



HAL
open science

Design of an LVDC grid based on renewable energy sources and multiple types of electrochemical storage elements

Kolja Neuhaus

► **To cite this version:**

Kolja Neuhaus. Design of an LVDC grid based on renewable energy sources and multiple types of electrochemical storage elements. Electric power. Université Paul Sabatier - Toulouse III, 2018. English. NNT: 2018TOU30306 . tel-02080092v2

HAL Id: tel-02080092

<https://laas.hal.science/tel-02080092v2>

Submitted on 6 Mar 2020

HAL is a multi-disciplinary open access archive for the deposit and dissemination of scientific research documents, whether they are published or not. The documents may come from teaching and research institutions in France or abroad, or from public or private research centers.

L'archive ouverte pluridisciplinaire **HAL**, est destinée au dépôt et à la diffusion de documents scientifiques de niveau recherche, publiés ou non, émanant des établissements d'enseignement et de recherche français ou étrangers, des laboratoires publics ou privés.



THÈSE

En vue de l'obtention du DOCTORAT DE L'UNIVERSITÉ DE TOULOUSE

Délivré par l'Université Toulouse 3 - Paul Sabatier

Présentée et soutenue par
Kolja NEUHAUS

Le 13 décembre 2018

**Conception d'un réseau LVDC à base de sources d'énergie durable
et de plusieurs types d'éléments de stockage électrochimiques**

Ecole doctorale : **GEET - Génie Electrique Electronique et Télécommunications :
du système au nanosystème**

Spécialité : **Génie Electrique**

Unité de recherche :

LAAS - Laboratoire d'Analyse et d'Architecture des Systèmes

Thèse dirigée par

Corinne ALONSO et Pierre Louis TABERNA

Jury

M. Alexandre DE BERNARDINIS, Rapporteur
M. Jean Paul FERRIEUX, Rapporteur
M. Georges DA COSTA, Examineur
M. Masakazu SUGIYAMA, Examineur
M. Mamadou-Bailo CAMARA, Examineur
M. Bruno ESTIBALS, Examineur
Mme Corinne ALONSO, Directrice de thèse
M. Pierre-Louis TABERNA, Co-directeur de thèse

ACKNOWLEDGEMENTS

Before going into the details of this Ph.D. thesis, I would like to express my thanks to a number of people without whom I would not have been able to accomplish the work described in this manuscript.

Firstly, I would like to express my sincere gratitude to my advisor Prof. Corinne ALONSO for the continuous support of my Ph.D. study and related research, and her immense knowledge; but also for her kindness, for her patience, her guidance and the motivation she has been able to provide to myself and other Ph.D. students. I could not have imagined having a better advisor and mentor for my Ph.D. study.

My sincere thanks also goes to Dr. Pierre-Louis TABERNA for his support as my co-advisor, for his kindness and for the immensely valuable insight he has given me in the field of battery storage as well as for permitting a healthy collaboration between the CIRIMAT and LAAS laboratories in this study.

Besides my advisors, I would like to thank the rest of my thesis committee: Prof. Jean Paul FERRIEUX, Prof. Masakazu SUGIYAMA, Prof. Bruno ESTIBALS, Dr. Alexandre DE BERNARDINIS, Dr. Georges DA COSTA and Dr. Mamadou-Bailo CAMARA for their insightful comments and encouragement, but also for the hard questions which incited me to widen my research from various perspectives.

I would like to express my sincere thanks to Prof. Marie-Pierre GLEIZE and to the entirety of the people participating in the NEOCAMPUS project. This project for an ecological, modern and connected renovation of the campus of Toulouse was a positive drive to my Ph.D. study and gave me an insight into the organization of wide spanning collaborations including multiple labs, industrials and students.

I thank all my fellow labmates for the stimulating discussions, the resourceful collaborations, and for all the fun we have had in the last four years. In particular, I am grateful to Ilias PAPAS for being the greatest office colleague that I could have imagined, and to Dr. Michael BRESSAN for enlightening me the first glance of research.

Last but not the least, I would like to thank my parents and my sister as well as my girlfriend for supporting me spiritually throughout writing this thesis and in my life in general.

TABLE OF CONTENTS

| | |
|---------------------|----------|
| INTRODUCTION | 7 |
|---------------------|----------|

| | |
|-------------------------------------|-----------|
| CHAPTER 1 : Energy and grids | 11 |
|-------------------------------------|-----------|

| | |
|---|-----------|
| 1.1. Solar energy production | 11 |
| 1.1.1. Solar Energy | 11 |
| 1.1.2. Photovoltaic systems | 12 |
| 1.1.3. Concentrated thermal solar power | 15 |
| 1.2. Energy storage | 17 |
| 1.2.1. Mechanical storage | 17 |
| 1.2.2. Thermal storage | 19 |
| 1.2.3. Electrochemical storage | 20 |
| 1.2.4. Chemical storage | 22 |
| 1.3. Microgrids | 22 |
| 1.4. LVDC grids | 23 |
| 1.5. Conclusion | 25 |

| | |
|--|-----------|
| CHAPTER 2 : Photovoltaic production and electrochemical storage | 29 |
|--|-----------|

| | |
|--|-----------|
| 2.1. Introduction | 29 |
| 2.2. PV and buildings: BIPV | 30 |
| 2.3. Modeling PV production | 36 |
| 2.3.1. Design of Solar Irradiation Model | 36 |
| 2.3.2. PV Energy Production | 37 |
| 2.4. Clustering of PV production data, the case of ADREAM | 42 |
| 2.4.1. Clustering daily power data using K-medoids algorithm | 42 |
| 2.4.2. Example of data treatment for the production and consumption profiles of the ADREAM BIPV. | 44 |
| 2.5. Instrumentation and specifications for the study of electrochemical storage elements | 46 |
| 2.5.1. Instrumentation for battery testing: | 46 |
| 2.5.2. Battery specifications: | 48 |
| 2.6. Studied electrochemical storage technologies | 49 |
| 2.6.1. Lead acid batteries | 50 |
| 2.6.2. Lithium iron phosphate batteries | 54 |
| 2.6.3. Lithium-ion Polymer batteries | 57 |
| 2.6.4. Lithium supercapacitor LIC chemical hybrid | 59 |
| 2.7. Modeling methodology for various electrochemical storage elements | 67 |
| 2.7.1. Open circuit voltage V_{oc} | 68 |
| 2.7.2. Internal resistance R | 69 |
| 2.7.3. Complete model | 70 |

| | |
|------------------------|-----------|
| 2.8. Conclusion | 72 |
|------------------------|-----------|

CHAPTER 3 : HYDROGEN AS A VECTOR OF ENERGY **75**

| | |
|---|------------|
| 3.1. Why Hydrogen? | 75 |
| 3.1.1. History | 76 |
| 3.1.2. Characteristics | 76 |
| 3.1.3. Usages of Hydrogen | 77 |
| 3.2. Hydrogen applications | 78 |
| 3.2.1. The automobile | 78 |
| 3.2.2. Space application | 81 |
| 3.2.3. Aeronautics | 82 |
| 3.2.4. Hydrogen uses in the industry | 83 |
| 3.3. Hydrogen storage | 83 |
| 3.3.1. High pressure gas Hydrogen | 84 |
| 3.3.2. Liquid Hydrogen storage | 85 |
| 3.3.3. Solid Hydrogen storage | 86 |
| 3.4. Hydrogen production through electrolysis | 86 |
| 3.4.1. Water electrolysis | 87 |
| 3.4.2. Alkaline Electrolysis: | 88 |
| 3.4.3. Acid Proton Exchange Membrane (PEM) electrolysis | 89 |
| 3.4.4. High temperature solid oxide electrolysis cell (SOEC) | 90 |
| 3.5. Cost of Hydrogen produced from electrolysis | 91 |
| 3.6. Solar Fuel: producing hydrogen from solar energy | 93 |
| 3.7. Electrolyzer study | 97 |
| 3.7.1. Experimental testing of electrolyzer cells | 98 |
| 3.8. Modeling of the Electrolyzer cell | 101 |
| 3.8.1. Automated identification with ZFitGUI: | 103 |
| 3.8.2. Manual parameter identification using ZFitGUI: | 104 |
| 3.8.3. Development of a precise manual parameter identification tool: SpecificFit | 106 |
| 3.8.4. Relation between each parameter and the voltage | 108 |
| 3.9. CONCLUSION | 109 |

CHAPTER 4 : Design of a LVDC microgrid for solar to hydrogen conversion **113**

| | |
|--|------------|
| 4.1. The joint H24 hydrogen production by CPV project | 114 |
| 4.2. LVDC synoptic dedicated to hydrogen production | 115 |
| 4.3. Triple junction high efficiency photovoltaic panels | 116 |
| 4.4. Distributed micro-boost converter architecture for CPV and command | 120 |
| 4.4.1. Boost converter design | 120 |

| | | |
|--|---|------------|
| 4.4.2. | Command circuits: | 122 |
| 4.4.3. | MPPT Command algorithm: | 126 |
| 4.4.4. | PCB design | 127 |
| 4.5. | Distributed micro-buck converter architecture for electrolyzer cells | 129 |
| 4.5.1. | Buck converter design | 129 |
| 4.5.2. | Simulation with ideal components: | 130 |
| 4.5.3. | Simulation with real components: | 131 |
| 4.5.4. | Synchronous Buck converter: | 131 |
| 4.5.5. | Command circuits: | 132 |
| 4.5.6. | Voltage Control Algorithm | 135 |
| 4.6. | Lithium-Carbon supercapacitor storage | 138 |
| 4.6.1. | Storage Sizing: | 138 |
| 4.7. | Conclusion | 140 |
| General Conclusion and Perspectives | | 144 |
| Table of Figures | | 148 |
| ANNEXES | | 152 |

INTRODUCTION

Maintaining quality of life with a good development of society implies drastic changes on each part of the energy provision sector, meaning energy production, energy transport, energy consumption and energy storage.

Historically, the most part of energy provision and distribution has been, organized in a vertical structure from producers to consumers. Public utilities, differentiating generation, transmission, distribution and supply steps are in charge of this type of transfer. This system was targeting to minimize the total system cost by exploiting economies of scale for each step, resulting in construction of large generation plants to be located near to primary fuel sources or near large industrial customers. The first oil crisis in 1973 induced a change in global awareness concerning the security and quality of energy supply as well as the imperative need to diversify the energy vector toward other sources. In this context of large centered energy production, the whole energy distribution was created to match loads to the generation, meaning that produced energy had to be consumed at all times and grids have been designed to transport energy from generation plants to consumers. In addition, grid operators have been lacking detailed knowledge of customer load profiles due to lack of smart metering technologies and therefore were only able to adapt consumption to production. In this period, some social influence factors such as high quality service expectations and environmental awareness were not as important as nowadays. As the general demographic, economic and technologic resource abundancy situations are changing progressively, the energy grids and its different uses must be adapted, taking into account new constraints. For example, by fixing objectives of developing energetic autonomy in specific States, to decrease pollutions in megalopolis progressively replacing fossil energies by sustainable ones.

In the years 2000, new systems based on high rates of renewable energies needed to break down existing monopoly structures on the energy markets. The previously vertical energy supply chain needed reorganization. In this new context, every element in the supply chain except grid operation could be subject to competition between different economic actors. On the production side, many different companies have their own energy production that can be issued from many decentralized sources. Even the consumer himself can supply energy to the general grid. On the consumer side, the choice of the energy provider is free. New uses such as self-production or self-consumption become viable options in the context of high rate of decentralized energy production, made possible by technology advances. The development of sustainable distributed generation such as photovoltaic systems, small hydraulic, wind turbines, small combined heat/power plants or solar thermal systems are an opportunity for carbon dioxide reduction and security of energy supply. But they also introduce new technological challenges, in particular the integration of a large quantity of small and intermittent energy sources in the existing grid, thus threatening the quality of energy supply and even in some cases the grid stability. Bidirectional energy flows in grids have been progressively introduced to handle local excess generation or economical billing problematics based on energy

provenance. In parallel, self-consumption and therefore uses of autonomous local networks have been developed to propose alternative solutions to classical grids.

In response to these challenges, the structure of energy grids has to be redesigned from a unidirectional system structure to a more interactive one where production and consumption can be mitigated at local levels if needed. Usage of new technologies such as smart sensors, digital data gathering and analysis, emerging electronic converters and commands [1] must constitute the core of future smart energy grids. Perfect matching of both energy production and consumption in quantity and quality could be coupled with appropriate controlled bidirectional grid structures. These key points allow the development of smart grids, responding to the overall and international necessity to reduce energy losses and using energy in its most primary form. For this purpose, along with technological advancement in electrical converters, new types of grid structures such as the LVDC grid emerge to minimize the number of conversion stages between energy production and local consumption. However, local grid structures such as LVDC or LVAC with a large rate of sustainable sources necessitate energy storage devices such as batteries which behave as buffers, storing intermittent energy produced. These grids could be isolated or interconnected to others. Consequently, combining production, storage, distribution and consumption in order to achieve an improvement in energy management is a real design challenge.

This thesis work was mostly carried out in the LAAS laboratory, more specifically in the ISGE team, given the great expertise and experience of the supervising team in the fields of photovoltaics, distributed microgrids and the full-scale experimental platform ADREAM. This research is financed through a larger academic project named NeoCampus, which aims for the development of a more durable and connected campus for the Université Paul Sabatier in Toulouse. NeoCampus is a major project including several laboratories of complementary scientific fields in order to tackle the different scientific and technological challenges for sustainable development. A collaboration with the RTS team of the CIRIMAT did emerge from this framework, mainly focusing on energy storage.

Furthermore, this work contributes to the international collaboration between the LAAS and the RCAST laboratories in the framework of the international associated laboratory CNRS NextPV. In fact, both teams decided to associate in the conception of a new high performance “Solar Fuel” system capable of continuous production of Hydrogen through the incorporation of storage elements.

The first chapter of this thesis sets the global energy context and the current state of solar electricity production with a particular focus on energy aiming to be injected in a power grid.

Chapter two is dedicated to the Building Integrated Photovoltaic (BIPV) problematic that is specific to the LAAS laboratory. Experimental resources are presented, including big data for photovoltaic production since 2012. The processing and the modeling of this data by using clustering methods to extract typical profiles helped us for the choice and study of specific storage elements adapted to BIPV applications. Using the experimental means available in the LAAS, several storage elements have been thoroughly studied in order to develop a generic equivalent circuit modeling methodology, while aiming towards the general study of the insertion of storage elements in grids.

In chapter three, the production and usage of Hydrogen in the energy sector is studied. In relation to the application chosen for the validation of this work, a focus is made on Hydrogen production through water electrolysis, modeling techniques for electrolyzers and specific tools that were elaborated for this purpose.

The fourth and last chapter of this thesis addresses the design and conception of the specific “Solar Fuel” microgrid application that is developed in collaboration with the RCAST.

CHAPTER 1 : Energy and grids

In the context of a global energy crisis as described in the introduction of this thesis, technological solutions are needed and researched in order to tackle these problems and try to build a better and more sustainable world for the future. The problematic of production, transport and consumption of energy today is one of the key factors in terms of the energy cost increases, overall availability of energy as well as its environmental and health related impact. Research for efficient alternatives that can see a short term implementation is of critical importance.

In this chapter, the major state of the art technologies used for renewable and durable solar energy production are presented. They are being developed as solutions to the energy crisis often associated to energy storage technologies able to cope with the intermittent nature of these sources to achieve stability and deliver quality energy supply. Several energy storages solutions including mechanical, thermal, electrochemical and chemical technologies that are used in the main grid are introduced. The development of micro-grids will be discussed as a tool for both renewable source integration and increasing energy efficiencies in energy provision. A focus is made particularly on LVDC grids linked to new applications with a majority of DC sources and DC loads

1.1. Solar energy production

1.1.1. Solar Energy

The sun is the most important source of energy for the earth, providing 174 petaWatt (PW) of incoming terrestrial solar radiation, resulting in an average solar irradiance of $I_0 = 1367 \pm 0.5$ W/m² outside of the atmosphere [2]. While this last value is often considered as a constant in solar radiation, it is in reality evolving for about 0.1 W/m² each year. Therefore it is readjusted every year through satellite measures. From this out of atmosphere solar radiation, around 30% is reflected by the atmosphere and 70% is absorbed by water and land masses. The part of the solar radiation that hits a given terrestrial surface is named solar producible. By measuring or estimating the solar producible in Watt per square meter (W/m²) in a specific area, it is possible to know how much power could theoretically be harvested from the sun in this zone and converted to electricity. Figure 1 shows a map representation of the solar irradiance levels on terrestrial surfaces from 2013.

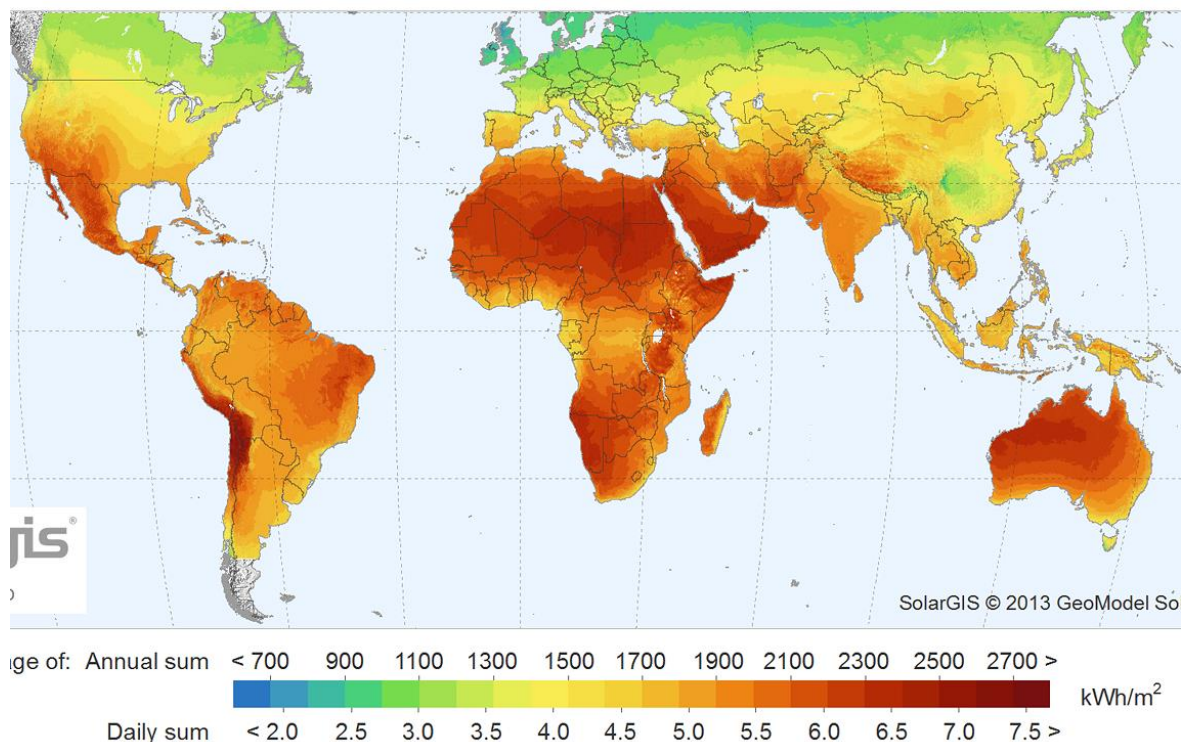


Figure 1: Map of the annual and daily solar irradiance on terrestrial surfaces in 2013 (Solargis)

A part of this incredible amount of energy represents a potential energy able to be harvested using either passive or active solar technologies. Passive solar technologies such as the positioning of a building, the construction materials used or the regulation of the airflow inside the building can increase the usage of the incoming solar radiation and its distribution. In this thesis, only active solar harvesting technologies for energy transformation and distribution have been studied.

Active solar technologies aim to convert solar energy into solar power by either transforming it into heat using thermodynamics or into electricity using the photovoltaic effect. These technologies include Photovoltaic systems (PV), concentrated solar power and solar water heating.

1.1.2. Photovoltaic systems

Closely related to the photoelectric effect, the photovoltaic effect corresponds to the excitation of an electron or another charge carrier to a higher energy state. When a photon is absorbed by a semi-conducting material such as silicon, its energy is transferred to an electron usually situated in the valence band [3]. If this energy is sufficient enough, the electron will pass into the conduction band, permitting it to move within the semiconducting material, resulting in the creation of a hole-electron pair. A hole-electron pair usually disappears spontaneously as electrons recombine with holes, but the recombination process can be reduced by creating a potential barrier, a static charge existing in a thin layer or junction. Electrical contacts are made by metal bases on the bottom of the cell and by metal grids on the top layer in order to allow maximal photon penetration. When these contacts are connected through an external circuit,

excess electrons from the n layer will flow through the circuit to recombine with the excess holes in the p layer, creating an electrical current. Figure 2 and Figure 3 show a schematic cross section of a standard silicon cell as well as a picture of a standard silicon panel.

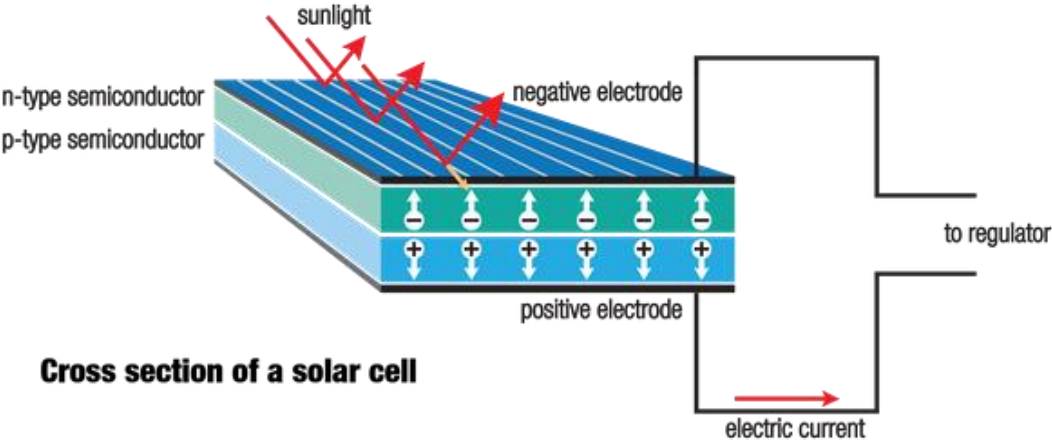


Figure 2: Cross section of a standard silicon solar cell [4]



Figure 3: Picture of a monocrystalline silicon PV cell [5]

Cell material, design and manufacturing methods come in many variations. Monocrystalline, Amorphous or polycrystalline silicon (Si), cadmium sulfide (CdS), gallium arsenide (GaAs) and others are used to produce photovoltaic cells.

While a silicon solar cell is considered having a good efficiency around 20% to 25% solar to electric power conversion with a theoretical maximum of 33.16% [6], higher efficiencies up to 46% [7] are obtainable by creating multi-junction photovoltaic cells. In this case, multiple p-n junctions made out of different semiconductor materials are created and stacked together. Each of the p-n junctions will be able to absorb photons in a specific wavelength of light, increasing the total wavelength range absorbed by the panel. Figure 4 shows an example of the different wavelength absorbed by a multi-junction solar cell.

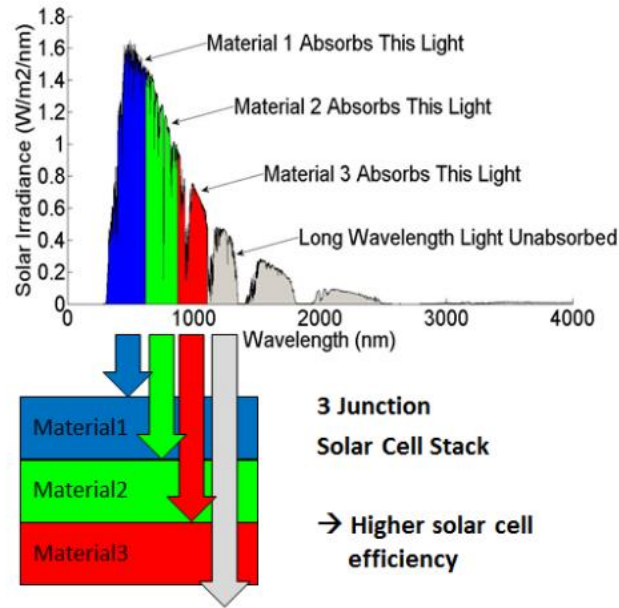


Figure 4: Schematic representation of the different Wavelength of the solar spectrum and their absorption through different materials in multi-junction PV cells [8]

In this example, Material 1 absorbs the lowest wavelength, transporting the highest power, while letting radiation in other wavelength travel through the material. Material 2 and Material 3 both absorb higher wavelength components, resulting in the absorption of an increased part of the total solar irradiance.

As the processes and materials used for this type of panels can be extremely expensive, they are manufactured in small surfaces (a few mm^2 to a few cm^2) for terrestrial applications and placed under concentrators such as Fresnel lenses in order to multiply the amount of incident solar radiation. Theoretically, an infinite number of junctions would have a limiting efficiency of 86.8% under highly concentrated sunlight [9]. In Japan, SUMITOMO Electric specializes in megawatt CPV installations worldwide in conjunction with solar trackers. Figure 5 shows a 1 MW CPV installation in Morocco build by this brand [10].



Figure 5: 1 MW CPV installation with trackers in Morocco, by SUMITOMO Electric

A study by NREL shown in Figure 6 presents the evolution of the best PV efficiencies achieved in research worldwide since 1975.

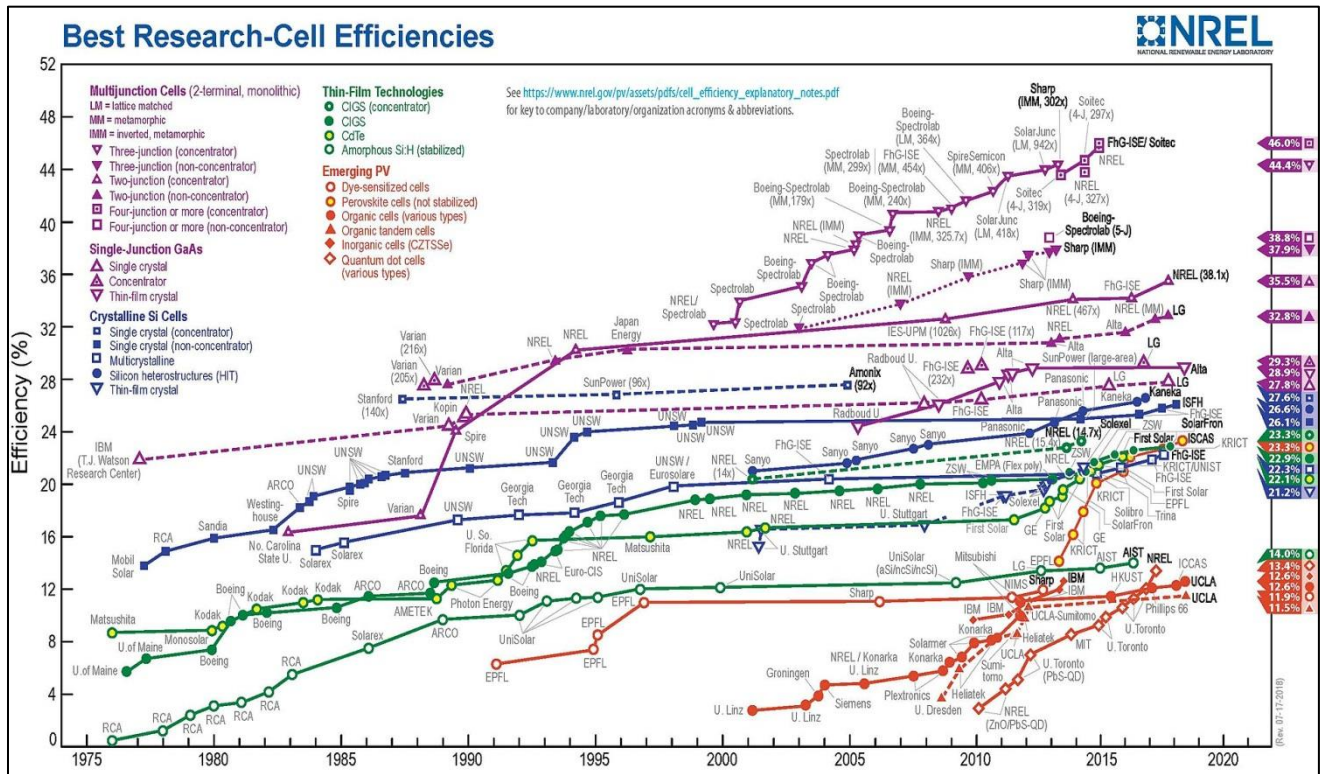


Figure 6: NREL study showing the best PV efficiencies achieved in research worldwide since 1975.

Solar PV systems generate no pollution and no greenhouse gas emission once installed, making them a good option for green energy generation. In addition, silicon is largely available on earth and PV systems show simple scalability in respect to power needs.

Compared to Hydro power and Wind power, PV power is the third renewable energy source in terms of total global capacity, with a total of over 390 GW installed worldwide in 2017 according to the international renewable energy agency (IRENA) [11].

1.1.3. Concentrated thermal solar power

Large areas of sunlight can be concentrated through mirrors or lenses focused on a small area via tracking systems. The concentrated light can be used directly as a source of heat or indirectly to produce solar thermoelectricity or both. Solar concentration can be achieved through parabolic trough, enclosed trough, Fresnel reflectors, dish-stirling and solar power towers.

Solar tower technology is based on flat mirrors placed on dual axis solar trackers and a central solar receiver on a high tower. A heat transfer fluid such as water-steam or molten salt is channeled through the receiver and heated at 500°C to 1000°C and used as a heat source for a thermoelectric system or directly as an energy storage. The major advantages of this technology are cheap maintenance as replacing mirrors is easy and high efficiency of the thermal processes. This type of technology can be adapted to special landscapes such as mountain flanks, offering

perfect relief for the mirrors as in the example shown in Figure 7 depicting the THEMIS solar thermal plant in the south of France that was inaugurated by EDF in 1982, also made compatible with pastures as cows are able to graze between the tracker devices.



Figure 7: THEMIS concentrated solar plant [12]

The solar furnace of ODEILLO, inaugurated in 1962 in southern France, Figure 8, is the world’s biggest solar furnace. This structure is used in order to achieve temperatures up to 3500°C at the focal point. While the ODEILLO system is mostly used for research in materials, this technology can also be used for energy production.



Figure 8: Concentrated solar Furnace ODEILLO, France [13]

As most of the installed renewable energy power, and especially solar power, is highly prone to meteorological intermittency, they are often paired with storage elements. The next part will

introduce the major energy storage technologies while solar intermittency will be further discussed in chapter 2.

1.2. Energy storage

An energy grid is a complex system that has to stay in a perfect balance in order to prevent power failures and blackouts. Energy grid managers need to be able to match precisely the supply of energy to the demand. Energy demand is predictable through statistics and general knowledge as there commonly is a higher demand in the evening when homes are powered and generally less demand on the weekend when industrial applications are less active. Historically, with a major part of fossil energy production such as coal or oil, energy demand could be matched hourly by turning the generators up or down precisely. Nuclear power, while using fossil uranium, has a very constant production with a slow inertia due to the chain reaction nature of the process and can only be turned up or down very slowly over several days. Therefore nuclear power production cannot be matched to demand and will sometimes produce too much energy and sometimes not enough. In order to balance energy in the grid, it is then necessary to either store the energy surplus or to activate additional on-spot production sources in order to compensate for the lack of energy.

With the highly needed increase of renewable energy production appears a new problem of energy balancing. The most used renewable energy sources are intermittent in nature as their production is based on meteorological conditions (such as solar irradiation). For this reason they are not reliable enough and impossible to match to the energy demand, energy storage is a necessity when using renewable sources.

A number of storage technologies exist that are each more adapted to certain types of applications or scales. These technologies can be classified into four groups which are mechanical storage, thermal storage, electrochemical storage and chemical storage.

1.2.1. Mechanical storage

Mechanical storage technologies make use of the potential gravitational force in order to keep a certain amount of energy available for later use.

The most widely used storage technology for large-scale grid balancing purposes is pumped storage Hydropower. Generators are used to pump water up into a reservoir when energy production is high and can be released in times of higher energy demand with lack of matching production. The working principle of a pumped storage installation is depicted in Figure 9.

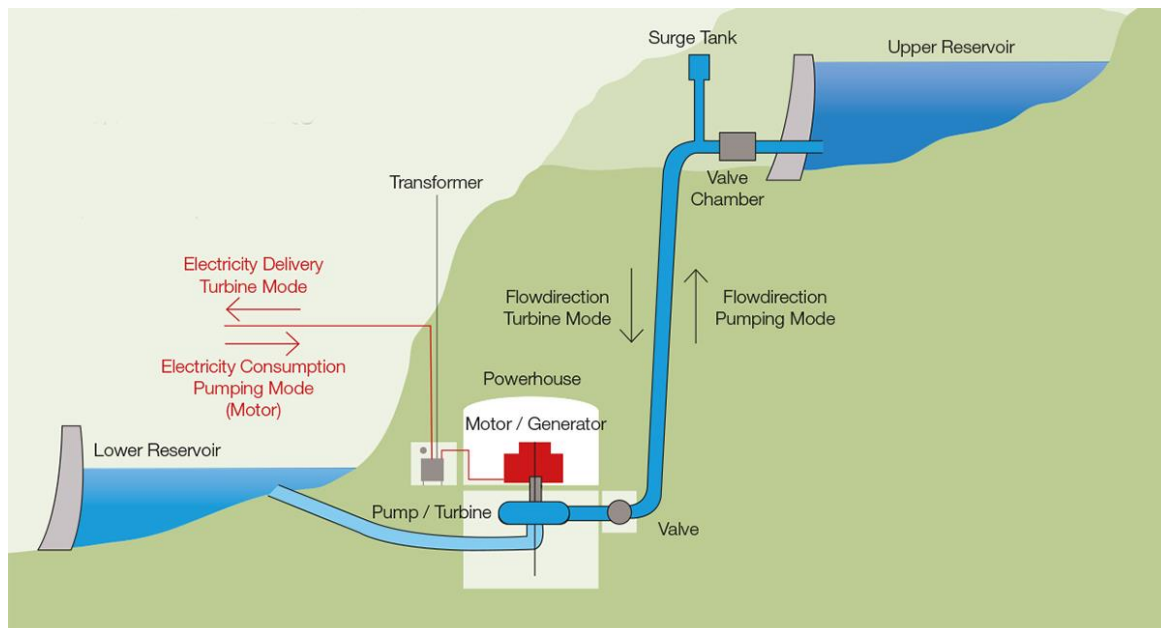


Figure 9: Schematic representation of the working principle of a pumped storage installation []

When energy is needed, the valves are opened and the water flows from the upper reservoir towards the lower reservoir, the turbine is activated by the water flow due to gravity. The generator is turned by the turbine and injects electrical energy into the grid through a transformer. When energy has to be stored, the electrical grid activates the motor, which in its turn activates the pump. Water is pumped up from the lower reservoir to the upper reservoir and is blocked there by the valves, storing its potential gravitational force for later use.

In France for example, where a majority of the energy comes from nuclear plants, six large pumped storage installations are used in order to provide up to 5GW of additional power in the evening when energy demand is high. The largest French pumped storage is the Grand'Maison Dam in the French Alps operated by EDF. It was made operational in 1985 and has an installed capacity of 1.8GW with a dam height of 140 m. It produces an annual average of 1.42 GWh of electrical energy and consumes an average of 1.72 GWh per year in pumping mode. As it can be activated within minutes, it is used as one of the biggest peak power sources in the country. A photograph of the Grand'Maison Dam is visible in Figure 10 below.



Figure 10: Picture of Grand'Maison Dam, the biggest pumped storage installation in France []

While Hydropower pump storage is a mechanical storage solution for large-scale grid energy storage, less conventional methods exist such as compressed air pumped into underground cavities or gravitational potential energy where the altitude of a solid mass increases for later usage of its potential gravitational energy. Flywheels are another example of mechanical storage but are commonly less used for renewable energy storage and more adapted for vehicles and trains. However, ENGIE and LEVISYS have recently installed a 10 kW flywheel as a storage for the regulation of energy flows in a smart grid in Toulouse [14].

1.2.2. Thermal storage

Energy can be stored by heating or cooling matter either using sensible heat or latent heat. Sensible heat storage describes the principle of storing energy into a certain matter by changing its temperature without changing all of its macroscopic variables like the volume or pressure. A multitude of materials can be used to store sensible heat such as salt mixtures, sands, crystalline bedrock or mixtures of gravel and water. This technology of heat storage is mostly used for Seasonal Thermal energy storage, where the materials are heated in the summer when excess energy from solar or wind power is more available and later used to heat water for usages in colder seasons. This is used for example in the Drake Landing solar community in Alberta, Canada [15], where thermal solar panels on building roofs produce thermal energy in the summer which is stored in a Borehole seasonal thermal storage tank underground to be used in the winter for heating as seen on the schematic in Figure 11 below.

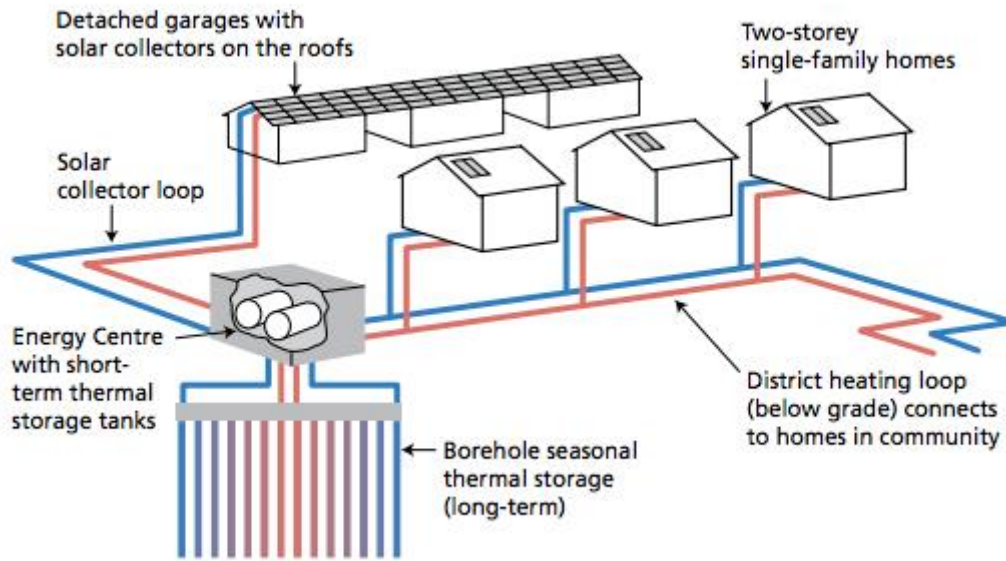


Figure 11: schematic of the thermal heating system installed in the Drake Landing Solar Community, Canada [15]

Latent heat energy storage uses thermal storage in matter without changing its temperature. This is possible when changing the phase of a mater from solid to liquid or from liquid to gas. Material with high latent heat capacity, known as phase change materials, are used for their capacity to store great amounts of energy in their phase change process and their ability to release this energy when changing back to their original state. For storage applications, these materials include inorganic systems (salt and salt hydrates), organic compounds such as paraffin or fatty acids and polymeric materials[16].

Naturally, given their thermal nature, these storage technologies are most adapted in applications using solar thermal energy production.

1.2.3. Electrochemical storage

According to the French research network on electrochemical energy storage RS2E [17], “Electrochemical energy storage is a method used to store electricity under a chemical form. This storage technique benefits from the fact that both electrical and chemical energy share the same carrier, the electron. This common point allows to limit the losses due to the conversion from one form to another.” Electrochemical storage devices exist in three different forms: rechargeable batteries, flow batteries and supercapacitors.

Rechargeable batteries, also called accumulators, store energy through a reversible electrochemical redox reaction. They are always composed of two metallic electrodes, a positive and a negative, separated by a liquid or solid electrolyte. Cell voltage is determined by the sum of the reduction potential and the oxidation potential of the electrodes. A multitude of sizes and shapes of accumulators exist, from small button cells to megawatt grid systems, and a large range of different materials can be used. The most renowned electrode and electrolyte materials are lead-acid, nickel-cadmium (NiCd), nickel-metal hydride (NiMH), Lithium-ion

(Li) and lithium-ion polymer (LiPo). During charging, the oxidization of the positive electrode's material produces electrons and the reduction of the negative electrode's material consumes electrons while the electrolyte serves either as a buffer for internal ion flow between electrodes like in Li-ion batteries or takes an active part in the reaction, as in lead-acid cells.

Flow batteries are rechargeable batteries where two fluids containing the active materials are pumped through a cell in order to promote redox reactions on both sides of an ion-exchange membrane, creating an electrical potential. Here, the electrodes are two different tanks containing active materials dissolved directly in the electrolyte. These mixtures are pumped into a compartment where a selective membrane permits the exchange of ions between the two liquids. This way, the energy and power components of the storage are separated and can be scaled independently. The cell capacity is function of the amount of electrolyte and the concentration of active ions while the power is function of electrode area within the cell. Common flow battery materials include Bromine-polysulfide, Vanadium-vanadium, Vanadium-Bromine, Zinc-Bromine and Zinc-cerium. Showing long service life, no standby losses and low maintenance, this technology is mostly used for long lifetime use in large scale applications due to the necessity of heavy installations (tanks, pumps, etc.). The charging and discharging of flow batteries is not affected by fluctuating power input and demand, making it a good choice for large photovoltaic or wind energy farms.

Supercapacitors are capacitors with very high capacitance values by combining electrochemical and electro-static principles, positioning them between electrolytic capacitors and rechargeable batteries. In fact, they can store ten to hundred times more energy per unit volume or mass than electrolytic capacitors, can accept and deliver charge much faster than batteries and tolerate an enormous number of charge and discharge cycles compared to rechargeable batteries. Supercapacitors use the double-layer effect [18] to accumulate ions on each of the two electrodes separated by an ion-permeable membrane (a separator) themselves separated via the electrolyte containing a mixture of positive and negative ions dissolved in a solvent. Applying a voltage at the electrochemical capacitors electrodes moves ions in the electrolyte to the opposite polarized electrode, forming a capacitive layer. Due to their high power density, supercapacitors can be used for applications needing large amounts of power with a high number of charge/discharge cycles. They are often used as a complement to rechargeable batteries to manage large power peaks and thus prolonging the battery lifetime by smoothing out the power profiles applied to them.

Recently, new types of electrochemical storage units named Lithium-ion capacitors (LIC) are being investigated. This technology combine the double layer storage principle of supercapacitors with the lithium ion electrode and electrolyte chemistry of lithium batteries. These specific elements show a better energy density than standard supercapacitors and are therefore investigated as hybrid storage elements accomplishing the role of current smoothing and energy storage in grids.

As we choose to use secondary batteries and Lithium capacitors for our studies, in the chapter 2 of this thesis, specific electrochemical storage elements are further described and analyzed as well as experimental setup and modeling techniques.

1.2.4. Chemical storage

Energy can be converted into both gaseous and liquid fuels through chemical reactions for being used as storage or as fuel in different types of engines. These processes are called power to gas and power to liquid.

Power to gas processes use the principle of water electrolysis, which is further detailed in chapter 3, in order to separate water into hydrogen and oxygen. Both of these gases can be stored and transformed again to electricity again via a fuel cell, but Hydrogen can also be used as a fuel in combustion systems. Combining the Hydrogen with carbon dioxide through a methanation reaction produces methane, which can be directly fed into the natural gas grid. Through partial reverse hydrogenation at high pressure and low temperature, methane can also be converted into Liquefied petroleum gas (GPT) also called propane or butane.

Power to liquid processes are similar to power to gas processes and can be achieved either through the methane route or the Fischer-Tropsch process [19].

In order to maximize efficiency of energy production, consumption and storage, new types of grid structures are emerging, combining all these technologies into microgrids.

1.3. Microgrids

As mentioned in the introduction of this thesis, starting in 2000 energy grids tend to integrate horizontal distribution methods instead of classical vertical distribution. With the growing need to integrate decentralized renewable energy sources, new types of local grids are emerging. By combining localized renewable energy sources, consumption and storage in micro-grid structures, the produced energy can be consumed or stored locally with minimal losses by applying control strategies.

While a number of definitions exist for microgrids, the Microgrid Exchange Group of the U.S. Department of Energy defines it as follows:

“[A microgrid is] a group of interconnected loads and distributed energy resources within clearly defined electrical boundaries that acts as a single controllable entity with respect to the grid. A microgrid can connect and disconnect from the grid to enable it to operate in both grid-connected or island mode [20].”

Micro-grids can be bi-directionally connected to the main grid through electronic converters in order to either inject excess energy production into the grid or to complement energy consumption at times when local production is not sufficient. They can also be isolated from the main grid or have the ability to be disconnected from the main grid. In the latter case, the interface with the main grid can be a synchronous AC connection with the advantage of simplicity or an asynchronous connection using a DC coupled electronic power converter [21], isolating the microgrid from the utility grid regarding power quality (frequency, voltage, harmonics).

Emerging from micro-grid development, the concept of the "Prosumer" was introduced as a new type of element in energy grids, defined by the U.S. department of energy [22] as an actor that is both an energy producer and an energy consumer. A Prosumer can be an industrial or public actor or even private housings, as long as they can communicate in a bi-directional way with a local micro-grid or the general grid directly.

In order to make bi-directionality possible and efficient, another key aspect of micro-grids is command and energy flow control. The energy exchanges inside of a micro-grid and between a micro-grid and the main grid must be managed in an optimal way. Data acquired through smart-metering technology is computed by either a centralized controller [23], which is able to determine an energy flow strategy based on fixed objectives, either in a decentralized manner with each resource responding to local conditions. Objectives can use multiple criteria such as maximizing self-consumption, optimizing cost efficiency and economic gains, minimizing general energy losses, maximizing grid energy input, and more while maintaining energy balance at all times[24],[25]. Chosen strategies can be implemented and applied through advanced converter command. A grid-connected microgrid must be presented to the main grid as a self-controlled entity providing frequency control [26], it has to be regulated in order to not exceed power line ratings, be able to maintain energy balance and to smoothly and safely connect and disconnect from the utility grid [27].

Micro-grids can be developed using different power scales and technologies depending on the application. With a goal to optimize energy efficiency, energy bus strategies and converter types must be adapted to production, consumption and storage parts of the micro-grid. As each stage of power conversion will induce energy losses depending on converter technology, dimensioning the right micro-grid bus for a given application is essential. Bus types vary in current (either AC or DC), low voltage (LV) or high voltage (HV). The choice of the bus type in a given micro-grid has to be compatible with its separate elements. An AC bus will be chosen for a micro-grid containing AC sources such as wind turbines and/or AC loads such as electrical motors. On the other hand, a DC bus will be preferred when the micro-grid contains DC sources such as PV panels and/or DC loads such as lighting or servers. The presence of storage elements can also take a significant part in the choice of the bus type as battery or supercapacitors act as both DC sources and loads.

Simulated, experimental and existent microgrid projects until 2016 are listed in the article [28], resuming conclusions from these project's experiences for future applications.

1.4. LVDC grids

As technology develops faster and faster, we now live in a DC world without realizing it as most of our commonly used electronic applications use direct current according to the International Electrotechnical Commission (IEC) [29]. Battery driven devices such as multimedia, mobile phones, LED lighting, electric vehicles, IT equipment and even electrical equipment using motors such as washing machines, fridges and fans being more and more equipped with DC motors are all DC loads. Ironically, many devices are sold and delivered

with AC/DC adapters to be used with standard AC wall sockets. In addition, as mentioned in part 1.4, a number of distributed renewable energy production technologies produce energy in DC. With the growing number of solar panels on roofs, small wind or micro-hydro turbines, electricity can be generated as close as possible to where it is consumed. Currently, these DC sources have their electricity converted to AC to be transferred through AC grids and transformed back into DC when being fed to the previously described electronic applications. This back and forth transformation induces unneglectable energy losses which could be reduced through the usage of DC microgrids.

A microgrid where the main power bus is using direct current and low voltage is defined as an LVDC microgrid. In DC, low voltage is defined as voltage levels below 1500 VDC, which is the limit for electrical arcing. It is to be noted that between 120 VDC and 1500 VDC, the risk of electric shock is still present but an LVDC bus functioning below 120V is considered low risk. As these standard definitions of voltage levels are existent, they need to be expanded to take into account new technological applications such as LVDC grids containing battery storage. In fact, battery voltage depends on the state of charge (SOC). The voltage of an LVDC bus based on battery storage can therefore have a changing voltage level inside of a specific range. The voltage ranges for LVDC microgrids per application type according to the IEC are described in Table 1 below.

Table 1: Voltage levels per application types in LVDC grids

| | |
|--------------|---|
| 3,6 – 5 V | Mobile phone charging (USB) |
| 9 V | Battery |
| 12 V | Car battery, lighting, indoor farming |
| 24 – 36 V | Electric scooters, electric bikes, high-power cordless tools, truck battery |
| 48 V | Telecom power and power over Ethernet |
| 400 V | Data centres, office buildings, hospitals, EV fast charging |
| Up to 1500 V | Urban railways |

Changing DC voltage levels is made easy today by using efficient DC/DC power converters, inducing significantly lower losses than AC/DC conversion. They also introduce the possibility for advanced and easily implementable control through the usage of solid state switching devices, paving the way for increasingly more intelligent power distribution systems.

For DC applications, other safety areas also have to be examined and developed further such as overvoltage protection, overcurrent protection, fault detection, corrosion, earthing, arcing and even digital protection, making the development of LVDC microgrids challenging [30]–[33].

1.5. Conclusion

As we have seen in this chapter, energy grids are evolving towards horizontally interconnected local microgrid structures. At the same time, the amount of renewable energy production that can be integrated into these grids is increasing thanks to the integration of storage technologies and improved control. As the first experimental applications are being conducted, one of the main conclusions to be heard from the scientific community is the ongoing need for knowledge of the interaction between renewable energy production, storage, loads and microgrids. In this specific context, this thesis work aims to contribute to the field of microgrid applications for a world with more renewable energy.

The ADREAM platform in the LAAS-CNRS laboratory is studied as an example of Building Integrated PV production that can be used as a basis for the modeling of PV producible and production as well as a load for microgrid applications in buildings. Through a partnership with the laboratory CIRIMAT, the question of the choice of electrochemical storage elements for microgrids has been discussed. In fact, researchers in the field of electrochemistry have a need for insight into specific applications of storage technologies applied to renewable energy and their impacts. This part of the thesis work is described in chapter two.

REFERENCES

- [1] B. Wang, M. Sechilariu, et F. Locment, « Intelligent DC Microgrid With Smart Grid Communications: Control Strategy Consideration and Design », *IEEE Transactions on Smart Grid*, vol. 3, n° 4, p. 2148-2156, déc. 2012.
- [2] J. A. Duffie et W. A. Beckman, *Solar Engineering of Thermal Processes: Duffie/Solar Engineering 4e*. Hoboken, NJ, USA: John Wiley & Sons, Inc., 2013.
- [3] J. Nelson, *The physics of solar cells*. London : River Edge, NJ: Imperial College Press ; Distributed by World Scientific Pub. Co, 2003.
- [4] en.stonkcash.com, « How Does Solar Energy Converted To Electricity », *Ace Energy*. [Online]: <http://en.stonkcash.com/how-does-solar-energy-converted-to-electricity/>. [11-nov-2018].
- [5] « Solar Energy Technologies Office | Department of Energy ». [Online]: <https://www.energy.gov/eere/solar/solar-energy-technologies-office>. [11-nov-2018].
- [6] S. Rühle, « Tabulated values of the Shockley–Queisser limit for single junction solar cells », *Solar Energy*, vol. 130, p. 139-147, juin 2016.
- [7] F. Dimroth *et al.*, « Four-Junction Wafer-Bonded Concentrator Solar Cells », *IEEE Journal of Photovoltaics*, vol. 6, n° 1, p. 343-349, janv. 2016.
- [8] « Solar Junction » Technology ». [Online]: <http://www.sj-solar.com/technology/>. [12-nov-2018].
- [9] M. A. Green, Éd., « Tandem Cells », in *Third Generation Photovoltaics: Advanced Solar Energy Conversion*, Berlin, Heidelberg: Springer Berlin Heidelberg, 2003, p. 59-67.
- [10] « Sumitomo Electric Starts Operation of Concentrator Photovoltaic Power Generation Pilot Plant | Press Release | Company Information | Sumitomo Electric Industries, Ltd ». [Online]: <https://global-sei.com/company/press/2016/11/prs103.html>. [11-nov-2018].
- [11] « Renewable Capacity Statistics 2018 ». [Online]: <http://www.irena.org/publications/2018/Mar/Renewable-Capacity-Statistics-2018>. [08-oct-2018].
- [12] « Themis - PROMES ». [Online]: <https://www.promes.cnrs.fr/index.php?page=themis>. [11-nov-2018].
- [13] « Odeillo - PROMES ». [Online]: <https://www.promes.cnrs.fr/index.php?page=odeillo>. [11-nov-2018].
- [14] « CP_Stockage_Energie_Smart_Grid_Toulouse.pdf ». .
- [15] « Drake Landing Solar Community ». [Online]: <https://www.dlsc.ca/>. [11-nov-2018].
- [16] K. Pielichowska et K. Pielichowski, « Phase change materials for thermal energy storage », *Progress in Materials Science*, vol. 65, p. 67-123, août 2014.
- [17] « Energy RS2E », *Energy RS2E*. [Online]: <http://www.energie-rs2e.com/en>. [19-oct-2018].
- [18] S. Bi *et al.*, « Molecular Insights into Electrical Double Layers in Graphene-Based Supercapacitors », *Nano-Micro Conf.*, vol. 1, n° 1, p. 01022, oct. 2017.

- [19] A. de Klerk, « Fischer–Tropsch Process », in *Kirk-Othmer Encyclopedia of Chemical Technology*, American Cancer Society, 2013, p. 1-20.
- [20] D. T. Ton et M. A. Smith, « The U.S. Department of Energy’s Microgrid Initiative », *The Electricity Journal*, vol. 25, n° 8, p. 84-94, oct. 2012.
- [21] A. Hirsch, Y. Parag, et J. Guerrero, « Microgrids: A review of technologies, key drivers, and outstanding issues », *Renewable and Sustainable Energy Reviews*, vol. 90, p. 402-411, juillet 2018.
- [22] « Consumer vs Prosumer: What’s the Difference? », *Energy.gov*. [Online]: <https://www.energy.gov/eere/articles/consumer-vs-prosumer-whats-difference>. [19-oct-2018].
- [23] A. Kaur, J. Kaushal, et P. Basak, « A review on microgrid central controller », *Renewable and Sustainable Energy Reviews*, vol. 55, p. 338-345, mars 2016.
- [24] D. E. Olivares *et al.*, « Trends in Microgrid Control », *IEEE Transactions on Smart Grid*, vol. 5, n° 4, p. 1905-1919, juill. 2014.
- [25] Z. Shuai *et al.*, « Microgrid stability: Classification and a review », *Renewable and Sustainable Energy Reviews*, vol. 58, p. 167-179, mai 2016.
- [26] J. M. Guerrero, P. C. Loh, T. Lee, et M. Chandorkar, « Advanced Control Architectures for Intelligent Microgrids—Part II: Power Quality, Energy Storage, and AC/DC Microgrids », *IEEE Transactions on Industrial Electronics*, vol. 60, n° 4, p. 1263-1270, avr. 2013.
- [27] O. Palizban, K. Kauhaniemi, et J. M. Guerrero, « Microgrids in active network management – part II: System operation, power quality and protection », *Renewable and Sustainable Energy Reviews*, vol. 36, p. 440-451, août 2014.
- [28] L. Mariam, M. Basu, et M. F. Conlon, « Microgrid: Architecture, policy and future trends », *Renewable and Sustainable Energy Reviews*, vol. 64, p. 477-489, oct. 2016.
- [29] « Brochure: LVDC: another way – en – IEC Basecamp ». .
- [30] A. Makhe, V. Bugade, S. Matkar, et P. Mothe, « Digital protection of LVDC and integration of Distributed generation », in *2016 International Conference on Energy Efficient Technologies for Sustainability (ICEETS)*, 2016, p. 942-946.
- [31] P. Nuutinen *et al.*, « LVDC rules – technical specifications for public LVDC distribution network », *CIREN - Open Access Proceedings Journal*, vol. 2017, n° 1, p. 293-296, 2017.
- [32] D. Wang, A. Emhemed, P. Norman, et G. Burt, « Evaluation of existing DC protection solutions on an active LVDC distribution network under different fault conditions », *CIREN - Open Access Proceedings Journal*, vol. 2017, n° 1, p. 1112-1116, 2017.
- [33] L. Li, J. Yong, L. Zeng, et X. Wang, « Investigation on the system grounding types for low voltage direct current systems », in *2013 IEEE Electrical Power Energy Conference*, 2013, p. 1-5.
- [34] US Department of Energy, *Buildings Energy Data Book*. 2011.

CHAPTER 2 : Photovoltaic production and electrochemical storage

2.1. Introduction

In the context of the evolution of the energy distribution grid and the growing integration of renewable energy sources described in chapter one, a specific focus can be made on buildings such as domestic homes or Buildings for tertiary, industrial or logistics use. As large scale production and distribution struggles to compensate constant growing energy demand, energy savings must be made at each scale.

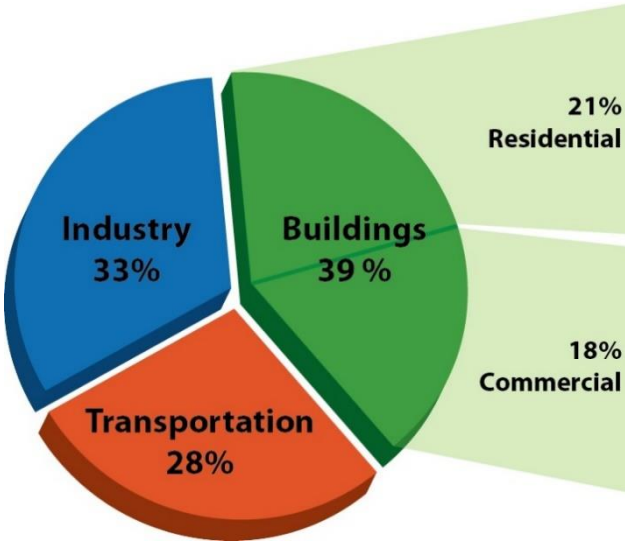


Figure 12: Distribution of energy consumption per activity sector (US department of energy)[34]

According to the U.S. department of energy, buildings are responsible for about 40% (Figure 12) of the global energy consumption. They represent one of the primary targets of world policies that aim to reduce energy consumptions. The final objective is the achievement of energy savings in the order of 25% by 2030 [35]. The concept of a net Zero Energy Building (ZEB) was defined in the scientific literature by 2006, but it had not been concretely translated into laws and norms, until the National Renewable Energy Laboratory (NREL) proposed some preliminary definitions in 2006 [36]. In 2009, Aalborg University expanded this concept with a state of the art synthesis of ZEB definitions [37]. Recent demonstrators tried to achieve a zero net energy consumption target over one-year-cycles. These demonstrations implied that the energy demand for heating and electrical consumption must be minimized. The reduced demand should be completely met by its own annual production of renewable energy [38][39]. Among the different renewable energy sources, solar energy has a high potential of exploitability due its wide availability.

Technological and structural drawbacks limit the development of this type of buildings. The main difficulty lies on the accurate evaluation of consumption (energy meters) and their impact

on environment (CO₂ emissions). The reliability of renewable sources is another major issue, as well as the insufficient knowledge of adapting their usage to building integrated systems (limited space, problematic thermal effects, high costs, and system complexity). In 2015, the International Energy Agency edited a report about different energy performance metrics and their evolution between 2000 and 2012 based on two scenarios of consumption and greenhouse emission reduction by 2025 [40].

In order to achieve the objective of an autonomous or positive energy building, the choice of the renewable sources depends on the availability of local energy resources. In this context, solar irradiation provides several suitable uses (solar heating, natural lighting, photovoltaic energy production). Since 1999, demonstrations of Building-Integrated Photovoltaics (BIPV) appear as a ZEB solution [41][42].

Smartgrid structures comprising renewable energy production and storage elements, as described in the previous chapter, can be adaptable to buildings in order to move towards ZEB standards. In addition to energy consumption optimization through thermal and electrical engineering, a better understanding of building integrated production and storage elements adapted to buildings is necessary. In this chapter, the ADREAM building and research facility in LAAS-CNRS is introduced. It was designed as a BIPV research platform for concept validation and development of new ZEBs. The PV production of the building's integrated Photovoltaic panels will be studied and then modeled through an estimation of solar radiation on its different surfaces. Followed by the description of a clustering method for the building's production and consumption data to define typical profiles in particular to better describe the intermittent behaviors. This research is useful for the design and sizing of energy storage elements in buildings. Different battery technologies that have been studied in the LAAS using a specific test bench dedicated to battery cycling. The main experimental results obtained by cycling will be described in this chapter as well as a methodology I have used to identify parameters of storage elements independently of their technologies. This flexible and reliable modeling methodology for electrochemical storage elements will be presented for usage in microgrid and ZEB applications.

2.2. PV and buildings: BIPV

Photovoltaic panels on buildings are usually installed on top of existing surfaces such as roofs or terraces using adapted structures. In the 1990s, Photovoltaic construction products made for direct integration as part of the building's structure were commercialized [43]. By using photovoltaic panels directly as parts of a building's structure, the concept of Building Integrated Photovoltaics, BIPV was created. The most used BIPV technologies today are crystalline silicon panels for rooftops or terraces, amorphous crystalline silicon panels for glass curtains or transparent skylight, and square crystalline silicon cells placed inside double or triple glass windows. Applications vary in a very wide range, from standard roof integration to photovoltaic windows, full scale building facades or vertical photovoltaic walls. A Dutch company even patented solar roof tiles in 2012 [44], which looks and acts like a regular roof tile in addition to producing electrical energy and inspired a similar product by renown company Tesla [45].

The ADREAM (French acronym for Embedded Reconfigurable Dynamic Autonomous and Mobile Architectures) building of LAAS-CNRS was inaugurated in 2012 [42]. Comprising a large surface of BIPV systems including roof, terrace, façade and vertical walls, it can be used as an experimental platform to validate numerous concepts on Smart Grids, micro-grids, as well as on Ambient Physical Cyber Systems. Figure 13 provides an aerial view of the building ADREAM, showing the totality of its BIPV surface.



Figure 13: Aerial view of the ADREAM building in LAAS-CNRS

Four different surfaces of the building are covered in photovoltaic panels, for a total PV power of 100 kW peak. Individual PV panels are grouped into strings which are each connected to a single inverter. For the purpose of clarity, a string of panels grouped with a converter will be called a PV system for the rest of this study. Details on the specific surfaces and PV system equipment are given in Table 2.

Table 2: Overview of ADREAM PV systems

| Placement (Angle) | PV Module (η) | Power (kWp) | Inverters (η) |
|-------------------------|---|-------------|---------------------------|
| Accessible Roof (45°) | TE2200 250Wc (15.9%) | 17.2 | 4 × 2.5kW TENESOL (94.6%) |
| | | | 1 × 5kW TENESOL (94.6%) |
| | | | 1 × 3.3kW TENESOL (94.8%) |
| Cladding (90°) | TE2200 250Wc (15.9%) | 13.4 | 2 × 6kW SMA (95.3%) |
| | | | 1 × 2.1kW SMA (95.2%) |
| Inaccessible Roof (10°) | TE2200 250Wc (15.9%) | 24 | 3 × 5kW TENESOL (94.6%) |
| | | | 3 × 2.5kW TENESOL (94.6%) |
| Facade (60°) | Double or Triple glazing PV cells (14.3%) | 38 | 6 × 5kW SMA (95.3%) |
| | | | 3 × 2.1kW SMA (95.2%) |

The solar cells used in this building are crystalline silicon cells from the brand TENESOL. Their datasheet is available in ANNEX 1. While panels are used as is on the roof and terrace surfaces (Figure 14), the separate cells are directly integrated inside of double and triple glazing for the façade and window surfaces as seen in Figure 15.



Figure 14: Regular crystalline silicon PV cells installed on the terrace and walls of the ADREAM building



Figure 15: Double and triple glazing PV façade of the ADREAM building

Today, ADREAM is entirely monitored through a large sensor network, which includes a meteorological station. The acquisition of multiple years of production and consumption data allows the extensive examination of the building's functioning, as well as its ongoing optimization. This process relies on a large amount of data (thermal, electrical, air quality, comfort, lighting, etc.) being stored every day in the platform's database through 6500 sensors. The database is accessible through a supervision tool (Figure 16) as well as a web interface inside of the laboratory. Specific data can be extracted for further studies.



Figure 16: ADREAM's supervision tool, user interface

Figure 17, Figure 18 and Figure 19 show the measured data for PV energy production for the years 2014, 2015, and 2016 respectively, with a sampling period of one hour. In addition, the same data sets with a sampling period of one day are represented in ANNEX 2.

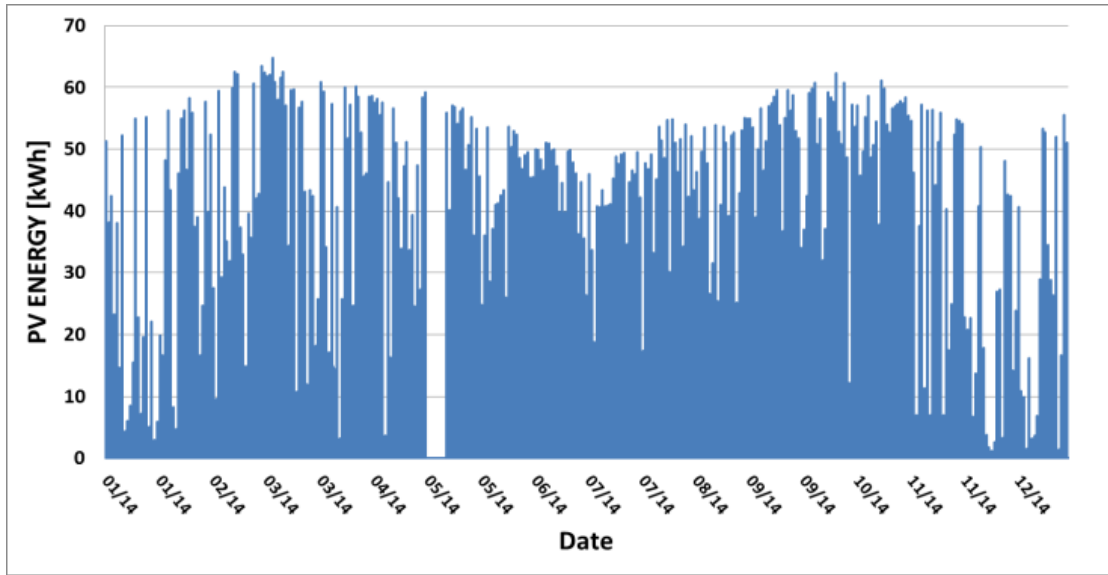


Figure 17: ADREAM's measured PV Energy Production (2014)

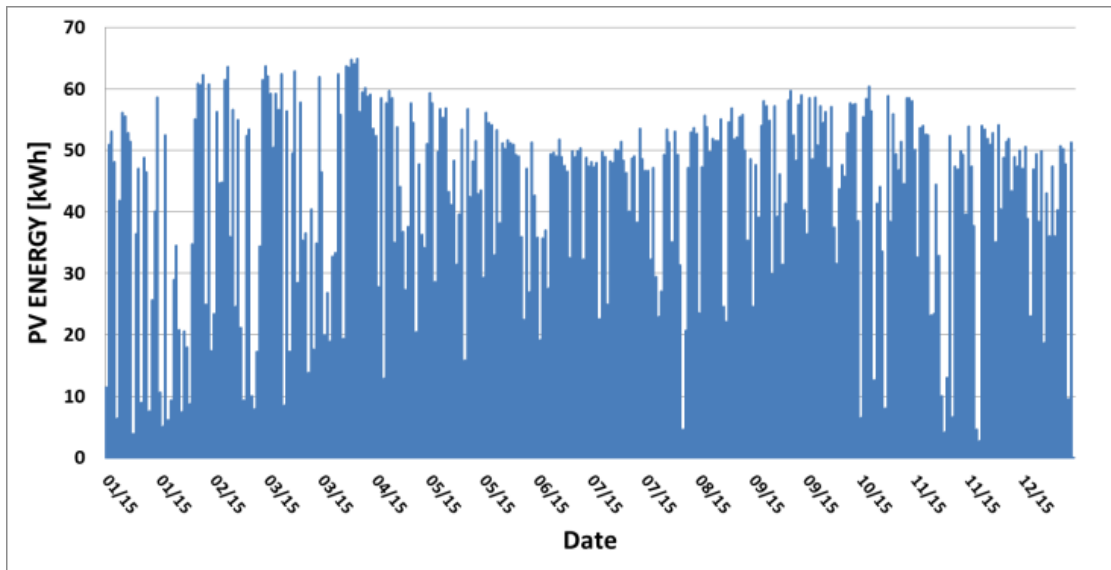


Figure 18: ADREAM's measured PV Energy Production (2015)

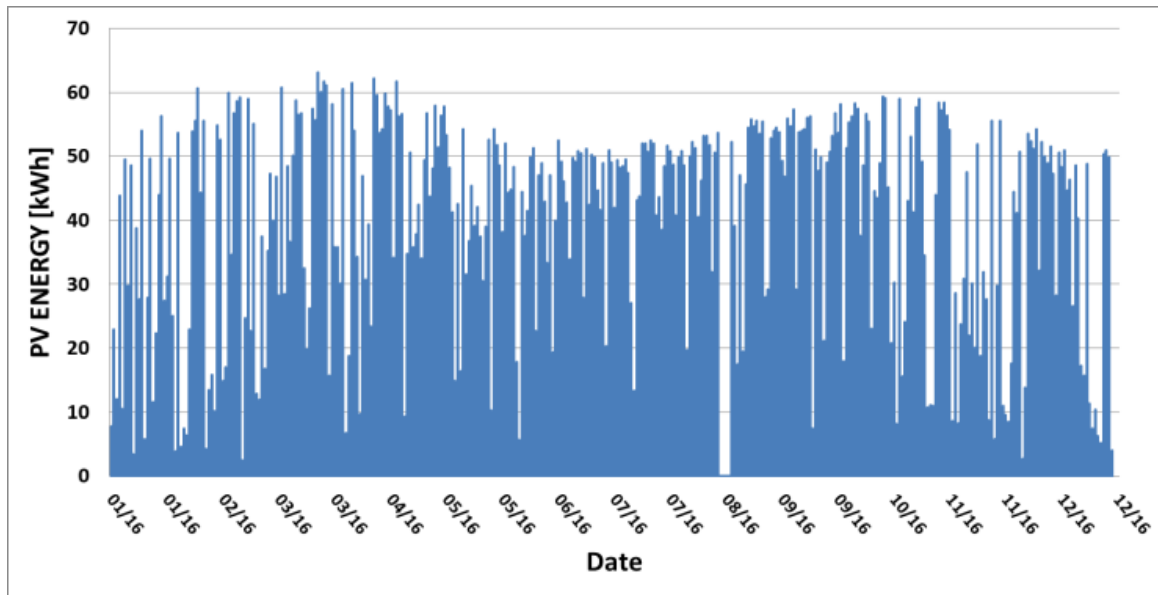


Figure 19: ADREAM's measured PV Energy Production (2016)

As it can be seen on these graphs, non-negligible periods of data are missing in the years 2014 and 2016. This is due to a malfunction in the sensor and database systems of the building. These respective periods will therefore be ignored in the simulations and results.

Recent scientific studies on the building are based on the concept of New Generation Energy Networks. The related domains include power electronics, data processing, security functioning, and automation. The resolution of the associated challenges demands the understanding of the different behaviors of connected systems in an electrical network, such as photovoltaic panels and inverters, through complete model elaboration and analysis. Each type of energy source (thermal or electrical) present in the building can be studied through a modular monitoring infrastructure. Additionally, the emulation of different consumption profiles (e.g. lighting, electronic equipment, data servers) coupled to human usages is possible.

Therefore, a modeling approach to energy management and optimization for the totality of the systems, integrating all the entities of production and consumption has been initiated. For this Thesis work, the part of PV production modeling is discussed in the following section.

2.3. Modeling PV production

In order to estimate the PV energy production for the building ADREAM, an optimized solar irradiation model was used to estimate the solar radiation on surfaces of different inclinations. This model was developed through Matlab and parts of it are based on previous PhD research [46] and renown models from the literature [47][48][49][50][51]. I participated in the optimization of the models before this PhD during my Master internship in LAAS.

2.3.1. Design of Solar Irradiation Model

Solar irradiation on terrestrial surfaces, as explained in chapter 1, is highly dependent on the composition of the atmosphere. Furthermore, estimating the solar radiation incoming on different surfaces with varying inclinations and properties is a complex matter. This subsection presents a model developed to estimate solar producible on ADREAM's PV surfaces by using the horizontal global irradiance measure provided by pyranometer of the meteorological station on the building's roof.

For the development of an optimized solar irradiation model, a good understanding of the composition of solar radiation on a terrestrial surface is necessary. Direct radiation (S), diffuse radiation (D) and reflected radiation (R) add together to form the global radiation (G) on a surface as given in equation (1) and illustrated in Figure 20.

$$G = S + D + R \quad (1)$$

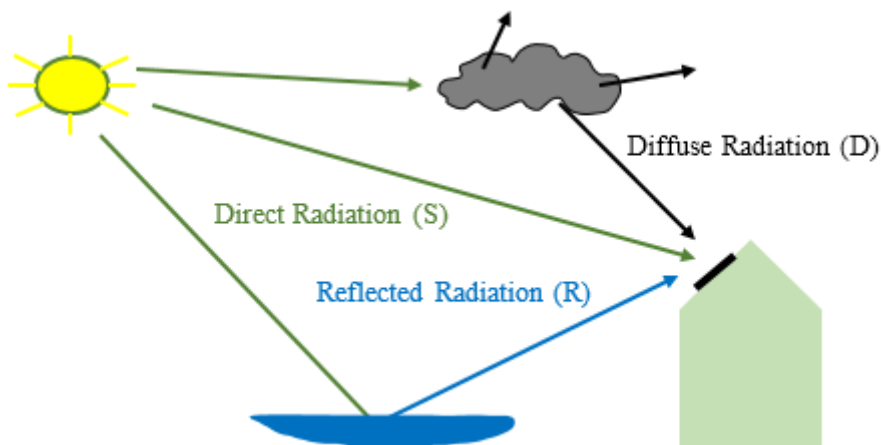


Figure 20: Division of the global radiation (G) into direct (S), diffuse (D) and reflected (R) radiation

For the estimation of the global irradiance on an inclined surface such as a PV panel, it is necessary to estimate each of these components for the given inclination 'i' as shown in equation (2).

$$G_i = S_i + D_i + R_i \quad (2)$$

The reflected part can be neglected based on the surrounding environment and the direct part (S , S_i) can be determined through geometric calculations. However, the estimation of the The reflected part can be neglected based on the surrounding environment and the direct part (S , S_i) can be determined through geometric calculations. However, the estimation of the diffuse component of the global irradiance on a given inclined surface is the determining and more complex part of a solar irradiation model. Many attempts to model D and D_i have been carried out in literature. The works of Temps and Coulson [47], and Klutcher [48] study the horizontal diffuse irradiance while Skarveith [49], Orgrill and Hollands [50], and Erbs [51] study the diffuse irradiance on a surface of given inclination. These existing models have been compared and combined into an optimized and calibrated solar irradiation model. The details of the complete model are shown in [52] and Figure 21 shows an overview of its structure.

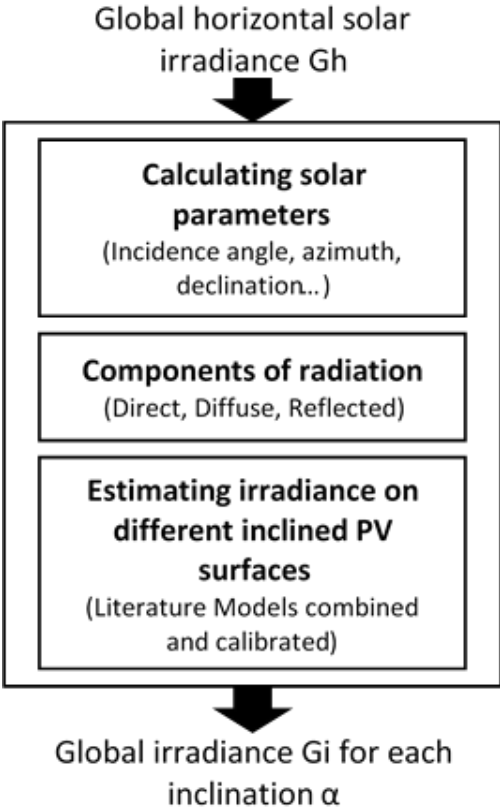


Figure 21: Simplified diagram of the solar irradiation model

As it can be seen in Figure 21, this model uses only one input, which is the global horizontal solar irradiance data for a given period of time.

2.3.2. PV Energy Production

Using this optimized model and global horizontal solar irradiance data from a pyranometer integrated in the ADREAM building, we can estimate the global irradiance on each inclined

photovoltaic surface for every minute of the year. This estimated data will be used to calculate the total PV power and total PV energy production of the platform.

Various PV systems are integrated in the ADREAM building. Each system is composed of a specific string of PV panels tilted at a given angle, connected to a single inverter as shown in Section 3.2, Table 1. Using equation (3), the electrical production of each individual PV system can be calculated, as the specific efficiencies of each subsystem are known.

$$P_{sys_i} = PV_{surface_i} * G_{i_{\alpha}} * \eta_{PV_i} * \eta_{INV_i} * (1 - MM_{loss}) * (1 - OHM_{loss}) \quad (3)$$

Where:

P_{sys_i} : Electrical power produced by the system 'i' [W];

$PV_{surface_i}$: Total PV surface in the string 'i' [m²];

$G_{i_{\alpha}}$: Global inclined irradiance arriving on a surface at angle α [W/m²];

η_{PV_i} : Efficiency of the PV panel technology used in string 'i';

η_{INV_i} : Efficiency of the inverter connected to string 'i';

MM_{loss} : Mismatch losses [%];

OHM_{loss} : Ohmic losses [%].

The total PV power ($P_{pvtotal}$) in Watt for the whole building is calculated by adding the power of all the PV systems.

$$P_{pvtotal} = \sum_i P_{sys_i} \quad (4)$$

The final goal of this type of model is to estimate the annual PV energy production in order to study the impact of BIPV in ZEBs as seen in the previous sections. As the input data from the buildings sensors has a period of one minute, the annual energy consumption can be calculated by integrating the total PV power $P_{pvtotal}$ over the examined time period. The results of the simulation are presented in Figure 22, Figure 23, and Figure 24. In addition, the same simulation result data sets with a sampling period of one day are visible in ANNEX 3.

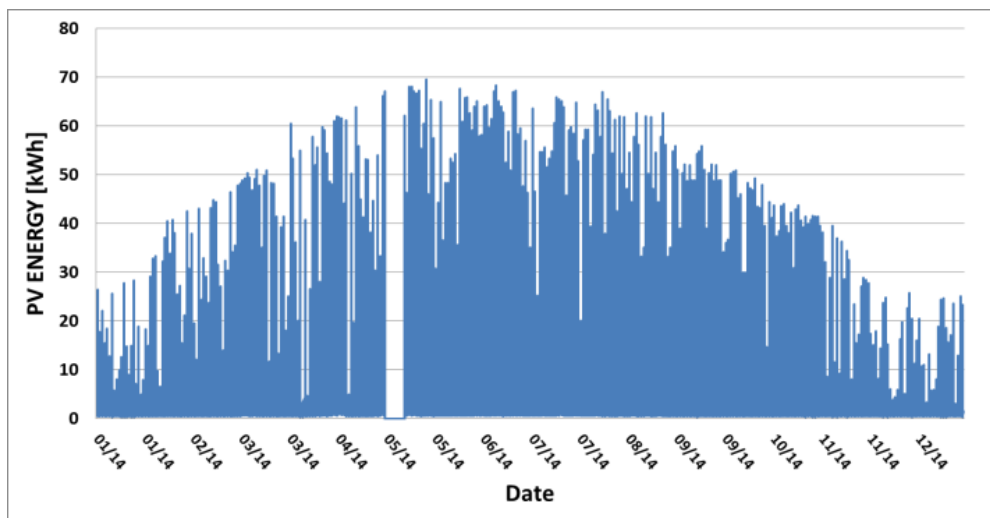


Figure 22: Simulated PV Energy Production with Matlab (ADREAM, 2014)

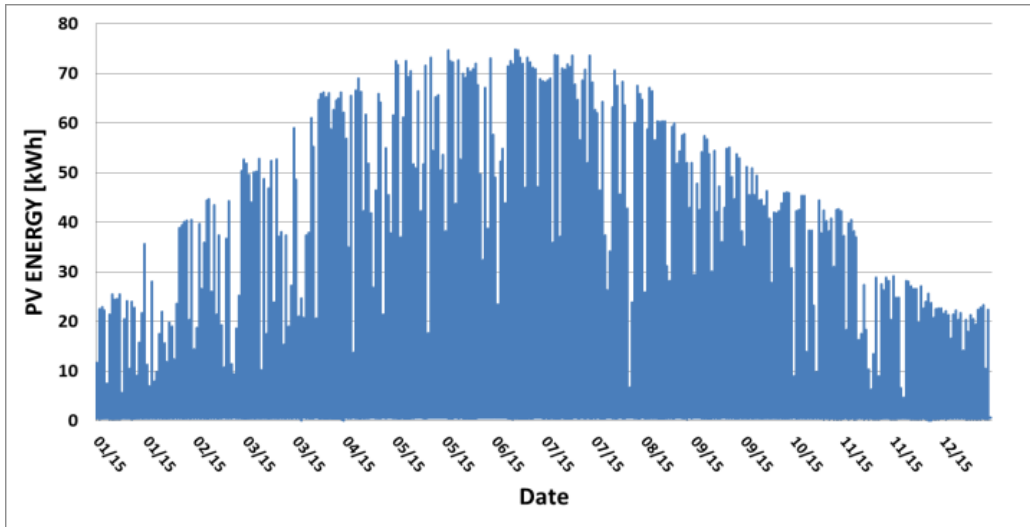


Figure 23: Simulated PV Energy Production with Matlab (ADREAM, 2015)

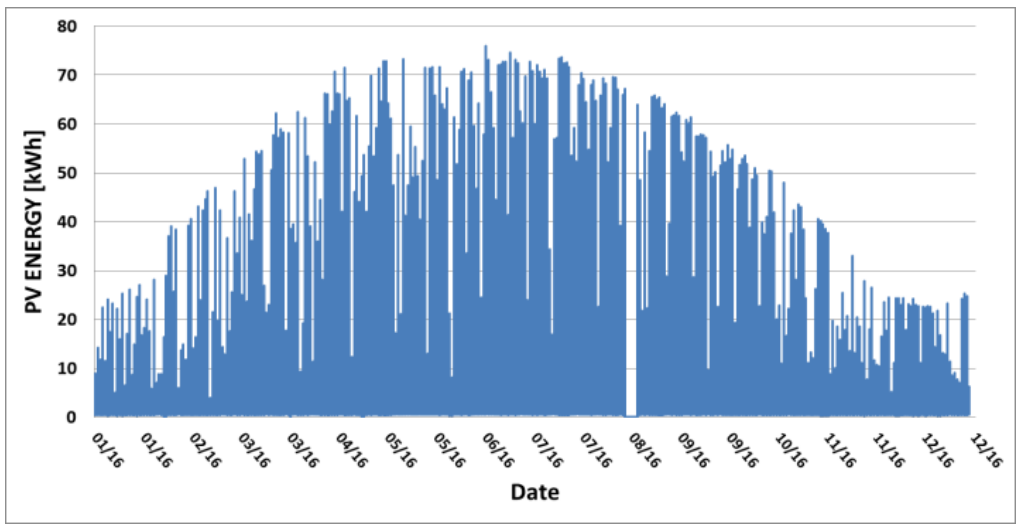


Figure 24: Simulated PV Energy Production with Matlab (ADREAM, 2016)

A comparison between these simulation results with the measured data on a yearly basis is shown on the graphs in Figure 25, Figure 26 and Figure 27 below.

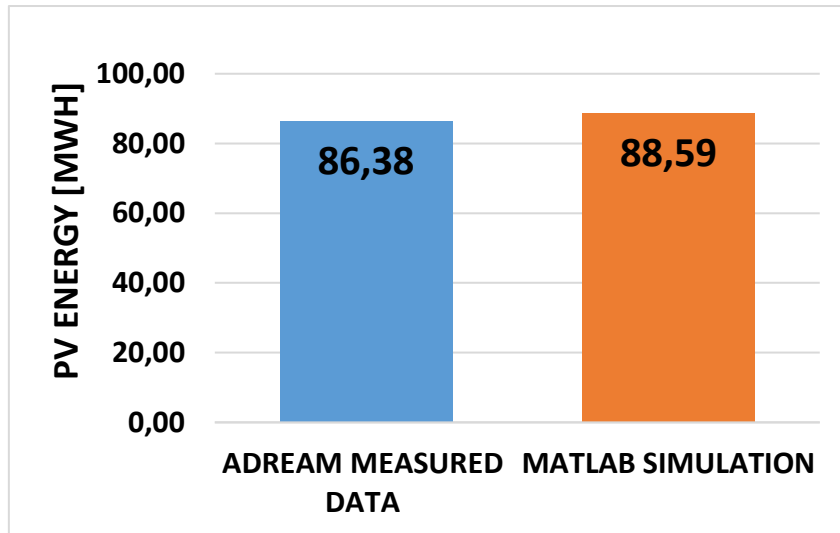


Figure 25: Annual Electrical Energy Production from ADREAM's PV Systems (2014), measured and simulated

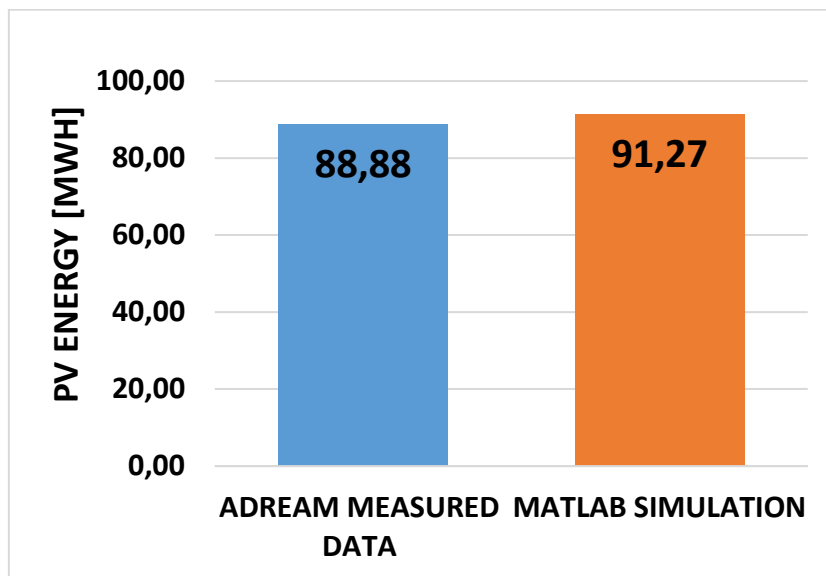


Figure 26: Annual Electrical Energy Production from ADREAM's PV Systems (2015), measured and simulated

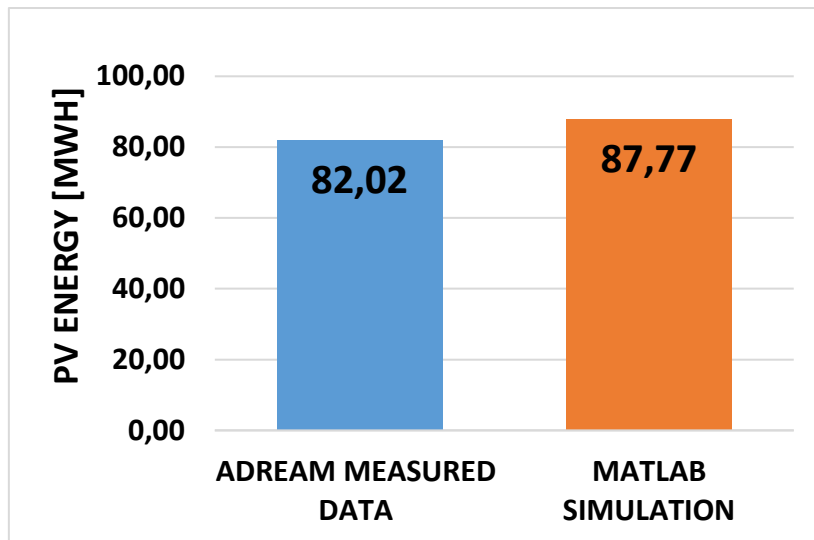


Figure 27: Annual Electrical Energy Production from ADREAM's PV Systems (2016), measured and simulated 6

As it can be observed, for 2014 the simulation overestimates the annual PV energy production by 5.41MWh (6.2% relative error). Similarly, for 2015, simulation overestimates the PV production by 7.91MWh (8.9% relative error). Finally, for the year 2016, the overestimation is 10.63MWh (13% relative error).

The cross-examination of the models' production over three years presents a systematic overestimation of the measured output. This phenomenon confirms the consistency of the model for variable sets of inputs.

This model was used in a comparison with another modelling work of PV production using traditional software Pleiades + Comfie. This collaborative work was presented in the ELECTRIMACS 2017 conference [53]. This modelling work is also usable for embedded mobile systems, and was used in an internal collaboration in LAAS for drone applications [54].

While the simulated and measured data for the yearly PV production is now available, it is a big amount of data and hard to analyze as it is. In order to be able to extract useful knowledge from this data regarding energy management and control, it has to be further examined. In the next section, a mathematical method for data analysis named Clustering is described and used to process both production and consumption data for the building and extract useful daily power curves based on scenarios.

2.4. Clustering of PV production data, the case of ADREAM

Storage technologies are more or less resistant to rapid variations in their power inputs and outputs. The study of the impact of rapid variations on storage elements is a common work in the community and is in need of realistic data sets for buildings and renewable energy production to simulate the impacts on batteries. A mathematical clustering method is used in this thesis work in order to identify useful information from ADREAM's data sets.

Cluster analysis or clustering is the task of grouping a set of objects in such a way that objects in the same group (called a cluster) are more similar to each other than to those in other groups (clusters). It is a common technique for statistical data analysis and is used to identify general trends or typical similarities in large data and has been proven to be usable for PV power data [55]. Cluster analysis can be achieved with many different methods and algorithms that differ in their notion of what constitutes a cluster and how to efficiently find them. This task can be described as an iterative knowledge discovery that involves many trials and iterations to find adequate clusters with desired properties.

Different types of cluster analysis algorithms exist in the literature and we have to choose the best adapted to our application. In the literature, four main types of clustering algorithms can be found. For each of these four types, the community has developed a multitude of specific algorithms. The four main types are the following:

Hierarchical clustering [56] calculates distance between objects (data points) to connect the closest objects as clusters. Each cluster is defined by the maximum distance that connects two objects in the cluster.

In centroid based clustering [57] each cluster is represented by a central vector (or centroid). Objects are assigned to clusters by their distance to the central vector of each cluster.

Distribution-based clustering uses mathematical probability distribution models such as Gaussian distribution. Clusters are then defined as objects belonging to the same distribution.

In density-based clustering [58], clusters are defined as areas of higher density than the remainder of the data set. Objects in these sparse areas are usually considered to be noise and border points.

In this work, the goal is to identify typical profiles representing general trends in daily electrical power production and consumption based on meteorological scenarios in order to better understand the typical daily behavior of PV sources and loads in the building depending on these scenarios. A centroid based clustering method is therefore chosen because this method uses central vectors to define the general behavior of each cluster. Each central vector can then be used as a typical daily power characteristic, representing one scenario.

2.4.1. Clustering daily power data using K-medoids algorithm

The most common centroid based clustering method is the K-means algorithm [59]. In this algorithm, the centroid of each cluster is defined as the mean value of the cluster. This algorithm is not directly usable in our application as we want to identify the most “typical” and

representative daily curves among the data but do not want to use a mean value which would make the data less realistic.

One centroid based clustering algorithm that is particularly adapted to this study is the K-medoids algorithm which is a derivate of the K-means algorithm. In this algorithm, the centroid element of each cluster is the one data that is the closest to the mean value of the cluster (the medoid). This means that in our application, the medoid of a cluster of daily power vectors (electrical power vs time) will be one of the real vectors of this cluster: the one that is closest to the middle of the cluster. Figure 28 presents a flowchart of the K-medoids method.

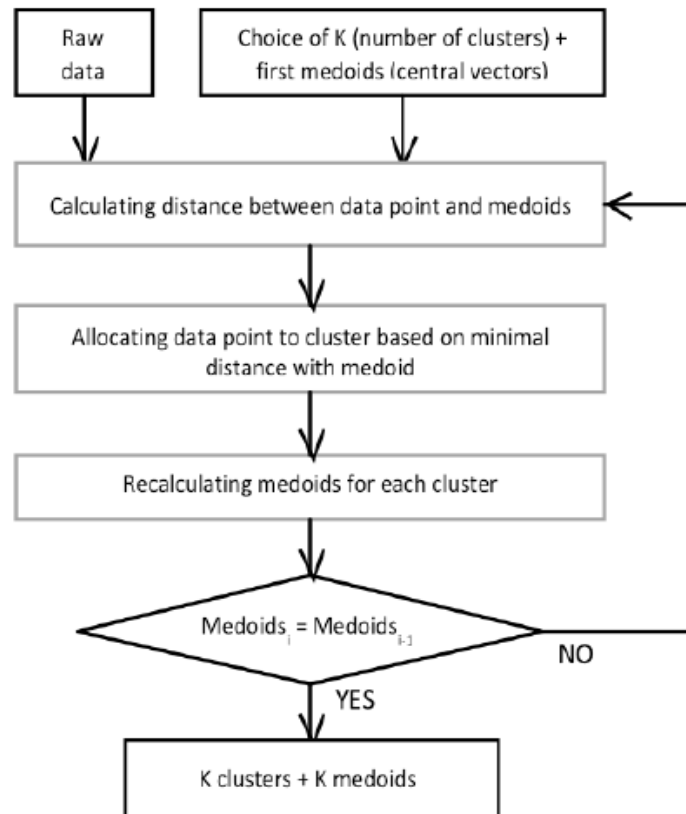


Figure 28: Algorithm for the K-medoids clustering method

The algorithm is initialized with the raw data. The number of desired clusters (K) is chosen by the user and one data (here one daily power vs time array) is chosen as medoid for each cluster. An iterative loop begins. For each data element, the distance between it and each medoid is calculated. Each data point is then assigned to the closest medoid, forming the clusters. After this step, the new medoid is selected in each cluster. The algorithm stops when the K medoids have not changed between two iterations. At this point, the raw data has been partitioned in K groups (clusters) of daily curves. Each cluster is represented by one central element (the medoid), a typical daily curve.

This data partitioning method is applied to two sets of data from the ADREAM platform: daily PV production data from the 100kWp of photovoltaic panels and electrical consumption data from the building.

2.4.2. Example of data treatment for the production and consumption profiles of the ADREAM BIPV.

Today, the ADREAM platform [42] in Toulouse provides with typical production and consumption data for a three-phased AC micro-grid supplying the energy optimized building described previously in this chapter.

It is important to quantify the different energy exchanges such as photovoltaic production or electrical consumption when conceiving a local low voltage grid (LVDC or LVAC). Only then it is possible to properly size the needed storage units and adapt the command circuits. To achieve this goal, we have decided to use a the K-medoids data clustering method explained above in order to identify specific and characteristic profiles for daily PV production and electrical consumption of the building.

Instantaneous power data from ADREAM with a sampling rate of one minute from 2015 as described in the previous section is used for this study. Using the K-medoids method explained above, this data is processed with a chosen number of clusters $K=4$. The following profiles depicted in Figure 29 are obtained:

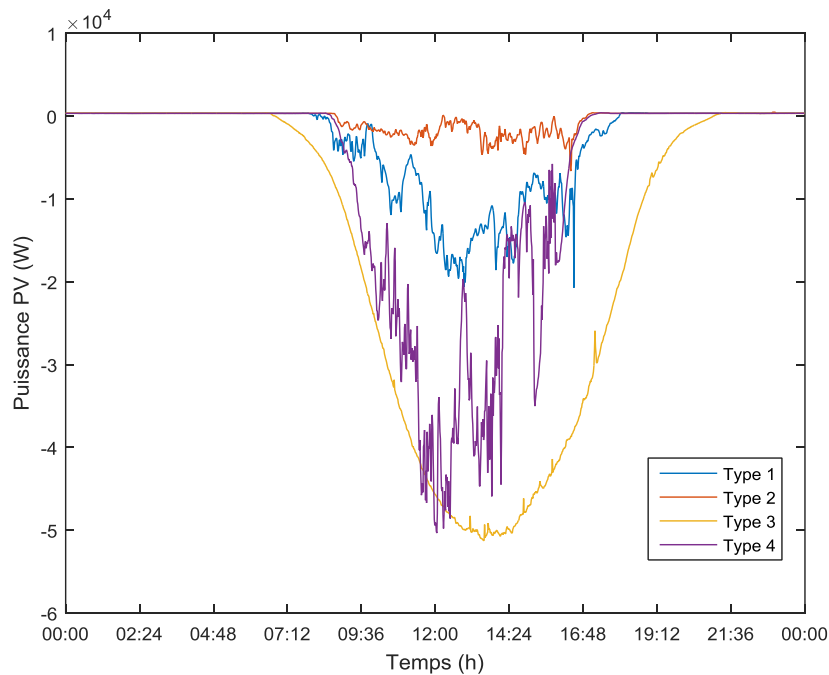


Figure 29: Different types of daily profiles for PV power production identified with K-medoids algorithm.

The four resulting medoids define typical daily PV production profiles. They can be labeled “low intermittent solar radiation”(type 1), “low uniform solar radiation”(type 2), “uniform strong solar radiation”(type 3) and as “strong intermittent solar radiation”(type 4). The shown PV power profiles are negative as these graphs represent “consumed power”. Identifying these daily production profiles is a necessary step to study realistic impact of PV intermittence on microgrids and storage devices.

As for PV production data, the K-medoids algorithm was used on the total electrical consumption data from ADREAM platform in 2015 with a one minute sampling rate. For this study a number of clusters of $K=3$ has been chosen. The following results (Figure 30) are obtained:

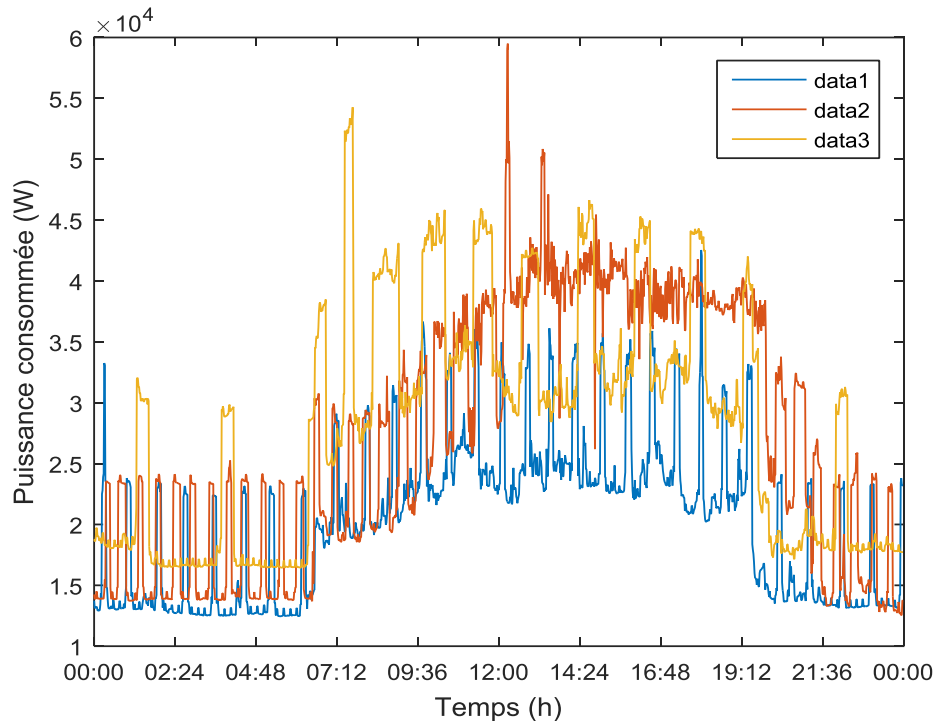


Figure 30: Different types of daily profiles for ADREAM’s power consumption identified with K-medoids algorithm.

These three different profiles are mostly varying in amplitude and thickness of the visible repeating power plateau. These plateaus are due to temporary activation of the heat pumps for both heating and cooling of the building. A change in overall amplitude between data1 and data3 curves is mostly due to different commands of hot water circulation pumps between winter and summer. These typical daily consumption profiles for the building give more information on the load behavior of the building's systems in a microgrid context than raw data available through sensors.

To sum up these clustering works on data of the BIPV building, it can be noticed that intermittences exist both on PV profiles and consumption profiles.

To conceive a local optimized energy grid based on photovoltaic sources, a good knowledge of the solar producible, its intermittency and its production are needed. In a first approach, studying typical PV production profiles could permits to identify the quantity of available and storable energy depending on the meteorological scenario. Four types of production profiles have been identified in addition to three types of consumption profiles for the ADREAM building. But it appears that the calculation task to deduce the quantity of stored energy needed for ADREAM was not easy. Nevertheless, these typical profiles constitute a valuable resource for studying the direct impact of intermittency of production and consumption on storage elements and energy management strategies in a microgrid context. This information can be

used either directly in the chemical design of future cells as a goal for withstandable inputs as well as in the design of electrical protections and energy management tools to prevent premature ageing of existent technologies.

One key point in energy transfer optimization is a better knowledge of storage units. For this purpose, a model of state of charge (SOC) in battery storage units is needed. Instrumentation for battery study installed in LAAS during the thesis is presented in the next section followed by the description of a fast modeling methodology developed for testing various types of electrochemical storage elements.

2.5. Instrumentation and specifications for the study of electrochemical storage elements

2.5.1. Instrumentation for battery testing:

At the beginning of this thesis work, a battery test bench had been installed in the electronic lab of the ADREAM platform. This battery test bench was composed of a battery cycling device from the brand BIO-Logic, a thermal enclosure and a pc using the software BT-LAB.

The battery cycler used for this thesis work is a BCS-815 from Bio-Logic represented in Figure 31 below. Further specifications are available in ANNEX 4.



Figure 31: BCS-815 battery cycler from Bio-Logic installed in the laboratory room of the ADREAM platform

This battery cycler has 8 four point channels with a voltage range from 0V to 9V $\pm 0.3\text{mV}$ and a current range of $\pm 15\text{A}$. Channels can be paralleled for up to $\pm 120\text{A}$ with 8 channels. Thermocouples are available on each channel for recording of cell temperatures from -25°C to $+2000\text{C} \pm 2^{\circ}\text{C}$. A built in EIS module permits electrochemical impedance spectroscopy applications on each channel from 10kHz to 10mHz.

The BCS-815 is piloted from a PC using the windows based BT-Lab software for battery cycling. The BT-Lab software offers a user friendly interface to program cycles for electrochemical storage elements. Several standard cycling methods are built in for easy use such as open circuit voltage measures, cyclic voltammetry, capacity determination, galvanostatic cycling or constant load discharge. The method that was used for most of the battery tests through this thesis work is the “Modulo Bat” method, permitting the user to craft desired battery test strategies by combining several test methods together.

A thermal enclosure (Figure 32) is used to be able to control environmental temperature for battery tests. As the temperature in the laboratory can change based on seasons and acclimatization, this device is used to keep the temperature around the tested battery cells constant through cycling tests. It can also be used to test the impact of higher or lower temperatures on battery efficiency and/or lifetime.



Figure 32: Thermal enclosure used with the BCS-815 for temperature control during battery tests

When testing battery cells, a number of standard designations are used in order to describe its functioning. The most common specifications will be described here.

2.5.2. Battery specifications:

According to the MIT [60], battery cell characteristics are defined as follows:

Capacity or Nominal Capacity (Ah for a specific C-rate) – The coulometric capacity, the total Amp-hours available when the battery is discharged at a certain discharge current (specified as a C-rate) from 100 percent state-of-charge to the cut-off voltage. Capacity is calculated by multiplying the discharge current (in Amps) by the discharge time (in hours) and decreases with increasing C-rate.

The theoretic capacity of a battery can be calculated using equation (5):

$$C_{th} = \frac{n_e \times 26.8 \times 1000}{M_{act}} \quad (5)$$

With:

n_e : The number of exchanged electrons ;

C_{th} : The theoretical massic capacity [Ah.kg⁻¹] ;

M_{act} : The molar mass of the active matter that limits the discharge reaction [g.mol⁻¹].

The effective capacity can be calculated using equation (6):

$$C_{eff} = I . t \quad (6)$$

With

C_{eff} : The effective capacity [Ah] ;

I : discharge current [A] ;

t : The discharging time after which the current reaches a specific value [h].

C- rates – When describing batteries, discharge current is often expressed as a C-rate in order to normalize against battery capacity, which is often very different between batteries. A C-rate is a measure of the rate at which a battery is discharged relative to its maximum capacity. A 1C rate means that the discharge current will discharge the entire battery in 1 hour. For a battery with a capacity of 100 Amp-hrs, this equates to a discharge current of 100 Amps. A 5C rate for this battery would be 500 Amps, and a C/2 rate would be 50 Amps.

State of Charge (SOC)(%) – An expression of the present battery capacity as a percentage of maximum capacity. SOC is generally calculated using current integration to determine the change in battery capacity over time. It can also be calculated from current capacity and nominal capacity or from the already used capacity by using equation (7):

$$SOC = \frac{C_r}{C_n} = \frac{C_n - C_u}{C_n} = 1 - DOD \quad (7)$$

With :

C_r : The remaining capacity in the battery ;

C_n : The nominal capacity ;

C_u : The used capacity ;

Depth of Discharge (DOD) (%) – The percentage of battery capacity that has been discharged expressed as a percentage of maximum capacity. A discharge to at least 80 % DOD is referred to as a deep discharge. It is the used capacity C_u divided by the nominal capacity C_n as shown in equation (8):

$$DOD = \frac{C_u}{C_n} \quad (8)$$

Nominal Voltage (V) – The reported or reference voltage of the battery, also sometimes thought of as the “normal” voltage of the battery.

Terminal Voltage (V) – The voltage between the battery terminals with load applied. Terminal voltage varies with SOC and discharge/charge current.

Open-circuit voltage (V) – The voltage between the battery terminals with no load applied. The open-circuit voltage depends on the battery state of charge, increasing with state of charge.

Cut-off Voltage – The minimum allowable voltage. It is this voltage that generally defines the “empty” state of the battery.

Charge Voltage – The voltage that the battery is charged to when charged to full capacity. Charging schemes generally consist of a constant current charging until the battery voltage reaching the charge voltage, then constant voltage charging, allowing the charge current to taper until it is very small.

Internal Resistance – The resistance within the battery, generally different for charging and discharging, also dependent on the battery state of charge. As internal resistance increases, the battery efficiency decreases and thermal stability is reduced as more of the charging energy is converted into heat.

Specific Energy (Wh/kg) – The nominal battery energy per unit mass, sometimes referred to as the gravimetric energy density. Specific energy is a characteristic of the battery chemistry and packaging. Along with the energy consumption of the vehicle, it determines the battery weight required to achieve a given electric range.

Specific Power (W/kg) – The maximum available power per unit mass. Specific power is a characteristic of the battery chemistry and packaging. It determines the battery weight required to achieve a given performance target.

Cycle Life (number for a specific DOD) – The number of discharge-charge cycles the battery can experience before it fails to meet specific performance criteria. Cycle life is estimated for specific charge and discharge conditions. The actual operating life of the battery is affected by the rate and depth of cycles and by other conditions such as temperature and humidity. The higher the DOD, the lower the cycle life.

2.6. Studied electrochemical storage technologies

Battery storage of electrical energy is one of the key points for successful renewable energy development. Several different technologies exist nowadays and it is essential to identify the

most adapted ones for usage in microgrids and energy-optimized building applications. Determinant factors for comparison [61] are battery lifetime (depending on depth of discharge DOD per cycle), the overall efficiency of the cells (ratio of charged/discharged energy), their price and their environmental footprint. These storage devices must be able to store as much as possible of the overproduction from renewable sources and must be able to reconstitute this energy as needed when the production is not sufficient to supply for the application's consumption. In this case the stored energy is discharged over several hours, meaning specific energy (Wh/kg) is more valuable than specific power. In the specific case of renewable energy production and more specifically PV energy production, the previously described intermittency is an important point for storage technologies as they can have a significant impact on the efficiency and the lifetime of electrochemical storage elements.

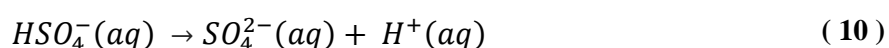
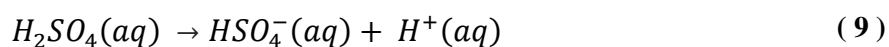
For our approach, four technologies of batteries have been selected a priori more adapted to a building context: Lead acid, Lithium iron-phosphate, Lithium polymer and hybrid LIC lithium-supercapacitor. Their main characteristics are summed up below.

2.6.1. Lead acid batteries

The lead acid battery technology [62] is the oldest rechargeable accumulator technology, existing since 1859. It is very commonly used today and different variations exist for different applications (energy storage, power storage). Its specific energy is relatively low (33 to 42 Wh/Kg) but is interesting for stationary energy storage due to its low cost. This technology constitutes the basis that has been proven to work for solar PV production in multiple types of applications.

In a charged lead accumulator, the positive electrode is formed by a solid layer of lead(IV) (PbO₂) oxide covering a lead alloy grid. The negative electrode is formed by a layer of lead (Pb) covering a lead alloy grid. The electrolyte is a solution of sulfuric acid H₂SO₄, which participates in the charge and discharge reactions of the cell.

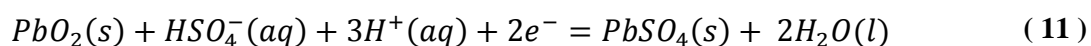
The dissociation of sulfuric acid produces bisulfate ions (also named hydrogen sulfate) HSO₄⁻ and sulfate ions SO₄²⁻ following equation (9) and (10):



The second acid reaction is weak; therefore sulfate ions are only present in low concentration. The redox reactions in lead acid batteries only involve the HSO₄⁻ ion. The discharge and charge reactions of the lead acid accumulator function as follows.

When discharging, two simultaneous reactions are happening:

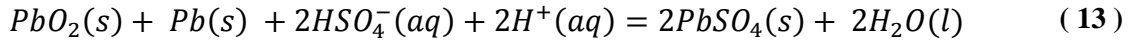
On the positive electrode (the cathode when discharging), the lead(IV) oxide is reduced into lead(II) sulfate :



On the negative electrode (the anode when discharging), the lead is oxidized into lead(II) sulfate.



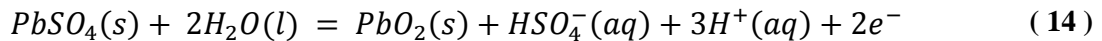
The global reaction inside of the cell can be written as follows:



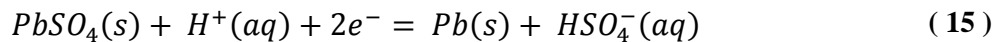
On both electrodes, a conductor (lead oxide and lead) becomes an isolating solid: lead(II) sulfate. This results in a significant increase in electrode volume and a decrease in electrolyte concentration during the discharge.

When charging, the precedent reactions are reversed:

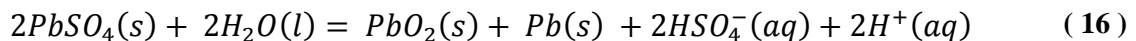
On the positive electrode (the anode while charging), the lead(II) sulfate is oxidized into lead(IV) oxide:



On the negative electrode (the cathode while charging), the lead(II) sulfate is oxidized into lead:



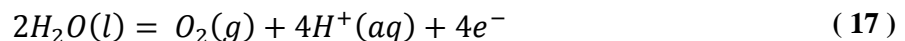
The global charge reaction is the following:



When the cell charges, electrolyte concentration rises as the water is consumed and hydrogen sulfate (VI) is produced.

At the end of charge, when no lead(II) sulfate is left at the contact of the electrodes, a gassing process is observed. In open accumulators, this gas is released, resulting in a loss of water in the electrolyte.

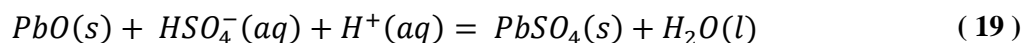
The valve-regulated lead-acid battery (VRLA) technology appearing in the 1950s solves this problem through gas recombination. VRLA batteries are sealed and do not release the gas formed by the reaction. The dioxygen formed on the positive electrode travels to the negative electrode and recombines with dihydrogen to form water. The negative electrode is oversized in comparison to the positive electrode. This way the lead sulfate is still present in the negative when it is used up in the positive electrode, therefore inducing an electrolysis reaction producing hydrogen:



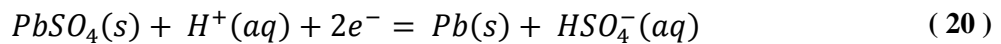
On this same electrode a reaction between dioxygen and lead goes as follows:



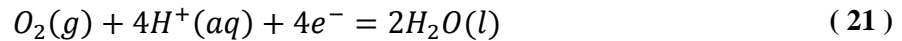
In the presence of the sulfuric acid solution, lead oxide reacts and forms lead sulfate:



As there is no hydrogen gassing at the negative electrodes surface due to the oversizing, the lead(II) sulfate is reduced into lead in the same way as in the normal charging process:



The global gas recombination equation can be written as follows:



This reaction permitted to create sealed lead-acid battery technologies such as AGM (Absorbent Glass Matt) or OPzV (using tubular electrodes) cells using a jellified electrolyte, minimizing maintenance. These specific types of lead acid batteries can have a lifetime of 500 to 1500 cycles at 80% DOD against 300 to 600 cycles for other lead acid technologies. Their self-discharge is a slow 3% to 10% per month [61].

The OPzV lead-acid battery technology has been chosen to be used as battery storage in the ADREAM platform's project named OPA for the previously cited reasons. In OPzV batteries, the positive electrode has a tubular form, increasing its cyclic lifetime. Classic OPzV are 2V cells with high capacity stacked into 6V or 12V modules. From the available products the OPzV cells from the brand Hoppecke were chosen for the ADREAM building. Table 3 below shows standard characteristics of a 2V Hoppecke OPzV cell.

Table 3: Standard characteristics of a 2V OPzV cell from Hoppecke

| Characteristics | OPzV Hoppecke |
|------------------------------|---|
| Nominal Voltage | 2V |
| Charge float voltage | 2.4V (2.35-2.45) |
| Minimum voltage (discharged) | 1.80 V (C10), 1.77 V (C5) |
| Charging current | 5 - 20 A / 100 Ah (C10) |
| Charging factor | 1.1 (110%) |
| T° range (°C) | min : -20°, max 45°, recommended : 15° - 35° optimal : 20°C |
| Cycle life time (20°C) | 8000 cycles (20% DOD) 2000 cycles (70% DOD) 1500 cycles (80% DOD) |
| Capacity (examples) | C10=310 Ah C5= 283 Ah |
| Density | 11.5 Ah/kg 23.1 Wh/kg |
| Self-discharge | 3% /month (25°) |

The goal of the OPA project developed inside of the ADREAM platform is to power a 600Wp computer server with 1kWp of PV panels by adding storage on a 50-60V DC bus. The sizing for the lead-acid battery pack for the OPA project was initiated in this thesis work with the choice to use OPzV battery packs for their long cycle life and their low maintenance making them well suited for PV applications.

In order to be able to supply the servers for 15h at maximum load, a quick calculation following equation (22) gives us the maximal installed storage capacity needed C:

$$C = 600W * 15h = 9000Wh \quad (22)$$

The total battery capacity needed for the OPA project is 9kWh. As battery packs come in 6V or 12V stacks, a comparison of the characteristics of the available packs is made following Table 4 below from the constructor's website.

Table 4: Characteristics of the different OPzV battery packs available

| Battery stack | Voltage | C10 capacity | Number of cycles at 50% DOD C10 | Purchase price | kWh price at C10 |
|---------------|---------|--------------|---------------------------------|----------------|------------------|
| OPzV 12V 70 | 12V | 51.0 Ah | 2500 | 374.10 € | 0.47 €/kWh |
| OPzV 12V 180 | 12V | 154.0 Ah | 2500 | 730.80 € | 0.32 €/kWh |
| OPzV 6V 300 | 6V | 250 Ah | 2500 | 677.50 € | 0.29 €/kWh |

According to this table, purchasing 6V 300 OPzV packs will net the same number of cycles and the same capacity for a lower price than the two other choices. A total number of 6 6V OPzV battery packs are needed to supply with a total of 9kWh of storage (equation X).

$$Number\ of\ stacks = \frac{9000Wh}{250Ah * 6V} = \frac{9000\ Wh}{1500\ Wh} \cong 6 \quad (23)$$

By connecting the six battery packs in series, a total voltage of 36V is obtained. The battery packs are therefore connected to the microgrid 50-60VDC bus through a reversible DC/DC converter.

Assuming maximum peak PV power of 1kWp is attained, the amount of time $T_{PVcharge}$ is needed to fully charge the battery packs:

$$T_{pvcharge} = \frac{9000\ Wh}{1000\ Wh} = 9\ h \quad \text{While all the PV power is connected to the battery} \quad (24)$$

$$T_{pvcharge} = \frac{9000\ Wh}{1000\ Wh - 600\ Wh} = 22.5\ h \quad \text{While the servers are powered by PV} \quad (25)$$

With more realistic hypothesis, PV power is not always at maximum peak power and can even be zero when meteorological conditions are bad. Therefore these approximations are very optimistic. More details on the realization of the OPA microgrid can be found in [63].

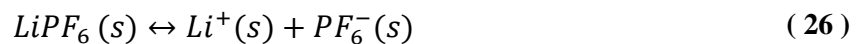
As the lead-acid technology is a mature battery technology today, its usage in building and PV storage in microgrids constitutes a basis for this type of application. In the following parts, three different technologies are described and tested for potential building microgrid applications.

2.6.2. Lithium iron phosphate batteries

Lithium-ion batteries [64] are industrially produced since the beginning of the 1990's and are the most used storage devices today on the electronic consumer market.

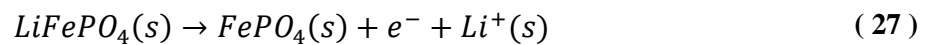
Mobile devices generally use mixed cobalt-lithium batteries LiCoO_2 for their high energy density. The lithium iron phosphate battery LiFePO_4 shows a bit lower energy density ($\sim 90\text{Wh/Kg}$) but a longer lifetime (2500-3000 cycles at 80% DOD) and a better security, which makes it especially adapted for stationary high energy density storage. The price of the LiFePO_4 technology is higher than for lead acid batteries but stays competitive due to its increased lifetime, meaning less replacing and maintenance costs. It also has a better resistance to fast discharges and deep discharges while maintaining a low self-discharge rate (around 3% per month). Low voltage variation while discharging greatly reduces the complexity of the voltage regulation for this technology. It is therefore one of the best adapted batteries for inhabited environment when used with a protection system against overvoltage and overcurrent.

In Lithium iron phosphate accumulators (LFP), the positive electrode is composed of lithium iron phosphate, LiFePO_4 covered in a conducting material such as carbon and doped with aluminum, niobium or zirconium cations in order to increase its conductivity. The negative electrode is composed of graphite deposited on a copper conductor. The electrolyte is a solution of lithium hexafluorophosphate LiPF_6 in an organic solvent, producing Li^+ and PF_6^- ions as follows:

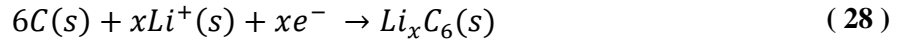


Due to the presence of Li^+ ions in the electrolyte, charge transfer between electrodes is made possible during charging and discharging of the battery cell. By replacing the cobalt used in other Lithium battery technologies with phosphates, the LFP technology is the most environmental friendly of the lithium batteries, as Fe is a very abundant material. LiFePO_4 makes the cathode structure more stable than in other lithium technologies, greatly reducing the risk of combustion.

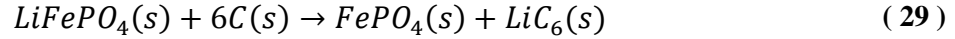
During the charging process, electrons from the positive electrode migrate to the negative electrode. On the positive electrode, LiFePO_4 liberates electrons, producing lithium ions:



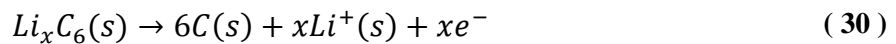
On the negative electrode, the accumulated electrons form a negative charge, attracting Li^+ ions that are present in the electrolyte solution. These Li^+ ions intercalate into the graphite material of the negative electrode, forming lithiated graphite.



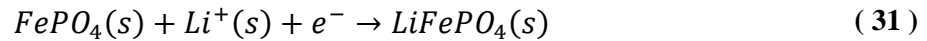
The global charge reaction can be written as follows:



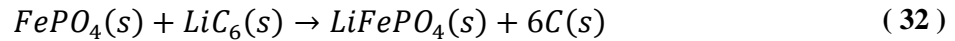
The inverse reactions occur when charging an LFP cell. Electrons are transferred from the negative electrode to the positive, liberating Li^+ ions contained in the graphite through an oxidation reaction:



Li^+ ions migrate inside of the electrode to intercalate into the crystalline structure of the FePO_4 from the positive electrode through the following reduction reaction:



The general discharge reaction reads as follows:



Charging an LFP cell is done with constant current until the maximal voltage of 3.6V is attained. End of charge has to be controlled precisely as overvoltage can lead to the explosion or combustion of the cell. Fast charging (2h for example) can be done when necessary but slightly reduces the lifetime of the cell. For the end of charge, fixing a constant voltage of 3.6V while letting the current drop until it is inferior to $C/24$ is recommended.

While discharging, the cell voltage stays stable around 3.2V for most of the capacity. A soft voltage regulation is needed to prevent the voltage from dropping below 2V or irreversible damage will be done to the cell. Fast peaks of discharge up to 10C are possible with this technology but it will reduce the cell's lifetime. One of the major drawbacks of the LFP accumulator is the premature ageing when it is not used. A cell's lifetime after manufacture when it is not being used is two to three years.

Single LFP cells from two different manufacturers have been tested in this thesis work. Cells from the brand ENIX and cells from the brand PHET as they are depicted in Figure 33: LFP cells from the brand ENIX and PHET where tested using the battery cycler described in the previous section. Datasheets for the ENIX cells can be found in ANNEX 5. Test cycles at different C-rates for the ENIX cells are visible in Figure 34for charges and figure Y for discharges. Test cycles for the PHET cells will not be shown or discussed as the test cells were of poor quality and did not show interesting results.



Figure 33: LFP cells from the brand ENIX and PHET

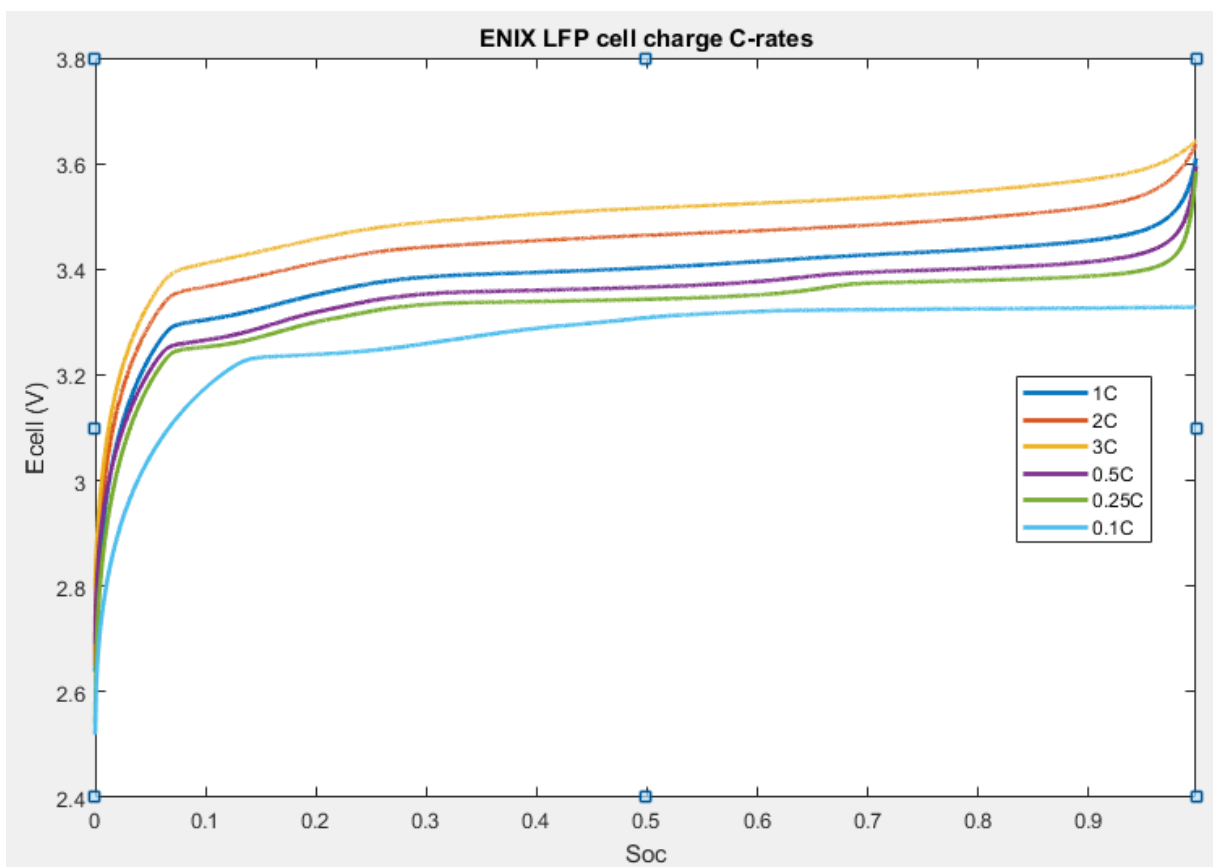


Figure 34: Charging cycles at different C-rates for the ENIX LFP cell

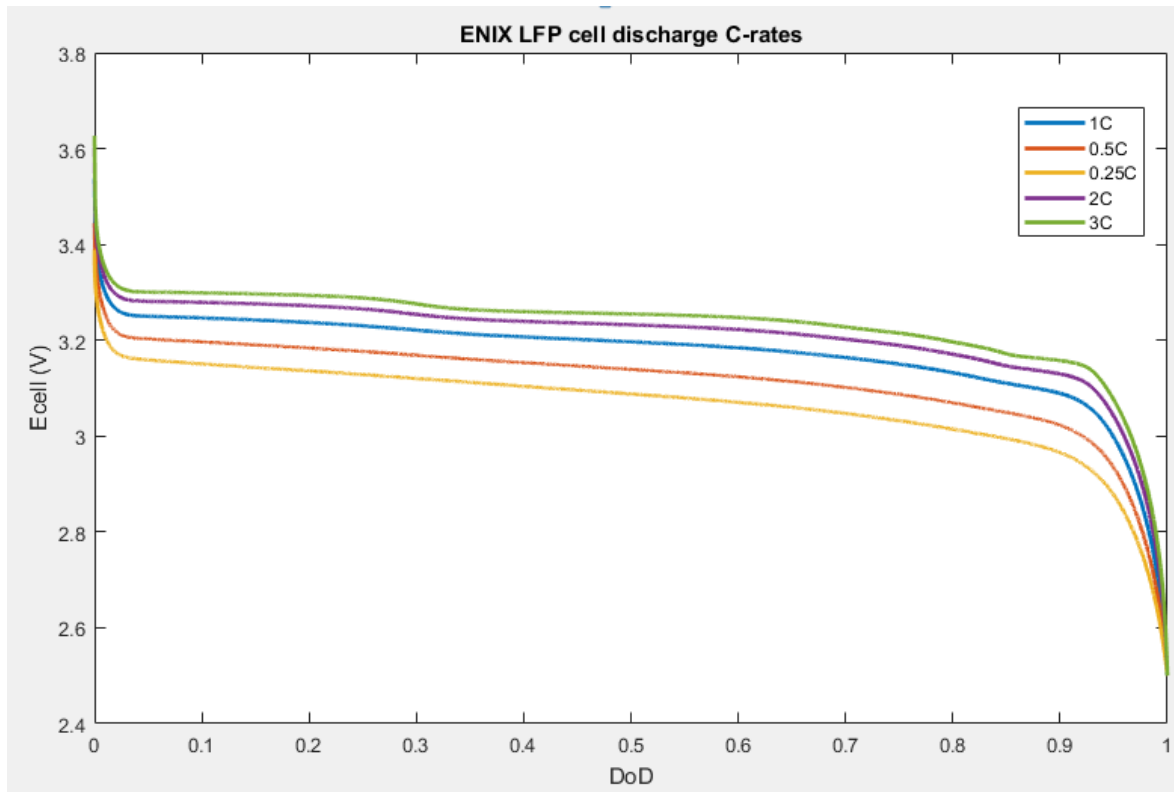


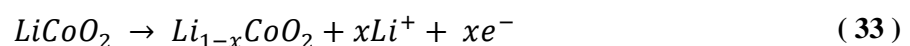
Figure 35: Discharging cycles at different C-rates for the ENIX LFP cell

On these graphs the nearly constant voltage during most of the charge and the discharge is clearly visible as well as the increase in voltage to 3.6V at the end of charge and the voltage drop to 2.5V at the end of discharge. It can be noted that the average voltage during most of the charging and discharging process is rising when increasing the charging/discharging current rate and that it is dropping when decreasing the charging/discharging current rate.

2.6.3. Lithium-ion Polymer batteries

Lithium Polymer (LiPo) cells use a solid polymer as electrolyte (SPE) such as polyacrylonitrile, polyethylene oxide or polymethyl methacrylate instead of an organic solvent with lithium-salt. Electrodes are composed of lithium cobalt oxide for the cathode and intercalated graphite for the anode. The main advantages of this technology are their easy shaping in space and weight and their low self-discharge (~5% per month), making them a good choice for embedded electronics. They also are one of the safest Lithium battery technologies as they can even be punctured (by a nail for example) without explosion or fire, even when fully charged. While they are mainly used in radio controlled equipment (RC modeling), LiPo cells can be used for autonomous mobile homes and have even been used for simple low energy housings for homeless people in the USA [65].

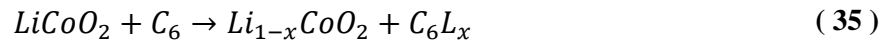
During the charging process, the cathode loses lithium in the form of Li^+ ions:



At the anode, Lithium ions are intercalated inside of the graphite carbon structure:



The general charging equation can be written as follows:



When discharging the cell, this reaction is inverted. Lithium ions are deintercalated from the graphite and reform lithium cobalt oxide on the anode side.

LiPo cells must be charged and discharged at lower current rate than other lithium technologies. With a C-rate of 1C, a LiPo cell has only a lifetime of about 300 cycles and about 500 cycles at 0.5C. Optimal charging and discharging rates are around 0.2C. For a nominal voltage of 3.7 V, the end of charge for a cell can be detected when 3.7 V are attained while the minimum discharge voltage is at 2.75 V. The optimal state of charge for storage of a LiPo battery is around 50% SoC.

The following LiPo cells shown in Figure 36 were tested in the laboratory, resulting in the charge and discharge curves visible in Figure 37 and Figure 38 below.

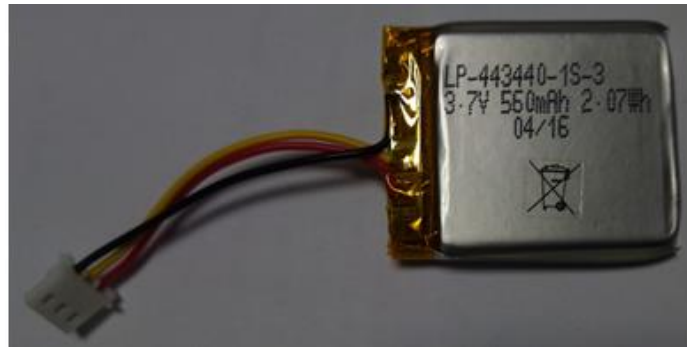


Figure 36: 3.7 V Lithium-polymer cell

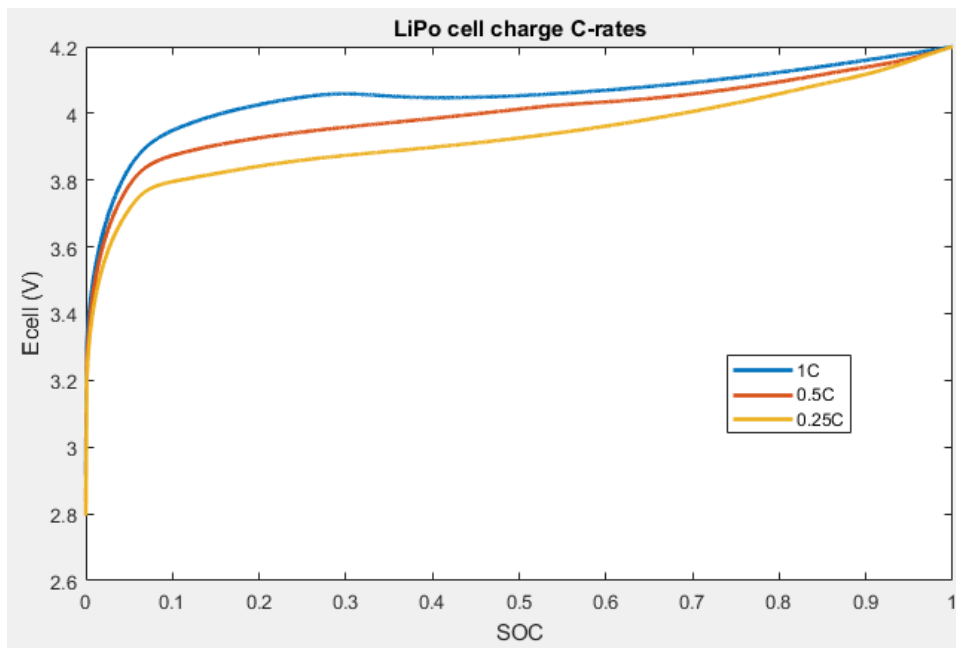


Figure 37: Charging cycles at different C-rates for the LiPo cell

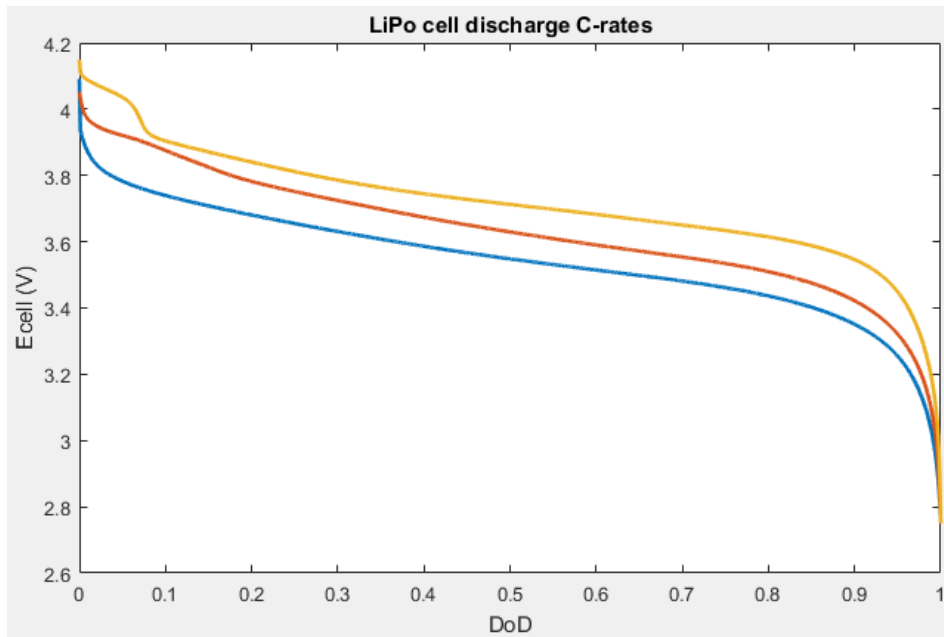


Figure 38: Discharging cycles at different C-rates for the LiPo cell

During the charge of the LiPo cell, the voltage increases rapidly at the beginning before stabilizing around 3.8V. The end of charge is achieved when the maximum cell voltage (here 4.2V) is reached. The curves on Figure 37 show no voltage increase at the end of charge as we observed for the LiFePO₄ cells.

During discharge, the behavior seems similar to LiFePO₄ cells. At 1C we observe a bulge at the beginning of the discharge. The manufacturer for these cells recommends using lower currents than 1C in order to preserve the lifetime of this technology.

2.6.4. Lithium supercapacitor LIC chemical hybrid

The intermittency of photovoltaic production can be problematic for energy storage. Hybrid systems using lead acid and lithium ion batteries with supercapacitors are largely studied in this domain and tend to improve the smoothing of production or consumption peaks directly related to intermittency.

Lithium supercapacitors (LIC) [66] are electrochemical hybrid storage devices that have been created recently by combining principles of lithium-ion batteries and double-layered supercapacitors (EDLC). EDLC is a technology halfway between batteries and electrolytic capacitors that are able to store more energy than a classical capacitor. The energy can be stored and released at high power as in a classical capacitor. The main goal of this hybridization is to combine the benefits of each technology in terms of energy density, power density, charge/discharge speed and lifetime. This new hybrid technology is emerging like a potential alternative to electrical hybridization of lithium-ion batteries and EDLC, being used both as energy and power source.

The positive electrode of an LIC cell is composed of active carbon, permitting the double-layer storage of charges similarly to EDLCs. The active carbon is structured in a way to create

maximal electrode surface, thus significantly increasing the retained charge. The negative electrode is composed of graphitic carbon doped with Li^+ ions, permitting the formation of LiC_6 when the cell is charged. Another type of negative electrode exists, using Li_2TiO_3 . The electrolyte is a saline Lithium ion solution in an organic solvent similar to that used in lithium-ion batteries. Figure 39 shows a simplified representation of an LIC cell given by the manufacturer JMenergy.

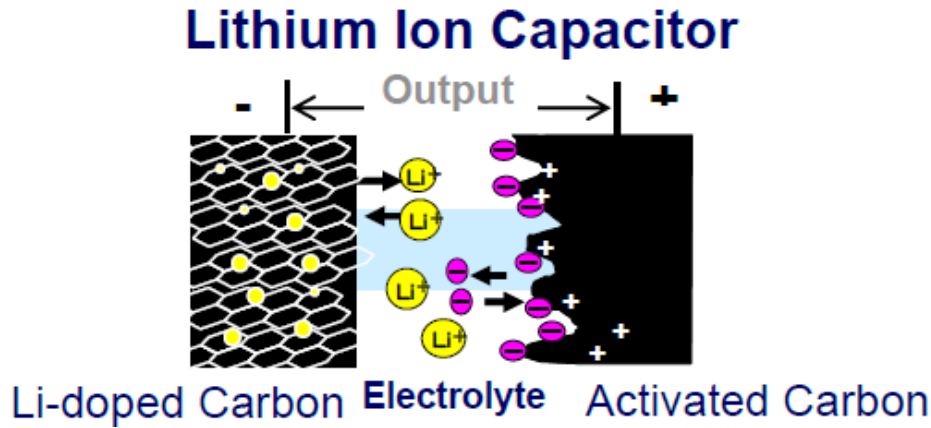


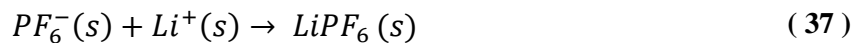
Figure 39: Simplified representation of the energy storage process in a LIC cell

Charging and discharging a LIC cell implies both a redox reaction on the negative electrode and a charge accumulation on the positive electrode.

In the discharging process, the LiC_6 inside the negative electrode is subject to an oxidation reaction:



Negative charges accumulated on the positive electrode are released and combine with Lithium ions liberated in the electrolyte:



This reaction is similar to that inside of the electrolyte of Lithium-ion batteries.

During the charging process, these reactions are inverted. The Li^+ ions from the electrolyte intercalate inside the carbon of the negative electrode through a reduction reaction involving additional free electrons:



A positive overcharge appears at the positive electrode, inducing a capacitive accumulation of electrons at the double-layer interface. This situation results in a difference of potentials between the two electrodes around 3V.

In a LIC cell, the cathode capacity is highly superior to the anode capacity, resulting in a higher change in potential on the anode during the charge/discharge. The voltage of a LIC cell has to be limited to never fall below 2.0V, which would cause irreversible damage to the cell. The charging of LIC cells is approximately 30% faster than that of an equivalent Lithium-ion battery

[66]. While the energy density is lower than that of a lithium-ion battery, the power density of a LIC cell is way higher, close to that of an EDLC supercapacitor.

Manufacturers show a very high number of capacitive cycles (>100 000) and a long lifetime, making this technology very interesting for stationary renewable energy structures. Additional studies are needed to verify daily cycling withstanding. This type of hybrid seems very promising for renewable energy applications. LAAS-CNRS, associated to CIRIMAT through the Neocampus project are studying this type of hybrid storage to improve their performance and modeling it.

LIC cells named ULTIMO from the brand JMenergy were tested using the battery cycler. Figure 40 is a picture of laminated ULTIMO cells while Table 5 presents the main characteristics of these cells.



Figure 40: ULTIMO laminated LIC cells, JMenergy

Table 5: Characteristics of an ULTIMO LIC cell

| Characteristic | LIC Ultimo 1100 |
|------------------------------------|-----------------|
| Capacitance | 1100 F |
| Rated voltage | 2.2V – 3.8V |
| Max charge voltage | 3.8V |
| Minimum discharge voltage | 2.2V |
| Absolute minimum discharge voltage | 2.0V |
| Charging current | Max : 50 A |
| Discharge current | Max : 360 A |

| | |
|------------------------|---|
| Internal resistance | 1.2 mΩ |
| T° range (°C) | min : -30°, max 70°, recommended : 10° - 35° optimal : 25°C |
| Cycle life time (20°C) | >100 000 cycles (80% DOD) |
| Energy density | ~10 Wh/kg |
| Power density | ~14 kW/kg |
| Self-discharge | < 1.7 % /month (25°) |

Results of cycles at different C-rates are presented in Figure 41 and Figure 42 below.

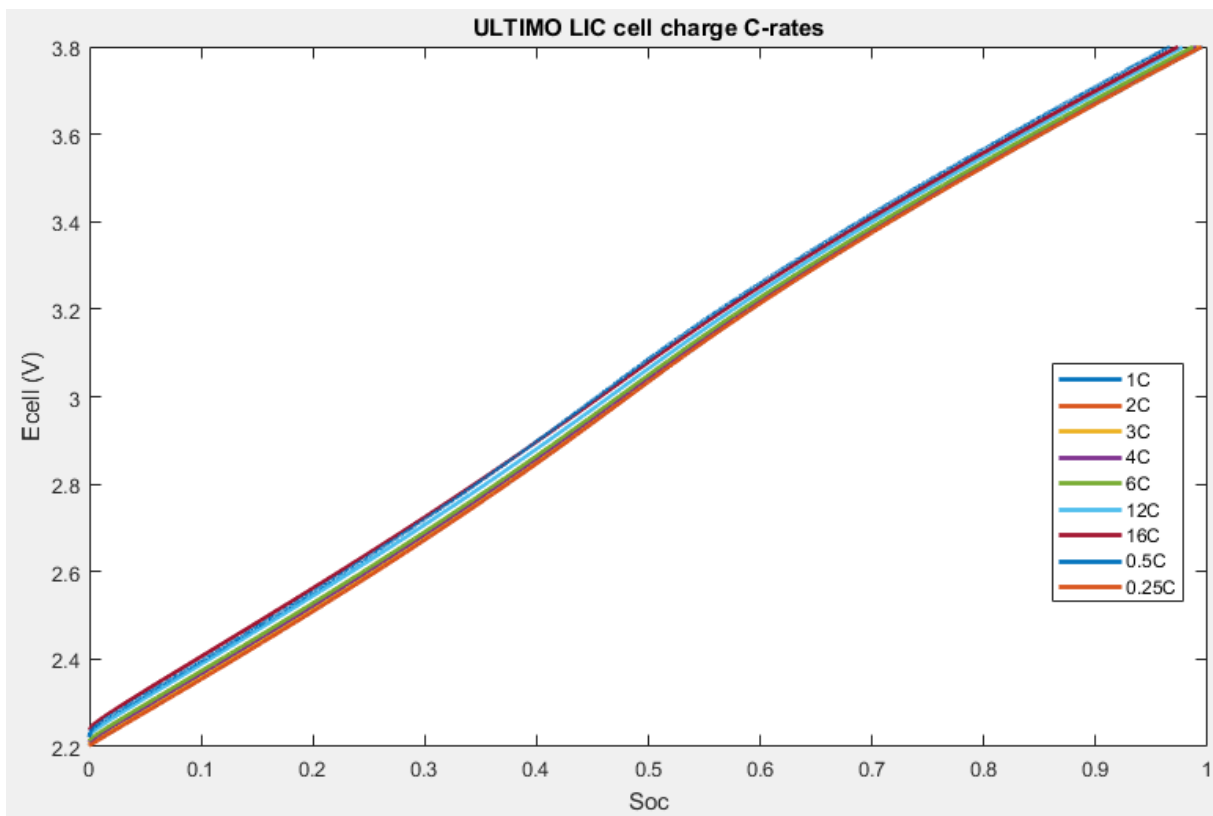


Figure 41: Charging cycles at different C-rates for a ULTIMO LIC cell

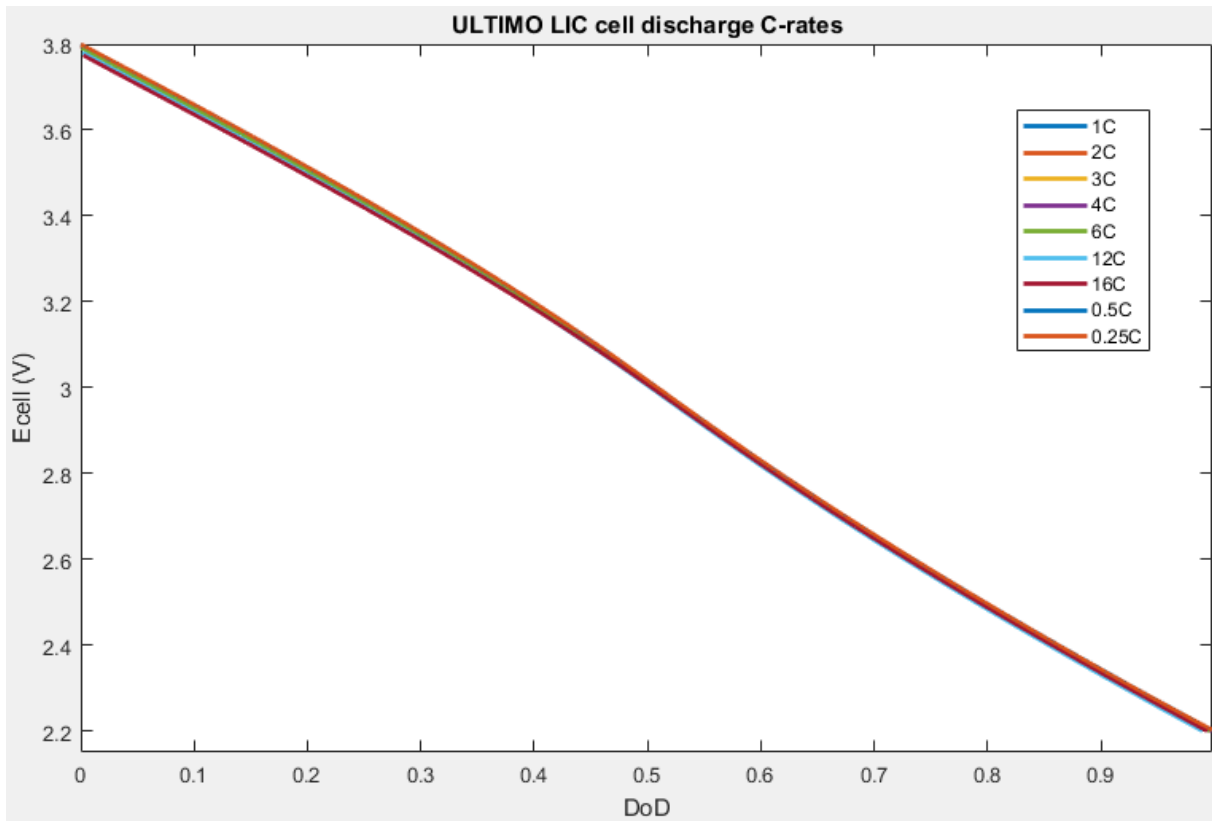


Figure 42: Discharging cycles at different C-rates for a ULTIMO LIC cell

According to these curves, the cell voltage E_{cell} during charging and discharging of the ULTIMO LIC cells does vary in an almost linear way in relation with the Soc of the cells. In this regard, the ULTIMO cell seems to act in the same way as a supercapacitor cell. As it can be seen on these graphs, the current only has a minimal influence on the cell voltage for ranges from 0.25C (125 mA) to 16C (8.0 A). This particularity greatly simplifies the evaluation of the Soc and DoD of this storage technology. In microgrid applications, this means that the only regulation needed for the ULTIMO LIC cell is a voltage control to stop the charging once the cell voltage reaches 3.8V and stop the discharge once it falls to 2.2V. In addition, the intermittency of PV production does not have a significant impact on the efficiency of this type of storage as the impact of different current regimes is neglectable. On the other side, the linear voltage to Soc relation means that the terminal voltage changes constantly during charge and discharge opposed to lithium batteries where the voltage stays the same for the biggest part of the cycle. This means that a converter with voltage regulation is needed in order to connect the LIC cells to a bus, as it is the case for supercapacitors.

For this new technology, the manufacturer announces 100 000 cycles at 80% DoD. We decided to experimentally test the cycle lifetime of two ULTIMO cells to validate this operation life. In order to simulate the ageing of the cells, they have been charged and discharged for 6000 cycles during a two month experiment (57 days). The cells are charged and discharged at 10C (5 A) from maximal voltage 3.8V to minimal voltage 2.2V. A special cycle is performed every 100 cycles, including 1h rest times after charging and discharging to measure the remaining capacity in the cell. During the experiment, the cells are kept in the thermal enclosure regulated at 25

°C. Results for the evolution of the discharged capacity in each cycle are shown in Figure 43 and Figure 44.

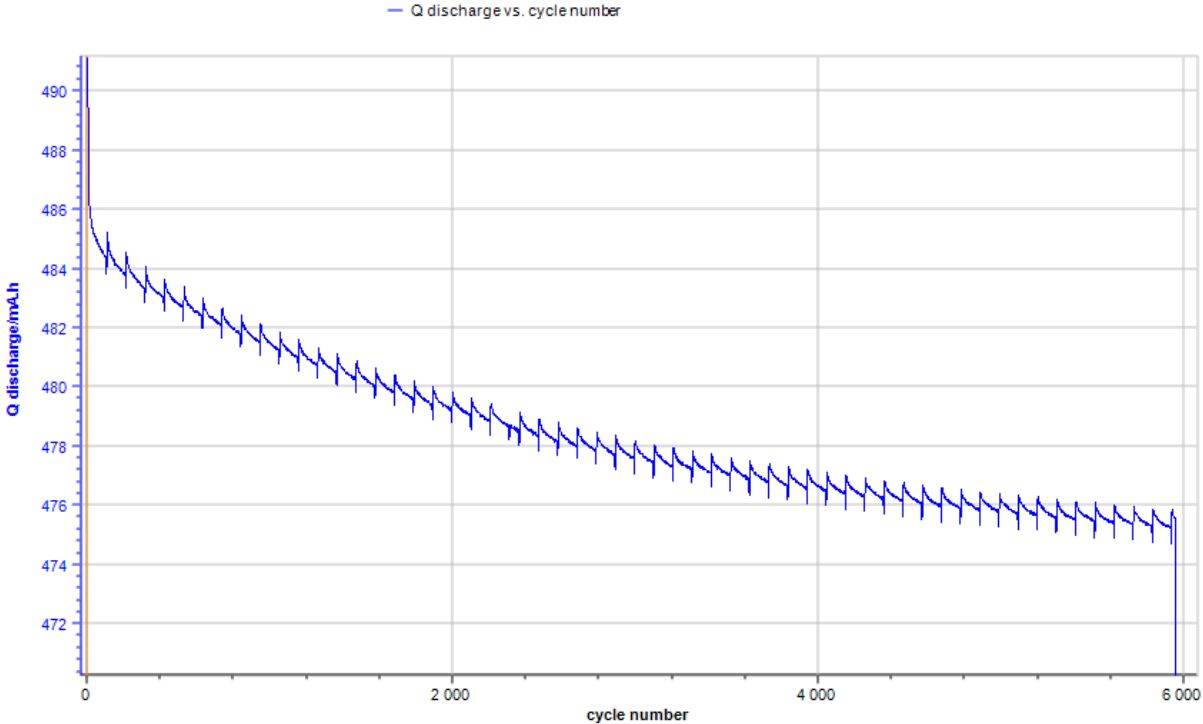


Figure 43: Evolution of the dischargeable capacity in ULTIMO cell 1 over 6000 cycles at 10C. With rest times every 100 cycles.

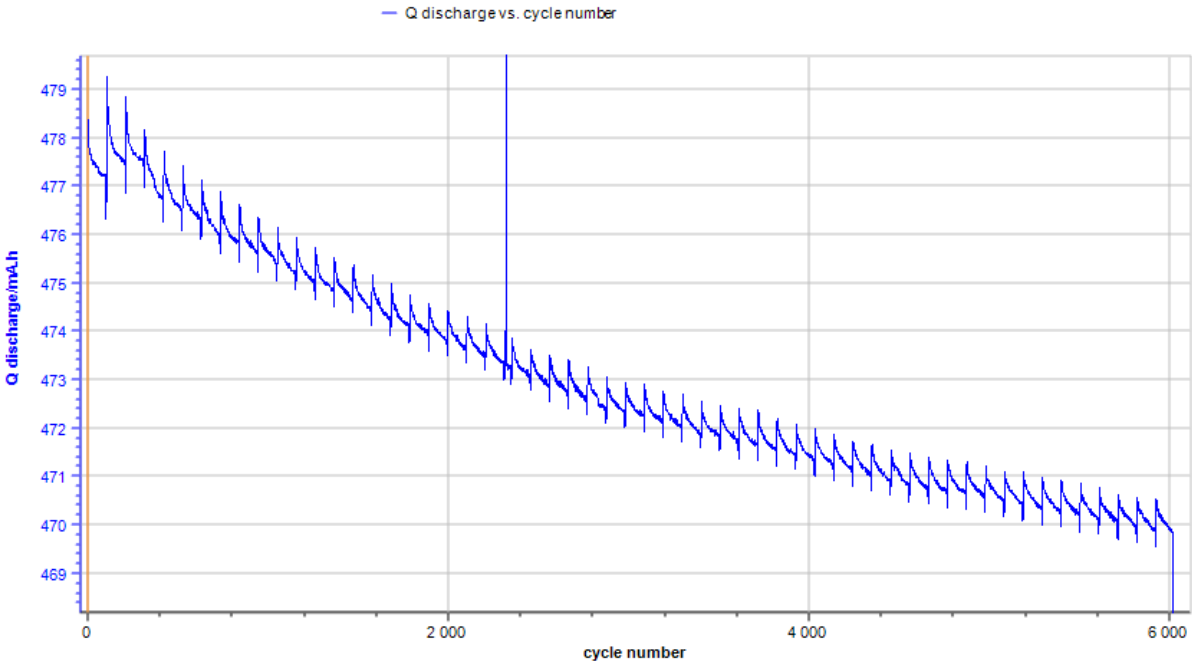


Figure 44: Evolution of the dischargeable capacity in an ULTIMO cell 2 over 6000 cycles at 10C. With rest times every 100 cycles.

For a discharged capacity of 485.2 mAh after 100 cycles, the ULTIMO cell 1 retains 475.9 mAh after 6000 cycles at 10C. This means that after these 6000 cycles the cell still has lost a percent of its capacity equal to:

$$Capacityloss_{cell1} = \frac{485.2 - 475.9}{485.2} * 100 = 1.92\% \quad (39)$$

For a discharged capacity of 479.2 mAh after 100 cycles, the ULTIMO cell 2 retains 470.5 mAh after 6000 cycles at 10C. This means that after these 6000 cycles the cell still has lost a percent of its capacity equal to:

$$Capacityloss_{cell2} = \frac{479.2 - 470.5}{479.2} * 100 = 1.82\% \quad (40)$$

From this observation we can deduce that an ULTIMO cell loses roughly 2 % of its initial capacity after 6000 cycles at 10C at a constant temperature. We can therefore assume that a cell can provide at least 60 000 cycles before reaching a capacity loss of 20% of its nominal capacity when cycled at 10C. By observing these curves, we can observe that the decrease in capacity is not linear. In fact, we observe a decrease in the capacity losses over cycling time, meaning that we can expect more than 60 000 cycles. As a result, we can realistically expect a cycle lifetime close to 100 000 cycles when the cells are used at 1C, at a current ten times lower than in our experiment.

To conclude this part, a comparison of typical voltages, average energy efficiency, cycle lifetime and cost is given in Table 6. Energy efficiency is given for charge/discharge cycles at 1C. Number of cycles is given for 1C until only 80% of the rated capacity is left in the cell.

Table 6: Comparison of the main characteristics of the four studied storage technologies

| Technology | Typical voltages | Energy efficiency (1C) | Cycle Lifetime (1C, 80% capacity) | Cost comparison |
|------------|---------------------------------|------------------------|---|-----------------|
| Lead acid | 1.8 V – 2.4 V 2 V nominal | ~ 70 % | 300 – 1500 cycles depending on technology | + |
| LiFePO4 | 2.5 V - 4.2 V 3.2 V nominal | 96 % - 99 % | ~ 2000 cycles | +++ |
| Li-Polymer | 2.75 V – 4.2 V 3.7 V nominal | 90 % – 97 % | 300 – 400 cycles | ++ |
| LIC | 2.2 V – 3.8 V | 99 % + | 100 000 cycles | +++++ |

When comparing these technologies, Lithium iron phosphate and LIC technologies seem to have the most interesting efficiencies and cycle lifetime, which are the most important parameters for microgrid applications including renewable energies. While both are very expensive, their cost should be reduced if they are used more widely due to mass production. In comparison, lead-acid batteries are cheaper because it is a mature technology that exists for a long time and is still the most used battery storage. LiPo batteries are cheaper but their relatively short cycle life does not justify their use outside of small scale applications. On the other hand, LiFePO₄ and LIC cells have a high voltage variation when compared to lead-acid batteries, meaning that they need more voltage control. On the other side, the impact of current rates is lower in LiFePO₄ cells and even more so on LIC cells thus reducing the control and converter electronics complexity. In addition, LIC cells are especially adapted to intermittency in comparison to the other technologies as they are capable of absorbing high currents peaks similarly to standard supercapacitors while still being able to store a reasonable amount of energy. Further testing of the LIC ULTIMO cells is still needed to justify their exact cycle lifetime in different conditions.

2.7. Modeling methodology for various electrochemical storage elements

For zero energy building applications, it is important to select the right storage technologies and hybridizations. For energy production to consumption system scale simulation purposes, a single and simple equivalent circuit modeling methodology for electrochemical storage elements has been developed. The goal of this modeling technique is to be fast and reproducible for every type of electrochemical storage element described in the previous part.

This methodology focuses on the study of a single elementary cell of the desired electrochemical storage element (ESE).

Within the framework of a global energy system modelization comprising energy production, consumption, storage and exchanges, different ESEs technologies must be modeled. As there are multitudes of usable ESE technologies, it is preferable to opt for a simple modeling methodology that requires few experimental tests. A simple equivalent circuit model with few parameters is obtainable through the method explained in this chapter. This method can be applied to single electrochemical cells for convenience and then extrapolated to bigger accumulators.

The performances of an ESE can be approximated using an equivalent circuit composed of a variable voltage source and a variable resistance as shown in Figure 45.

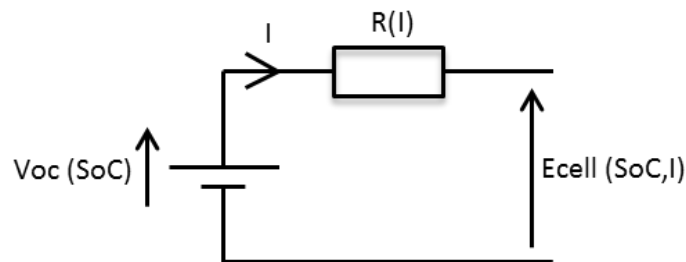


Figure 45: Schematic of the V_{oc} , R equivalent circuit storage model

The voltage source V_{oc} represents the open circuit voltage of the cell and can be expressed in function of its state of charge (SoC). The series resistance R represents the internal resistance of the cell which varies with the intensity of the current I . The total voltage E_{cell} in the cell can be expressed through equation (41).

$$E_{cell} = V_{oc}(SoC) + R(I) * I_{bat} \quad (41)$$

Where I_{bat} is the charge/discharge current applied to the cell.

The proposed modelizing method consists in the identification of the parameters V_{oc} and R for each electrochemical storage technology as follows.

2.7.1. Open circuit voltage Voc

A relation exists between the open circuit voltage Voc and the state of charge of the battery cell, SoC. The cell is charged or discharged by steps in order to determine this relation. Between each step of charge the cell is let to rest until it reaches Voc for that specific state of charge.

Figure 46 shows an example of charge by steps for a LiFePO4 (Li-iron phosphate) from the brand ENIX at it's nominal charge current 1C (1,5A). In this example, a 50mAh charge is applied to the cell for each step, then the cell is let to rest until the voltage has stabilized when $|dV/dt| < 5mV/h$.

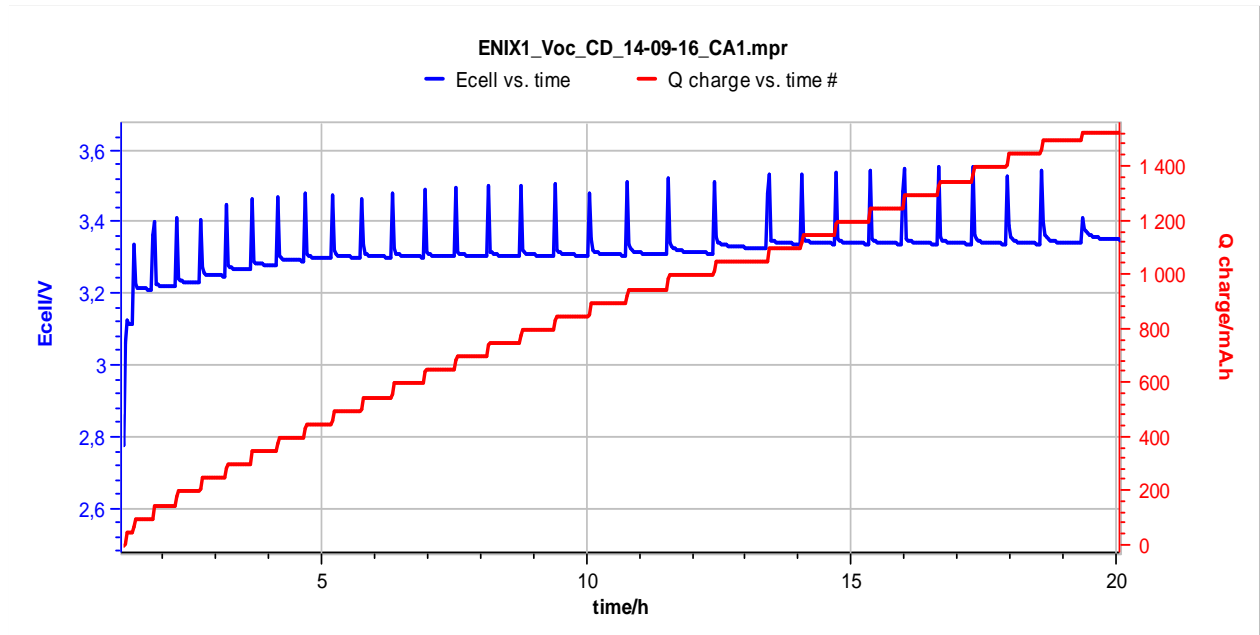


Figure 46: Cell voltage and Ah during step by step charging

A single value of Voc is read for each corresponding SoC. SoC is calculated as described in equation (42):

$$SoC = CAh / Cref \quad (42)$$

Where CAh is the capacity in the battery at the current step (50mAh for the first point)

Cref is the total reference capacity of the cell once it is fully charged. Here Cref = 1528 mAh in our example.

After the full charge or discharge by steps is complete, it is now possible to trace the Voc=f(SoC) in a graph. It is then possible to approach the curve by a function as shown in Figure 47.

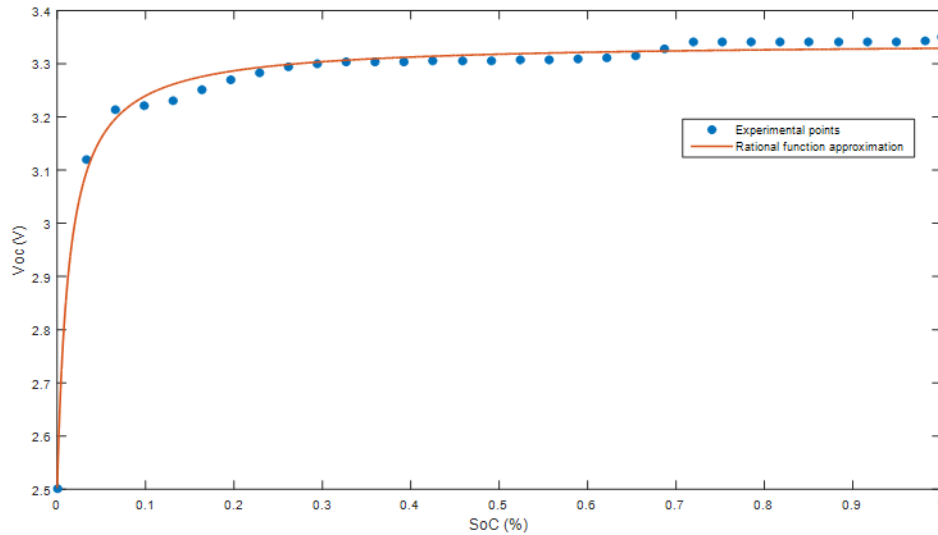


Figure 47: Approaching Voc(SoC) relation with a rational function for an ENIX LiFePO4 cell

In this example, a rational function will be chosen to approximate the Voc(Soc) parameter for this Li-iron phosphate cell. In other cases like supercapacities or lead batteries, a polynomial function could be more appropriate.

This Voc(SoC) relation represents the voltage source in the equivalent circuit model. In order to further complete the model, the internal resistance parameter must be expressed in function of charge/discharge current.

2.7.2. Internal resistance R

The internal resistance of a battery cell can be expressed in multiple ways. However, for simplicity and reproducibility of this modeling technique, the resistance is expressed in function of the charge or discharge current applied to the cell. For this purpose, multiple charge/discharge cycles at different currents have to be done. Figure 48 below shows an example of points of internal resistance for different charge rates: 1C, 2C, 3C, 0.5C, 0.25C and 0.1C for the Li-iron phosphate cell from ENIX. The function is represented on a logarithmic scale in order to approach it with a polynomial function $\log(R) = f(\log(I))$.

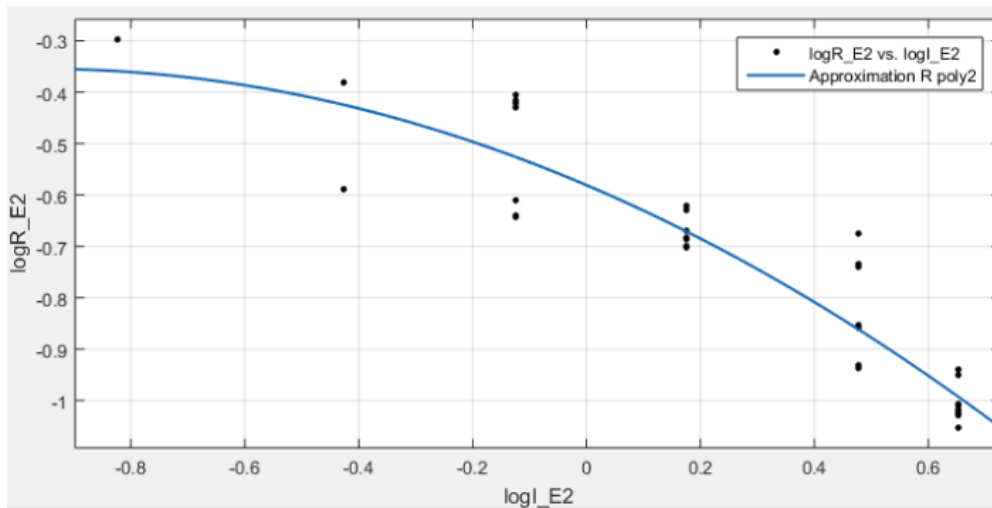


Figure 48: Approaching R(I) relation for an ENIX LiFePO4 cell on a logarithmic scale

Once this relation between resistance and charge/discharge current has been identified, it is used as the series resistance in the equivalent circuit model.

2.7.3. Complete model

Once the two parameters (V_{oc} and R) for this model have been determined, it is possible to combine them for the equivalent circuit model in order to obtain a relation between the total cell voltage E_{cell} , the state of charge SoC and the current I . Figure 49 shows an example of final model curves vs experimental charge curves of the ENIX LiFePO4 cell.

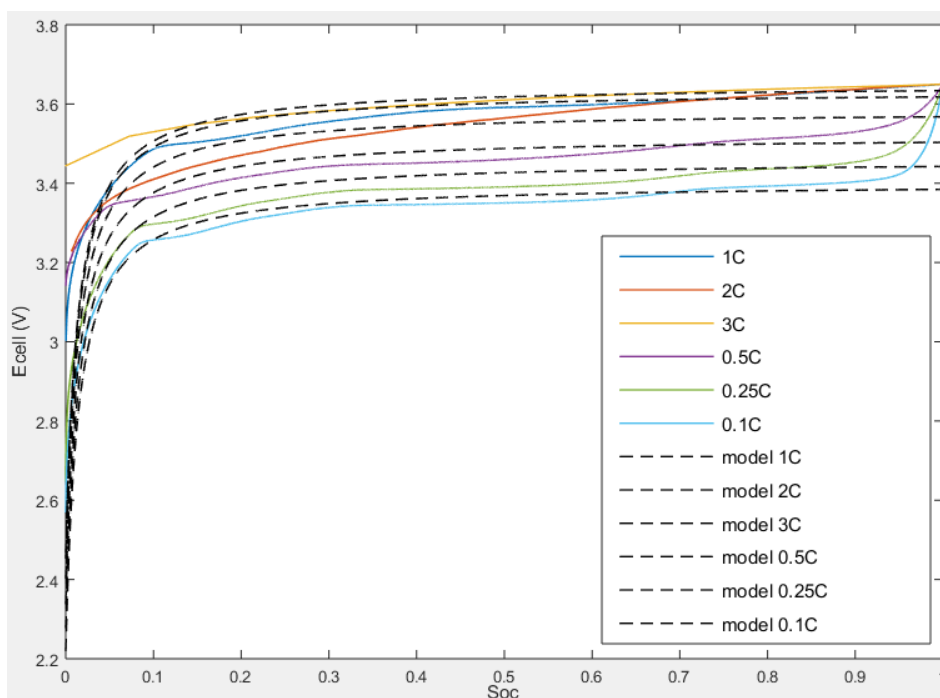


Figure 49: Experimental measures compared to EC model at different current rates for ENIX LiFePO4 cell

When comparing the experimental data with the model data, it can be noticed that the start and end of charge are not very accurately reproduced by the model due to its simplicity, not including capacitive elements. The limitations of such a model are clearly visible on this graph. For the purpose of entire system (building) scale energy simulations, this is not a major problem as most of the usable energy in the cell is transferred during the more stable and linear part of the model.

The relative root mean square error (RRMSE) is used to compare the model to the experimental data for each rate of current. Equation (43) gives the expression of RRMSE and results are shown in

Table 7.

$$RRMSE = \left[\left\{ \frac{\sum_{i=1}^N (y_i - x_i)^2}{N} \right\}^{\frac{1}{2}} \right] / \bar{x} \quad (43)$$

Table 7: Relative Root Mean Square Error between model and experimental data at different current rates

| Charge Rate | I (A) | RRMSE |
|-------------|-------|--------|
| 0.1C | 0,15 | 0,0135 |
| 0.25C | 0,375 | 0,0153 |
| 0.5C | 0,75 | 0,0222 |
| 1C | 1,5 | 0,0196 |
| 2C | 3 | 0,0177 |
| 3C | 4,5 | 0,0686 |

The RRMSE is below 10% (0.1) in general, which is a standard goal for this type of model. It is observable that the error is increasing with charging current. This is due to the fact that the model's Voc parameter is determined at nominal current. Higher currents also increase the cell's temperature, which decreases efficiency. The influence of temperature is not studied in this model and needs further investigation.

In the context of ZEB and microgrid research, energy system models are a crucial point for future building design. In order to develop a complete energy system model, each element of the system is modeled separately. A simple, reproducible and accurate modeling approach for

electrochemical storage elements has been produced. This methodology aims to be applicable for each electrochemical storage technology usable in ZEB and microgrids. In addition, the model's parameters V_{oc} and R are determined through a very limited number of experimental steps: a single step by step cycle charge or discharge and a few charge-discharge cycles at different current rates. This modeling technique can be used for rapid determination of an appropriate energy model for new electrochemical storage technologies to be used in larger-scale system simulation.

The work on the presented modeling methodology forms the basis for uncovering and examining further perspectives. The proposed model can be used to compare general characteristics of different storage elements usable in ZEB and microgrids. A comparison of the model's accuracy and reproducibility with more complex models such as predictive models and neural network models can be done for additional validation. The impact of cell temperature is another point of improvement to be investigated.

2.8. Conclusion

Through this chapter, we have shown that the study of intermittency and their impact on storage elements was more difficult than we initially planned, especially as PV is not the only element generating intermittency. Consequently, studies on charge profiles for the ADREAM building are also complex. Although the results of these first studies are promising, the decision has been made with the supervising team that we would not continue the studies on storage elements and the energy storage needed for ADREAM. We estimated that the research time needed to obtain relevant results was too long and this work was continued by other researchers and PhD students in the ISGE team through new projects. The seven typical profiles resulting from the clustering work will be used in the future for comparative studies of performance on several storage technologies, which was the primary goal of their identification. Another goal was to develop a simple method to identify model parameters for diverse storage elements by using few tests, even if their characteristics were different. Beyond consumption and production data, the insertion of storage elements between both parts greatly depends upon the choice of the microgrid architecture. In this context, we sought to illustrate the utility of storage in a microgrid through a concrete application. We identified that Solar Fuel applications were presenting the characteristics we had been looking for, and would permit us to validate several concepts both in modeling and in modular distributed architectures. The chapters 3 and 4 describe our approach by introducing the Hydrogen energy vector, not only as a contender to electrochemical storage but also as a system load, needing specific I-V profiles, high performance conversion and dedicated storage elements.

REFERENCES

- [35] « Energy - European Commission », *Energy*. [Online]: <https://ec.europa.eu/energy/en/topics/energy-%20strategy/2030-energy-strategy>. [28-oct-2018].
- [36] P. Torcellini, S. Pless, M. Deru, et D. Crawley, « Zero Energy Buildings: A Critical Look at the Definition; Preprint », National Renewable Energy Lab. (NREL), Golden, CO (United States), NREL/CP-550-39833, juin 2006.
- [37] A. J. Marszal et P. Heiselberg, « A Literature Review of Zero Energy Buildings (ZEB) Definitions », 2009.
- [38] A. J. Marszal *et al.*, « Zero Energy Building – A review of definitions and calculation methodologies », *Energy and Buildings*, vol. 43, n° 4, p. 971-979, avr. 2011.
- [39] L. Wang, J. Gwilliam, et P. Jones, « Case study of zero energy house design in UK », *Energy and Buildings*, vol. 41, n° 11, p. 1215-1222, nov. 2009.
- [40] « Building Energy Performance Metrics », *IEA webstore*. [Online]: <https://webstore.iea.org/building-energy-performance-metrics>. [28-oct-2018].
- [41] S.-H. Yoo, E.-T. Lee, et J.-K. Lee, « BUILDING INTEGRATED PHOTOVOLTAICS: A KOREAN CASE STUDY », *Solar Energy*, vol. 64, n° 4, p. 151-161, déc. 1998.
- [42] « ADREAM | Laboratory for Analysis and Architecture of Systems ». [Online]:<https://www.laas.fr/public/en/adream>. [28-oct-2018].
- [43] P. Eiffert et G. J. Kiss, *Building-Integrated Photovoltaic Designs for Commercial and Institutional Structures: A Sourcebook for Architects*. DIANE Publishing.
- [44] « ZEP - Home ». [Online]: sur: <https://zepbv.nl/>. [24-oct-2018].
- [45] « Tesla Solar Roof ». [Online]: <https://www.tesla.com/solarroof>. [24-oct-2018].
- [46] M. Bressan, « Développement d'un outil de supervision et de contrôle pour une installation solaire photovoltaïque », phdthesis, Université de Perpignan, 2014.
- [47] R. C. Temps et K. L. Coulson, « Solar radiation incident upon slopes of different orientations », *Solar Energy*, vol. 19, n° 2, p. 179-184, janv. 1977.
- [48] T. M. Klucher, « Evaluation of models to predict insolation on tilted surfaces », *Solar Energy*, vol. 23, n° 2, p. 111-114, janv. 1979.
- [49] A. Skartveit et J. A. Olseth, « A model for the diffuse fraction of hourly global radiation », *Solar Energy*, vol. 38, n° 4, p. 271-274, janv. 1987.
- [50] J. F. Orgill et K. G. T. Hollands, « Correlation equation for hourly diffuse radiation on a horizontal surface », *Solar Energy*, vol. 19, n° 4, p. 357-359, janv. 1977.
- [51] D. G. Erbs, S. A. Klein, et J. A. Duffie, « Estimation of the diffuse radiation fraction for hourly, daily and monthly-average global radiation », *Solar Energy*, vol. 28, n° 4, p. 293-302, janv. 1982.
- [52] K. Neuhaus, « Optimisation de modèles d'ensoleillements à des fins d'estimation de production photovoltaïque du bâtiment ADREAM ». LAAS-CNRS, Université Paul Sabatier, 2015.

- [53] K. Neuhaus, I. PAPAS, B. Estibals, et C. Alonso, « COMPARISON OF ELECTRICAL ENERGY PRODUCTION USING TWO SOLAR IRRADIATION MODELS OF BIPV », in *Electrimacs 2017*, Toulouse, France, 2017, p. 7p.
- [54] V. M. Gutierrez, F. Defay, V. Boitier, et H. Schneider, « [STUDY OF PHOTOVOLTAIC CELLS IMPLANTATION IN A LONG-ENDURANCE AIRPLANE DRONE] », p. 62.
- [55] A. A. Munshi et Y. A.-R. I. Mohamed, « Photovoltaic power pattern clustering based on conventional and swarm clustering methods », *Solar Energy*, vol. 124, p. 39-56, févr. 2016.
- [56] B. Everitt, Éd., *Cluster analysis*, 5th ed. Chichester, West Sussex, U.K: Wiley, 2011.
- [57] S. Lloyd, « Least squares quantization in PCM », *IEEE Transactions on Information Theory*, vol. 28, n° 2, p. 129-137, mars 1982.
- [58] M. Ester, H.-P. Kriegel, J. Sander, et X. Xu, « A Density-based Algorithm for Discovering Clusters a Density-based Algorithm for Discovering Clusters in Large Spatial Databases with Noise », in *Proceedings of the Second International Conference on Knowledge Discovery and Data Mining*, Portland, Oregon, 1996, p. 226-231.
- [59] A. K. Jain, « Data clustering: 50 years beyond K-means », *Pattern Recognition Letters*, vol. 31, n° 8, p. 651-666, juin 2010.
- [60] « A Guide to Understanding Battery Specifications », p. 3.
- [61] J. Valencia, « Handbook Of Batteries 3rd Edition ».
- [62] *Générateurs électrochimiques*. 2018.
- [63] J. Dulout, C. Alonso, L. Séguier, et B. Jammes, « Development of a photovoltaic low voltage DC microgrid for buildings with energy storage systems », in *ELECTRIMACS 2017*, Toulouse, France, 2017, vol. 2017, p. 6p.
- [64] G.-A. Nazri et G. Pistoia, Éd., *Lithium Batteries*. Boston, MA: Springer US, 2003.
- [65] B. Scrosati, « Lithium Batteries: from early stages to the future », in *Lithium Batteries*, B. Scrosati, K. M. Abraham, W. Van Schalkwijk, et J. Hassoun, Éd. Hoboken, NJ, USA: John Wiley & Sons, Inc., 2013, p. 21-38.
- [66] D. Porcarelli, D. Brunelli, et L. Benini, « Characterization of lithium-ion capacitors for low-power energy neutral wireless sensor networks », in *2012 Ninth International Conference on Networked Sensing (INSS)*, Antwerp, Belgium, 2012, p. 1-4.

CHAPTER 3 : HYDROGEN AS A VECTOR OF ENERGY

Today, Hydrogen applications seem to achieve a high level of technological maturity equally on the production of H₂, electricity and storage of H₂ on large ranges of voltage, power and energy. Many fuel cells and electrolyzers can now be used with security and considered as « black boxes » once the system is put into service as it is done for batteries. Given the limited experience of the LAAS-CNRS supervisor team of this PhD work in the field of H₂, it seemed necessary to carry out a more consequent state of the art allowing us technological choices without having to take into account the security measures related to Hydrogen. The initial objective of the team beyond the acquisition of new knowledge was to find stackable elements with low power and energy per element. The aim was study new electrolyzers easily in our laboratory while choosing elements that could be representative of the field to allow the validation of different concepts of PV insertion in grids, design of dedicated converters and the choice of best suited storage element. For all of these reasons, we choose a small scale electrolyser cells in the Watt scale.

In this chapter, before presenting preliminary electrolyser test studies, a synthesis of the state of Hydrogen systems is carried out. The objective of this synthesis is to show the potential it offers and the technological maturity reached in certain applications, as much in the transport as on the electric network applications. At the end of this chapter, specific studies made within this laboratory to obtain electrolyzer models are described. The idea of obtaining a relatively simple model of electrolyser described in this chapter follows the system modeling approach begun in Chapter 2 on the search for simple models of storage elements. However, although in the literature, hydrogen is increasingly represented as a potential storage vector, as an alternative to electrochemical storage, the models of electrolyzers and especially the identifications of their parameters were not obvious. The approach we have taken in this way should make it easier in the future to identify the parameters and, in addition, the data treatment that was needed to make them more reliable. For questions of time and to answer the specifications of the project "H₂ production of hydrogen by CPV", we first treated the production of hydrogen without taking care of its use, supposing that the aspects of storage or injection into a network could be done later.

3.1. Why Hydrogen?

While the world is entering a new era threatened by extreme climatic changes as well as the exhaustion of fossil fuels; political forces, industrial actors and the general public start to realize that the implementation of a new energetic paradigm is needed. From this context, Hydrogen emerges among other technologies as a possible large scale vector of energy management, storage and transportation. Hydrogen has been used in the industry for more than two centuries for its interesting chemical properties, but it also has the scary taste of a highly explosive

combustive labeled on top of it. The diffusion of educated knowledge concerning this gas is decisive in order to achieve a larger social acceptability of hydrogen as a vector of energy.

3.1.1. History

The usage of Hydrogen starts at the beginning of the XVIth century with the Swiss alchemist Paracelsus [67] who studied properties of the Vitriol and sulfuric acid applied on iron. He stated that he was intrigued by the inodorous gas emerging from his experiment.

In the middle of the XVIIIth century, the British chemist Henri Cavendish resumes the work of Paracelsus, leading to the discovery of the inflammability of this gas by Swiss chemist Theodore Turquet de Mayerne in 1703, naming it “inflammable air”. This work was continued by a number of chemists among which the famous French Lavoisier. A communication to the Academy of Science was issued in 1783, giving it its current name: Hydrogen, which means “gas which produces water”.

Starting in 1782, one of the first usages of Hydrogen was made by the Montgolfier brothers, using it as traction for hot air balloons.

At the beginning of the XIXth century, Hydrogen penetrated many industrial sectors such as chemistry, petrochemistry and fertilizer manufacturing. In the meantime, the gas was progressively used for domestic use and street lighting in a nearly half to half mix with carbon monoxide in a large number of countries, including France. It was later replaced by natural gas. Hydrogen has since then been increasingly used in diverse industrial sectors for its chemical properties and energetic performances.

3.1.2. Characteristics

Hydrogen is a gas of many qualities. It is neither toxic nor polluting, making it widely usable. It is the lightest of all gases, making it very volatile at four times the diffusion speed of natural gas. Hydrogen-air mixtures can ignite with very low energy input, 1/10 that required igniting a gasoline-air mixture and is the most energetic fuel by mass unit (2.2 times that of natural gas). Its presence is very abundant on earth in its atomic form, associated to oxygen and carbon but it is very rare in its molecular form H_2 , therefore processes are needed to extract it. In contrast, some of its attributes can be critical for development of Hydrogen technologies. In fact, its low ignition energy makes hydrogen-air mixtures very likely to detonate or ignite even through an invisible spark or a static spark from a person. High security measures are therefore preconized, even if the gas has an exaggerated false bad reputation due to incidents such as the Hindenburg accident [68] or the Hydrogen bomb.

Table 8 presents the main characteristics of this gas in comparison to methane (CH_4).

Table 8: Main characteristics of Hydrogen

| Characteristic | Hydrogen H ₂ | Methane CH ₄ |
|-------------------------------------|--|--|
| Lower calorific value | 10.8 MJ/m ³ – 118.8 MJ/kg 3.0 kWh/m ³ - 33.3 kWh/kg | 35.8 MJ/m ³ – 46.8 MJ/kg 9.9 kWh/m ³ – 13.9 kWh/kg |
| Higher calorific value | 12.7 MJ/m ³ – 141.7 MJ/kg 3.5 kWh/m ³ - 39.4 kWh/kg | 39.8 MJ/m ³ – 55.5 MJ/kg 11.1 kWh/m ³ – 15.4 kWh/kg |
| Gas density at 20.3K | 1.34 kg/m ³ | - |
| Gas density à 273K | 0.08988 kg/m ³ | 0.708 kg/m ³ |
| Liquid density at 20.3K | 70.79 kg/m ³ | - |
| Theoretical liquefaction energy | 14 112 J/g (3.92kWh/kg) | |
| Auto-ignition temperature in air | 858K | 853K |
| Flame temperature in air at 20 °C | 2 384K | 2223K |
| Ignition limits in air (vol %) | 4-75 | 5-15 |
| Detonation speed in air | 2.0 km/s | 0.7 km/s |
| Stoichiometric mixture in air (vol) | 29.53 % | 10.5 % |

3.1.3. Usages of Hydrogen

Hydrogen can be described as a potential energy carrier. Its potential energy can be liberated in different ways depending on the application, be it by using its chemical characteristics or through consumption to fuel other applications. It plays an important role in industrial chemical reactions. In the petrochemical industry, large quantities of H₂ are used for reactions.

In physics and engineering, Hydrogen can be used in a variety of ways. Liquid Hydrogen is used in cryogenic research, including superconductivity studies [69]. It is used as a rotor coolant in generators as it has the highest thermal conductivity of any gas and it can be used as a shielding gas in atomic hydrogen welding [70].

In the field of semiconductors, Hydrogen is used for its properties to stabilize amorphous silicon and carbon materials [71]. It can be a potential electron donor in oxide materials [72].

As an energy carrier, it can be used directly as a transfer, transport or storage vector for energy grids. In energy applications, its potential energy is mostly released through combustion, or through recombination with Oxygen to produce electricity.

3.2. Hydrogen applications

Hydrogen is considered today as the best ally of renewable energies and constitutes a good complement to electrical energy. Several industrial sectors have identified this point and are developing their products towards hybridization with Hydrogen. These sectors using Hydrogen include but are not limited to the automobile sector, the aeronautics sector, the space industry and the chemical industry.

3.2.1. The automobile

The Hydrogen car is the best step towards the promise of a zero emission vehicle. More specifically, the fuel cell electric vehicle is propelled by an electrical motor in the same way as in the battery electric car (conventional electric car) with the only difference being that the electrical energy is produced directly on board, through a fuel cell consuming Hydrogen.

A fuel cell stack is composed of multiple cells comprising two electrodes separated by a polymer membrane which functions as an electrolyte. Electricity, heat and water are produced by the chemical reaction between the hydrogen injected in the Anode and the Oxygen injected in the Cathode. The Hydrogen vehicle only evacuates water, which makes it a cleaner alternative to regular diesel or gasoline cars.

The following Table 9 shows a comparison of characteristics between fuel cell electric cars and battery electric cars.

Table 9: Comparison of characteristics of fuel cell cars with regular electric cars

| | Fuel cell car | Regular electric car |
|--------------------------|----------------------|---|
| Autonomy (Km) | 400 to 500 | 150 to 200 |
| Energy Efficiency | 35% H2 to movement | 75% Electricity to movement |
| Full recharge | 3 to 5 minutes | 7 to 8 hours Or 5 to 7 minutes for interchangeable batteries |
| Cost today | ~70 to 80K€ | ~25K€ |

Architecture of a fuel cell vehicle

A fuel cell vehicle is mostly composed of the following elements:

- A Hydrogen tank pressurized between 700 bars for lightweight vehicles and 350 bars for heavier ones such as buses.
- A PEM fuel cells unit, comprising multiple stacks of PEM fuel cells.
- An electrochemical storage device such as a battery or supercapacitors which can function in hybridization with the fuel cell units and for electric command.
- An electric motor.
- A compressor to pressurize the air fed to the fuel cell, which has to be at around 1 to 3 bars depending on the technology used.
- Heat exchangers and a radiator to evacuate the heat produced by the fuel cell stack.
- Converters and sensors for control command and energy management.

Figure 50 represents a generic and simplified architecture for a fuel cell car.

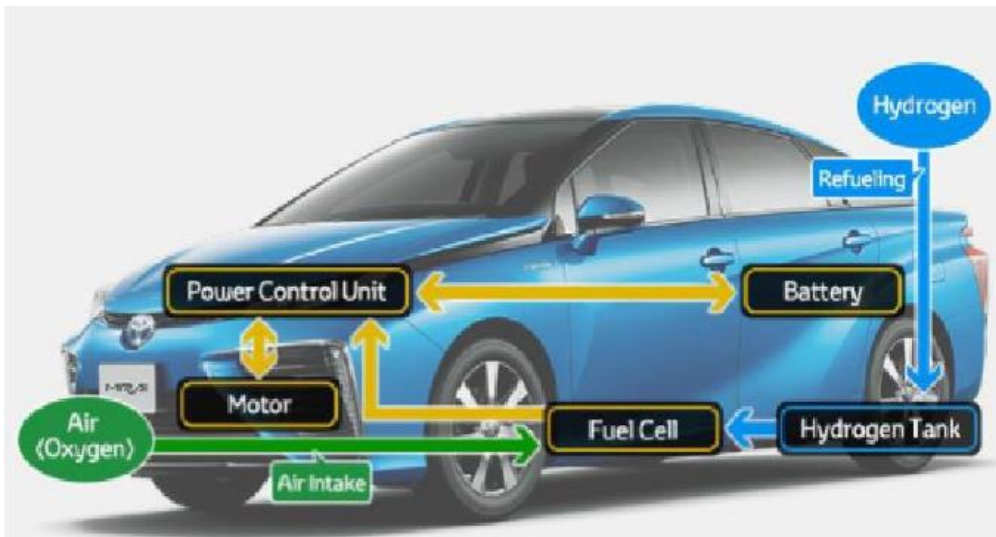


Figure 50: Simplified representation of a fuel cell car architecture

As the need for energy alternatives to classic fuel cars increases on the market both ecologically and economically, most significant automobile industrials have tried their luck at developing a fuel cell hybrid vehicle. Figure 51, Figure 52, Figure 53 and Figure 54 depict several modern or representative fuel cell car models from different Brands.



Figure 51: 2009 - Peugeot 307 cc FiSyPAC hybrid electrical prototype, equipped with JCS Li-ion batteries and a CEA-PSA 20kWe fuel cell stack as a « range extender »



Figure 52: Toyota - FCHV-adv model 2009. Advanced fuel cell vehicle with four high pressure hydrogen tanks at up to 700 bar, precursor to the more known Toyota Mirai.



Figure 53:2010 - Hyundai Tucson iX35 FCEV hybrid. Equipped with 21 kW Li polymer battery, 100 kW Bipolar metallic fuel cell and a 5.6 kg Hydrogen tanks at 700 bars – It achieved an autonomy of 640 km.



Figure 54: 2015 - TOYOTA Mirai, with a 114 kW fuel cell (155 horses), and a 1.6 kWh Ni-Mh battery.

Advantages of fuel cell cars:

First of all, fuel cell cars are more ecological than classic fuel and diesel cars, as they do not reject carbon dioxide. As a matter of fact, water and heat are the only rejection of this type of vehicle. This is an incredibly valuable asset given the emerging changes in political views concerning climate change, especially in Europe. Secondly, unlike fossil fuels, Hydrogen abundant on earth and there will surely never be any natural shortage. With theoretical hydrogen to electricity efficiencies of 85-90% for fuel cells, fuel cell vehicles can save a lot of energy while maintaining high autonomies over long distances. A fuel cell car will consume about 1 kg of Hydrogen per 100km on average, which makes it one of the most autonomous among hybrid vehicles.

Implications:

Despite all of these qualities, wide range commercialization of Fuel cell vehicles is still in its infancy, why is that?

On the market, fuel cell cars still are extremely expensive and are rivaling only on the luxury car market. The Toyota Mirai for example has a cost of nearly 80k€, which compares to the average 25k€ French citizens usually pay for a new unused car. This high price is partly due to

the high production cost of adapted fuel cells containing platinum, a very rare and extremely costly material. Repairing and maintenance for fuel cell vehicles also has a heavy cost as the technology requires very specific knowledge and materials.

The alternation of hydration and dehydration cycles inside of a fuel cell progressively damages the membrane between the electrodes. In addition, free radicals are produced as a secondary effect of the reaction and accelerate the membranes degradation. These two effects affect the lifetime of fuel cells used in vehicles, making it difficult to last for more than 150 000 km before changing the fuel cell.

For previously mentioned reasons, Hydrogen is considered a high risk gaz. Hydrogen recharge stations for fuel cell cars are therefore expensive to build and to maintain, making them rare with only a few hundred existing across the world. In France, the company Air Liquide has constructed fifteen Hydrogen stations equipped with pressurized Hydrogen gaz at 700 bars. The recharge rate in these stations is around 3 minutes for 5kg of Hydrogen.

Transporting Hydrogen remains difficult today. Both compressors and energy used for compression as well as fuel tanks are expensive, making transportation costly in a compressed form. Achieving liquid state is only possible within extremely low temperatures; making it equally difficult for a transportation chain.

As Hydrogen is an extremely volatile and inflammable gas, storing it in vehicles requires extreme caution and very controlled conditions, as an unlucky choc to the reservoir can lead to an explosion. For these reasons, fuel cell cars have special temperature restrictions, as the water inside of the cells could freeze. These factors make the Hydrogen and fuel cells hard to store inside of vehicles.

Finally, as clean as fuel cell cars are, it is really the Hydrogen production process that determines the ecological footprint of this technology. In fact, the most used process is steam reforming from hydrocarbons, which emits carbon dioxide. Other techniques include partial oxidation of methane, coal gasification, biomass gasification and water electrolysis.

Most actors of the automobile industry are convinced that hybrid electric fuel cell vehicles will have an important spot in the future. Decisive projects have already hit the market for Korean brand Hyundai and Japanese brands Toyota and Honda. More of the same type should follow in 2018-2019.

3.2.2. Space application

Hydrogen has been used as fuel for space travel since the very beginning as it has the highest energy concentration, making it the most lightweight fuel and a perfect match for space industry. A liquid Hydrogen and liquid Oxygen mix is still used today to fuel Astrium's European Ariane 5 rocket (Figure 55) which tanks a total of 28 tons of liquid Hydrogen at -252.87°C and 162 tons of Oxygen at -183°C. Here, the Hydrogen combustion started from mixing it with Oxygen creates a huge amount of water steam which expands at high speed through the nozzle of the Vulcain motor. This high speed gas ejection propels the aircraft strongly enough to leave the atmosphere.



Figure 55: Rocket Ariane 5 takeoff

3.2.3. Aeronautics

Hydrogen is a clean energy source with a high potential for aeronautics applications where it can be used through fuel cells similarly to fuel cell cars. The electrical energy generated from the fuel cells by mixing the tanked Hydrogen and the Oxygen from the atmosphere is used to power various instruments, especially when the plane is on the ground. The French brand Air Liquide has developed mobile Hydrogen refueling solutions that can be used in airports. These stations are hybrid trucks that can roll up directly next to the plane and can tank up to 300 liters of Hydrogen.

Other Hydrogen applications in the aeronautics domain such as satellite planes, drones and the more classic zeppelin balloons are depicted in the following figures.



Figure 56: Hydrogen satellite plane designed by ONERA, France



Figure 57: Hydrogen drone designed by the company Intelligent Energy using fuel cells.



Figure 58: Hydrogen zeppelin balloon used in the 1930s.

In airports, Hydrogen is also used for maintenance and logistics in order to reduce pollution and costs when using lift trucks, nacelles and baggage trucks. Hydrogen recharge stations can be implemented directly inside the airport to refuel those equipments.

3.2.4. Hydrogen uses in the industry

Hydrogen is highly used in different sectors of industry. The biggest one is the chemical industry, where Hydrogen is used for producing ammoniac (NH_3) which is the basis for most fertilizers. Hydrogen is also used in chemical creation of amines, ethanol and oxygenated water. It is also used in to increase the level of saturation of unsaturated fats and oils, in the production of methanol and as a reducing agent of metallic ores.

In the petrochemical industry, Hydrogen is consumed in very high amounts for Hydrocracking to achieve thermolysis and decompose petroleum into its high value components as well as hydrotreatment, desulfuration and lightening of heavy hydrocarbures.

In the energy sector, new global warming and greenhouse gas reduction policies as well as fossil fuel scarcity are all factors that encourage the development of the Hydrogen domain as a fuel and storage technology for renewable energy production.

3.3. Hydrogen storage

The development of safe and efficient methods of hydrogen storage is a prerequisite for the use of hydrogen with fuel cells for the applications cited above and more. Hydrogen is a very volatile gas and occupies a significant volume at atmospheric pressure. In order to store it, this volume has to be reduced and therefore the density increased. Three different techniques are used today to store Hydrogen in different states which are high pressure gas, liquid Hydrogen and solid Hydrogen formed from absorption or adsorption. These three storage techniques will be discussed in this section.

3.3.1. High pressure gas Hydrogen

Today, Hydrogen gas storage is possible in composite reservoirs in opposition to historically used steel reservoirs. Composite materials are more lightweight, and have a better resistance to high pressure, making it possible to store Hydrogen gas at 700 bars. An example of a composite storage unit is shown in Figure 59. It is composed of a waterproof envelope, a working composite structure and a protective layer.



Figure 59: Composite Hydrogen reservoir from the brand Toyota

From an economic point of view, the amount of stored energy is compared to the energy required to achieve this given storage. Figure 60 below depicts the energy cost of pressurizing Hydrogen with different methods. As we can see on the “Multistage” curve, the energy required to pressurize Hydrogen at 700 bars is roughly 12% of the amount of stored energy using multistage pressurizing, which is the most used technique.

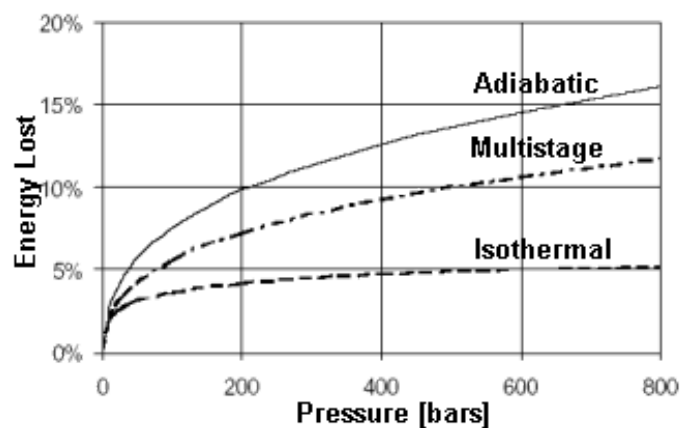


Figure 60: Energy loss by pressurizing Hydrogen for different techniques

Gaseous Hydrogen storage is mastered in Europe by the French Firm Air Liquide which claims that it is an economic storage technique as pressurizing to 700 bars only costs 10% of its lower calorific value and is very fast. Higher pressures are a technological challenge and the 700 bar reservoirs are still very cumbersome. In addition, the cylindrical form makes it hard to incorporate into vehicles and special security measures have to be taken as the risk with handling Hydrogen is high.

3.3.2. Liquid Hydrogen storage

A liquid Hydrogen storage tank is much lighter than a gas tank. Therefore it is mostly used in special applications as the high cost of the liquefaction process is hard to justify for other types of applications. In fact, energy loss in the liquefaction process is highly dependent on plant capacity, as shown in figure X below. Losses are 30% in the best case.

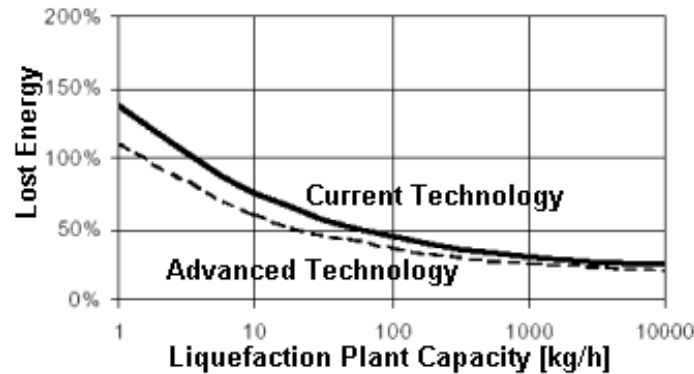


Figure 61: hydrogen liquefaction cost in comparison to stored energy and dependance on plant capacity

Hydrogen liquefaction temperature is 20 K (-252°C) in atmospheric pressure conditions. A density of 70 Kg/m³ can be obtained for liquid Hydrogen. Two types of processes are used for Hydrogen liquefaction: the Claude cycle and the Brayton Cycle.

The Claude Cycle, named after the founder of Air Liquide, uses three steps of cooling in order to liquefy Hydrogen. The three steps are described in Table 10 below.

Table 10: The three steps of the Claude Cycle developed by Air Liquide.

| Temperature in K | Method used for each cooling step |
|------------------|---|
| 300K to 230K | Mechanical freezing unit |
| 230K to 80K | Calorific heat exchange cycle with liquid Nitrogen (N ₂) |
| 80K to 20K | Calorific heat exchange cycle based on Joule-Thomson refrigeration using dihydrogen (H ₂) |

The Brayton cycle was invented by Barber in 1791 and later applied by George Brayton. It is also known as Joule cycle. This process is based on a thermodynamic exchange with liquid Helium (He) and is a very easy and fast way to liquefy Hydrogen. In order to perform this process it is required to liquefy Helium first, which greatly reduces the energy efficiency though.

Liquid Hydrogen stored in a tank designed for automobiles is estimated to lose 5% of its capacity per day, making it usable for fleets like taxis or buses but not for personal vehicles. This process is called “boil off”. In addition, Hydrogen molecules exist in two forms, ortho (anti-parallel electron spin) and para (parallel electron spin). While room temperature Hydrogen is a mixture of both, liquid hydrogen turns into pure para Hydrogen over the course of a few days. This process releases enough heat to turn the liquid Hydrogen into gas over that period.

For this reason, Hydrogen has to be catalytically converted to all para Hydrogen in the liquefaction process or even a perfect cryogenic tank would lose about 30% of its Hydrogen in just two days. This conversion immensely adds to the cost and complexity of liquefaction.

For all the reasons previously described, liquid Hydrogen is very unlikely to be used in common applications outside of critical areas such as space travel.

3.3.3. Solid Hydrogen storage

Storage of Hydrogen in solids is achievable in two different ways: Adsorption and Absorption.

Adsorption storage

Adsorption, also called physisorption, is the increase of density of a gas at the surface of a solid through intermolecular forces. Adsorption increases with pressure and inversely with temperature. Being purely physical, adsorption is entirely reversible. It decreases with pressure and with rising temperature. Activated carbons, which are highly porous amorphous carbon materials, are mostly chosen as Hydrogen sorption material but the process is possible with a variety of different materials. Adsorption storage has a relatively low volumetric density but the materials are cheap so it can be a cost efficient storage solution.

Absorption storage

Absorption, also called chemisorption is the reversible chemical combination of Hydrogen with atoms of a large variety of metals or metallic alloys to form hydrides. This permits to store Hydrogen particles inside of other materials in a solid state without needing very high pressure and ambient temperature with high volumetric density. In opposition to adsorption, materials for absorption are more expensive and catalyzers must be used to accelerate the reactions.

As a recent example, the company McPhy in France used the absorption process to create a new Hydrogen storage technology named McStrore, storing Hydrogen in a solid state in form of discs using equation (44) below.



The resulting solid is fireproof and has a high concentration. One disk of approximately 30 cm diameter and 1.5 cm thickness can contain 600 liters of Hydrogen, which means 50 gram Hydrogen gas. This completely reversible technology can easily be paired with renewable energy production as it can absorb variations of production of the energy sources or electrolyzer cells. The Hydrogen can be released by heating the disk with an energy efficiency of nearly 90%.

3.4. Hydrogen production through electrolysis

Electrolysis is the electrochemical process of forcing non spontaneous redox reactions by applying a reverse current equal or higher than that given by the equivalent spontaneous redox reaction. Let's take the historical example of Fluorine. Fluorine is so highly reactive that it's

impossible to isolate it through standard chemical reactions. In 1886, the French scientist Henri Moissan managed to isolate Fluorine by applying a current to a melted mix of anhydrous Potassium Fluoride and Hydrogen Fluoride. Today, Fluorine is still produced industrially using this technique.

An electrolyser cell (EC) is an electrochemical cell powered by an external electrical source, triggering a non-spontaneous chemical reaction. Figure 62 below depicts an electrolyser cell used in the Dow process for industrial Magnesium production. Here, the electrolyte is melted Magnesium Chloride. When an external electrical current passes through the cell, reduction of Magnesium cations and oxidation of anion chlorides occur, forming gaseous dichloride. Similar to a battery, oxidation is produced at the anode and reduction happens at the cathode.

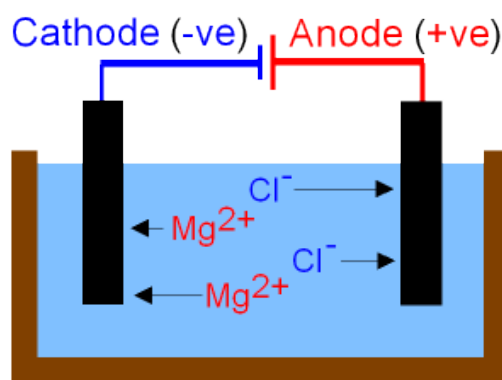
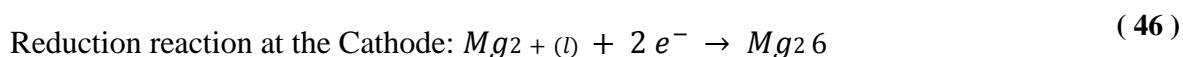
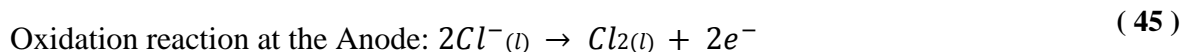


Figure 62: simplified schematic of Magnesium electrolysis

The negative pole of the electrical source is connected to the cathode (-) while the positive pole of the source is connected to the anode (+). The following reactions occur:



Electrons are travelling through the external connection from the anode to the cathode while cations migrate from the cathode to the anode through the electrolyte. In opposition to galvanic cells, electrolysis cells have both of their electrodes inside the same compartment with only one electrolyte with a specific pressure and concentration.

3.4.1. Water electrolysis

Water electrolysis is used to produce Hydrogen from an external electrical source such as the power grid, but also renewable sources such as photovoltaics or wind energy. In a water electrolysis process, the water molecule (H_2O) is dissociated into dioxygen (O_2) and dihydrogen (H_2) following equation (47).



Water dissociation enthalpy is: $\Delta\text{H} = 285 \text{ kJ/mol}$

This dissociation needs an external energy input which depends on the enthalpy and the entropy of this reaction. The theoretical dissociation potential at 298K is 1.481 V. Classical industrial water electrolysis cells use potentials around 1.7V up to 2.1V, attaining efficiencies of 70% to 85% using the higher calorific value of Hydrogen: 3.55kWh/Nm³. Industrial water electrolysis cell energy consumption spans from 3 to 4 kWh/Nm³ of produced Hydrogen. Minimal theoretical water input rate for a water electrolysis cell is 0.8L/Nm³ of Hydrogen, but is close to 1L/Nm³ in reality. Purified water must be used in this process in order to reduce impurities which accumulate inside of the cell as well as negative effects from chlorides on the electrodes. In fact, the ionic conductivity of the water used must be inferior to a few $\mu\text{S}/\text{cm}$.

A water electrolysis cell is constituted of two electrodes (anode and cathode) connected through an external DC current source and separated by an electrolyte permitting ionic conduction. Standard electrolytes are acid or basic aqueous solutions, polymer proton exchange membranes and ceramic dioxygen conduction membranes, mostly determining the different water electrolysis technologies. The next part will focus on explaining these different technologies.

Water electrolysis cell technologies

Water electrolysis cells exist in two types of structures: mono-polar and bipolar. Both structures can use three different types of electrolytes: alkaline, proton exchange membrane (PEM) or solid oxides (SOEC).

The first water electrolysis cells were using mono-polar electrodes, where the anode was connected to the electrical positive (+) and the cathode to the electrical negative (-). This type of cell was connected in parallel in electrical circuits.

Bipolar systems use dual electrodes, used as anode on one side and as cathode on the other side. Bipolar electrolysis cells are therefore connected in series in electrical circuits and the electron conduction from the anode to the cathode takes place inside of the electrode, creating a low ohmic voltage drop due to its thickness. Bipolar cell structures offer a better current density and are more compact. Nevertheless, they also present the technical difficulty of having the same electrode in an oxidation process on one side and in a reduction process on its other side. Today, most industrial systems are based on bipolar technology while small scale cells can still be manufactured as mono-polar technology.

In addition, water electrolyzers have to be waterproof and isolated as well as being resistant to corrosion in a variety of temperature and pressure conditions in order to attain maximal efficiency.

3.4.2. Alkaline Electrolysis:

Alkaline electrolysis is the most used process of water electrolysis in the industry and is therefore much matured. Ranging from a capacity of 0.5 up to 800 Nm³/h of produced Hydrogen, Alkaline cells use an aqueous Potassium Hydroxide solution at a concentration varying with temperature (typically 25% mass at 80° up to 40% mass at 160°C). Sodium can also be used but it has a lower ionic conductivity at equivalent temperature and more abundant

chloride and sulfate impurities. A schematic of the structure of an alkaline water electrolysis cell can be seen in Figure 63.

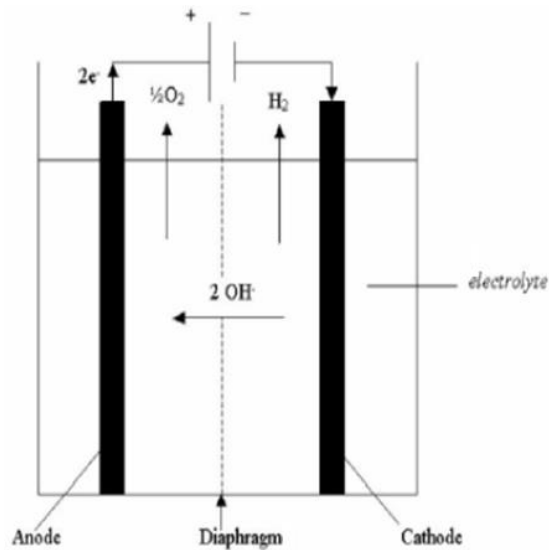
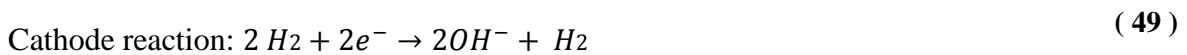
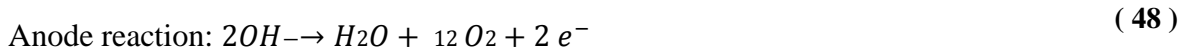


Figure 63: Simplified schematic of alkaline electrolysis

Reactions at the anode and the cathode are given in equations X and Y:



Multiple research laboratories are conducting R&D on alkaline fuel cells aiming to replace the liquid electrolyte by solid OH⁻ ion conduction membranes. In case of a future success of this research, this type of solid membranes could also be applied to alkaline electrolyzer cells.

3.4.3. Acid Proton Exchange Membrane (PEM) electrolysis

Acid electrolysis uses a solid electrolyte membrane constituted of polymers capable of proton conduction. Figure X shows a schematic of a classical PEM electrolyzer cell.

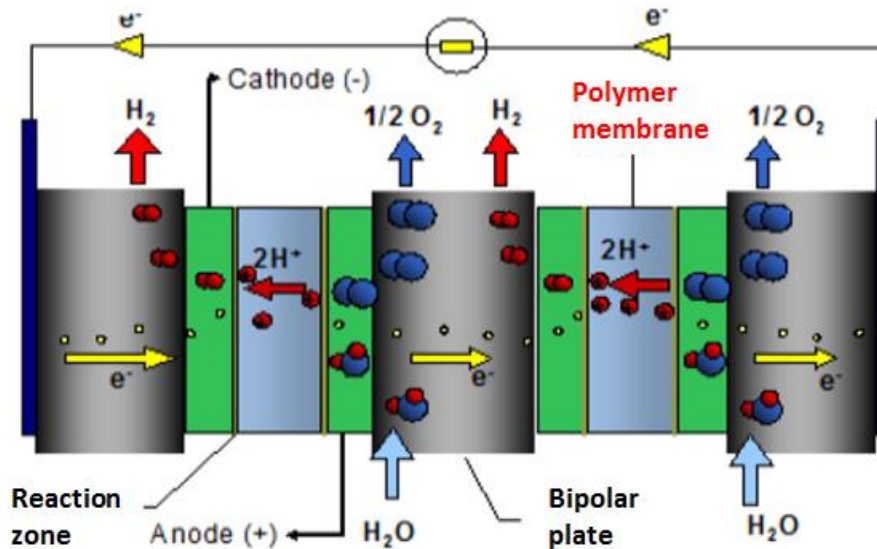
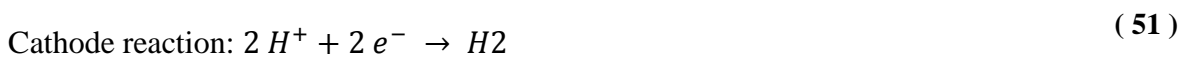
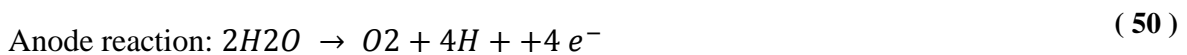


Figure 64: Schematic of a PEM electrolyzer cell

Equations X and Y give the reactions at the anode and at the cathode of the PEM electrolyzer cell:



This water electrolysis technology presents a large number of advantages such as not having a problematic liquid electrolyte, being very compact and easy to manufacture, being very simple in design, having very limited corrosion issues and a slightly higher efficiency than other technologies. In addition, PEM cells are less affected by perturbations on the external DC source, making it best suited for renewable energy applications suffering intermittencies. However, the polymer membrane and the electrodes composed of noble metals highly increase the cost of this technology when compared to alkaline electrolysis. Nevertheless, PEM electrolysis profits from research and development on PEM fuel cells and also from the cost reduction due to plant capacity increase for fuel cells and is therefore considered becoming a promising technology for the future of water electrolysis. Today, small scale PEM electrolysis is used in several applications such as submarines or in space for generating Oxygen.

3.4.4. High temperature solid oxide electrolysis cell (SOEC)

This technology directly emerged from SOFC and PCFC fuel cell technologies. A solid oxide electrolyzer cell uses a solid oxide or ceramic electrolyte at high temperatures between 500°C and 800°C. This type of cell can operate at pressures from 1 bar to a few hundred bars and reaches maximal efficiency when provided with both stable current and heat inputs, reaching up to 80%. Due to these specifications, they are most useful when paired with solar concentrators or high temperature nuclear reactors. Figure 65 depicts a schematic of an SOEC.

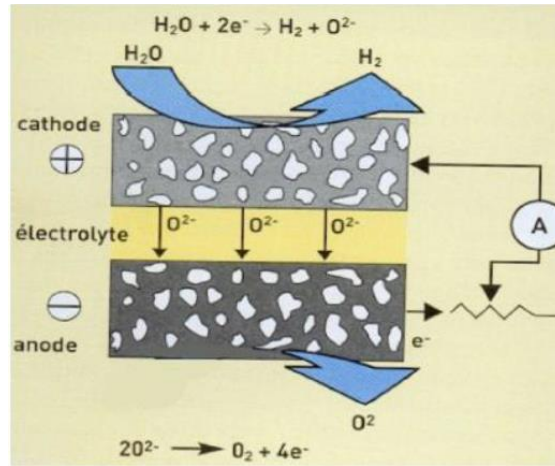


Figure 65: Schematic of high temperature SOEC electrolysis cell

Reactions at the anode and at the cathode of an SOEC are respectively given in equations (52) and (53):



Research and development on SEOC technology is ongoing in CERAMATEC in the USA as well as in the French CEA. The company Sylfen6 associated with Boeing and Sunfire designed a 50kW SOEC demonstrator for the US Navy in February 2016.

For the experimental part of this thesis work presented in Chapter 4, PEM water electrolyzer cells are used due to the small scale of the experimental prototype as well as safety and simplicity reasons.

3.5. Cost of Hydrogen produced from electrolysis

Even in a preliminary state, the development of a new energy vector needs a scientific analysis and a life cycle analysis, but also a global economic analysis including capital costs, operation costs and maintenance costs.

First of all, the cost of Hydrogen produced through water electrolysis is directly related to the cost of local electrical energy, and therefore to the means of producing said electrical energy. For renewable energy production plants, the majority of the costs are the capital cost of the equipment. Depending on authors and hypothesis (scale, performance and cost), renewable energy costs between 27 and 55 \$/GJ (100-200€/MWh) which translates into a cost of 4 to 6 \$/kg of Hydrogen when referring to the equivalent higher calorific value, given a functioning period of more than 7000h/year.

At this stage of development, numbers have to be considered with extreme caution. In fact, very little experimental return is available on real performance and cost of modern water electrolysis technology. But even in its current R&D status, preliminary economic analyses do not disqualify this new technology.

As an example, with the hypothesis of a massive hydrogen production based on wind farms and deep cavity storage in the region Rhône-Alpes in France, the prospective cost of Hydrogen produced through water electrolysis in 2050 could be around 0.6 to 0.9\$/kg (0.5-0.7€/kg).

The French organism CGSP (“Commissariat general à la stratégie et à la prospective”) for general strategy and prospection has published a study on the cost of water electrolysis in 2014. The graph from Figure 66, taken from this study, compares the price of Hydrogen produced through water electrolysis from two different technologies to the price of Hydrogen produced through steam metal reforming and natural gas in Europe.

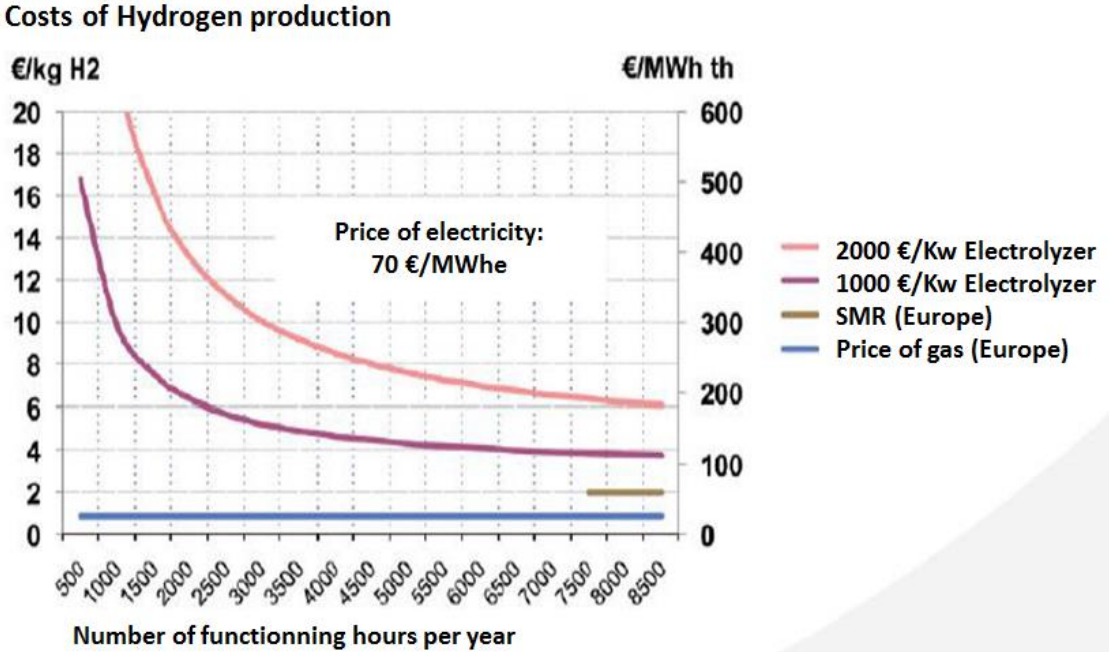


Figure 66: Comparison of the price of produced Hydrogen through water electrolysis using two different technologies and the price of Hydrogen produced through steam metal reforming in Europe. CGSP study

In this study, six different scenarios for Hydrogen production through water electrolysis are prospected, with varying characteristics. Results of this study are shown in Table 11 below.

These scenarios use the following special hypothesis for renewable energy production, storage, or electrolysis:

1. Alkaline Electrolysis.
2. PEM electrolysis using wind farm energy sources.
3. PEM electrolysis with estimated performance for the years 2025-2030.
4. Same as scenario 3 but using photovoltaic energy sources.
5. Same as scenario 3 but using oversupply from renewable energies. In this scenario, storage cost is considered zero as this energy would otherwise be lost.
6. Theoretical perfect best case scenario for awaited future Hydrogen production for comparison.

Table 11: Comparison of the cost of produced Hydrogen over 6 scenarios using different hypothesis. CGSP study.

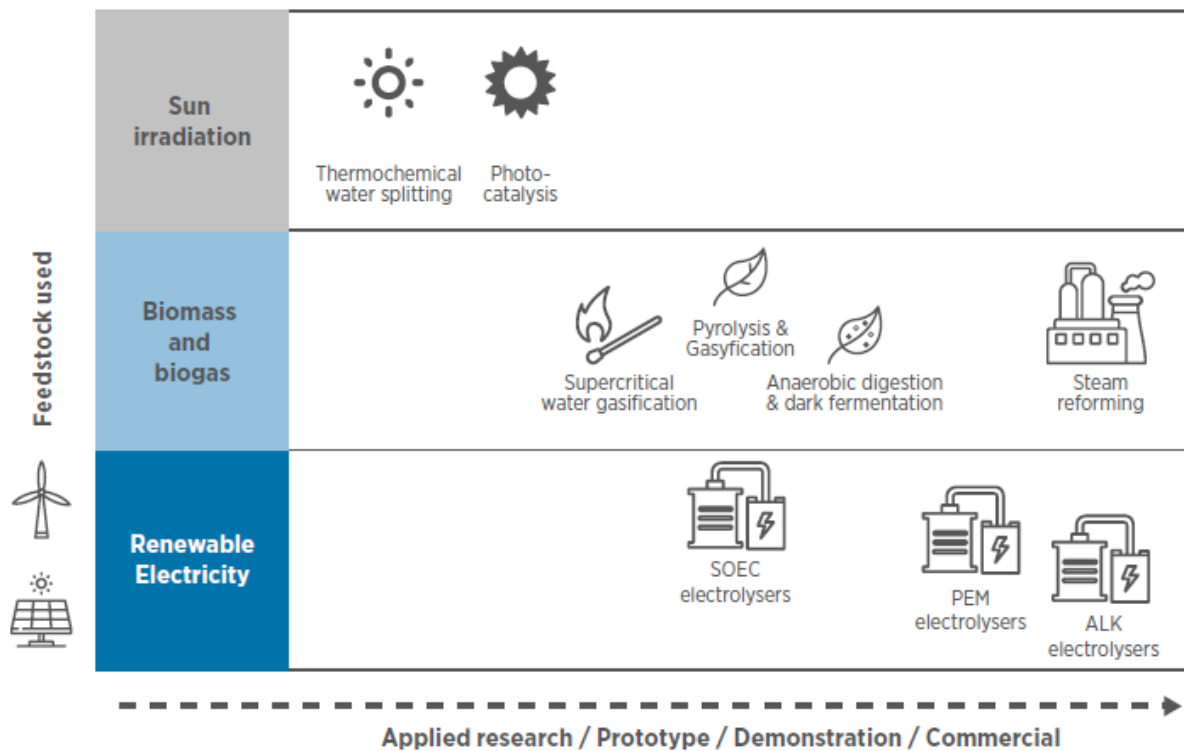
| Scenario | | 1 | 2 | 3 | 4 | 5 | 6 |
|----------------------------|-------|------|------|------|------|------|------|
| Cost of the EC | €/kW | 2000 | 2500 | 800 | 800 | 800 | 800 |
| Efficiency of electrolysis | | 60 % | 50 % | 80 % | 80 % | 80 % | 80 % |
| Annual production | kWh | 7000 | 2000 | 2000 | 1000 | 500 | 7000 |
| Cost of stored electricity | €/MWh | 70 | 70 | 70 | 140 | 0 | 60 |
| Cost of produced Hydrogen | €/kg | 7,0 | 18,3 | 6,1 | 12,2 | 10,5 | 3,7 |
| | €/MWh | 68 | 177 | 59 | 118 | 102 | 36 |

The very specific concept of producing Hydrogen through electrolysis based on renewable solar energy sources, as in scenario 4 and 5 of Table 11, is classified under “Solar fuel”.

3.6. Solar Fuel: producing hydrogen from solar energy

As we saw throughout this chapter, Hydrogen is an energy carrier and not a source of energy. It can be produced in a variety of ways using different production methods and energy sources. Within the context of decarbonisation of the energy sector set by the Paris agreement, the production of Hydrogen from renewable energy sources is preferred to other sources.

Several pathways exist for Hydrogen production from renewable energy. The International Renewable Energy Agency (IRENA) recently published a report on Hydrogen production from renewable power [73]. This study provides a comparison in maturity of the different Hydrogen production technologies with renewable sources as we can see in Figure 67.



Notes: ALK = alkaline; PEM = proton exchange membrane; SOEC = solid oxide electrolyser cell.

Figure 67: Comparison of maturity for different Hydrogen production methods based on renewable energies. IRENA 2018

Among these technologies, we find PEM electrolyzers supplied by renewable electricity such as solar PV. The specific field of solar fuel Hydrogen produced using PV power has been an ongoing topic of research in the world.

In Ajaccio, Corsica, the MYRTE platform is producing solar Hydrogen since 2012 [74]. With 560 kW PV power and a 210 kW PEM electrolyser cell, the platform provides the local energy grid with renewable energy without the influence of solar intermittency. By combining Fuel cells with heat exchangers, this installation provides the electricity and hot water for about 200 local housings. The University of Corsica, the French Environment and Energy Management Agency (ADEME) and the company AREVA are associated in this project to conduct research on solar to Hydrogen conversion. The MYRTE PV plant is visible in Figure 68 while Figure 69 and Figure 70 respectively depict the electrolyzer station and the Hydrogen and Oxygen storage tanks of the station.



Figure 68: Solar PV installation of the MYRTE platform in Ajaccio



Figure 69: Electrolyser station for solar Hydrogen production of the MYRTE platform in Ajaccio



Figure 70: Hydrogen and Oxygen storage tanks at MYRTE platform in Ajaccio

In South Australia, the government has announced the construction of a 15MW renewable Hydrogen plant in January 2018. This project is described as a “globally-significant demonstrator project” for the Hydrogen and energy sector. It aims to supply the power grid and enable renewable wind and solar energy to be exported outside of Australia.

In Japan, the government aims for an 80 % reduction in greenhouse gas (GHG) emission by 2050. In order to achieve this, the increase in renewable energy production is an absolute key necessity. Being an insular state without the convenience of largely available international grid interconnections, Japan more than other states needs to include energy storage to mitigate the intermittency of renewable energy production. In 2015, 95 % of Japan’s energy supply is imported and the decision to stop nuclear energy production after Fukushima has increased this dependency. To tackle this problem, the Japanese government supports its industrial energy sector with the goal to become one of the first “Hydrogen societies”. As a result, 2400 Hydrogen vehicles are in usage in Japan today with 101 operational H₂ charging stations around the archipelago. The objective for the government is to increase this number to 40000 Hydrogen vehicles and 160 stations in 2020, and even further to 800 000 vehicles for 900 stations in 2030 [75]. The Japanese government aims to halve the installation price of Hydrogen recharge stations by 2020 and to increase the part of Hydrogen that is produced using renewable sources.

Figure 71 shows a recent installation in Huis Ten Bosh Hotel in Japan () includes Hydrogen production from solar power through water electrolysis, storage tanks and fuels cells to produce local electricity and heat.

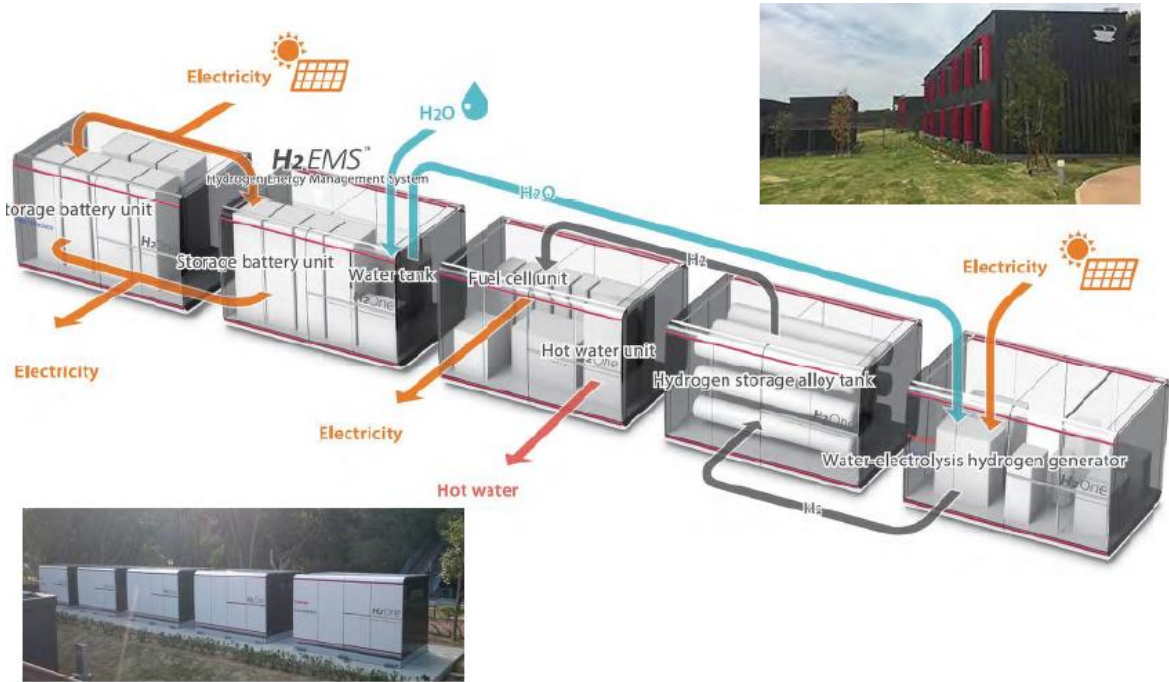


Figure 71: Hydrogen energy supply in Hsui Ten Bosh Hotel, using Batteries, electrolyzer cells and fuel cells for local energy supply

With this in mind, Japanese research institutes are studying the usage of Hydrogen both as energy storage for renewable production and the direct use of Hydrogen in vehicles or in gas distribution through pipelines and combustion like traditional CH₄ gas. As the space is limited

for production of solar energy in Japan, the study goes further by imagining a potential intercontinental Hydrogen transport to fuel the state's energy grids. The first step for this revamped energy supply system is the development of technological solutions for solar to Hydrogen conversion. In the University of Tokyo, the RCAST and more specifically the team of Prof. Sugiyama are conducting research on the association of high efficiency multi-junction PV cells with concentration (CPV) with PEM water electrolyzer cells. Figure 72 contains pictures of the CPV and electrolysis installations for experimental research in the University of Tokyo.

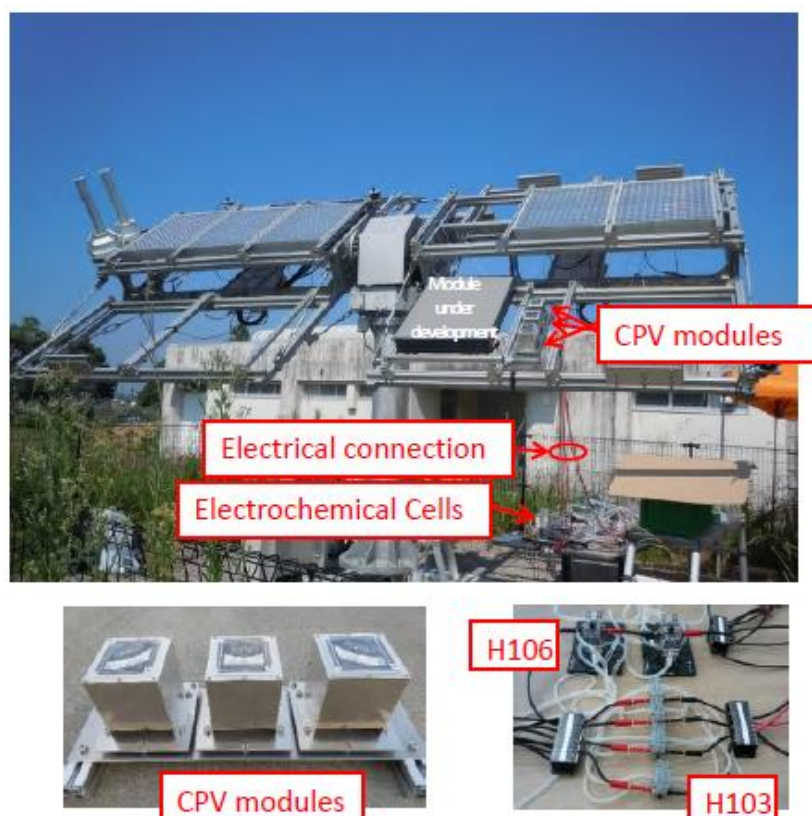


Figure 72: CPV and Electrolyzer installations in the University of Tokyo

As this research team has a great expertise in the fields of CPV and electrolysis, achieving a 24.4 solar to hydrogen conversion [3], a joint research project with our team in LAAS was initiated. The aim of this project is the design of a small scale microgrid for solar to hydrogen conversion. Preliminary studies on the electrolyzer cells used in this project were carried out between the LAAS and the RCAST to produce precise models and identify key parameters for our application.

3.7. Electrolyzer study

Electrolyzers are electrochemical systems that need specific working conditions. The efficiency of the electrolysis reaction depends heavily on these working conditions. In order to better understand the functioning of a cell and to be able to optimally size the control electronics, both experimental tests and a modeling approach were conducted on electrolyzer cells (EC).

3.7.1. Experimental testing of electrolyzer cells

For the Hydrogen production in the joint project between LAAS and RCAST, two small scale PEM electrolyzer cells from the brands H-TEC and HORIZON have been studied. The two cells are visible on Figure 73.

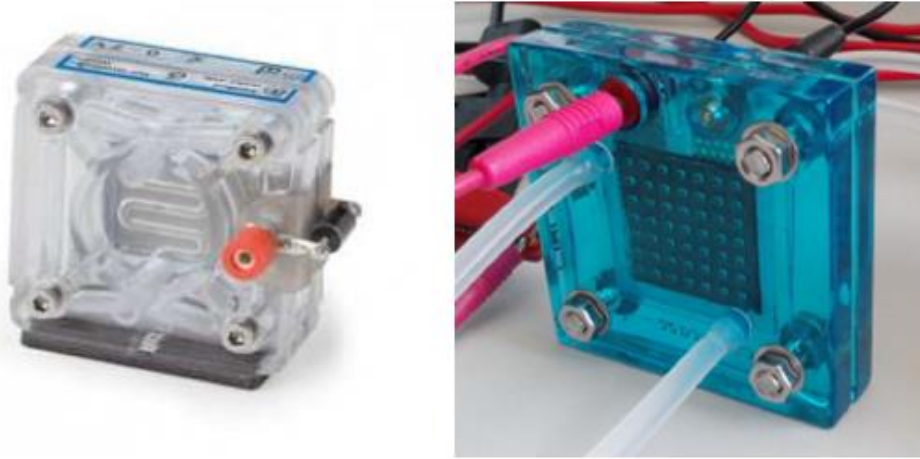


Figure 73: Electrolyzer cells from the brand H-Tec (left) and Horizon (right).

We chose to optimize energy efficiency over maximum production. This is why we conducted tests on these ECs with the goal to determine which cell would be the most efficient and how to connect it in an optimal way to a microgrid for achieving maximal efficiency. The cells were both tested for their specific voltage ranges and current limits as specified in Table 12.

Table 12: Specifications for the two different ECs

| specifications | H-Tec cell | Horizon cell |
|-----------------------------------|------------|--------------|
| Maximal current limit | 2 A | 1 A |
| Minimum voltage to start reaction | 1.5 V | 1.5 V |
| Absolute maximum voltage | 2.5 V | 2 V |

For the efficiency tests, the cells are connected to a programmable DC voltage source. Two sealed graduated reservoirs for the produced Hydrogen and Oxygen connected to the cells through plastic tubes (Figure 74). A stopwatch is used to measure the time of the experiments.



Figure 74: The two electrolyzers connected to graduated reservoirs via plastic tubes, experimental setup

The following calculations are used to determine the efficiency of the cells for each test.

The consumed electrical energy:

$$\text{Consumed energy (Ws)} = \text{Voltage (V)} * \text{Current (A)} * \text{period (s)} \quad (54)$$

The equivalent energy for Hydrogen:

$$\text{Equivalent energy (Ws)} = \text{volume of H}_2 \text{ (cm}^3\text{)} * \text{LCV of H}_2 \text{ (J/cm}^3\text{)} \quad (55)$$

$$\text{With LCV of H}_2 = 10800 \text{ kJ/Nm}^3 = 10.8 \text{ J/cm}^3$$

$$\text{And } 1 \text{ J} = 1 \text{ Ws}$$

The cell efficiency:

$$\text{Efficiency (\%)} = \frac{\text{Equivalent energy}}{\text{Consumed energy}} * 100 \quad (56)$$

The cells are tested separately using the same voltage source. The voltage is increased progressively from the minimum voltage to the maximum voltage for each cell with increments of 0.1 V. For each voltage level, a startup time of 1 minute is given to the cell before starting the experiment. After this startup time, the H₂ production of the cell and the current is measured during a period of 1 minute. Experimental test results are shown in Table 13 and Table 14.

Table 13: Experimental test results for the H-Tec EC

| Voltage (V) | Current (A) | Consumed energy (Ws) | Volume of Hydrogen (cm ³ /min) | Equivalent energy (Ws) | Efficiency (%) |
|-------------|-------------|----------------------|---|------------------------|----------------|
| 1,6 | 0,15 | 14,40 | 0,5 | 5,40 | 37,5 |
| 1,7 | 0,39 | 39,78 | 1,5 | 16,20 | 40,72 |
| 1,8 | 0,5 | 54,00 | 4,0 | 43,17 | 80,00 |
| 1,9 | 0,78 | 88,92 | 6,0 | 64,76 | 72,83 |
| 2 | 1,02 | 122,40 | 8,0 | 86,35 | 70,55 |
| 2,1 | 1,26 | 158,76 | 9,5 | 102,54 | 64,58 |
| 2,2 | 1,48 | 195,36 | 11,0 | 118,73 | 60,77 |
| 2,3 | 1,7 | 234,60 | 13,0 | 140,32 | 59,81 |
| 2,4 | 1,92 | 276,48 | 15,0 | 161,90 | 58,56 |

For the Horizon cell, voltages of 1.92 V and 1.95 V were tested in order to reach the current limit (1 A) without exceeding it too much.

Table 14: Experimental test results for the Horizon EC

| Voltage (V) | Current (A) | Consumed energy (Ws) | Volume of Hydrogen (cm ³ /min) | Equivalent energy (Ws) | Efficiency (%) |
|-------------|-------------|----------------------|---|------------------------|----------------|
| 1,6 | 0,24 | 23,04 | 1,5 | 16,20 | 70,31 |
| 1,7 | 0,53 | 54,06 | 3,5 | 37,80 | 69,92 |
| 1,8 | 0,68 | 73,44 | 5,0 | 54,00 | 73,52 |
| 1,9 | 0,93 | 106,02 | 6,5 | 70,20 | 66,21 |
| 1,92 | 0,98 | 112,90 | 7,0 | 75,60 | 66,96 |
| 1,95 | 1,08 | 126,36 | 8,0 | 86,40 | 68,37 |

Figure 75 shows a graphic representation of the compared efficiencies for both cells versus the cell voltage.

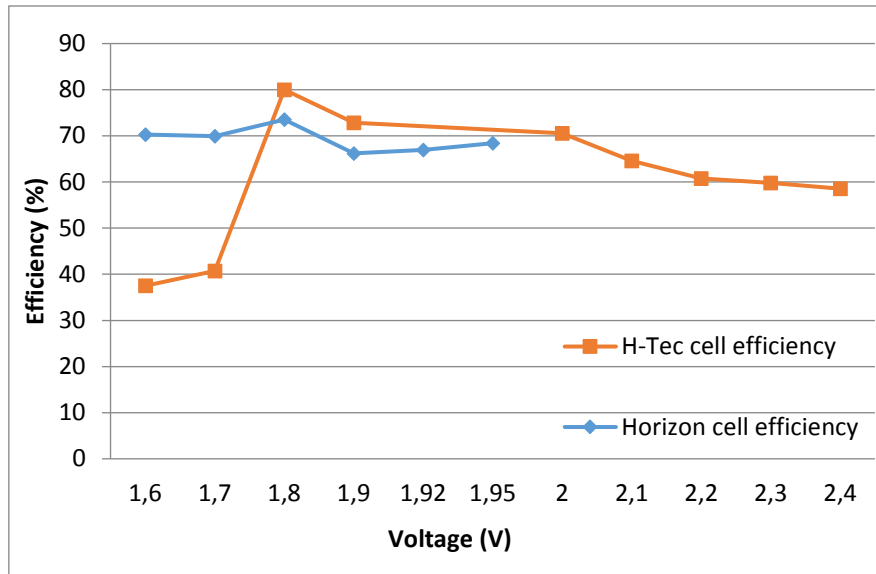


Figure 75: Graphic comparison of the H-Tec and Horizon EC

After examining the experimental results obtained in our lab and shown in table 6 and figure 26, a maximum efficiency can be achieved for the H-TEC cell if it is supplied by 1.8V. At this working point, a current of 0.5A is needed with an efficiency of 80.0%. In similar working conditions, the HORIZON cell showed an efficiency of 73.5% at 1.8V with a current of 0.68A. In the first approach and for this energy scale of PEM electrolyzer cell, 1.8V seems to be the optimal voltage level. In addition, it appeared during these tests that electrolyzer cell's performance suffers from repeated startup phases and needs a consistent voltage source. Fixing the input voltage of the cells at a constant 1.8V is therefore desired. Due to its higher efficiency, the H-Tec cell will be used for the rest of this project.

In addition, it appeared during these tests that the performance of the electrolyzer cells suffers from repeated startup phases and needs a consistent voltage source. Fixing the input voltage of the cells at a constant 1.8V is therefore desired.

3.8. Modeling of the Electrolyzer cell

In order to improve knowledge of the cell's behavior, we developed a modeling approach to produce a Matlab Simulink model of the H-Tec EC. The chosen approach is an electrical equivalent circuit modeling based on electrochemical impedance spectroscopy like the one described in [77]. The produced model aims to be working in conjunction with the models of storage elements described in the Chapter 2.

Electrochemical impedance spectroscopy (EIS) is an experimental technique to analyse the complex impedance of an electrochemical system [78] in response to frequency modulation of the voltage. The RCAST laboratory shared with us a set of experimental data from EIS performed on the H-Tec EC. This data can be represented on a Nyquist plot as presented in the example of Figure 76, depicting the Nyquist plot for the H-Tec cell at 1.65 V gained from the EIS test data.

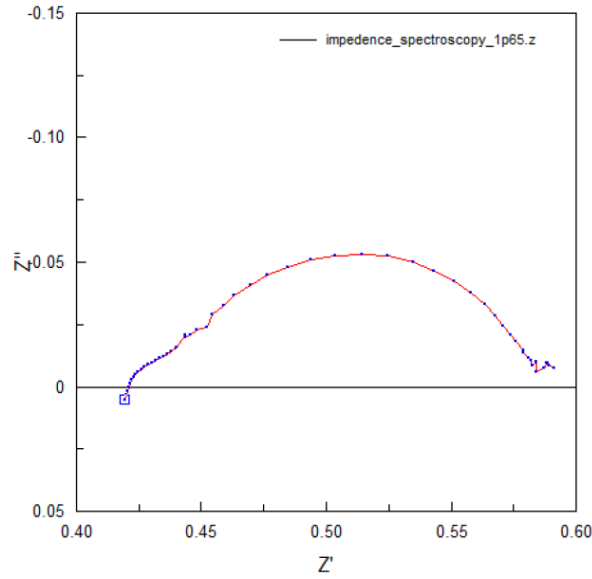


Figure 76: example of Nyquist plot for H-Tec cell for a 1.65 V supply. EIS data

Sets of data for voltages of 1.45V, 1.5V, 1.55V, 1.575V, 1.6V, 1.625V, 1.65V, 1.675V, 1.7V are available. As experimental of EIS at 1.8 V or above did not produce exploitable Nyquist curves with our material, we decided to model the behavior of the EC for these voltage values with the perspective to be able to extrapolate it's behavior at 1.8 V. On a first analysis of the data, it appears that the Nyquist plots for all the voltages have the same general shape with changes in numeric values. We can observe two successive arcs with a section chord and height in the complex plane depends on the level of voltage. An arc in the complex plane is specific to the Constant Phase Element (CPE). A CPE is an equivalent impedance element used in electrochemistry to describe a component with a phase that does not vary with frequency.

The complex impedance of a CPE is expressed as follows:

$$Z_{CPE} = \frac{1}{P_1 \cdot j\omega^{P_2}} \quad (57)$$

This type of impedance is purely imaginary and needs a parallel resistance in order to model the real part of the arc.

As we observe two arcs, two CPEs P_1 and P_2 can be identified in conjunction with their respective parallel resistors R_{P1} and R_{P2} .

The Y-intercept in the Nyquist plot (Figure 76) corresponds to an additional series resistance as it is only in the real pane.

Based on these observations, we propose the following model for the EC:

$$Z_{EC} = R_S + \frac{R_{P1}}{1 + j \cdot R_{P1} \cdot P_1 \omega^{P_2}} + \frac{R_{P2}}{1 + j \cdot R_{P2} \cdot P_3 \omega^{P_4}} \quad (58)$$

For the equivalent model graphically represented in Figure 77 below:

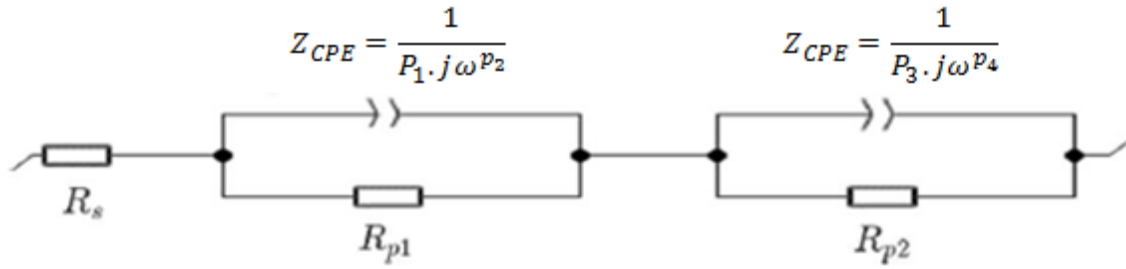


Figure 77: Schematic of the equivalent circuit model for the H-Tec EC

The different parameters of this model, R_s , R_{p1} , R_{p2} , P_1 , P_2 , P_3 and P_4 must be identified from the Nyquist plots of the EIS results for each voltage. The goal will be identify the response of each parameter to the variation of voltage.

3.8.1. Automated identification with ZFitGUI:

The first method used to identify the parameters is the use of a Matlab tool called ZFitGUI (Complex impedance Fit Graphical User Interface). It is a toolbox available for download which permits both automated and manual Nyquist plot fitting. For using the automated identification, the program must be given a model structure and a first approximation of the desired value for each parameter. This means that the user must already be close to obtaining an accurate model.

For the first parameter approximation, the following hypotheses have been taken:

The serial resistance R_s must be close to the Y-intercept on the Nyquist plot.

$$R_s \approx \min(\operatorname{Re}(Z)) \quad (59)$$

The parallel resistance values R_{p1} and R_{p2} must be close to the maximum real impedance for each arc on the Nyquist plot.

$$R_s + R_{p1} + R_{p2} \approx \max(\operatorname{Re}(Z)) \quad (60)$$

The other parameters (P_1 , P_2 , P_3 and P_4) are arbitrarily fixed to 1.

The first result obtained with these approximations had the expected curve form but did not correspond to the experimental curve obviously. Through repeated automatic fitting, the curve from Figure 78 was obtained, representing in blue the experimental data at 1.5 V and in red the best automatic fitting result from ZFitGUI. Complete results for all data are given in ANNEX 6.

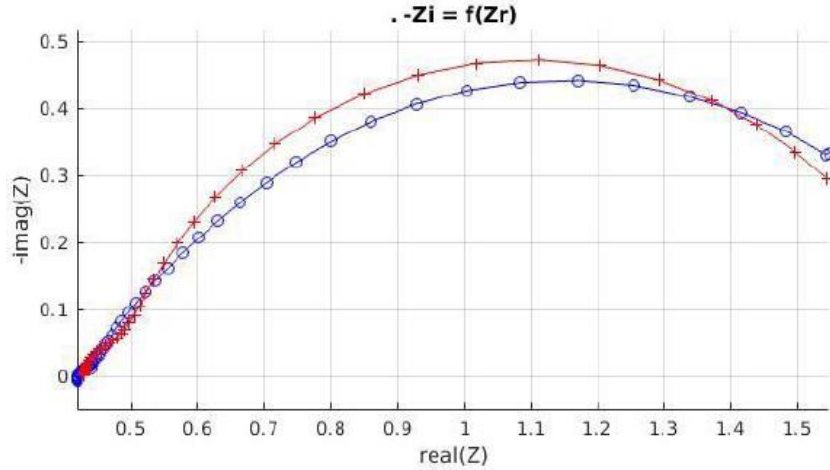


Figure 78: Nyquist plot of Experimental data (Blue) and Best automatic fit using ZFitGUI (Red) for 1.5 V data

These results are not satisfying at all, especially for the higher voltage levels. In addition, incoherencies were noted between multiple automatic fitting iteration for the same data sets. No relations between the model parameters and the voltage could be identified from this approach and the automatic identification of the parameters with ZFitGUI is discarded.

3.8.2. Manual parameter identification using ZFitGUI:

The second approach to identify the model parameters was to use the interface of ZFitGUI manually in order to try and fit the impedance curve more precisely. This was done by iteratively fixing the starting value of each parameter by hand and to repeat a trial and error process to fit model and experimental curves. For this method, a strategy has to be made. It is possible to fit the model perfectly for low frequencies but it will be worse at high frequencies. It is also possible to fit the model perfectly for high frequencies but it will be a bad fit at low frequencies. The chosen strategy in this identification is the choice of the overall “best-fit”, compromising both low and high frequency accuracy.

The results obtained with this method can be seen in ANNEX 7. Figure 79 shows an example of manual fitting for the Nyquist plot at 1.5 V.

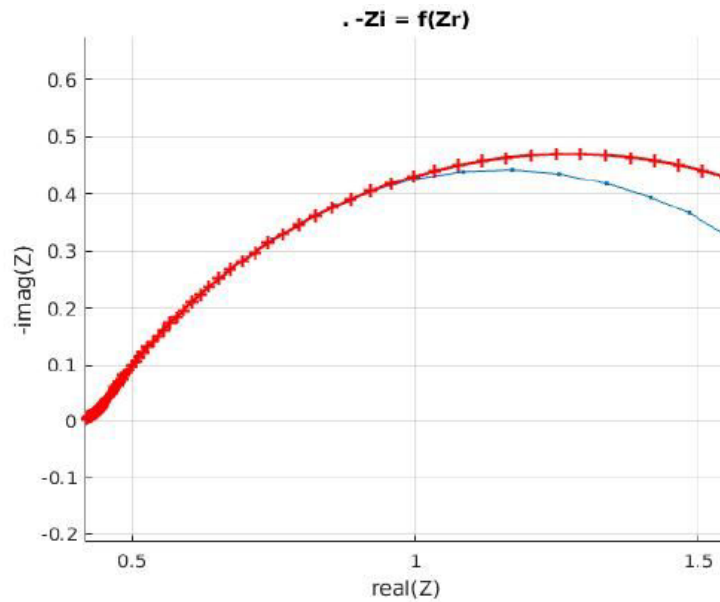


Figure 79: Nyquist plot of Experimental data (Blue) and manual fit using ZFitGUI (Red) for 1.5 V data

Cross examination of the manual fitting results shows more satisfying results as the automatic fitting, especially in the higher frequencies (low real impedance). We have made the following observations from the manual fitting process and the results given in ANNEX 7:

The influence of R_s :

When the serial resistance R_s is increased, the whole impedance curve moves in the ascending order on the real axis, without influencing the shape of the curve. However, the value of R_s is not exactly the value of the Y-intercept in the Nyquist plot.

Influence of R_{P1} :

When R_{P1} increases, the limit between the end of the first arc and starting of the second arc is shifted to the right on the real axis. Naturally, this also affects the position of the end of the second arc.

Influence of P_1 and P_3 :

P_1 affects the distribution of the frequencies along the two arcs. The smaller P_1 is, the more the points are gathered around the limit between the two arcs. This also changes the shape of the curve around the limit between both arcs.

P_3 also affects the distribution of the points. The smaller P_3 , the more the points are gathered towards the end of the second arc. This does not affect the shape of the curve as much as P_1 .

Influence of P_2 and P_4 :

Increasing P_2 increases the height of the first arc and increasing P_4 increases the height of the second arc, without modifying the arc's radius. This only slightly affects the global shape of the curve.

Limits of the ZFitGUI tool:

While ZFitGUI has permitted a rough and unsatisfying first model through automatic fitting and a more precise manual fitting through trial and error, it is a limited tool for our modeling approach.

It was not conceived to manually identify model parameters. To modify the parameters, the user has to open a text box and enter all the parameters in a single field, which is extremely tedious for complex models. It would be optimal to have a more graphic interface to tune parameters precisely and visualize the result in real time.

ZFitGUI does not have a solution to quantify the quality of a set of parameters identified through fitting. An indicator for the comparison of model parameters and experimental data would be adequate.

While it is possible to fit the curves, it is impossible to know if two points of the same frequency are aligned or not. In addition, the model has a different number of points than the experimental curve, which makes it hard to identify frequencies on the Nyquist plot.

For all of the above cited reasons, we decided to create a dedicated Matlab toolbox to make the manual identification of model parameters easier and more accurate.

3.8.3. Development of a precise manual parameter identification tool: SpecificFit

A Matlab tool was developed to permit easier identification of parameters for the EC model. This tool permits the user to use sliders or separate text fields in order to change the value of each parameter, for up to 10 parameters. Different frequency points are shown in different colors on the Nyquist plot, permitting an easy identification of equivalent points between data and model. In addition, the SSEM (Sum of Squared Error relative to Mean) between the experimental curve and the model is calculated as an indicator of fitting quality.

On the other hand, this tool is only meant for manual identification of this specific type of model and has a high CPU utilization as it constantly recalculates the model after each change of parameter. It could certainly be further optimized to achieve better calculation times.

Figure 80 shows the control interface of the SpecificFit Matlab tool with sliders and text boxes for each parameter. It also allows each parameter to be locked in for the model.

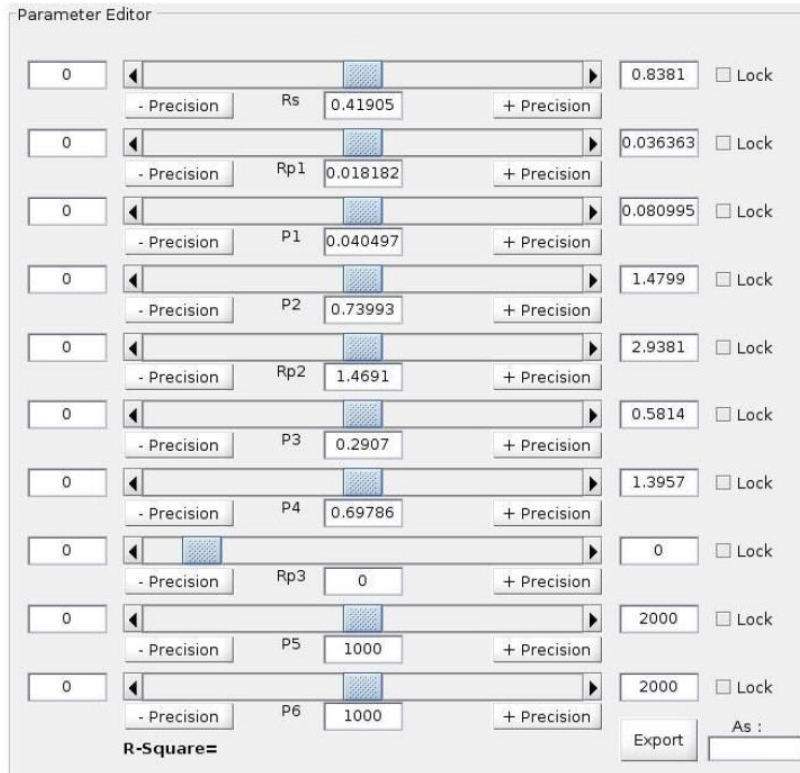


Figure 80: Parameter control interface of the SpecificFit Matlab tool

By manually calibrating the EC model's parameters, the best results were obtained, with a high correspondence between experimental data and model. The results of the complete identification process are accessible in ANNEX 8. F shows an example of result for the Nyquist plot at 1.5V identified with SpecificFit.

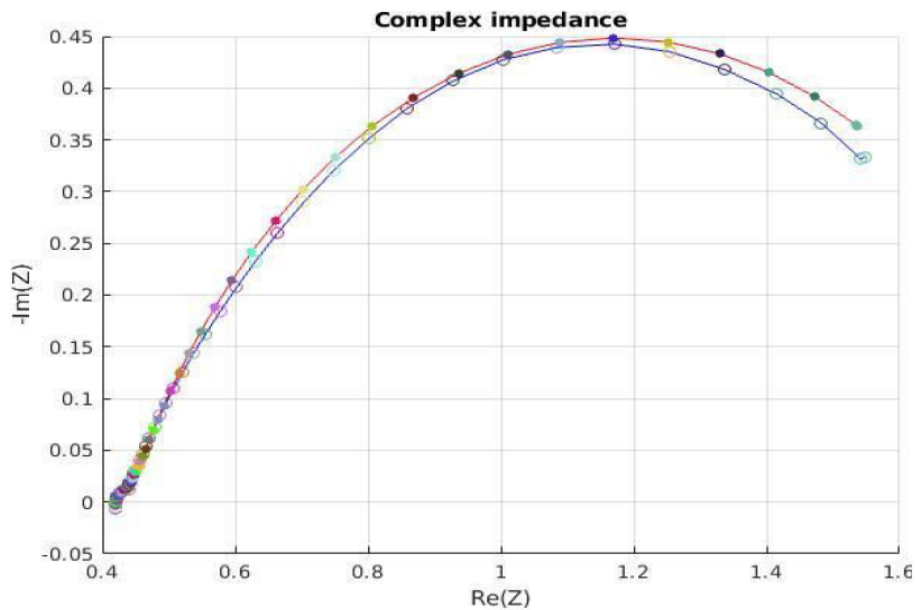


Figure 81: Nyquist plot of Experimental data (blue curve with circles) and manual fit using SpecificFit (red curve with points) for 1.5 V data

This parameter identification is selected for the final model of the H-Tec EC. The corresponding parameters for each voltage are listed in Table 15 below.

Table 15: Identified parameters for the EC equivalent circuit model

| Voltage (V) | R_s (Ω) | R_{P1} (Ω) | R_{P2} (Ω) | P_1 | P_2 | P_3 | P_4 | SSEM (%) |
|-------------|--------------------|-----------------------|-----------------------|--------|--------|--------|--------|----------|
| 1.45 | 0.4233 | 0.02035 | 0.02840 | 0.7754 | 10.20 | 0.3858 | 0.6754 | 99.9870 |
| 1.50 | 0.4191 | 0.01818 | 0.04050 | 0.7399 | 1.4691 | 0.2907 | 0.6979 | 99.9860 |
| 1.55 | 0.4179 | 0.01667 | 0.02887 | 0.8124 | 0.4272 | 0.2269 | 0.7229 | 99.9897 |
| 1.60 | 0.4204 | 0.01853 | 0.02578 | 0.8124 | 0.2543 | 0.1481 | 0.7824 | 99.9898 |
| 1.65 | 0.4210 | 0.01773 | 0.02524 | 0.7892 | 0.1493 | 0.1384 | 0.7854 | 99.9629 |
| 1.675 | 0.4214 | 0.01750 | 0.02692 | 0.7966 | 0.1262 | 0.1320 | 0.8012 | 99.9456 |
| 1.70 | 0.4284 | 0.01522 | 0.04332 | 0.7025 | 0.1105 | 0.1293 | 0.7604 | 99.8871 |

3.8.4. Relation between each parameter and the voltage

Once the parameters for each test voltage have been identified, relations between the value of the parameter and the voltage can be established.

From the parameters chosen in Table 15, a curve of parameter value versus voltage can be drawn for each parameter. All the curves are visible in ANNEX 9. Figure 82 shows the curve relating CPE parameter one (P_1 and P_3) to the cell voltage as an example.

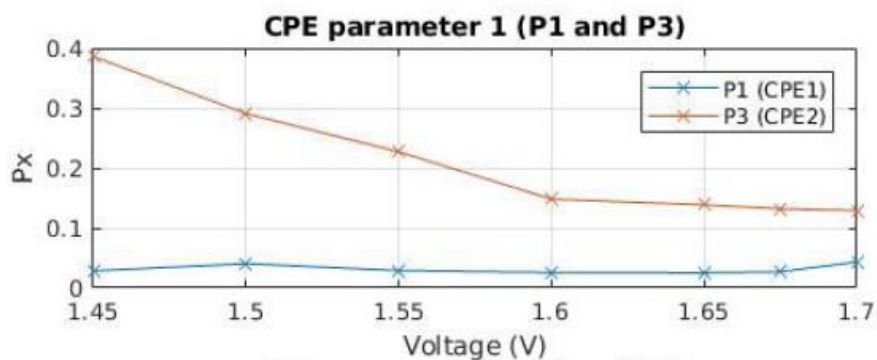


Figure 82: CPE parameter 1 (P_1 and P_3) versus EC voltage

From these curves, a parameter value can be interpolated or extrapolated for any usable voltage of the EC. Using these interpolations and extrapolations, a Simulink block model is created that

constructs the complex impedance of the EC for the voltage and frequency given as input. The model's implementation as a Simulink block is visible in Figure 83:

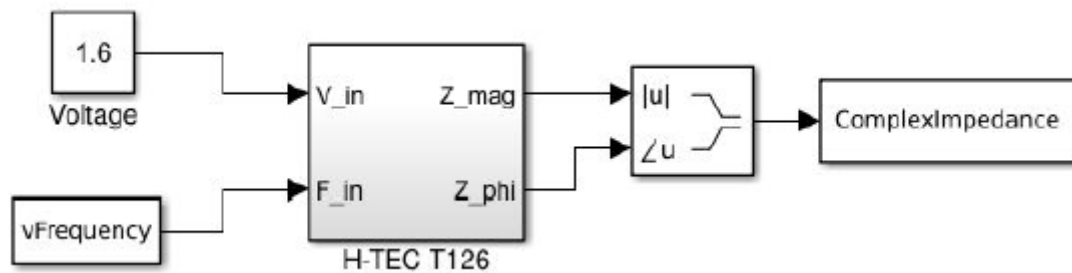


Figure 83: EC impedance model implemented as Simulink block

The Simulink model of the EC is adapted to validate designs for our experimental system. According to the experimental study the chosen H-Tec EC needs a DC converter with constant output voltage regulation. Using these results and the models developed for the EC, we are able to design an adapted converter stage.

In addition, the SpecificFit Matlab tool we developed is a powerful tool to identify model parameters for the study of all types of electrolyzer cells. It can be used in the future to model the bigger scale electrolysis systems that we aim to install in LAAS. One of the main questions with electrolyzer modeling is the question of scalability. It is important to know if the knowledge of behavior of ECs is scalable with higher power levels and bigger cells. We hope to be able to answer this question by studying bigger ECs, modeling them and comparing them to our small scale elements both in simulation and future experimental applications.

3.9. CONCLUSION

In this chapter, Hydrogen is studied as a vector of energy at different scales. As it is a technology approaching maturity and more and more targeted towards in energy systems, the laboratory LAAS wishes to extend its expertise towards this particular sector. Nevertheless, advancing with precaution in this new field, the validation of concepts at low power and energy scales was necessary. The research work on small electrolyzer cells in the Watt scale was therefore done in conjunction with the RCAST.

After a preliminary selection, experimental tests have permitted the choice of the cell showing the highest efficiency. We have observed that the efficiency of these cells decreases rapidly for lower voltages than 1.8 V. Above this voltage, the efficiency slightly decreases, making a slight variation in voltage possible above this value. A toolbox for modeling of the EC through GEIS technique and fitting of Nyquist plots has been developed. The proposed model as well as the parameter identification approach serve as a basis for the design of the dedicated DC/DC converter for the EC. The totality of the design and the development of laboratory prototype is described in the next chapter.

REFERENCES

- [67] L. Dobbin, « Paracelsus and the discovery of hydrogen », *J. Chem. Educ.*, vol. 9, n° 6, p. 1122, juin 1932.
- [68] G. A. DiLisi, « The *Hindenburg* Disaster: Combining Physics and History in the Laboratory », *The Physics Teacher*, vol. 55, n° 5, p. 268-273, mai 2017.
- [69] W. N. Hardy, « From H₂ to cryogenic H masers to HiTc superconductors: An unlikely but rewarding path », *Physica C: Superconductivity*, vol. 388-389, p. 1-6, mai 2003.
- [70] A. Durgutlu, « Experimental investigation of the effect of hydrogen in argon as a shielding gas on TIG welding of austenitic stainless steel », *Materials & Design*, vol. 25, n° 1, p. 19-23, févr. 2004.
- [71] P. G. L. Comber, D. I. Jones, et W. E. Spear, « Hall effect and impurity conduction in substitutionally doped amorphous silicon », *The Philosophical Magazine: A Journal of Theoretical Experimental and Applied Physics*, vol. 35, n° 5, p. 1173-1187, mai 1977.
- [72] A. Janotti et C. G. Van de Walle, « Hydrogen multicentre bonds », *Nature Materials*, vol. 6, n° 1, p. 44-47, janv. 2007.
- [73] IRENA, « Hydrogen from renewable power: Technology outlook for the energy transition », *Report*, p. 52, sept. 2018.
- [74] « MYRTE hydrogen energy storage test powers up in Corsica », *Fuel Cells Bulletin*, vol. 2014, n° 6, p. 8, juin 2014.
- [75] N. YOUSFI STEINER, « Contribution à la Résilience de Systèmes Piles à Combustible Tolérance aux défauts et à la dégradation ». HDR Université de Bourgogne Franche-Comté, 14-déc-2018.
- [76] A. Nakamura *et al.*, « A 24.4% solar to hydrogen energy conversion efficiency by combining concentrator photovoltaic modules and electrochemical cells », *Applied Physics Express*, vol. 8, n° 10, p. 107101, oct. 2015.
- [77] J. van der Merwe, K. Uren, G. van Schoor, et D. Bessarabov, « A study of the loss characteristics of a single cell PEM electrolyser for pure hydrogen production », in *2013 IEEE International Conference on Industrial Technology (ICIT)*, Cape Town, 2013, p. 668-672.
- [78] J.-B. Jorcin, M. E. Orazem, N. Pébère, et B. Tribollet, « CPE analysis by local electrochemical impedance spectroscopy », *Electrochimica Acta*, vol. 51, n° 8, p. 1473-1479, janv. 2006.

CHAPTER 4 : Design of a LVDC microgrid for solar to hydrogen conversion

In the context of the global evolution of energy networks, hydrogen (H_2) can be plenary considered as a new vector of energy as shown in Chapter 3. The production of H_2 from PV and CPV systems is a challenge for the future for multiple reasons summed up through the concept of “Power to gas” and its problematic linked to new types of optimized energetic microgrids. In the LIA NextPV, which is a joint international research CNRS lab, the labs LAAS-CNRS (Toulouse) and the RCAST (Tokyo) decided since 2014 to develop a join ambitious multi-physic project named “H24 hydrogen production by CPV”. The main goal of these researches was based on the need for high performances of systems named “solar to fuel” constituted of Concentrated PV sources or several CPV cells able to produce electricity at high efficiencies (more than 31% solar to electricity efficiency) and electrolyzers able to produce H_2 at high efficiencies. Previous studies published in the literature had shown all the difficulties to match the two systems with two world records [76], [79] showing limits around 30% of energy efficiency but obtained in lab environment with artificially powered light. In this type of records, elements are in small power scales and directly connected without electronic interfaces as seen in Figure 84.

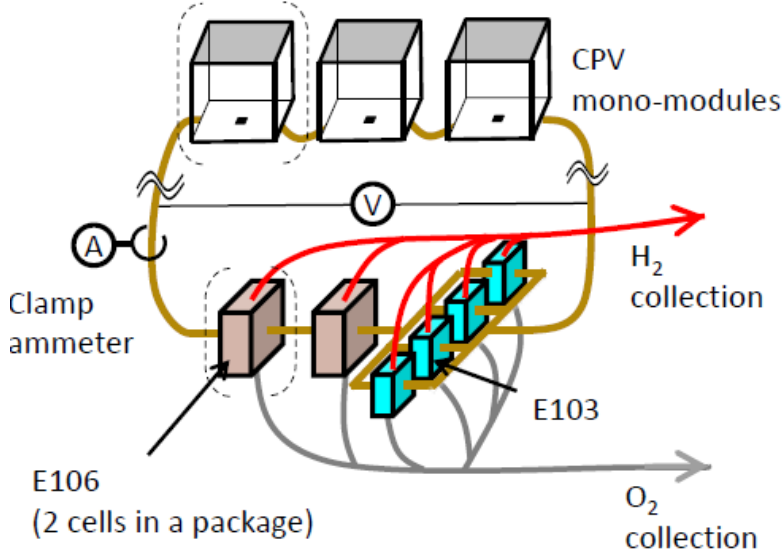


Figure 84: Solar to hydrogen conversion system using CPV mono modules and small scale electrolyzer cells with direct connection. RCAST

In this context, the solar to hydrogen (STH) efficiency is defined as the ratio between the equivalent energy of the quantity of produced hydrogen and the energy of the solar radiation incoming on the PV panels. This means that the higher the efficiency of each component is, the higher the total STH efficiency will be.

Through the association of LAAS and RCAST, we aim to study the integration of a solar to hydrogen system in a micro-grid structure using electronic power converters and storage elements.

4.1. The joint H24 hydrogen production by CPV project

The joint project between the LAAS-CNRS and the RCAST was focused on the design of an optimized Solar to Hydrogen conversion system able to work in real terrestrial conditions even with intermittencies. After several discussions, it was decided to study the use of a dedicated DC bus as an optimal interface working like a LVDC micro-grid including dedicated DC/DC converters and storage elements and specific control laws. This micro-grid was inspired by the LVDC designed and realized previously in LAAS to supply BIPV related DC loads (lighting, sensors and datacenters) [63], [80]. This ambitious project aims to combine the knowledge of RCAST on CPV technology and Electrolysis with the knowledge of LAAS for design of distributed power structures and microgrids with the integration of renewable energy sources helped by the CIRIMAT on modeling of storage elements. Previous works of these 3 labs needed for this work can be seen in [76], [81]–[87].

As a Ph.D. student, I was given the opportunity to contribute to the NextPV project by designing a small power scale solar to hydrogen conversion system to study the relevance of elementary blocks and help to the design of a real solar to fuel supply. This specific application came as a great opportunity to provide some concepts of my thesis with an example of an experimental microgrid application based on a real project. My contribution started with the discussion of the general design of the microgrid, followed by the study of each element that was necessary for its development.

The starting point for this project was a previous research work that was conducted by the team of Prof. Sugiyama concerning the direct connection between CPV panels and electrolyzer cells to achieve a high efficiency solar to hydrogen conversion [76] in 2014. While constituting a promising result, this study showed that a simple direct connection did not permit any energy flow control from the load to the charge and did not enable the harvesting of the maximum available solar energy in intermittent meteorological conditions. The structure we propose for the NextPV project to achieve a continuous production of solar hydrogen is to introduce a real DC bus constituted by several DC/DC converters such as the one previously designed in LAAS to study LVDC grids in buildings and for data centers. This experimental grid named OPA Platform was supplied by 1 kWp PV sources assisted by several storage elements such as Lead-acid batteries and Supercapacitors [88]. The schematic of this microgrid is shown in Figure 85. In its isolated state, the OPA micro-grid is able to supply DC loads during more than 24h.

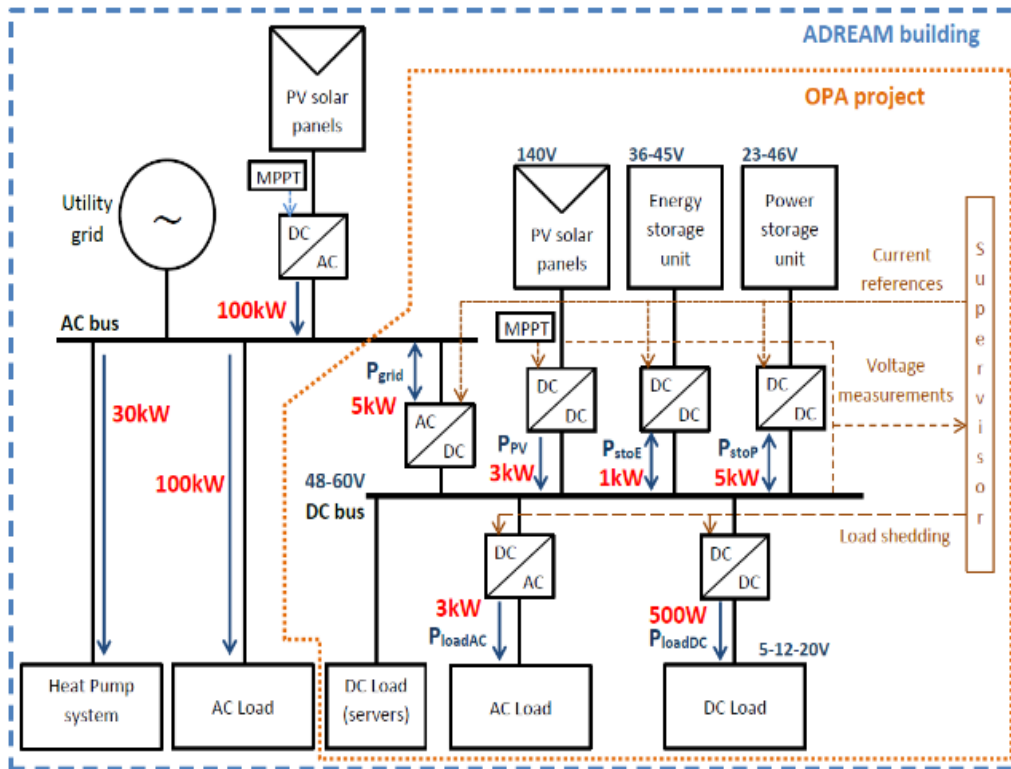


Figure 85: Schematic of the OPA micro-grid in LAAS-CNRS

4.2. LVDC synoptic dedicated to hydrogen production

Figure 86 represents a design schematic of the general system with its different elements. All of the component designed are separately discussed in the following parts of this Chapter.

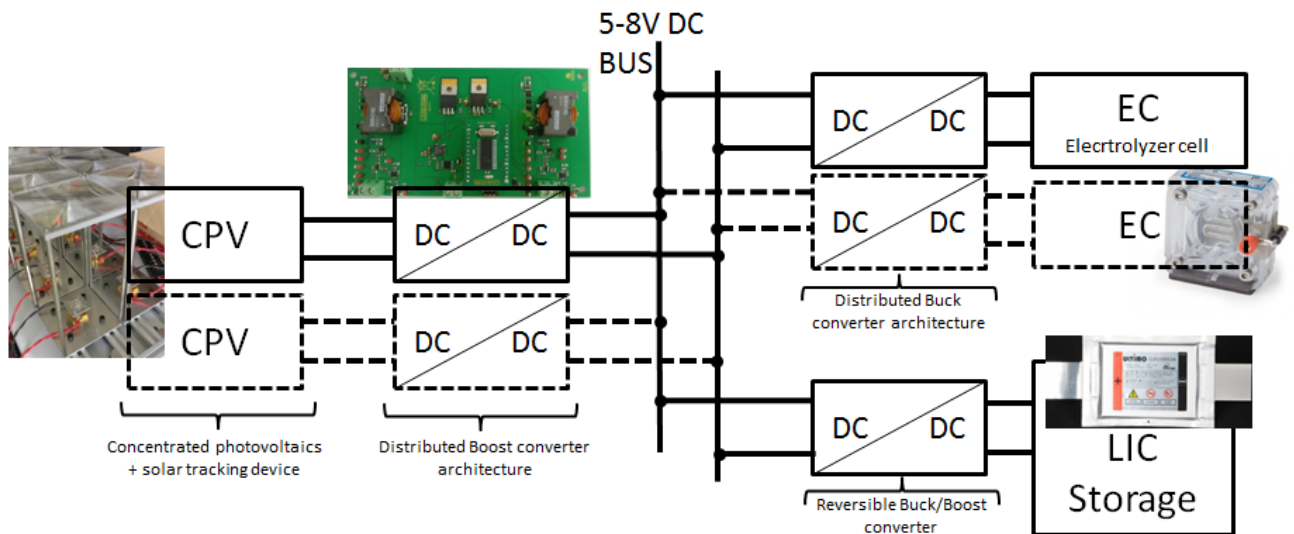


Figure 86: General design schematic of the NextPV system structure

We decided to use previous knowledges of each lab, in particular in CPV sources, to build the LVDC. First, we studied multi-junction CPV cells provided by Prof. Sugiyama's team. A

dedicated prototype board was built to provide different configurations of CPV cells and easily connect new DC/DC architectures. In LAAS, a new two-axis solar tracking system was installed on the roof of the ADREAM building to be able to make tests in real conditions. Details of this part are described in this Chapter.

In this global context, my first contribution was to design elementary DC/DC Boost converters and their dedicated controls for the CPV cells in order to enable harvesting of the maximum power available at any time. As multi-junction CPV cells are more sensible and precious elements than normal silicon PV cells and are more prone to disparity, we decided to design a distributed converter architecture. This type of converter structure, using a micro converter for each other element, was previously studied in LAAS [85]. It permits a special fine-tuning of the functioning point for each cell, enables the possibility of easy power scaling and reduces maintenance at the expense of an increase in initial costs. Today, PCB prototypes of converters were created and validated experimentally.

Once the CPV production system was successfully designed, a second study was focused on the choice of elementary electrolyzers compatible in power, voltage and current with CPV cells. Two small scale electrolyzer cells that had been tested and suggested by the RCAST team were also tested in LAAS. This part was described in chapter 3. We chose the more efficient of the two cells for our prototype and decided to model to study its behavior and design its own electronic interface. During the modeling phase based on experimental data provided by the RCAST team, we identified that the tools we had for analyzing the data and modeling the cells were not sufficient. We made the decision to develop our own Matlab tool to analyze the data properly and create an appropriate model. Following this, we started the design of a converter for the electrolyzer cell and first validated it through simulation. On the Hydrogen production side, I decided to apply the same methodology to design the interface DC/DC system as for the CPV part. Thus, a distributed Buck converter architecture was designed to enable each electrolyzer cell to function at its optimal functioning point with all the same advantages.

In addition, with the suggestion of CIRIMAT and for simplifying the storage solution, the joint team performed a preliminary study on the possibility to use ULTIMO LIC storage cells for this specific microgrid. This type of hybrid storage was not really well known and its behavior in the specific context of microgrids was an excellent opportunity to further study it. Indeed, linked to its own properties, it presents high potential to store enough energy for our application and achieve a constant hydrogen production by also being able to prevent intermittencies. All these different steps of design and development constitute my contribution to the NextPV project. Details of each step are given in this Chapter.

4.3. Triple junction high efficiency photovoltaic panels

As the main goal of the solar to hydrogen conversion system is to achieve maximal conversion efficiency, the choice was made to use multi-junction solar cells. The RCAST laboratory from the University of Tokyo, Japan, specializes in research on materials for multi-junction PV cells. The team of Prof. Sugiyama provided eight experimental cells that were shipped to LAAS for this application. These 2 mm² cells are composed of a three junction GaInP/GaAs/Ge

superposition capable of absorption in a wavelength spectrum ranging roughly from 300 nm to 1700 nm in comparison to 1100 nm [89] for standard silicon cells capable of attaining an efficiency of around 31% [76]. Figure 87 is a picture of one of the cells.



Figure 87: Triple junction cell with solar prism.

As it can be seen, the cell is equipped with a prism. This optical device is used in order to redistribute the solar rays incoming on the tiny cell in an homogeneous way. As these cells have a high efficiency, their production process is expensive and use expensive materials. In order to maximize the usage of the cells, each cell is equipped with a Fresnel lens that concentrates sunlight onto the cell’s surface. This concept is named concentrated photovoltaics (CPV). By adding this type of lens, up to an equivalent of 40 suns can be concentrated into the prism, which distributes this radiation homogeneously on the cell. The characteristics of the Fresnel lenses that were used can be seen in ANNEX 10.

The concentration of sunlight enhances the irradiation on the cell surface but also increases the temperature at the same time. As PV cell energy production decreases with the increase of cell temperature, a way to dissipate the surplus heat is needed. For our application, a thermal heat sink consisting of a larger heat conducting surface is installed beneath the cells. Figure 88 presents a picture and a simplified schematic of the cell with Fresnel lens and thermal dissipation.

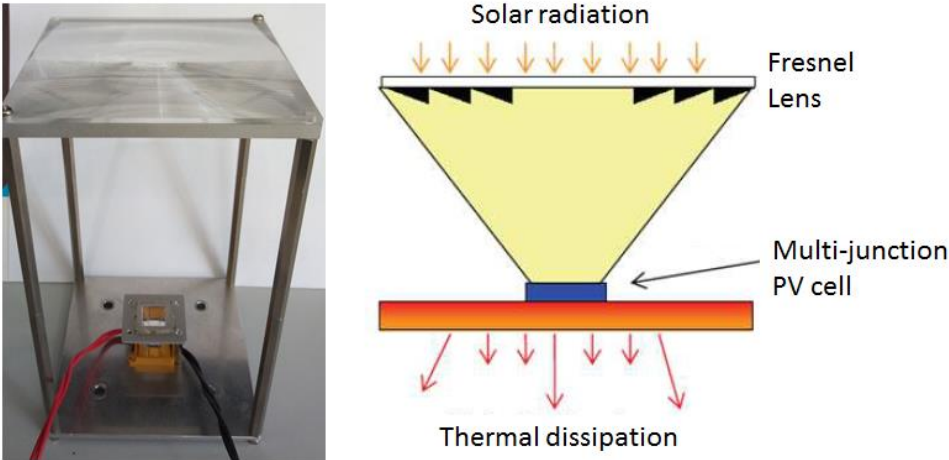


Figure 88: Multi-junction PV cell with Fresnel lens, prism and thermal dissipation, picture (left) and schematic (right)

Naturally, a Fresnel lens concentrates the sunrays in one focal point which position depends on the incidence angle of the direct solar radiance on the upper surface. In order to place the focal point onto the prism in the middle of the lens, the lens has to be perpendicular to the direct solar radiation. In other words, the whole CPV structure must be faced towards the sun at all moments.

The CPV cells are placed on a two-dimensional solar tracking system able to follow the position of the sun through the day. In LAAS-CNRS, a solar tracker from the brand Solarkit represented in Figure 89 was installed.



Figure 89: Two-axis solar tracker installed in the LAAS laboratory

This solar tracker uses two separate DC motors, one for inclination and the other for orientation. More detail on the motor specifications is visible in ANNEX 11. The motors are controlled by a microprocessor using a Time Derived Astronomical Positioning System (TDAPS) algorithm. This control algorithm calculates the position of the sun in the sky from the local time by using solar parameters similarly to the algorithm used in the solar irradiance model described in Chapter 2. The angular precision of this solar tracking system is 0.5° , which is sufficient to maintain the focal point of the Fresnel lenses accurately on the PV cells through the day.

The cells have been tested under real sun, using a CP160 solar tracer. Using this device, I-V curves have been traced with and without concentration. I-V curves of a cell tested under real sunlight around 750 W/m^2 irradiance with and without the Fresnel lens concentration are represented on Figure 90. This level of irradiance is a representative example of a day with clear sky in Toulouse, France.

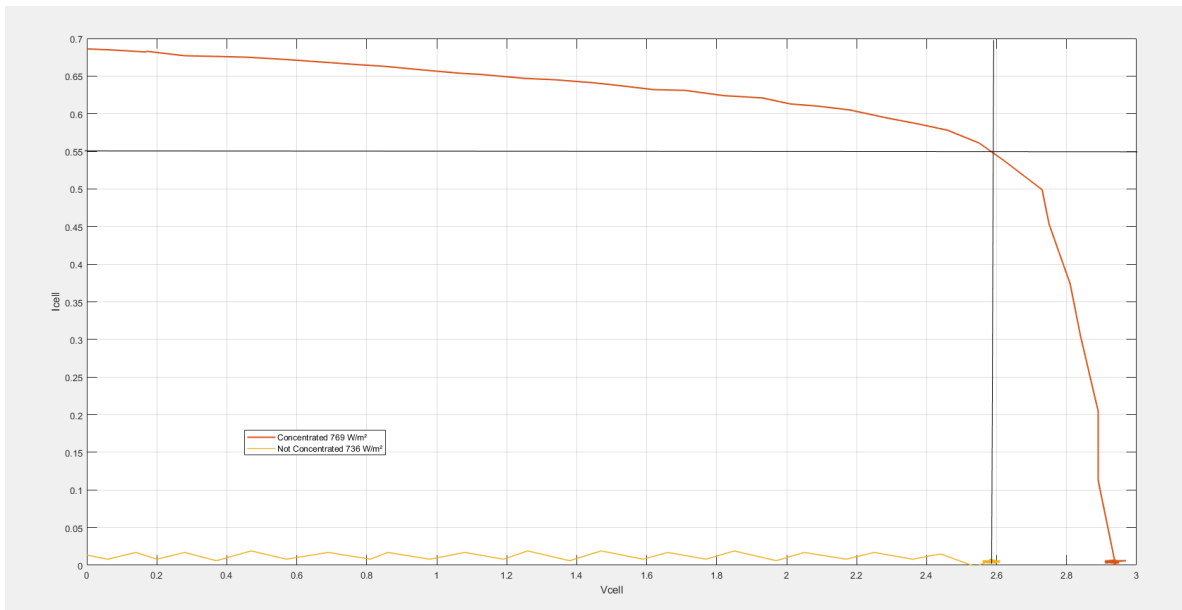


Figure 90: I-V curve of a multi-junction cell with Fresnel lens (orange) and without Fresnel lens (yellow). Measured under real sun at $\sim 750 \text{ W/m}^2$.

According to these curves, the cell voltage with concentration varies between 0 V and 3 V and the cell current varies between 0 A and 0.7 A.

Figure 91 shows an I-V curves for two different cells under concentration and at different irradiance levels from 633 W/m^2 to 683 W/m^2 of real sunlight.

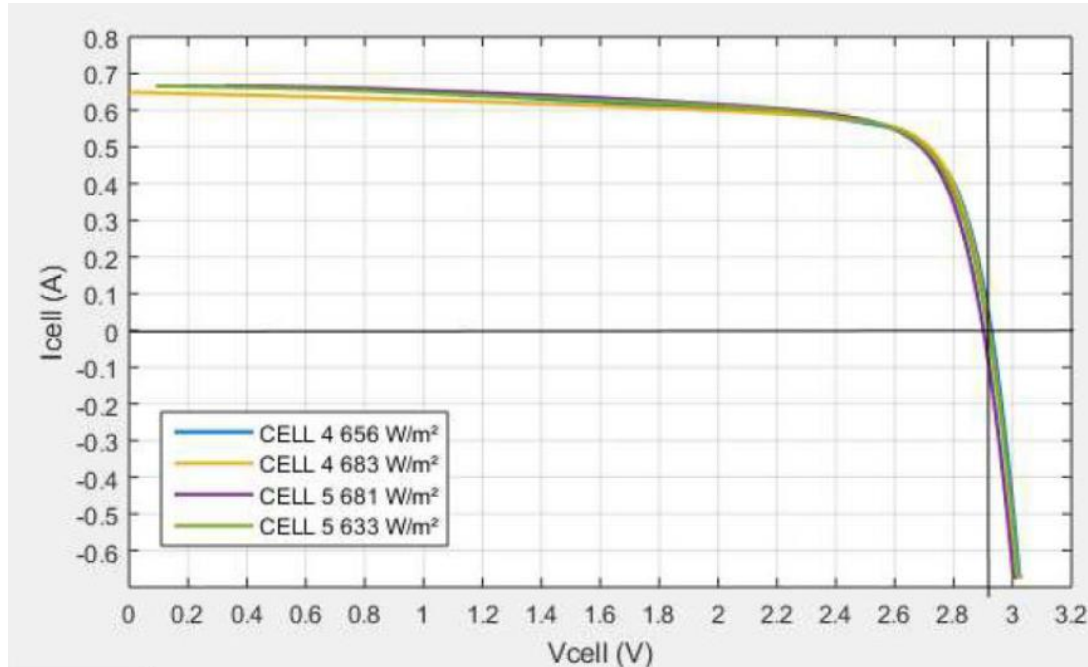


Figure 91: I-V curves for two different cells at different irradiance levels

The curves from Figure 91 show that even if the behavior is generally the same for these two cells, a disparity exists. Results of previous studies conducted by the team of RCAST on a larger batch of cells are visible in Figure 92. These results further confirm our observation on the disparity between cells.

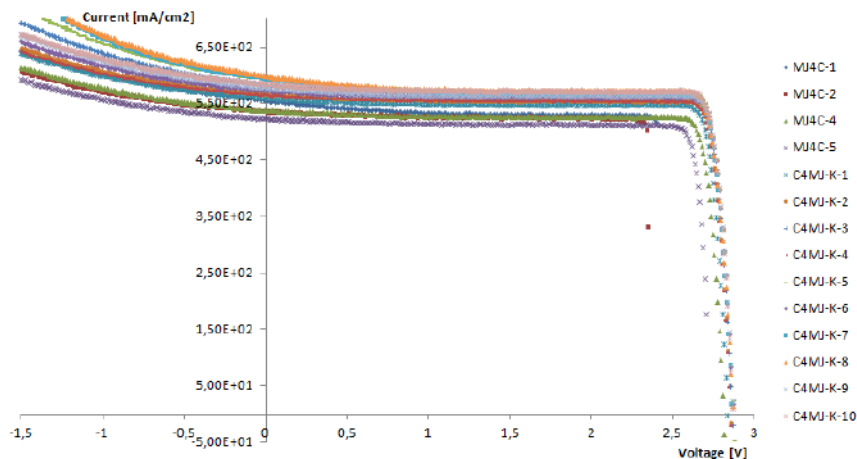


Figure 92: I-V curve results from previous tests at RCAST, Tokyo

According to the curves from Figure 90 and Figure 91, the maximum power should be harvested between 2.6 V and 2.8 V and around 0.5 A. At standard test conditions (STC), these cells have a maximum power output around 2 W each.

As for standard silicon PV panels, CPV need maximum power point tracking (MPPT) control in order to harvest the maximal power available at any moment. For this purpose, we developed a converter architecture for the CPV cells including an MPPT command.

4.4. Distributed micro-boost converter architecture for CPV and command

In order to enable MMPT control for the CPV cells, electronic power converters are needed. We chose to connect each cell separately to the LVDC grid through a micro Boost converter. This concept named distributed converter architecture has the advantage of permitting fine-tuned control for each individual cell, overcoming the problems of cell disparity, partial shadows, soiling and other types of malfunctions. Distributed converter architecture also brings great flexibility through modularity in dimensioning of systems, power scaling and maintenance. If more cells have to be added to a system in order to increase power output, the cells are easily added with their own converter.

4.4.1. Boost converter design

A prototype micro Boost converter for the CPV cells was developed during this thesis with specifications adapted to the NextPV project application. We chose a standard Boost converter structure as depicted in Figure 93 that will switch at 100 kHz.

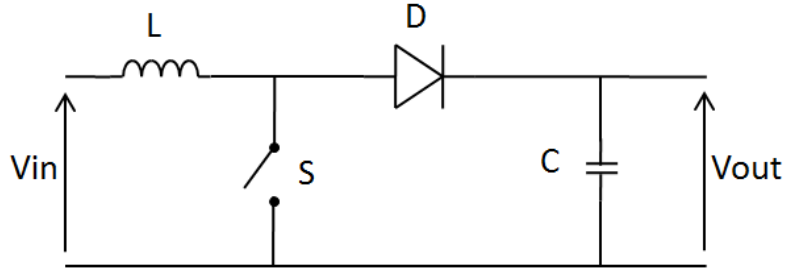


Figure 93: standard Boost converter structure

For the realization of this converter for small power, the choice of components is primordial to ensure a good efficiency.

We calculate the minimum inductance L_{min} to have a lowest series resistance while maintaining the current ripple ΔI_{max} below 10%. Equation (61) is used for the calculation

$$L_{min} = \frac{V_{in} * \alpha}{\Delta I_{max} * F} = \frac{2.7 * 0.8}{0.5 * 0.1 * 100e^3} = 432 \mu H \quad (61)$$

A 470 μH inductance with a series resistance $R_L=100$ m Ω from the brand Murata is chosen for our application.

The minimum output capacity is calculated using the maximum output current. The maximum output current of the converter would be the maximum PV current for one cell, meaning around 1A. With this in mind, Equation (62) can be used to calculate the capacity value:

$$C_{min} = \frac{I_{OUTmax} * \alpha}{\Delta V_{outmax} * F} = \frac{1 * 0.8}{2.7 * 0.1 * 100e^3} = 29 \mu F \quad (62)$$

We chose an output capacitor with a value of 33 μF for our application. A second 1 nF capacitor is added in parallel for filtering, as it will redirect electromagnetic noise to the ground.

For the switching cell, we compared five different n-type MOSFET transistors in simulation for 100 kHz frequency. The total losses for each of the tested switches were calculated by adding conduction losses, commutation losses, parasitic capacity losses (C_{oss}) and gate losses. A comparison of the losses depending on current is shown in Figure 94.

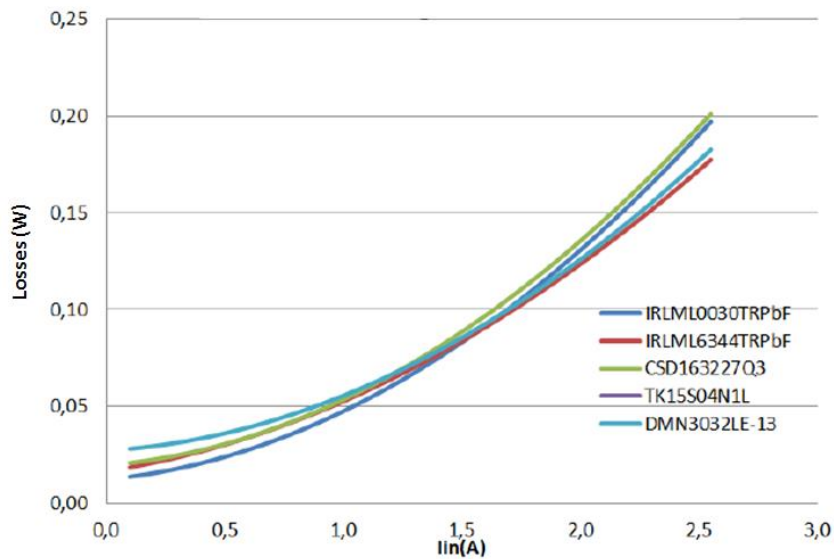


Figure 94: Comparison of losses in five selected n-type MOSFET switches for small power applications. Simulation at 2.7 V, 100 kHz

Based on these simulation results, the IRLML003TRPbF has the smallest losses around 20 to 50 mW for a current up to 1 A. We chose this MOSFET switch for our application.

Two different diodes with low losses were tested in simulation. For a duty-cycle of $\alpha=0.6$, the results in Figure 95 were obtained.

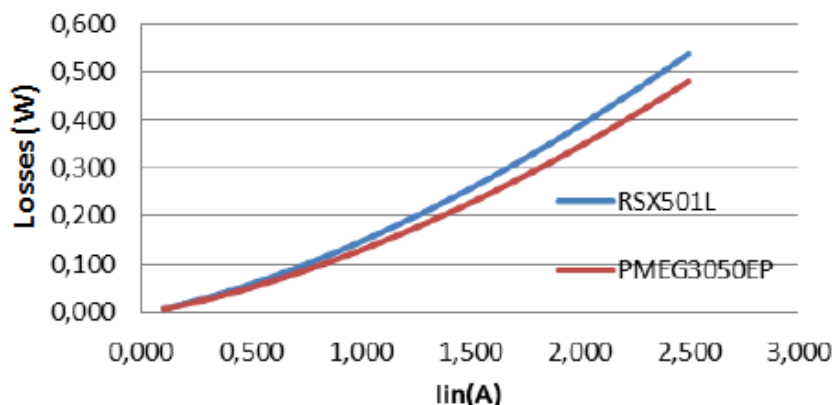


Figure 95: Comparison of the losses in two diodes at 100 kHz and $\alpha=0.6$

From these results, we can see that the PMEG3050EP diode has slightly lower losses. We therefore chose to use this diode in our application. In addition, we chose to use three diodes in parallel in order to divide the current in each diode and further reduce the losses.

Now that the power part of the converter is set, the command part needs to be designed.

4.4.2. Command circuits:

The command part of the converter is composed of regulated power supply, a microprocessor, drivers and sensors.

Regulated Power supply

The command part of the converter is made of active components that need a regulated voltage supply. This regulated power supply is sized for multiple converters so we need only one for two to six converter cells. Due to the fluctuating level of the bus voltage (5 V to 8 V supplied by the storage), we need a stable voltage V_{reg} supplying the command circuits with 5 V DC independently from the bus voltage and 3.3 V for the microcontroller. We use two steps for the voltage regulation in order to reduce the thermal impact on the components and to avoid using a heat sink as the converter is supposed to stay as compact as possible. We use a generic step down converter from Texas Instruments to produce a 5.5 V supply by using the circuit from the schematic in Figure 96.

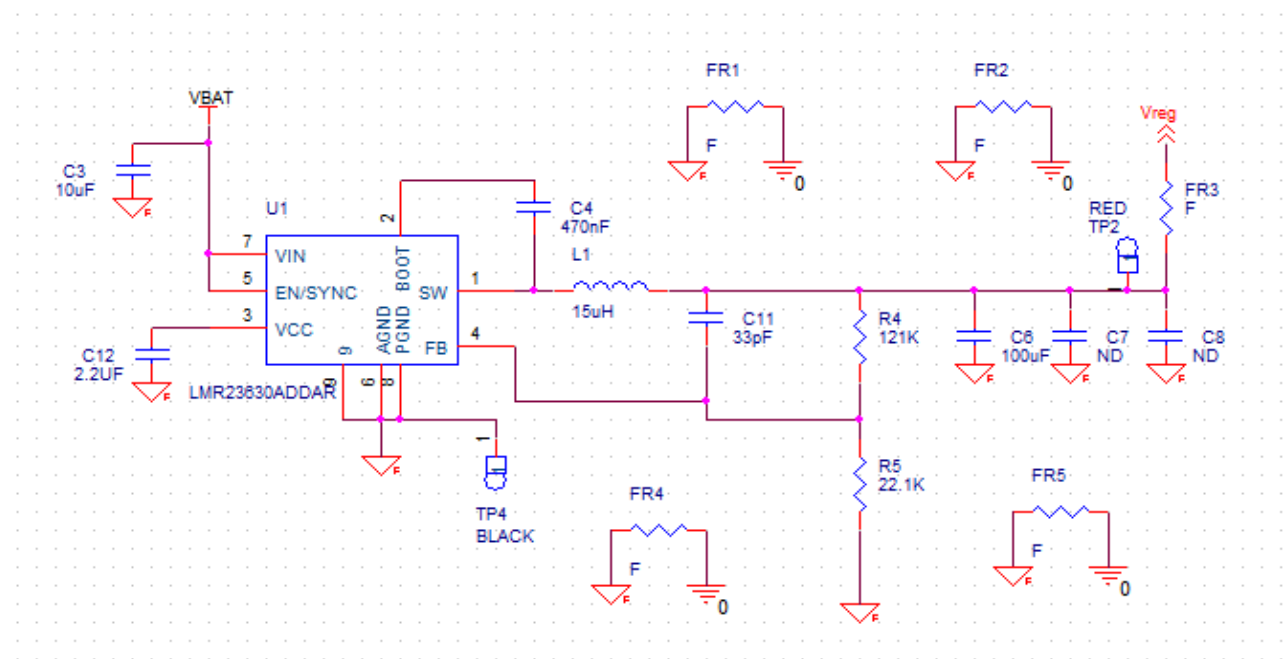


Figure 96: Schematic of the 5.5 V supply for the command circuits

The output of this supply stage is used as an input for two voltage regulators from TI to produce a stable supply for the MOSFET drivers (5V, V_{driver}) and the Microprocessor (3.3V, V_{cc}). The schematic of this circuit is visible in Figure 97

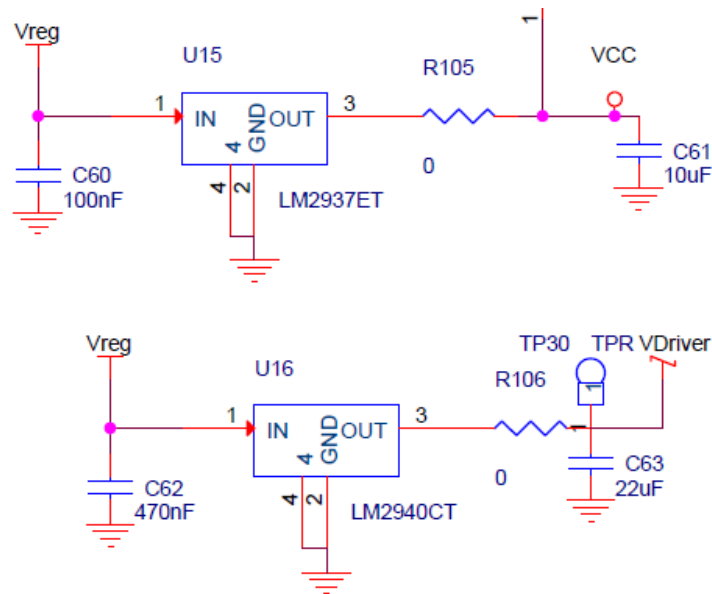


Figure 97: Schematic of the 5V and 3.3V voltage regulation to supply drivers and microprocessor

This regulated power supply is sized for multiple converters so we need only one for two to six converter cells. The first converter card contains two micro Boost converters and this power supply chain. But further converters will be able to make use of this same supply chain, reducing the costs and complexity of their manufacturing.

MOSFET driver

Drivers are used to power up the MOSFET gate as the microcontroller outputs do not provide sufficient power. For our application, we chose the ZXGD3002E6TA MOSFET driver as it has the required specifications for the chosen switch.

Sensors

We need sensors in order to measure voltage and current at the output of the converter. These values will be needed in the calculation of the duty cycle α in the regulation algorithm. High value resistance (100 k Ω for example) can be used to measure the voltage while protecting the microcontroller inputs from current. An instrumentation amplifier as seen in Figure 98 is used to measure the current.

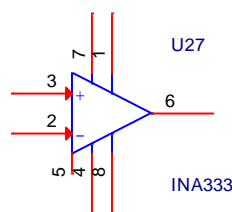


Figure 98: Instrumentation amplifier used for the measure of current

Microprocessor

The microprocessor is used to generate the command signals for the converter switches as well as for the output voltage regulation algorithm. For this converter, we chose a PIC18LF27K40

microcontroller. This microcontroller has a sufficient number of inputs and outputs for two micro Boost converters and is well suited for our application. It also has an extra low power mode to reduce the consumption of the command part. The channels RA0 to RA3 are used as inputs for the voltage and current sensors for two converters, while RC0 to RC3 are used for the output PWM signal. A 20 MHz quartz connected to RA7 and RA8 sets the microcontroller's internal clock. A schematic of the microcontroller connections is visible in Figure 99.

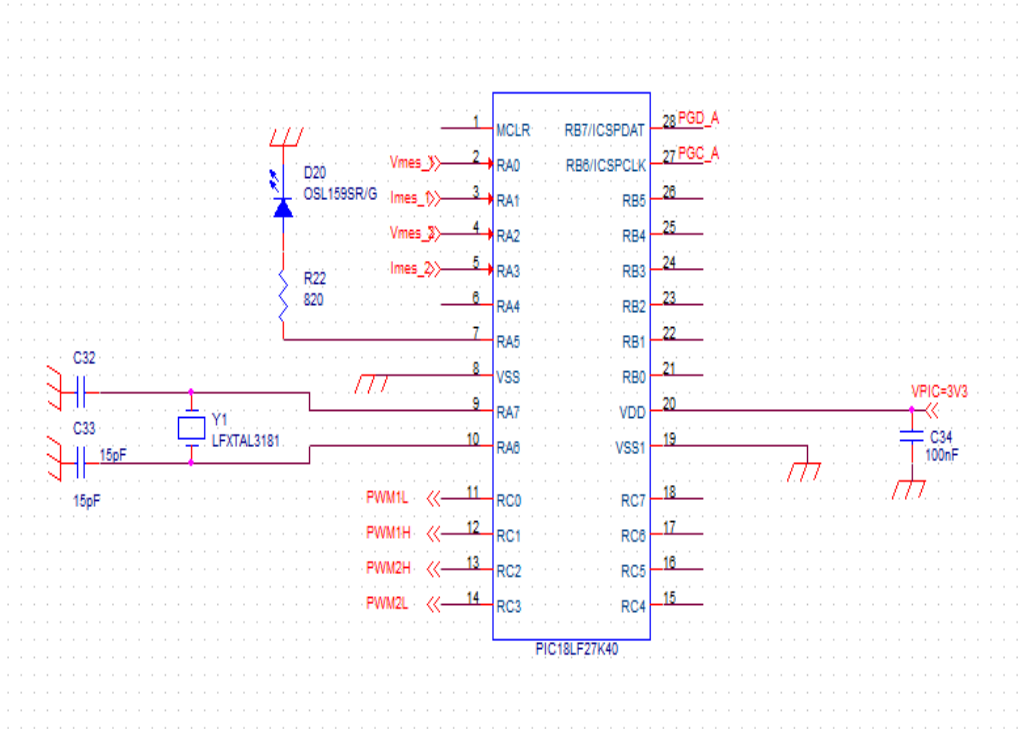


Figure 99: Schematic of the PIC18LF27K40 microcontroller and connections for the Buck converter.

This microcontroller has a single Analog to Digital Converter (ADC). In order to acquire four input values, the ADC has to be switched from one channel to another. After the acquisition of the four measured values is complete, the MPPT control algorithm can be launched in order to calculate the new duty cycle value α for each converter.

The schematic in Figure 100 presents the design made for the Boost converter and depicts where the MPPT command is applied and where the PV current and voltage are measured.

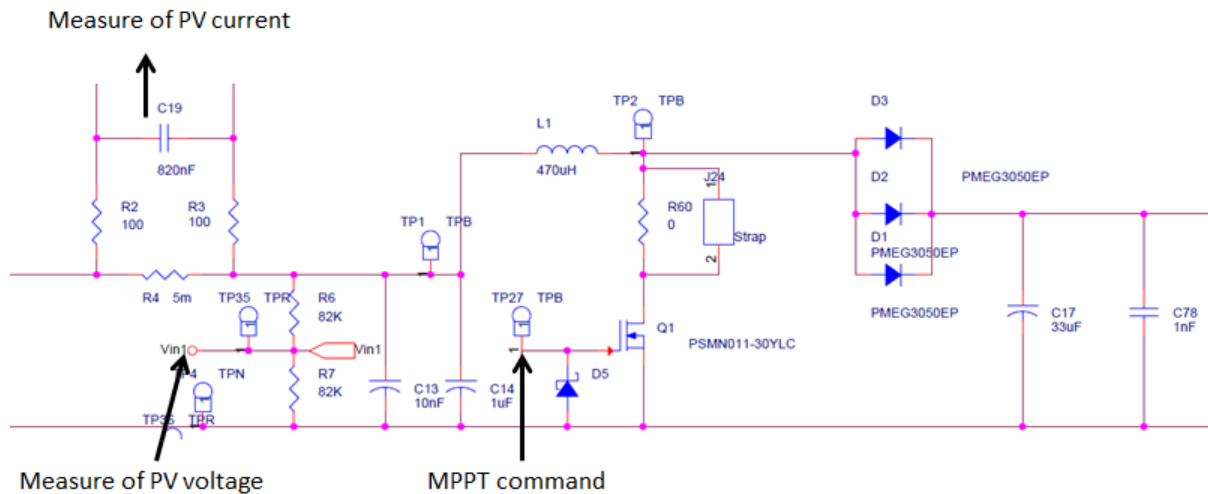


Figure 100: Schematic of the converter design showing measure points and MPPT command input

Once the design is fixed, the MPPT command algorithm needs to be developed.

4.4.3. MPPT Command algorithm:

While several MPPT command algorithms exist in the literature such as Perturb and Observe (P&O), Incremental condition or V_{OC} fraction, we chose to use a Hill Climbing algorithm as it permits the highest efficiency between these techniques.

The Hill Climbing method consists in the periodic measurement of PV current and voltage. From these measures, the power is calculated for that instant. This power is then compared to the previous calculation of the PV power. The duty cycle is increased or decreased by a fixed step depending on the result of the comparison. This way, the functioning point moves up the power curve (Figure 101) and ends up oscillation around the peak of the curve, which is the maximum power point.

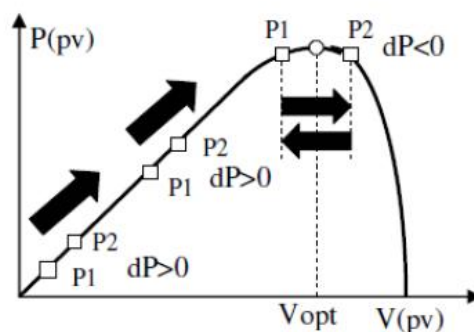


Figure 101: Movement of the functioning point on the PV power curve during Hill Climbing MPPT.

The Hill climbing algorithm is explained as a flowchart in Figure 102.

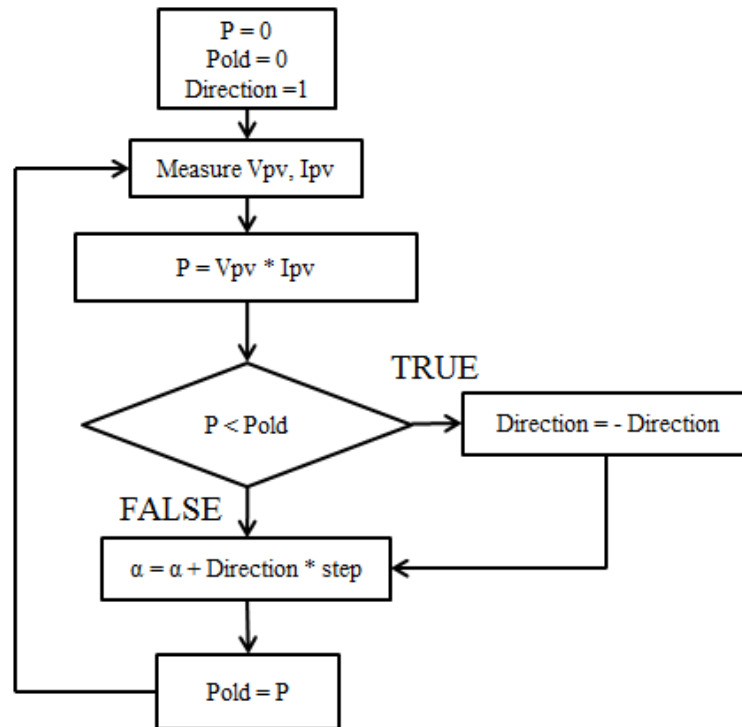


Figure 102: Flowchart of the Hill Climbing MPPT algorithm implemented for this converter

For the real implementation of the control algorithm and the generation of the PWM signal in the microcontroller, we used the software MPLABX. The measure of the voltage and the current is executed using a timer interruption. This timer's interruption flag enables the calculation of the power and the modification of the duty-cycle α .

4.4.4. PCB design

We developed the routing and the PCB card with the help of the technical team of the laboratory using the software Allegro. We developed a card containing two converters, the command circuits with one microcontroller, and one power supply for the command part. A picture of the finished card is visible on, with the detail of each part.

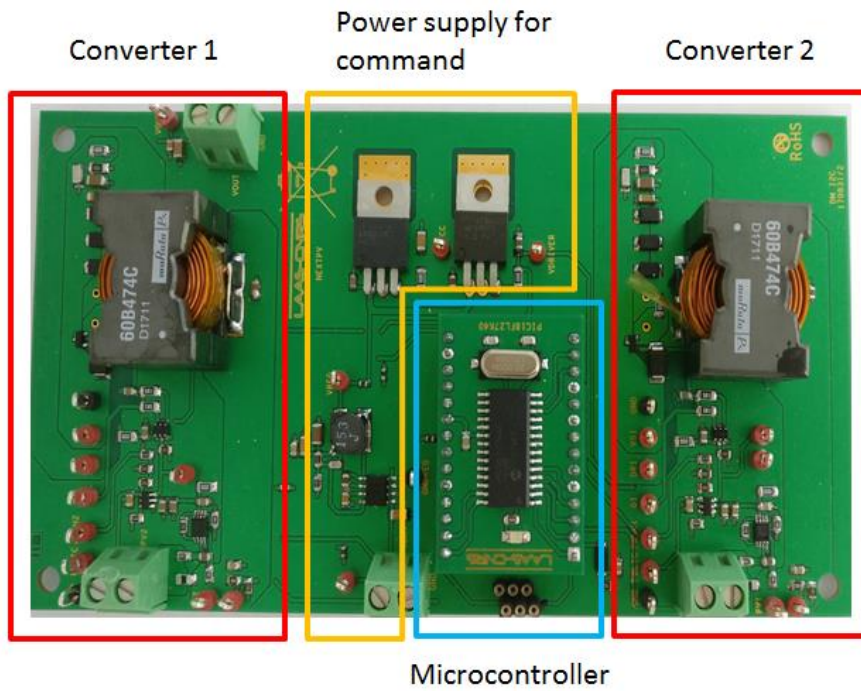


Figure 103: Picture of the card containing two Boost converters, one microcontroller and one supply circuit for the command part.

Additional converters for additional cells will not need the power supply part as it is sized to be able to supply the command part for up to six converters. This means that if more converters are added to the distributed architecture, they will only need their own microcontroller (one for two converters) and a connection to the first card's power supply.

A power efficiency ranging from 92% to 94% is achieved with this card for the desired current range from 0.2 A to 0.5 A, and for higher currents.

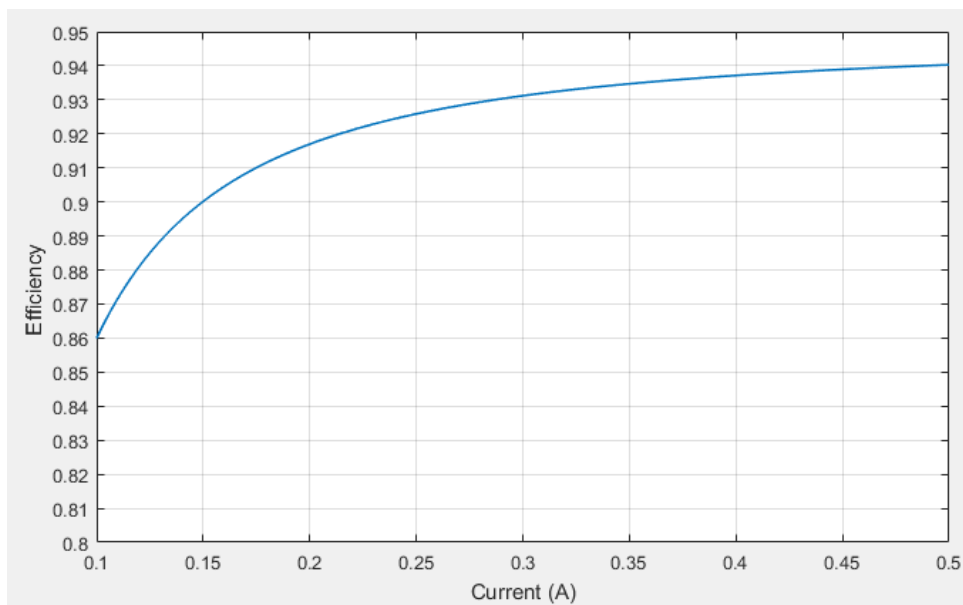


Figure 104: Efficiency versus current for the Boost converter card, $\alpha=0.5$

The power converter design for the CPV part of the project is validated. The output of the converters will feed the LVDC bus. On the other side of the bus, the goal is to supply the electrolyzers in order to produce hydrogen in the most optimized way.

4.5. Distributed micro-buck converter architecture for electrolyzer cells

In the Chapter 3, we concluded that the optimal way to produce Hydrogen using the H-Tec electrolyzer cells is to regulate their input to a constant 1.8 V DC. To step down from a 5-8 VDC bus, we naturally chose a Buck converter. Similarly to the CPV cells, we chose to design distributed micro converter architecture for the same reasons, being flexibility in scaling and maintenance, modularity and fine-tuned control for each cell. The designed converter does not need to be reversible and will switch at 100 kHz as this frequency will not influence the functioning of the EC. The goal is to achieve an efficiency between 93% and 98% at 1.8 V and 0.5 A to 0.8 A, with maximal ripple of 5%.

4.5.1. Buck converter design

The first power converter structure we chose for this application was a standard asynchronous Buck converter as seen on Figure 105:

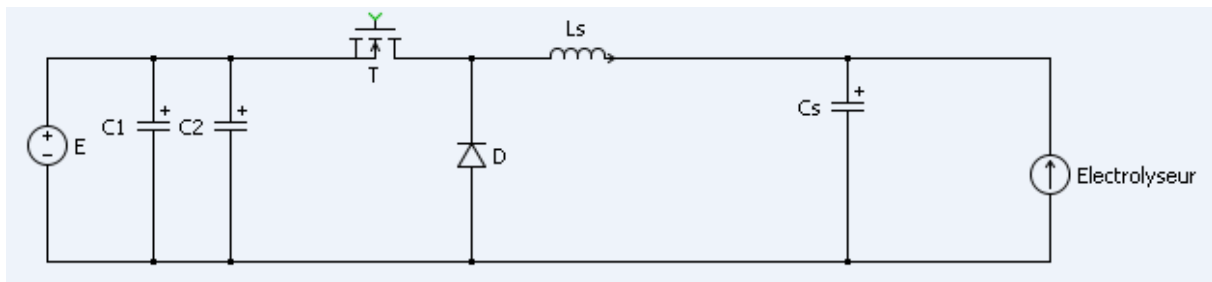


Figure 105: Schematic of the asynchronous Buck converter structure with ideal components

For this converter structure, we need to size the filter (L_s , C_s) and the power switches (T and D) as follows.

The smoothing coil L_s :

In a DC/DC converter, the maximum current ripple is obtained at a duty cycle $\alpha = 0.5$. With this in mind, the minimum smoothing inductance L_{smin} can be calculated as follows:

$$L_{smin} = \frac{V_{bus}}{4 * \Delta I_{max} * F} \quad (63)$$

In order to minimize the ripple, we chose to calculate with maximum values of the parameters. This means:

$$V_{bus} = 8V ; \Delta I_{max} = 5\% * 0.8 ; F = 100kHz$$

Resulting in $L_{smin} = 500\mu H$

For the choice of this coil, a compromise has to be made so that it can accept a current of 0.8 A while having a series resistance as low as possible to increase the efficiency.

The filter capacitor:

In the same way as for the current ripple, the maximum voltage ripple is obtained for a duty cycle $\alpha = 0.5$. The minimal capacity needed for the capacitor of the filter is given by equation (64):

$$C_{S_{min}} = \frac{V_{bus}}{32 * \Delta V_{out_{max}} * F^2 * L_{min}} \quad (64)$$

Using the same hypothesis as for the inductance, we use the maximal values for the calculation:

$$V_{bus} = 8V ; \Delta V_{out_{max}} = 5\% * 1.8 ; F = 100kHz$$

Leading us to: $C_{S_{min}} = 0.55 \mu F$

The two additional capacitors C1 and C2 are decoupling capacitors. These are classically added at the input of the converter. Voltage stability is assured as close as possible to the switching cell with a larger capacity C2 while the smaller capacity of C1 works as an interference suppressor, redirecting electromagnetic stress to the ground [Luc Lasne book]. These two converters are dimensioned to withstand the input voltage V_{bus} . Their internal series resistance has little impact on the converter's efficiency as their mean current is almost zero under periodic conditions.

Switching cell:

The switching cell for this converter architecture is composed of a transistor and a free-wheeling diode. For high switching frequencies (100 kHz in our case), an n-type MOSFET switch is the most appropriate. For sizing, the MOSFET must be able to withstand the bus voltage V_{bus} when it is open and the maximum current of the load (EC) when it is closed. The diode is chosen with the same constraints, with a target of minimal losses.

4.5.2. Simulation with ideal components:

After dimensioning the elements of the Buck converter circuit, a first simulation is conducted, using ideal components in order to validate the conception. Simulations are done with the Plexim toolbox in Matlab/Simulink. The curves presented in Figure 106 show the values of current and voltage in steady state conditions using ideal components.

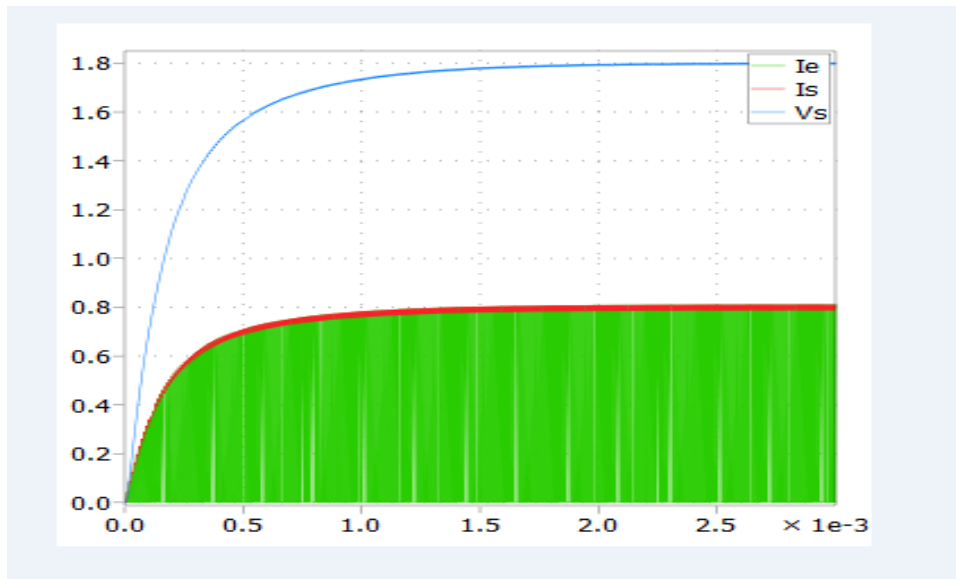


Figure 106: Simulation results with ideal components. Input current (green), output current (red) and output voltage (blue) in steady state conditions.

As the components are ideal in this simulation, the efficiency is without any surprise almost equal to 100 %. From the curves in Figure 106, we can conclude that the design is functional.

4.5.3. Simulation with real components:

Now that the design is validated through the ideal component simulation, we simulate the same converter with real components, including losses, as seen in Figure 107 below.

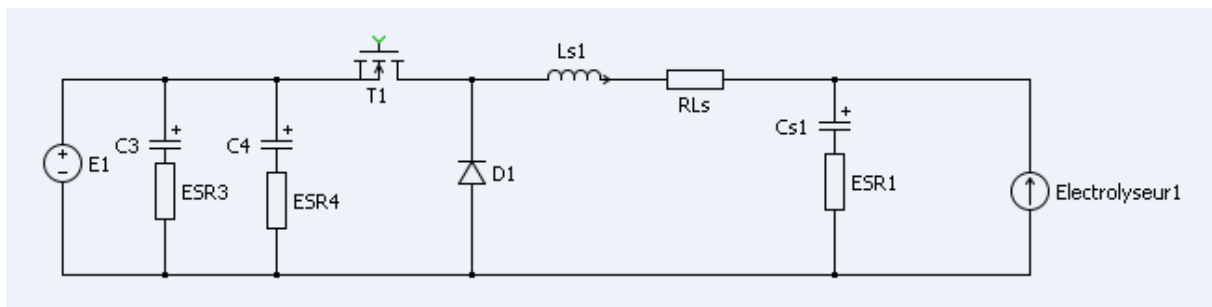


Figure 107: Schematic of the asynchronous Buck converter structure with real components

When integrating the specific losses for the different components, an efficiency of 91 % is estimated through simulation. This efficiency is too low for our application. As a potential solution, we decide to replace the diode by a second MOSFET switch.

4.5.4. Synchronous Buck converter:

As a solution to improve the efficiency of the converter in conduction mode, we chose to use a synchronous Buck structure by replacing the free-wheeling diode by a second MOSFET switch in parallel with a diode. Figure 108 shows a schematic of the synchronous Buck converter.

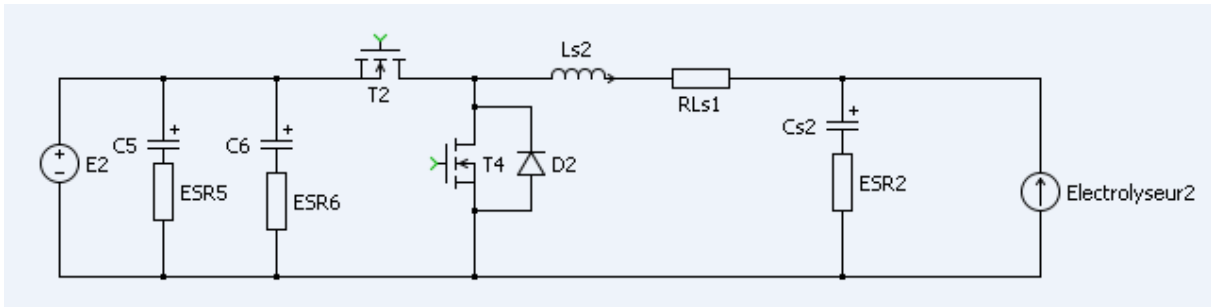


Figure 108: Schematic of the synchronous Buck converter structure with real components

Simulations of the synchronous Buck yield efficiency around 96 %, which corresponds to the project specifications. Although the efficiency is higher, this structure is more subtle in terms of control. The two switches must be fed a complementary PWM signal while managing downtimes. The parallel diode D2 helps with the conduction during switching times.

Now that the structure permitting efficiency higher than 93 % is chosen, the command for the converter must be designed.

4.5.5. Command circuits:

The command part of the converter is composed of regulated power supply, a microprocessor, drivers and sensors.

Regulated Power supply

For the voltage regulated power supply for the command circuits (5 V and 3.3 V), we used exactly the same design as in the Boost converter. Please refer to part 4.3 for more information on this part of the circuits.

This regulated power supply is again sized for multiple converters so we need only one for two to six converter cells. The first converter card will contain two micro Buck converters and this supply chain but further converters will be able to make use of this same supply chain, reducing the costs and complexity of their manufacturing.

MOSFET driver

Drivers are used to power up the MOSFET gate as the microcontroller outputs do not provide sufficient power. In our case, the main MOSFET switch is not connected to the ground, making it hard to command without a driver. For our synchronous Buck application, we need a driver with a complementary double output in order to command both MOSFETs in an optimal way. We chose the MCP14700 double MOSFET driver. Figure 109 shows a schematic of this driver.

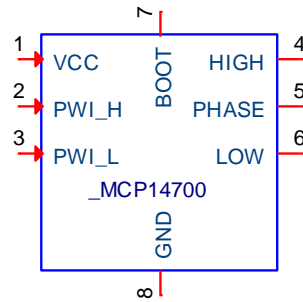


Figure 109: MCP14700 double MOSFET driver for the Buck converter

Sensors

We need sensors in order to measure voltage and current at the output of the converter. These values will be needed in the calculation of the duty cycle α in the regulation algorithm. As for the Boost converter, High value resistance (100 k Ω for example) can be used to measure the voltage while protecting the microcontroller inputs from current. The same instrumentation amplifier as in the Boost converter in part 4.3 is used to measure the current.

Microprocessor

The microprocessor is used to generate the command signals for the converter switches as well as for the output voltage regulation algorithm. For this converter, we chose to use the same PIC18LF27K40 microcontroller as for the micro Boost converter described in part 4.3.

Voltage control

As explained previously, we want to control the output voltage of our micro Buck converter to be constant at 1.8 V. To do this, a control algorithm needs to be developed. In order to design an appropriate control loop, we must first study the system in open loop.

To simplify this design step, the electrolyzer cell will be treated as a pure resistance. While this is not totally true in reality, it permits to describe the system easily when it comes to a constant output voltage. With this hypothesis, the system can be described by equation (65) below:

$$\frac{V_s(P)}{\alpha(P)} = \frac{E}{1 + \left(\frac{L_s}{R_{EC}} + R_{EC} \times C_s\right)P + L_s \times C_s P^2} \quad (65)$$

Where α is the duty cycle and $R_{EC} \cong 2.80 \Omega \cong \frac{V_s^2}{P_N}$

The step response of this system in open loop mode is studied in Matlab/Simulink and provides the resulting curves visible in Figure 110:

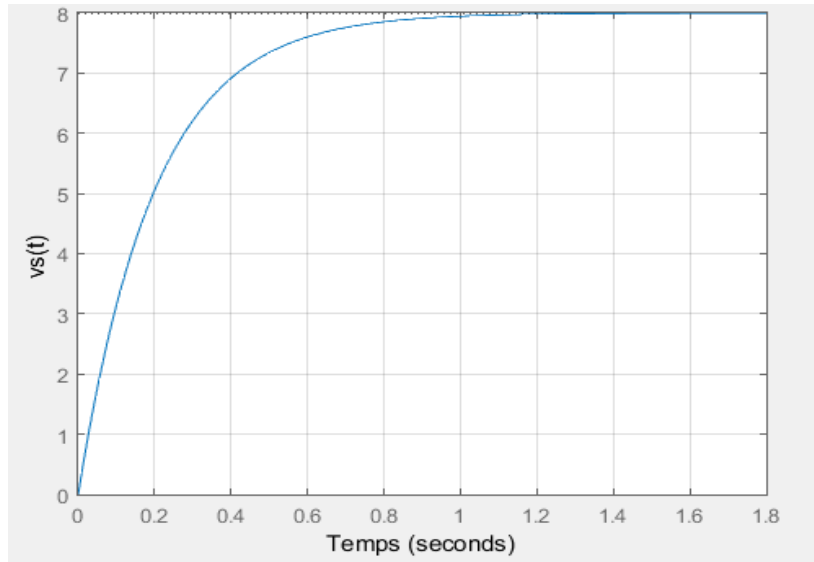


Figure 110: Step response of the converter system in open loop for the Buck converter

The step response behavior of this model can be modeled by the following equation:

$$G(p) = \frac{V_s(P)}{\alpha(P)} = \frac{K}{1 + TP} \quad (66)$$

With $K = 8V$: the static gain in permanent regime;

$T=0.261$ s: the time constant.

We wish to regulate the output voltage V_s to 1.8 V with a time response inferior to one millisecond ($T_{r95\%} \leq 1ms$) and a good static precision. A proportional integral (PI) corrector described by equation (67) is designed to satisfy these requirements.

$$C(P) = K_1 \frac{1 + T_1P}{T_1P} \quad (67)$$

As the desired time response $T_{r95\%}$ is small in comparison to the time constant T of the $G(P)$ system, we use the pole compensation method to calculate K_1 and T_1 as follows:

$$K_1 = \frac{3 \times T_1}{K \times T_{r95\%}} = 97.875 \quad \text{and} \quad T_1 = T = 0.261s \quad (68)$$

Figure 111 show the Simulink simulation for the closed control loop for the voltage regulation.

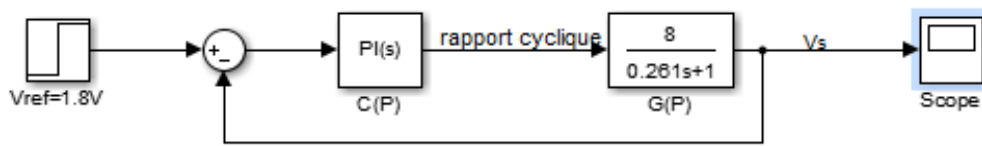


Figure 111: closed control loop for the voltage regulation in the Buck converter

The step response of the system in closed loop in simulation can be seen in Figure 112

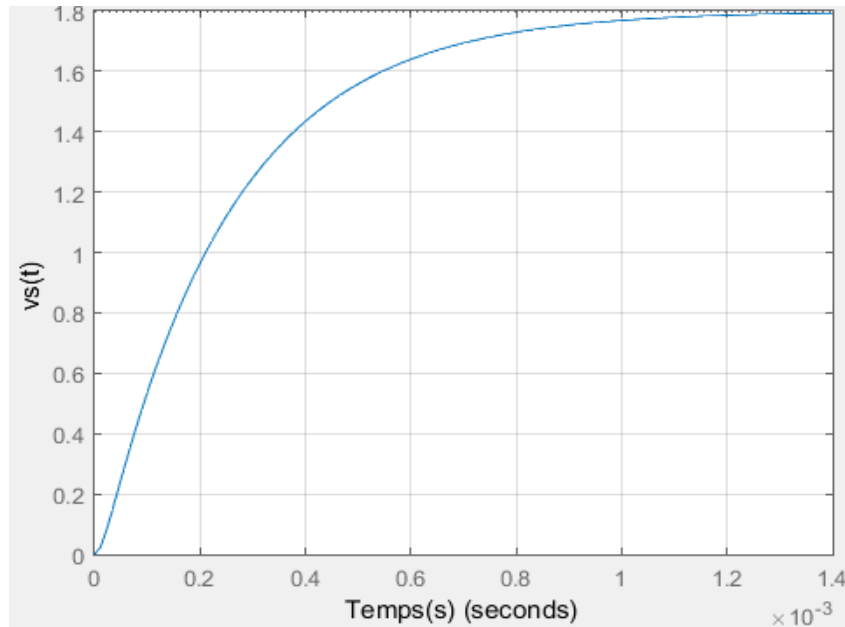


Figure 112: Step response in closed loop for the Buck converter

On this this simulation result curve a regulation at 1.8 V with the desired time response is observed. This result is satisfactory and permits to establish the control algorithm that will be implemented in the microcontroller.

4.5.6. Voltage Control Algorithm

From the previous closed loop simulations, we can create a control algorithm that will be implemented in the microcontroller. This algorithm will use the measured value of output voltage of the converter and compare it to the reference 1.8 V, calculating the error. The summed error is calculated by adding the current error to the previous error sum. The new result of the PI corrector is calculated by adding the error times the proportional gain K_1 to the error sum times the integral gain K_1/T_1 . Before implementing the PI result as the new duty-cycle (DC), we make sure that it does not exceed limits of the duty-cycle (maxDC and minDC). This algorithm is repeated after a determined time step dt . The flowchart in Figure 113 describes the implementation of this algorithm in a simplified way. For the real implementation in the microcontroller, the calculation of the PI and the refreshing of the duty-cycle value will be determined by the timer flag from the ADC measure acquisition.

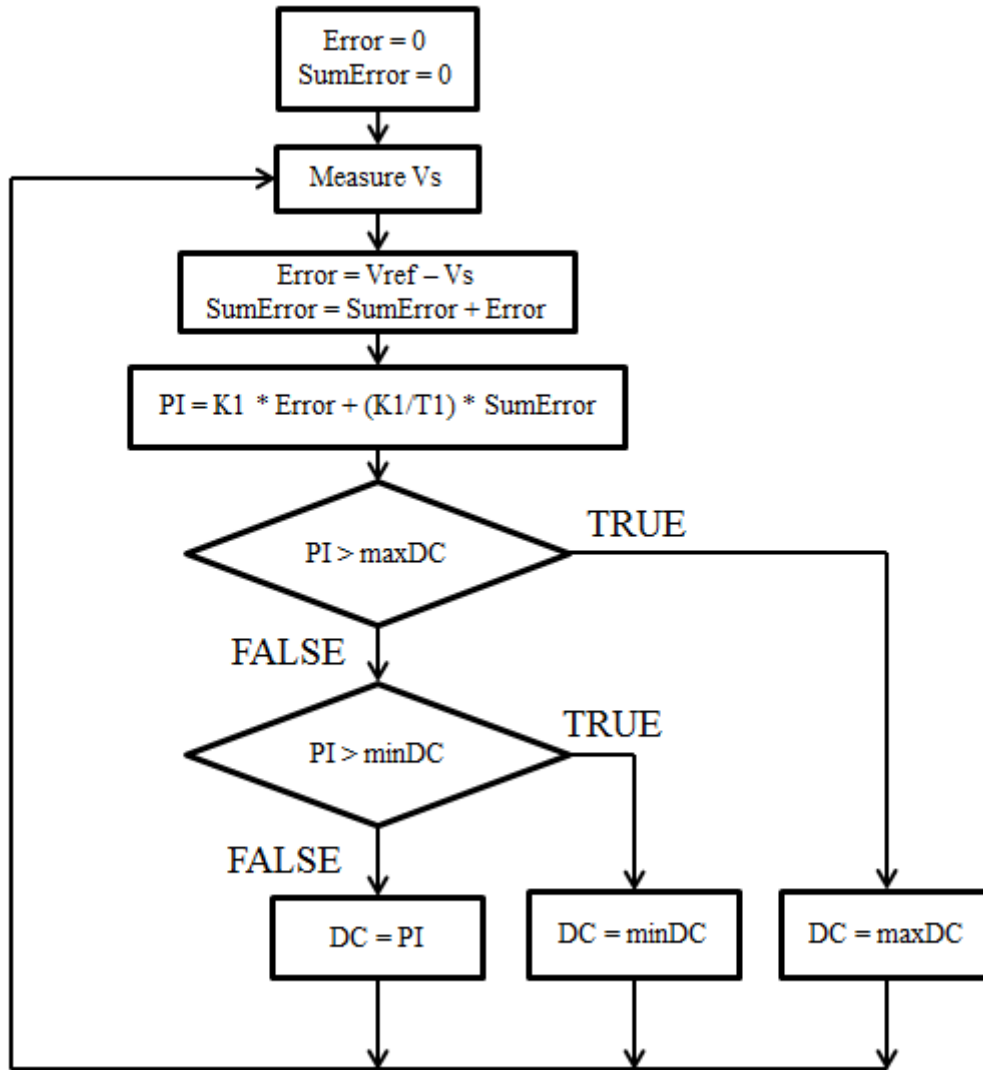


Figure 113: Flowchart of the simplified implementation of voltage regulation using the PI controller.

After performing these simulations and preparing for implementation of the command, the PCB layout of the card was designed with the help of the electronic tech department of the lab. It contains two micro Buck converters, one microcontroller with command circuits for both converters and the power supply circuit for the command part. The schematics for the design are visible on Figure 114.

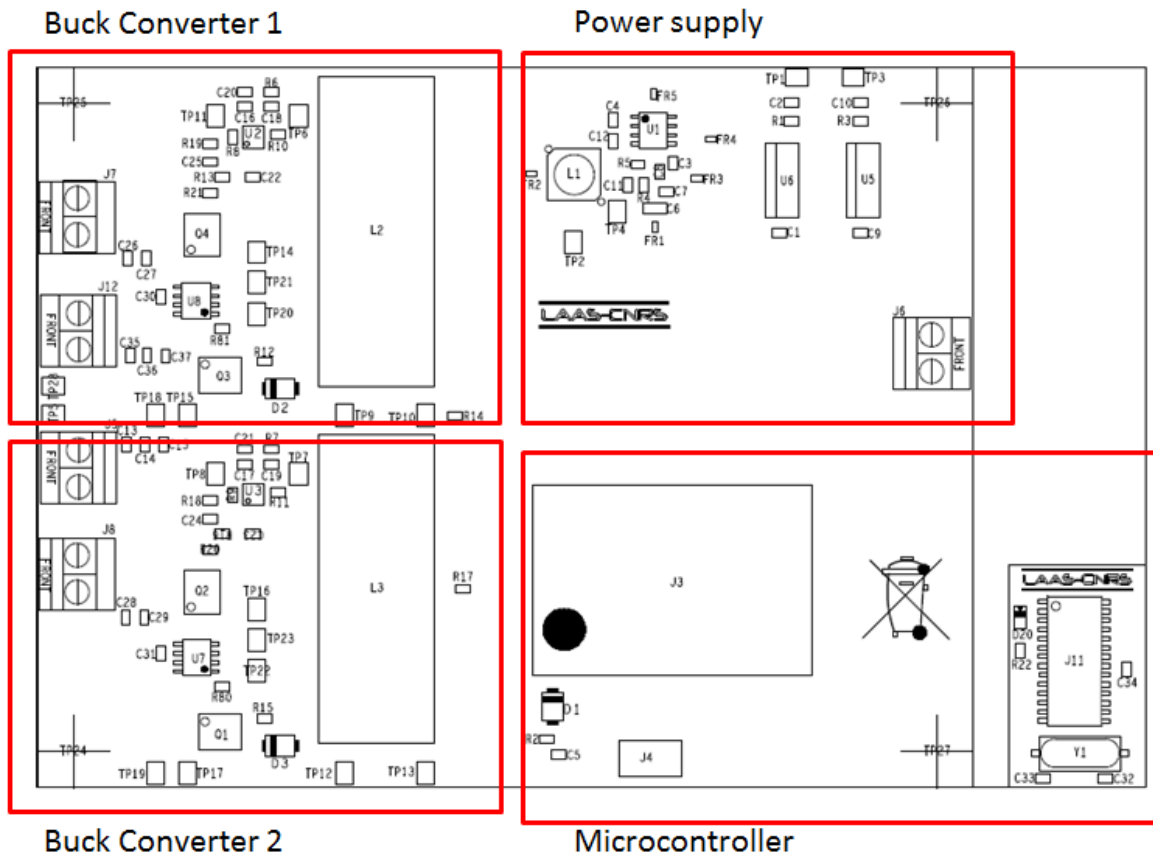


Figure 114: Schematics for the design of the Buck converter PCB containing two converters, one microcontroller and a power supply for the command part.

As the prototype card is still in the fabrication process, we do not have experimental results. The contribution of this thesis work for the distributed Buck converter stage is mostly in design and simulation.

The next step for the development of this project is the energy storage using the LIC supercapacitors described in Chapter 2 of this manuscript.

4.6. Lithium-Carbon supercapacitor storage

The energy storage part for this project by using LIC capacitors is mostly a perspective at this time. As this thesis work is the first in the team to incorporate Hydrogen study and electrolysis, a focus was made on that part of the project.

4.6.1. Storage Sizing:

Still, in order to design the whole project, a primary sizing of the storage elements had to be done. With the choice of the DC bus voltage of 5 V to 8 V, the ULTIMO LIC cell described in Chapter 2 of this manuscript is well adapted. As seen in Chapter 2, it is particularly well adapted to absorb intermittencies of the solar production, making it well suited to our CPV application. It will serve to store excess energy and supply energy to the ECs when necessary. In addition it will also ensure that the current fed to the ECs is not as fluctuating as the intermittent CPV production, and it will be able to smooth out the current profiles for the load.

The voltage range of the ULTIMO LIC cell is between 2.2 V (fully discharged) and 3.8 V (fully charged). This means that a series association of two cells would have a voltage range of 4.4 V to 7.6 V. This corresponds strategically with the DC bus voltage chosen for the project, which is 5 V to 8 V. Two ULTIMO cells connected in series will have the same capacity as a single cell: 500 mAh. With this in mind, we can connect multiple packs of two cells in series in order to increase the total storage capacity as in Figure 115.

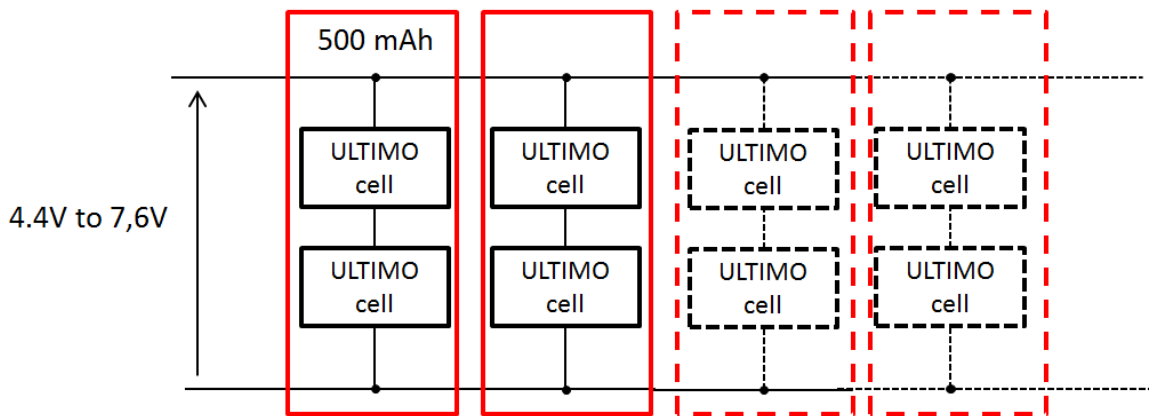


Figure 115: Possible series/parallel association of ULTIMO cells for the NextPV project

As seen in part 4.4, one H-Tec electrolyzer cell working at 1.8 V draws a current of 0.5 A, meaning a power of 0.9 W. This means that we need 0.9 Wh to supply it for one hour. The time “t” for which a supercapacitor can provide a given power P is given by equation (69):

$$t = \frac{1}{2P} C (V_{Max}^2 - V_{min}^2) \quad (69)$$

Where C =1100 F, is the capacity in Farad (F);

$V_{\max} = 3.8 \text{ V}$ is the maximal voltage of the cell when it is fully charged, in Volt (V).

$V_{\min} = 2.2 \text{ V}$ is the minimum voltage of the cell when it is fully discharged, in Volt (V).

For a power $P = 0.9\text{W}$ consumed by the load, we can calculate the total time t_{ULTIMO} needed to fully discharge one ULTIMO cell. This calculation is done without taking into account losses in the circuit and is only meant to be an indication for sizing.

$$t_{ULTIMO} = \frac{1100}{2 * 0.9} * (3.8^2 - 2.2^2) = 5867 \text{ s} = 97 \text{ min} = 1.63 \text{ h} \quad (70)$$

Experimental results of a 0.9 W constant power discharge of an ULTIMO cell are visible on Figure 116 and confirm this approximation.

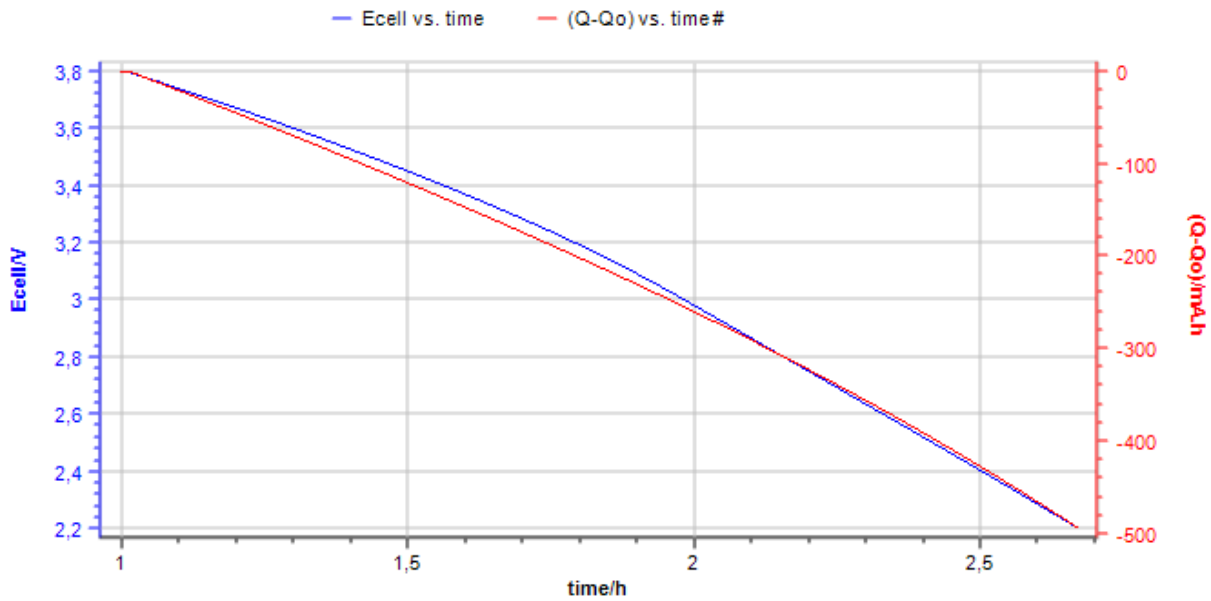


Figure 116: Experimental results of discharging ULTIMO cell at a constant power $P=0.9 \text{ W}$. V_{cell} vs time (V, blue) and discharged Capacity (mAh, red).

Now if we use a pack containing two ULTIMO cells in series as described in Figure 115, we obtain the following time:

$$t_{ULTIMOpack} = \frac{550}{2 * 0.9} * (7.6^2 - 4.4^2) = 11\,733 \text{ s} = 196 \text{ min} = 3.26 \text{ h} \quad (71)$$

This means that a pack containing two ULTIMO cells connected in series can potentially power one H-Tec electrolyzer for about three hours and fifteen minutes. Based on this, we will be able to scale our storage system depending on the intended autonomy of the system.

If we want to have sufficient energy storage to supply one electrolyzer for 24h without solar irradiation, we need to use more than 7 packs of two cells in parallel, meaning more than 14 single ULTIMO cells. Given the price of this new storage technology, this could be problematic for larger power scales. In order to be able to make realistic conclusions, comparative studies using battery storage hybridized with supercapacitors are needed.

Storage management:

Within a system comprising renewable energy production and energy consumption, it is primordial to manage energy flows going through the storage systems optimally. In addition, management systems are needed in order to protect the storage units and prolong their lifetime. In our specific application, two factors have to be taken into account: storing excess energy from PV production that cannot be immediately used by the load and providing the load with sufficient power when the PV power is not enough. In addition to this, the cell recharge has to be stopped when its maximum voltage is attained and its discharge has to be stopped once its minimum voltage is reached.

The potential management system built around the LIC storage elements can at this point be described through a set of rules:

- Using a bi-directional DC/DC Buck Boost converter structure for energy transfer between the bus and the storage elements.
- Allowing charge of the storage elements when PV power is superior to 0.9 W (per EC) and storage voltage is inferior to maximum voltage (7.6 V for packs of two cells in series).
- Allowing the discharge of the storage elements when PV power is inferior to 0.9 W (per EC) and when storage voltage is superior to minimum voltage (4.4 V for packs of two cells in series).
- Keeping the control circuits for each converter powered at all times when the system is powered on.

Applying these rules can be done either through a complete supervisor system connected to the other elements or in a more limited way through the control of the reversible DC/DC converter alone.

This step of the project still needs a lot of work, development and experimentation. This preliminary work will provide information for the next researcher working on this part of the project.

4.7. Conclusion

In this chapter we have presented the main results linked to the joint RCAST-LAAS project to produce H₂ with high efficiencies during 24h in real working conditions. To achieve the LVDC system structure which is my main contribution to this NextPV project, I started studying and designing each different element. CPV cells have been tested and a solar tracker has been installed to permit their usage. An elementary Boost converter architecture has been designed for one CPV cell and a PCB prototype containing two converters was created, enabling the use of a standard MPPT algorithm. Once this part was validated, the choice of an EC studied for our application was done. After better understanding the behavior of the EC following the studies presented in chapter 3, a Buck converter architecture has been designed, with the goal to enable the EC to work at the maximum efficiency point. We have simulation results but for time reasons, the experimental boards are not validated. Similarly, the study of DC/DC converters dedicated for LIC elements is not achieved.

A small scale solar to hydrogen conversion system has been designed with the goal of maximum hydrogen production efficiency. It has been shown that the individual stages of the conversion

chain have each have a specific efficiency. At its current stage of development, with a CPV system efficiency of roughly 31%, each elementary converter efficiency being around 95% with prototypes done in our lab and an electrolysis efficiency of 80%, we can look forward in the future to obtain an average STH solar to hydrogen conversion efficiency around 23 % in a large range of working conditions compared to 24.4 % in direct connection obtained in specific working conditions. This proposed system designed with distributed converter architectures presents numerous advantages with a maximal level of fine-tuned control for each of the elements and ensures optimal working conditions for the electrolyzer cells as long as solar irradiation is available. Unfortunately, this project needs more time to be achieved to definitively conclude on its own performances. The storage part must be studied with the addition of more comparative solutions. The LIC storage part for this solar to Hydrogen conversion system still needs development. A short preliminary study on sizing and achievable autonomy with the inclusion of ULTIMO LIC cells has been performed and constitutes a basic for further investigation in this field. But for cost reasons, this solution must be compared with another one, constituted by two storage elements, one dedicated for power demands and the other for energy demands, each one designed with its own DC/DC stage in order to have definitive results concerning the most adapted solution of storage part for this application.

REFERENCES

- [79] J. Jia *et al.*, « Solar water splitting by photovoltaic-electrolysis with a solar-to-hydrogen efficiency over 30% », *Nature Communications*, vol. 7, p. 13237, oct. 2016.
- [80] J. Dulout, « Optimal sizing and energy management of storage systems for renewable sources deployment, design of a LVDC microgrid », phdthesis, Université Toulouse 3 Paul Sabatier (UT3 Paul Sabatier), 2017.
- [81] W. Yanwachirakul *et al.*, « Design of free-barrier InGaAs/GaNAs multiple quantum well solar cells with 1.2 eV energy gap », *Jpn. J. Appl. Phys.*, vol. 56, n° 8S2, p. 08MA04, juill. 2017.
- [82] Z. Lin, P.-L. Taberna, et P. Simon, « Electrochemical double layer capacitors: What is next beyond the corner? », *Current Opinion in Electrochemistry*, vol. 6, n° 1, p. 115-119, déc. 2017.
- [83] Y. Liu, B. Soucaze-Guillous, P.-L. Taberna, et P. Simon, « Understanding of carbon-based supercapacitors ageing mechanisms by electrochemical and analytical methods », *Journal of Power Sources*, vol. 366, p. 123-130, oct. 2017.
- [84] G. Godillot, P.-L. Taberna, B. Daffos, P. Simon, C. Delmas, et L. Guerlou-Demourgues, « High power density aqueous hybrid supercapacitor combining activated carbon and highly conductive spinel cobalt oxide », *Journal of Power Sources*, vol. 331, p. 277-284, nov. 2016.
- [85] Y. El Basri, « Reconfigurable distributed power architecture for the optimisation of photovoltaic energy ». Ph.D. Thesis, Université Paul Sabatier, LAAS, 2013.
- [86] A. Gutiérrez Galeano, M. Bressan, F. Jiménez Vargas, et C. Alonso, « Shading Ratio Impact on Photovoltaic Modules and Correlation with Shading Patterns », *Energies*, vol. 11, n° 4, p. 852, avr. 2018.
- [87] M. Bressan, A. Gutierrez, L. Garcia Gutierrez, et C. Alonso, « Development of a real-time hot-spot prevention using an emulator of partially shaded PV systems », *Renewable Energy*, vol. 127, p. 334-343, nov. 2018.
- [88] J. Dulout, A. Luna Hernandez, A. Anvari-Moghaddam, C. Alonso, J. Guerrero, et B. Jammes, « Optimal Scheduling of a Battery-based Energy Storage System for a Microgrid with High Penetration of Renewable Sources », 2017.
- [89] S. W. Glunz, R. Preu, et D. Biro, « Crystalline Silicon Solar Cells », in *Comprehensive Renewable Energy*, Elsevier, 2012, p. 353-387.
- [90] K. Neuhaus, J. Dulout, et C. Alonso, « LVDC grid based on PV energy sources and multiple electrochemical storage technologies », in *Smart World Congress 2016 (2016SWC)*, Toulouse, France, 2016, p. 8p.
- [91] K. Neuhaus, C. Alonso, et P.-L. Taberna, « Adaptable equivalent circuit model for electrochemical storage elements as a part of energy system modeling for ZEB », in *2017 IEEE SmartWorld, Ubiquitous Intelligence & Computing, Advanced & Trusted Computed, Scalable Computing & Communications, Cloud & Big Data Computing, Internet of People and Smart City Innovation (SmartWorld/SCALCOM/UIC/ATC/CBDCOM/IOP/SCI)*, San Francisco, CA, 2017, p. 1-6.

General Conclusion and Perspectives

During this thesis work, we have been able to study the influence of the intermittency of the solar energy. Modeling efforts were necessary to apprehend the quality of the solar producible, which is an essential point in CPV applications. After synthesizing the existing models from the literature, we decided to process the experimental data from the 100 kWc solar platform ADREAM that were gathered over several years. This study led to a collaborative analysis and evaluation of simulation tools together with my colleague Ilias Papas, who is conducting a thesis on modeling energy in buildings. We focus our works on the modeling of the local solar producible for the conception of BIPV type buildings and compared the model's results with the experimental data of ADREAM [53]. The evaluated tools were Matlab on one hand, as a flexible way of implementing equivalent models, and on the other hand Pleiade, Comfie and TRNsys, which are more dedicated tools for thermal and building applications. For the most part of this thesis, Matlab Simulink stays the one most appropriate simulation tool, permitting an easy association of the different multidisciplinary models developed during this thesis and for the sizing of the different elements. As the precision of the solar producible and PV models are mostly set by the user, the models of other elements are chosen accordingly. The models of storage elements need to be kept relatively simple in order to limit the complexity of implementation and calculation times.

Based on the expertise of the supervising team, it seems clear to us that the usage of solar PV will become much more flexible in the future through the usage of specifically dedicated storage elements. For this reason, the first collaboration approach between LAAS and CIRIMAT was to conduct research on the impact of PV production on several types of storage elements, in order to incorporate these specific constraints directly into the design of new dedicated storage units. The first difficulty we faced was the choice of the most appropriate storage technologies for the study. A systematic study of experimental data from the PV plant of ADREAM was initiated, by using mathematical tools to deduce our first choices and develop a better understanding of the charging and discharging constraints implied by the PV source. Given the experimental data that was gathered over many years, the intermittency of the PV sources turns out to be very frequent and sometimes extremely abrupt on the ADREAM platform located in Toulouse. This has reaffirmed the fact that PV power cannot be massively injected into power grids as it is. In fact, it needs to be associated with storage elements that are at least able to "smooth out" the PV production, making it acceptable, predictable or controllable depending on the applications. Although it is acknowledged that the parameters of a battery are evolving differently in time depending on the way they are used, it is still difficult today to study the design of elements specifically adapted to buildings and PV.

As a consequence, the supervising team of this thesis wished to realize clustering studies that are described in the chapter 2 [90], with the goal to produce typical profiles of PV production and load. The idea is that through the identification of specific "building" profiles, the conception of elements of storage dedicated to this application could become more convenient and would help to avoid the surprises of premature ageing in battery cells. These profiles have

allowed us to prechoose storage elements that seemed to be the most appropriate to the building application. This opened up to another question regarding the quantity of energy that needed to be stored. The answer to this question turns out to be very complex, surpassing the choice of technology and including the issue of purchase and maintenance cost and the environmental impacts ranging from manufacturing processes to recycling. As this subject turned out to be too wide and out of the frame of our study, we choose to focus on a concrete application of concepts.

As the development of precise models for each type of storage element is way too time consuming, the research of a systematic identification methodology of parameters was suggested. It would allow to easily compare storage element families. The main results of this approach are documented in the chapter 2 and have otherwise been published in a conference[91].

Both for PV and CPV applications, the LVDC (Low Voltage Direct Current) microgrid concept seemed most appropriate for a connection with storage elements, when considering their direct impact on the power grid or on a load.

As the concept of LVDC involves dedicated distributed converters per source, per storage element and per load, we have been looking for an example of application that would illustrate the impacts in a PV system including storage.

Considering the existence of the collaboration between the LASS and the RCAST through the LIA NextPV and the discussions concerning the Hydrogene production from renewable sources, which is primordial for the energy transition in Japan, a “Solar Fuel” type application appeared as an appropriate context for the previously developed concepts.

Considering the small experience of LAAS concerning the Hydrogen energy vector, it seemed insightful to conduct a bibliographical synthesis to better apprehend the state of the art and the technological maturity of the different applications which need the production of hydrogen and its storage. More precisely, this part was launched in conjunction with the RCAST in order to better comprehend the behavior of the different elements, especially eletrolyzers. Experimental impedance spectroscopy tests have permitted the identification of literature model parameters. This led me to develop a data-processing tool dedicated to the identification of optimized parameters, which brought an increase in precision to this type of models. The details for this development are described in Chapter 3.

After we identified the priority of the energy flows between CPV, Hydrogen production through electrolysis and storage as well as the associated security measures, Chapter 4 explains the scientific approach for the conception of the “Solar Fuel” dedicated LVDC grid. In-depth studies on the characteristic dispersion in CPV cells from construction to usage (Temperature, irradiance...) had been carried out in RCAST, and were usable for the design of the first distributed architectures and to evaluate the energy gain in comparison with a classical single converter. As previous studies of the LAAS had demonstrated the contribution of distributed architectures in terms of PV production, the choice of a distributed converter architecture has also been made specifically for CPV in this application. In fact, CPV cells profit greatly from the ability to fine-tune their working conditions individually.

Knowing the performances of the energy sources, of the storage elements and of the load, the systematic approach for the design of dedicated converters for each of these elements and their specific command laws are described in chapter 4. The research of performance for each of the converters took more time than planned due to the complexity of the system and the microgrid dedicated to this application could not be completed in time.

To this day the converters dedicated to the CPV have been entirely validated while the experimental testing of the prototype for the converter dedicated to electrolyzers is ongoing. The characterization studies on the chosen storage elements and the models developed in chapter 2 will permit the conception of converters dedicated to the storage elements and the experimental validation of the complete microgrid.

These points constitute by default the first perspectives of this work, which is to conclude the laboratory scale microgrid, permitting the validation of all the concepts discussed in this thesis. In a short term perspective, the finalization of the prototype will permit the pursuit of comparative studies between distributed architectures and standard converter architectures that are used in grids today.

In the longer term, given the preliminary results uncovered during this thesis and through a new collaboration with the University of Corsica, the LAAS has decided to extend its existing platform to introduce electrolyzer cells, PMFC fuel cells and hydrogen storage tanks on a scale that is compatible with the existing DCAC grid existing in the ADREAM building. These major works constitute a direct perspective to the results of this thesis since the architecture that has been chosen for the association of the hydrogen vector with the PV plant of ADREAM will be based on the distributed LVDC architecture presented in this thesis. This installation will be an experimental basis to validate if our concept is viable at larger scales, permitting scalability and adaptability.

The first work on clustering methods to identify typical profiles for BIPV should be corroborated with similar studies on PV production data for other geographical locations in the world. On the long run, this could permit to establish norms for BIPV or storage design, such as the norms that exist for typical driving trajectories for the design of electric cars. This would help the electrochemical community to better understand the specific issue of the integration of renewable energies and the design of specially adapted storage elements.

Table of Figures

FIGURE 1: MAP OF THE ANNUAL AND DAILY SOLAR IRRADIANCE ON TERRESTRIAL SURFACES IN 2013 (SOLARGIS)..... 12

FIGURE 2: CROSS SECTION OF A STANDARD SILICON SOLAR CELL [4] 13

FIGURE 3: PICTURE OF A MONOCRYSTALLINE SILICON PV CELL [5] 13

FIGURE 4: SCHEMATIC REPRESENTATION OF THE DIFFERENT WAVELENGTH OF THE SOLAR SPECTRUM AND THEIR ABSORPTION THROUGH DIFFERENT MATERIALS IN MULTI-JUNCTION PV CELLS [8] 14

FIGURE 5: 1 MW CPV INSTALLATION WITH TRACKERS IN MOROCCO, BY SUMITOMO ELECTRIC..... 14

FIGURE 6: NREL STUDY SHOWING THE BEST PV EFFICIENCIES ACHIEVED IN RESEARCH WORLDWIDE SINCE 1975..... 15

FIGURE 7: THEMIS CONCENTRATED SOLAR PLANT [12] 16

FIGURE 8: CONCENTRATED SOLAR FURNACE ODEILLO, FRANCE [13] 16

FIGURE 9: SCHEMATIC REPRESENTATION OF THE WORKING PRINCIPLE OF A PUMPED STORAGE INSTALLATION [] 18

FIGURE 10: PICTURE OF GRAND'MAISON DAM, THE BIGGEST PUMPED STORAGE INSTALLATION IN FRANCE [] 19

FIGURE 11: SCHEMATIC OF THE THERMAL HEATING SYSTEM INSTALLED IN THE DRAKE LANDING SOLAR COMMUNITY, CANADA [15] 20

FIGURE 12: DISTRIBUTION OF ENERGY CONSUMPTION PER ACTIVITY SECTOR (US DEPARTMENT OF ENERGY)[34]..... 29

FIGURE 13: AERIAL VIEW OF THE ADREAM BUILDING IN LAAS-CNRS..... 31

FIGURE 14: REGULAR CRYSTALLINE SILICON PV CELLS INSTALLED ON THE TERRACE AND WALLS OF THE ADREAM BUILDING 32

FIGURE 15: DOUBLE AND TRIPLE GLAZING PV FAÇADE OF THE ADREAM BUILDING 33

FIGURE 16: ADREAM'S SUPERVISION TOOL, USER INTERFACE 33

FIGURE 17: ADREAM'S MEASURED PV ENERGY PRODUCTION (2014) 34

FIGURE 18: ADREAM'S MEASURED PV ENERGY PRODUCTION (2015) 34

FIGURE 19: ADREAM'S MEASURED PV ENERGY PRODUCTION (2016) 35

FIGURE 20: DIVISION OF THE GLOBAL RADIATION (G) INTO DIRECT (S), DIFFUSE (D) AND REFLECTED (R) RADIATION 36

FIGURE 21: SIMPLIFIED DIAGRAM OF THE SOLAR IRRADIATION MODEL 37

FIGURE 22: SIMULATED PV ENERGY PRODUCTION WITH MATLAB (ADREAM, 2014) 38

FIGURE 23:SIMULATED PV ENERGY PRODUCTION WITH MATLAB (ADREAM, 2015) 39

FIGURE 24: SIMULATED PV ENERGY PRODUCTION WITH MATLAB (ADREAM, 2016) 39

FIGURE 25: ANNUAL ELECTRICAL ENERGY PRODUCTION FROM ADREAM'S PV SYSTEMS (2014), MEASURED AND SIMULATED..... 40

FIGURE 26: ANNUAL ELECTRICAL ENERGY PRODUCTION FROM ADREAM'S PV SYSTEMS (2015), MEASURED AND SIMULATED..... 40

FIGURE 27: ANNUAL ELECTRICAL ENERGY PRODUCTION FROM ADREAM'S PV SYSTEMS (2016), MEASURED AND SIMULATED 6... 41

FIGURE 28: ALGORITHM FOR THE K-MEDOIDS CLUSTERING METHOD..... 43

FIGURE 29: DIFFERENT TYPES OF DAILY PROFILES FOR PV POWER PRODUCTION IDENTIFIED WITH K-MEDOIDS ALGORITHM. 44

FIGURE 30: DIFFERENT TYPES OF DAILY PROFILES FOR ADREAM'S POWER CONSUMPTION IDENTIFIED WITH K-MEDOIDS ALGORITHM. 45

FIGURE 31: BCS-815 BATTERY CYCLER FROM BIO-LOGIC INSTALLED IN THE LABORATORY ROOM OF THE ADREAM PLATFORM 46

FIGURE 32: THERMAL ENCLOSURE USED WITH THE BCS-815 FOR TEMPERATURE CONTROL DURING BATTERY TESTS 47

FIGURE 33: LFP CELLS FROM THE BRAND ENIX AND PHET 56

FIGURE 34: CHARGING CYCLES AT DIFFERENT C-RATES FOR THE ENIX LFP CELL 56

FIGURE 35: DISCHARGING CYCLES AT DIFFERENT C-RATES FOR THE ENIX LFP CELL 57

FIGURE 36: 3.7 V LITHIUM-POLYMER CELL 58

FIGURE 37: CHARGING CYCLES AT DIFFERENT C-RATES FOR THE LIPO CELL..... 58

FIGURE 38: DISCHARGING CYCLES AT DIFFERENT C-RATES FOR THE LIPO CELL 59

FIGURE 39: SIMPLIFIED REPRESENTATION OF THE ENERGY STORAGE PROCESS IN A LIC CELL..... 60

FIGURE 40: ULTIMO LAMINATED LIC CELLS, JMENERGY 61

FIGURE 41: CHARGING CYCLES AT DIFFERENT C-RATES FOR A ULTIMO LIC CELL..... 62

FIGURE 42: DISCHARGING CYCLES AT DIFFERENT C-RATES FOR A ULTIMO LIC CELL..... 63

| | |
|---|-----|
| FIGURE 43: EVOLUTION OF THE DISCHARGEABLE CAPACITY IN ULTIMO CELL 1 OVER 6000 CYCLES AT 10C. WITH REST TIMES EVERY 100 CYCLES..... | 64 |
| FIGURE 44: EVOLUTION OF THE DISCHARGEABLE CAPACITY IN AN ULTIMO CELL 2 OVER 6000 CYCLES AT 10C. WITH REST TIMES EVERY 100 CYCLES..... | 64 |
| FIGURE 45: SCHEMATIC OF THE VOC, R EQUIVALENT CIRCUIT STORAGE MODEL..... | 67 |
| FIGURE 46: CELL VOLTAGE AND AH DURING STEP BY STEP CHARGING | 68 |
| FIGURE 47: APPROACHING VOC(SOC) RELATION WITH A RATIONAL FUNCTION FOR AN ENIX LiFePO ₄ CELL..... | 69 |
| FIGURE 48: APPROACHING R(I) RELATION FOR AN ENIX LiFePO ₄ CELL ON A LOGARITHMIC SCALE | 70 |
| FIGURE 49: EXPERIMENTAL MEASURES COMPARED TO EC MODEL AT DIFFERENT CURRENT RATES FOR ENIX LiFePO ₄ CELL..... | 70 |
| FIGURE 50: SIMPLIFIED REPRESENTATION OF A FUEL CELL CAR ARCHITECTURE | 79 |
| FIGURE 51: 2009 - PEUGEOT 307 CC FISYPAC HYBRID ELECTRICAL PROTOTYPE, EQUIPPED WITH JCS LI-ION BATTERIES AND A CEA-PSA 20kWe FUEL CELL STACK AS A « RANGE EXTENDER » | 79 |
| FIGURE 52: TOYOTA - FCHV-ADV MODEL 2009. ADVANCED FUEL CELL VEHICLE WITH FOUR HIGH PRESSURE HYDROGEN TANKS AT UP TO 700 BAR, PRECURSOR TO THE MORE KNOWN TOYOTA MIRAI..... | 79 |
| FIGURE 53: 2010 - HYUNDAI TUCSON iX35 FCEV HYBRID. EQUIPPED WITH 21 kW LI POLYMER BATTERY, 100 kW BIPOLAIR METALLIC FUEL CELL AND A 5.6 KG HYDROGEN TANKS AT 700 BARS – IT ACHIEVED AN AUTONOMY OF 640 KM. | 80 |
| FIGURE 54: 2015 - TOYOTA MIRAI, WITH A 114 kW FUEL CELL (155 HORSES), AND A 1.6 kWh NI-MH BATTERY. | 80 |
| FIGURE 55: ROCKET ARIANE 5 TAKEOFF | 82 |
| FIGURE 56: HYDROGEN SATELLITE PLANE DESIGNED BY ONERA, FRANCE | 82 |
| FIGURE 57: HYDROGEN DRONE DESIGNED BY THE COMPANY INTELLIGENT ENERGY USING FUEL CELLS. | 82 |
| FIGURE 58: HYDROGEN ZEPPELIN BALOON USED IN THE 1930S..... | 83 |
| FIGURE 59: COMPOSITE HYDROGEN RESERVOIR FROM THE BRAND TOYOTA | 84 |
| FIGURE 60: ENERGY LOSS BY PRESSURIZING HYDROGEN FOR DIFFERENT TECHNIQUES | 84 |
| FIGURE 61: HYDROGEN LIQUEFACTION COST IN COMPARISON TO STORED ENERGY AND DEPENDANCE ON PLANT CAPACITY | 85 |
| FIGURE 62: SIMPLIFIED SCHEMATIC OF MAGNESIUM ELECTROLYSIS..... | 87 |
| FIGURE 63: SIMPLIFIED SCHEMATIC OF ALKALINE ELECTROLYSIS | 89 |
| FIGURE 64: SCHEMATIC OF A PEM ELECTROLYZER CELL..... | 90 |
| FIGURE 65: SCHEMATIC OF HIGH TEMPERATURE SOEC ELECTROLYSIS CELL..... | 91 |
| FIGURE 66: COMPARISON OF THE PRICE OF PRODUCED HYDROGEN THROUGH WATER ELECTROLYSIS USING TWO DIFFERENT TECHNOLOGIES AND THE PRICE OF HYDROGEN PRODUCED THROUGH STEAM METAL REFORMING IN EUROPE. CGSP STUDY ... | 92 |
| FIGURE 67: COMPARISON OF MATURITY FOR DIFFERENT HYDROGEN PRODUCTION METHODS BASED ON RENEWABLE ENERGIES. IRENA 2018..... | 94 |
| FIGURE 68: SOLAR PV INSTALLATION OF THE MYRTE PLATFORM IN AJACCIO..... | 95 |
| FIGURE 69: ELECTROLYSER STATION FOR SOLAR HYDROGEN PRODUCTION OF THE MYRTE PLATFORM IN AJACCIO..... | 95 |
| FIGURE 70: HYDROGEN AND OXYGEN STORAGE TANKS AT MYRTE PLATFORM IN AJACCIO..... | 95 |
| FIGURE 71: HYDROGEN ENERGY SUPPLY IN HSUI TEN BOSH HOTEL, USING BATTERIES, ELECTROLYZER CELLS AND FUEL CELLS FOR LOCAL ENERGY SUPPLY | 96 |
| FIGURE 72: CPV AND ELECTROLYZER INSTALLATIONS IN THE UNIVERSITY OF TOKYO..... | 97 |
| FIGURE 73: ELECTROLYZER CELLS FROM THE BRAND H-TEC (LEFT) AND HORIZON (RIGHT. | 98 |
| FIGURE 74: THE TWO ELECTROLYZERS CONNECTED TO GRADUATED RESERVOIRS VIA PLASTIC TUBES, EXPERIMENTAL SETUP | 99 |
| FIGURE 75: GRAPHIC COMPARISON OF THE H-TEC AND HORIZON EC..... | 101 |
| FIGURE 76: EXAMPLE OF NYQUIST PLOT FOR H-TEC CELL FOR A 1.65 V SUPPLY. EIS DATA | 102 |
| FIGURE 77: SCHEMATIC OF THE EQUIVALENT CIRCUIT MODEL FOR THE H-TEC EC | 103 |
| FIGURE 78: NYQUIST PLOT OF EXPERIMENTAL DATA (BLUE) AND BEST AUTOMATIC FIT USING ZFITGUI (RED) FOR 1.5 V DATA..... | 104 |
| FIGURE 79: NYQUIST PLOT OF EXPERIMENTAL DATA (BLUE) AND MANUAL FIT USING ZFITGUI (RED) FOR 1.5 V DATA | 105 |
| FIGURE 80: PARAMETER CONTROL INTERFACE OF THE SPECIFICFIT MATLAB TOOL..... | 107 |
| FIGURE 81: NYQUIST PLOT OF EXPERIMENTAL DATA (BLUE CURVE WITH CIRCLES) AND MANUAL FIT USING SPECIFICFIT (RED CURVE WITH POINTS) FOR 1.5 V DATA..... | 107 |
| FIGURE 82: CPE PARAMETER 1 (P ₁ AND P ₃) VERSUS EC VOLTAGE..... | 108 |
| FIGURE 83: EC IMPEDANCE MODEL IMPLEMENTED AS SIMULINK BLOCK..... | 109 |

| | |
|---|-----|
| FIGURE 84: SOLAR TO HYDROGEN CONVERSION SYSTEM USING CPV MONO MODULES AND SMALL SCALE ELECTROLYZER CELLS WITH DIRECT CONNECTION. RCAST | 113 |
| FIGURE 85: SCHEMATIC OF THE OPA MICRO-GRID IN LAAS-CNRS | 115 |
| FIGURE 86: GENERAL DESIGN SCHEMATIC OF THE NEXTPV SYSTEM STRUCTURE | 115 |
| FIGURE 87: TRIPLE JUNCTION CELL WITH SOLAR PRISM. | 117 |
| FIGURE 88: MULTI-JUNCTION PV CELL WITH FRESNEL LENS, PRISM AND THERMAL DISSIPATION, PICTURE (LEFT) AND SCHEMATIC (RIGHT) | 117 |
| FIGURE 89: TWO-AXIS SOLAR TRACKER INSTALLED IN THE LAAS LABORATORY..... | 118 |
| FIGURE 90: I-V CURVE OF A MULTI-JUNCTION CELL WITH FRESNEL LENS (ORANGE) AND WITHOUT FRESNEL LENS (YELLOW). MEASURED UNDER REAL SUN AT $\sim 750 \text{ W/m}^2$ | 119 |
| FIGURE 91: I-V CURVES FOR TWO DIFFERENT CELLS AT DIFFERENT IRRADIANCE LEVELS | 119 |
| FIGURE 92: I-V CURVE RESULTS FROM PREVIOUS TESTS AT RCAST, TOKYO | 120 |
| FIGURE 93: STANDARD BOOST CONVERTER STRUCTURE | 121 |
| FIGURE 94: COMPARISON OF LOSSES IN FIVE SELECTED N-TYPE MOSFET SWITCHES FOR SMALL POWER APPLICATIONS. SIMULATION AT 2.7 V, 100 KHZ..... | 122 |
| FIGURE 95: COMPARISON OF THE LOSSES IN TWO DIODES AT 100 KHZ AND $\alpha=0.6$ | 122 |
| FIGURE 96: SCHEMATIC OF THE 5.5 V SUPPLY FOR THE COMMAND CIRCUITS | 123 |
| FIGURE 97: SCHEMATIC OF THE 5V AND 3.3V VOLTAGE REGULATION TO SUPPLY DRIVERS AND MICROPROCESSOR | 124 |
| FIGURE 98: INSTRUMENTATION AMPLIFIER USED FOR THE MEASURE OF CURRENT | 124 |
| FIGURE 99: SCHEMATIC OF THE PIC18LF27K40 MICROCONTROLLER AND CONENNECTIONS FOR THE BUCK CONVERTER. | 125 |
| FIGURE 100: SCHEMATIC OF THE CONVERTER DESIGN SHOWING MEASURE POINTS AND MPPT COMMAND INPUT | 126 |
| FIGURE 101: MOVEMENT OF THE FUNCTIONING POINT ON THE PV POWER CURVE DURING HILL CLIMBING MPPT..... | 126 |
| FIGURE 102: FLOWCHART OF THE HILL CLIMBING MPPT ALGORITHM IMPLEMENTED FOR THIS CONVERTER | 127 |
| FIGURE 103: PICTURE OF THE CARD CONTAINING TWO BOOST CONVERTERS, ONE MICROCONTROLLER AND ONE SUPPLY CIRCUIT FOR THE COMMAND PART..... | 128 |
| FIGURE 104: EFFICIENCY VERSUS CURRENT FOR THE BOOST CONVERTER CARD, $\alpha=0.5$ | 128 |
| FIGURE 105: SCHEMATIC OF THE ASYNCHRONOUS BUCK CONVERTER STRUCTURE WITH IDEAL COMPONENTS | 129 |
| FIGURE 106: SIMULATION RESULTS WITH IDEAL COMPONENTS. INPUT CURRENT (GREEN), OUTPUT CURRENT (RED) AND OUTPUT VOLTAGE (BLUE) IN STEADY STATE CONDITIONS. | 131 |
| FIGURE 107: SCHEMATIC OF THE ASYNCHRONOUS BUCK CONVERTER STRUCTURE WITH REAL COMPONENTS | 131 |
| FIGURE 108: SCHEMATIC OF THE SYNCHRONOUS BUCK CONVERTER STRUCTURE WITH REAL COMPONENTS..... | 132 |
| FIGURE 109: MCP14700 DOUBLE MOSFET DRIVER FOR THE BUCK CONVERTER..... | 133 |
| FIGURE 110: STEP RESPONSE OF THE CONVERTER SYSTEM IN OPEN LOOP FOR THE BUCK CONVERTER..... | 134 |
| FIGURE 111: CLOSED CONTROL LOOP FOR THE VOLTAGE REGULATION IN THE BUCK CONVERTER | 135 |
| FIGURE 112: STEP RESPONSE IN CLOSED LOOP FOR THE BUCK CONVERTER | 135 |
| FIGURE 113: FLOWCHART OF THE SIMPLIFIED IMPLEMENTATION OF VOLTAGE REGULATION USING THE PI CONTROLLER. | 136 |
| FIGURE 114: SCHEMATICS FOR THE DESIGN OF THE BUCK CONVERTER PCB CONTAINING TWO CONVERTERS, ONE MICROCONTROLLER AND A POWER SUPPLY FOR THE COMMAND PART..... | 137 |
| FIGURE 115: POSSIBLE SERIES/PARALLEL ASSOCIATION OF ULTIMO CELLS FOR THE NEXTPV PROJECT | 138 |
| FIGURE 116: EXPERIMENTAL RESULTS OF DISCHARGING ULTIMO CELL AT A CONSTANT POWER $P=0.9 \text{ W}$. V_{CELL} VS TIME (V, BLUE) AND DISCHARGED CAPACITY (MAH, RED)..... | 139 |
| FIGURE 117: ADREAM'S MEASURED PV ENERGY PRODUCTION (2014), DAILY SUM | 154 |
| FIGURE 118: ADREAM'S MEASURED PV ENERGY PRODUCTION (2015), DAILY ENERGY SUM..... | 154 |
| FIGURE 119: ADREAM'S MEASURED PV ENERGY PRODUCTION (2016), DAILY ENERGY SUM..... | 155 |
| FIGURE 120: ADREAM'S SIMULATED PV ENERGY PRODUCTION (2014), DAILY ENERGY SUM | 156 |
| FIGURE 121: ADREAM'S SIMULATED PV ENERGY PRODUCTION (2015), DAILY ENERGY SUM | 156 |
| FIGURE 122: ADREAM'S SIMULATED PV ENERGY PRODUCTION (2016), DAILY ENERGY SUM | 157 |
| FIGURE 123: RESULTS FOR THE AUTOMATED CHARACTERIZATION OF THE COMPLEX IMPEDANCE AT 1.45V, USING ZFitGUI | 161 |
| FIGURE 124: RESULTS FOR THE AUTOMATED CHARACTERIZATION OF THE COMPLEX IMPEDANCE AT 1.5V, USING ZFitGUI | 161 |
| FIGURE 125: RESULTS FOR THE AUTOMATED CHARACTERIZATION OF THE COMPLEX IMPEDANCE AT 1.55V, USING ZFitGUI | 162 |

| | |
|---|-----|
| FIGURE 126: RESULTS FOR THE AUTOMATED CHARACTERIZATION OF THE COMPLEX IMPEDANCE AT 1.6V, USING ZFitGUI | 162 |
| FIGURE 127: RESULTS FOR THE AUTOMATED CHARACTERIZATION OF THE COMPLEX IMPEDANCE AT 1.65V, USING ZFitGUI | 163 |
| FIGURE 128: RESULTS FOR THE AUTOMATED CHARACTERIZATION OF THE COMPLEX IMPEDANCE AT 1.675V, USING ZFitGUI | 163 |
| FIGURE 129: RESULTS FOR THE AUTOMATED CHARACTERIZATION OF THE COMPLEX IMPEDANCE AT 1.7V, USING ZFitGUI | 164 |
| FIGURE 130: RESULTS FOR THE MANUAL CHARACTERIZATION OF THE COMPLEX IMPEDANCE AT 1.45V, USING ZFitGUI | 165 |
| FIGURE 131: RESULTS FOR THE MANUAL CHARACTERIZATION OF THE COMPLEX IMPEDANCE AT 1.5V, USING ZFitGUI | 165 |
| FIGURE 132: RESULTS FOR THE MANUAL CHARACTERIZATION OF THE COMPLEX IMPEDANCE AT 1.55V, USING ZFitGUI | 166 |
| FIGURE 133: RESULTS FOR THE MANUAL CHARACTERIZATION OF THE COMPLEX IMPEDANCE AT 1.6V, USING ZFitGUI | 166 |
| FIGURE 134: RESULTS FOR THE MANUAL CHARACTERIZATION OF THE COMPLEX IMPEDANCE AT 1.65V, USING ZFitGUI | 167 |
| FIGURE 135: RESULTS FOR THE MANUAL CHARACTERIZATION OF THE COMPLEX IMPEDANCE AT 1.675V, USING ZFitGUI | 167 |
| FIGURE 136: RESULTS FOR THE MANUAL CHARACTERIZATION OF THE COMPLEX IMPEDANCE AT 1.7V, USING ZFitGUI | 168 |
| FIGURE 137: RESULTS FOR THE MANUAL CHARACTERIZATION OF THE COMPLEX IMPEDANCE AT 1.45V, USING SPECIFICFIT..... | 169 |
| FIGURE 138: RESULTS FOR THE MANUAL CHARACTERIZATION OF THE COMPLEX IMPEDANCE AT 1.5V, USING SPECIFICFIT..... | 169 |
| FIGURE 139: RESULTS FOR THE MANUAL CHARACTERIZATION OF THE COMPLEX IMPEDANCE AT 1.55V, USING SPECIFICFIT..... | 170 |
| FIGURE 140: RESULTS FOR THE MANUAL CHARACTERIZATION OF THE COMPLEX IMPEDANCE AT 1.6V, USING SPECIFICFIT..... | 170 |
| FIGURE 141: RESULTS FOR THE MANUAL CHARACTERIZATION OF THE COMPLEX IMPEDANCE AT 1.65V, USING SPECIFICFIT..... | 171 |
| FIGURE 142: RESULTS FOR THE MANUAL CHARACTERIZATION OF THE COMPLEX IMPEDANCE AT 1.675V, USING SPECIFICFIT..... | 171 |
| FIGURE 143: RESULTS FOR THE MANUAL CHARACTERIZATION OF THE COMPLEX IMPEDANCE AT 1.7V, USING SPECIFICFIT..... | 172 |
| FIGURE 144: RELATION BETWEEN THE SERIES RESISTOR AND THE SUPPLY VOLTAGE FOR THE H-TEC CELL | 173 |
| FIGURE 145: RELATION BETWEEN THE PARALLEL RESISTOR Rp1 AND THE SUPPLY VOLTAGE FOR THE H-TEC CELL..... | 173 |
| FIGURE 146: RELATION BETWEEN THE PARALLEL RESISTOR Rp2 AND THE SUPPLY VOLTAGE FOR THE H-TEC CELL..... | 174 |
| FIGURE 147: RELATION BETWEEN THE CPE ELEMENT PARAMETERS P1, P2, P3, P4 AND THE SUPPLY VOLTAGE FOR THE H-TEC CELL | 174 |

ANNEXES

ANNEX 1: TENESOL PV panel datasheet

► TE2200

Caractéristiques électriques TE2200

| Puissance typique | Wc | 250' | 260' |
|-------------------------------|-----|-------|------|
| Puissance minimale | | 245 | 255 |
| Puissance maximale | | 255 | 265 |
| Limite de classe de puissance | Wc | -5/+5 | |
| Limite de classe de puissance | % | ± 2.0 | |
| Tension à puissance max. | (V) | 30.3 | 30.5 |
| Intensité à puissance max. | (A) | 8.3 | 8.5 |
| Tension circuit ouvert | (V) | 37.3 | 37.5 |
| Courant de court circuit | (A) | 8.6 | 8.8 |

Tests réalisés dans les conditions standards STC : Ensoleillement 1000 W/m²; Am 1,6; Température 25 °C.
(') : Module disponible sur demande.

| Puissance à 45°C / 800W/m² | Wc | 185.8 | 191.6 |
|----------------------------|-----|-------|-------|
| Tension à puissance max. | (V) | 27.7 | 27.9 |
| Intensité à puissance max. | (A) | 6.7 | 6.9 |
| Tension circuit ouvert | (V) | 34.7 | 34.9 |
| Courant de court circuit | (A) | 7.0 | 7.1 |

Tests NOCT réalisés avec une puissance maximale (en Wc) avec une température de jonction de 45 °C et un éclairement de 800 W/m²; Am 1,6; Température ambiante 20 °C; Vitesse de vent à 1 m/sec.

| Influence de la température | |
|---------------------------------------|---------------|
| Coefficient de température: Tension | - 129,0 mV/°C |
| Coefficient de température: Courant | + 4,4 mA/°C |
| Coefficient de température: Puissance | - 0,46 %/°C |
| NOCT | 45°C |

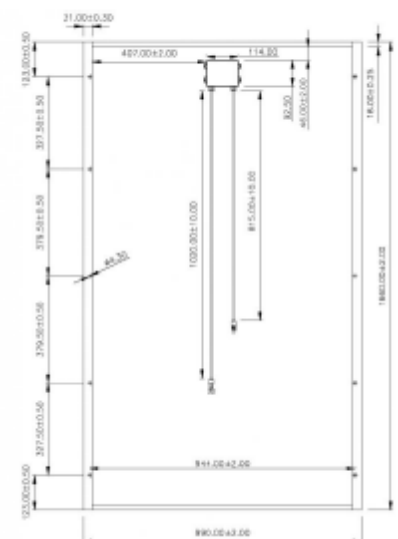
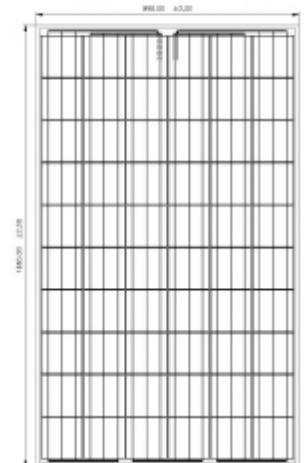
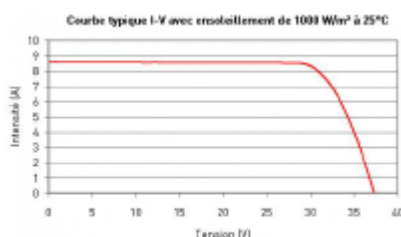
| Cellules | |
|-------------|----------------------|
| Taille | 156 x 156mm |
| Disposition | 60 cellules / 6 x 10 |
| Type | Monocristallin |

| Informations générales | |
|-------------------------------|------------------|
| Tension maximale du système | 1000 V |
| Courant inverse maximum | 17 A |
| Diodes | 3 by-pass |
| Connectique | Connecteurs Tyco |
| Boîte de jonction | IP55 |
| Poids | 19 kg |
| Température de fonctionnement | -40 / +85°C |

| Certifications | |
|----------------|----------------------|
| | IEC 61215 + IEC61730 |

| Garantie | |
|------------------------|--|
| Garantie produit | 10 ans |
| Garantie puissance (*) | 25 ans - 80 % de la puissance minimale 10 ans - 90 % de la puissance minimale |

| Dépendance à l'éclairement | | | |
|----------------------------|-------|-------|-----|
| Éclairement (W/m²) | Pm | Vpm | Ipm |
| 1000 | 1 | 1 | 1 |
| 800 | 0,799 | 0,999 | 0,8 |
| 500 | 0,497 | 0,994 | 0,5 |
| 400 | 0,394 | 0,988 | 0,4 |
| 300 | 0,291 | 0,970 | 0,3 |
| 200 | 0,187 | 0,936 | 0,2 |
| 100 | 0,088 | 0,862 | 0,1 |



ANNEX 2: ADREAM measured PV production data, daily sum

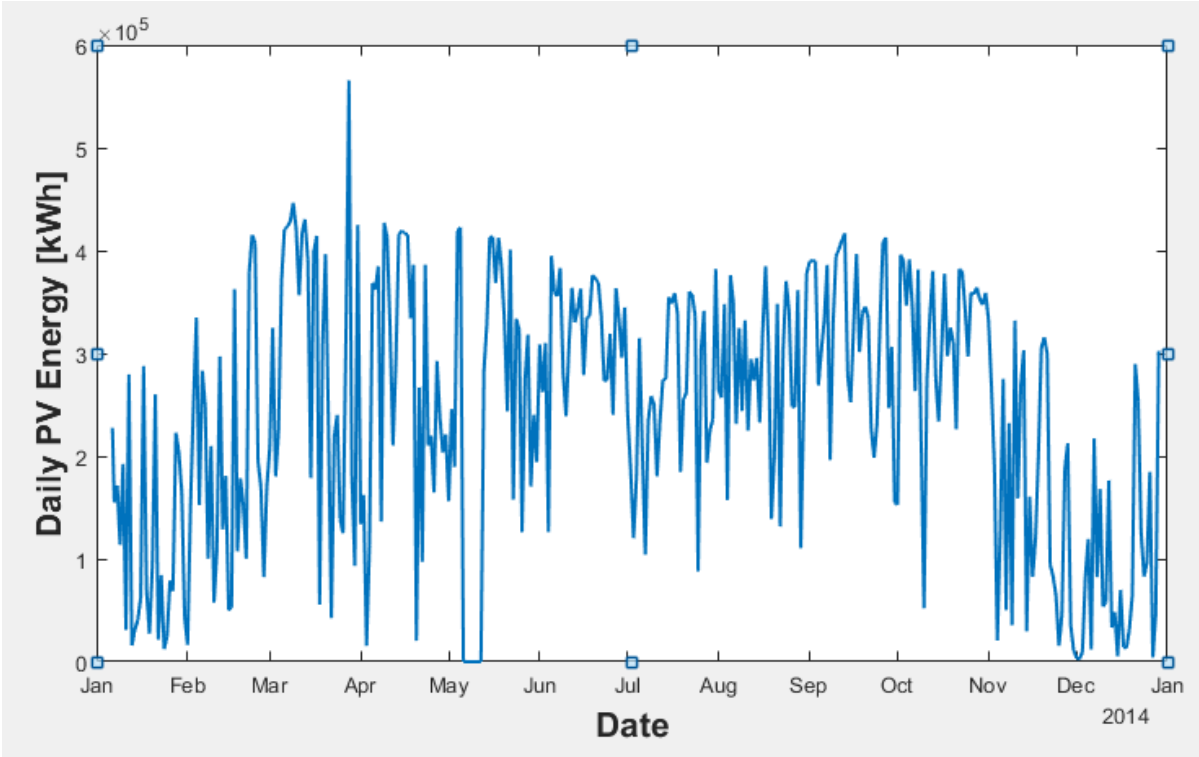


Figure 117: ADREAM's measured PV Energy Production (2014), daily sum

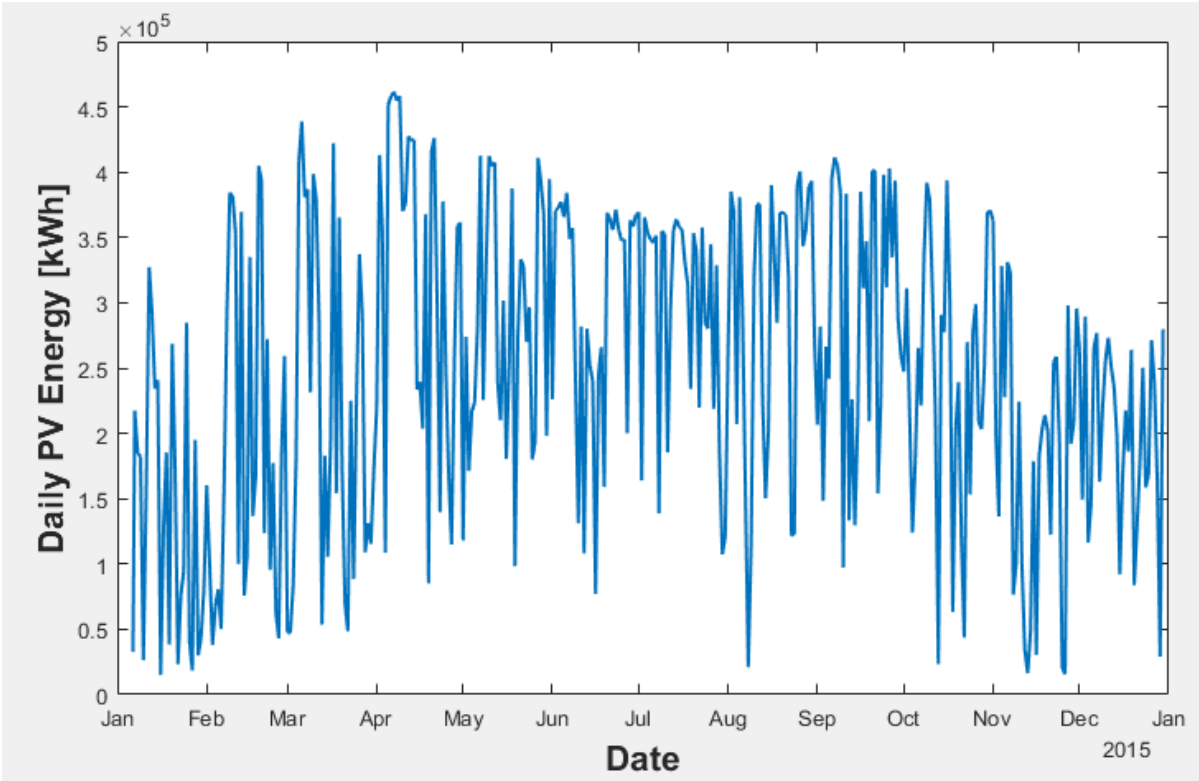


Figure 118: ADREAM's measured PV Energy Production (2015), daily energy sum

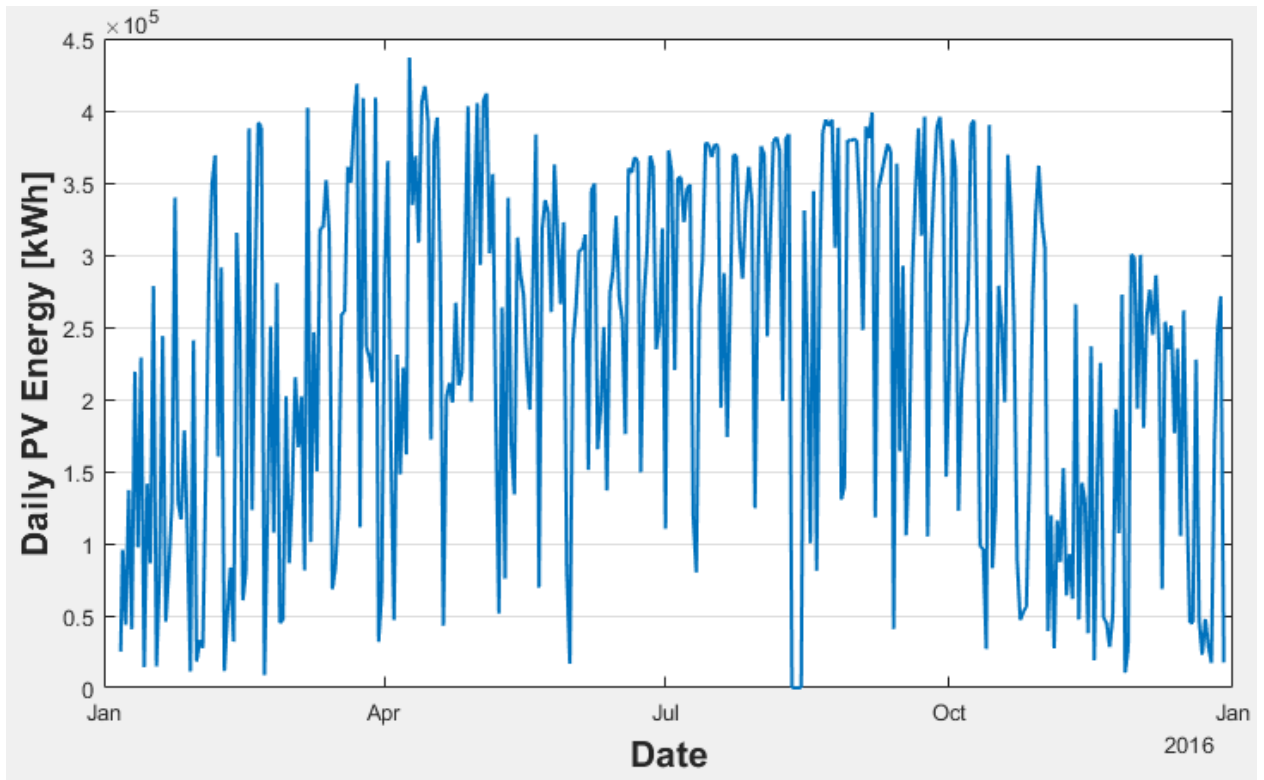


Figure 119: ADREAM's measured PV Energy Production (2016), daily energy sum

ANNEX 3: ADREAM Simulated PV production, daily sum

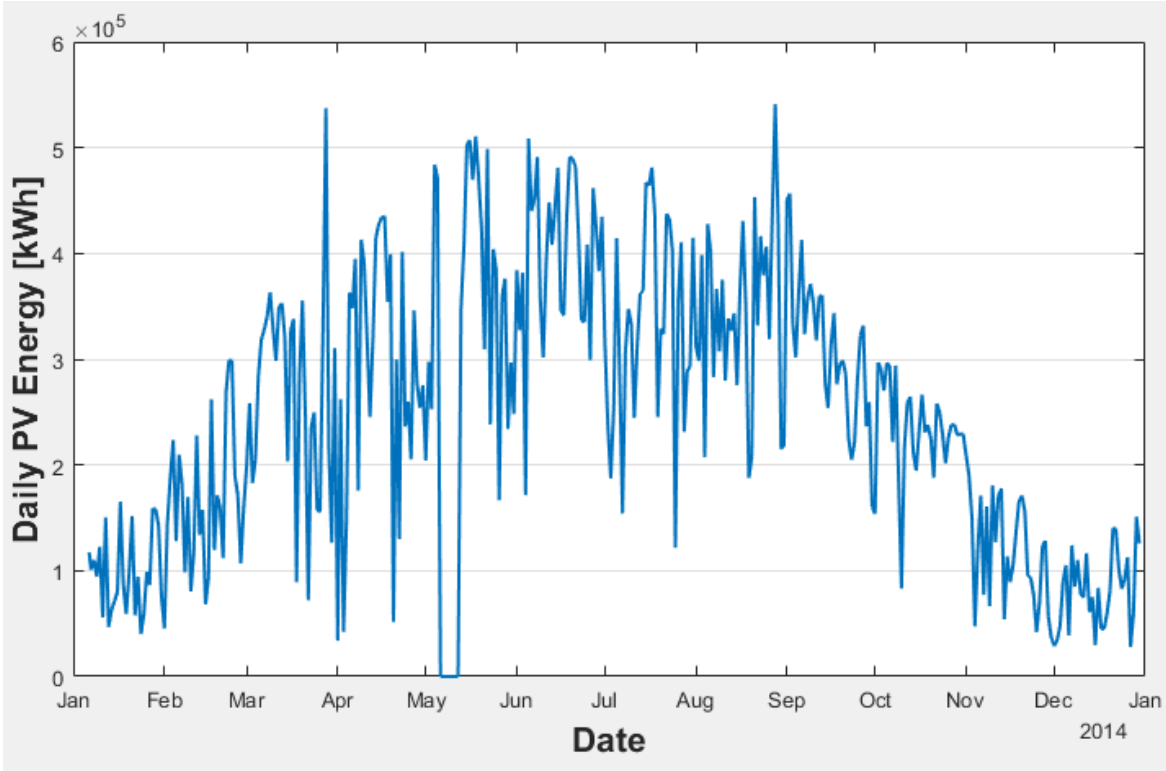


Figure 120: ADREAM's simulated PV Energy Production (2014), daily energy sum

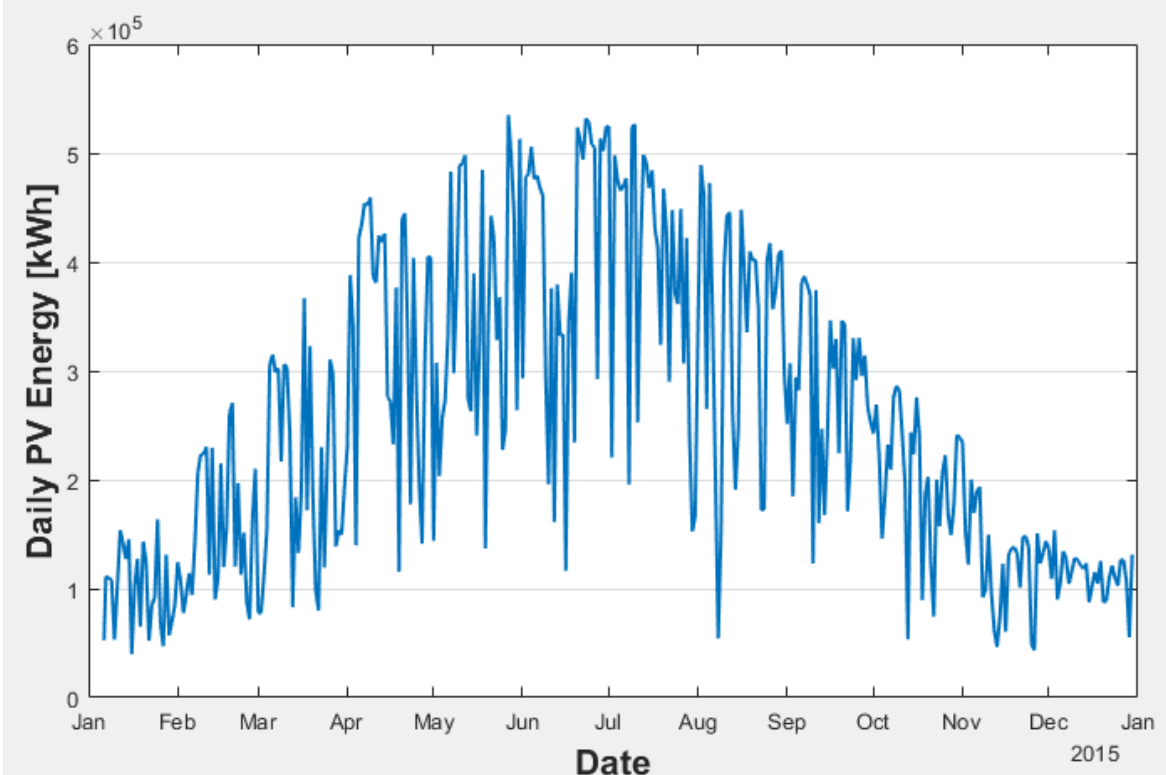


Figure 121: ADREAM's simulated PV Energy Production (2015), daily energy sum

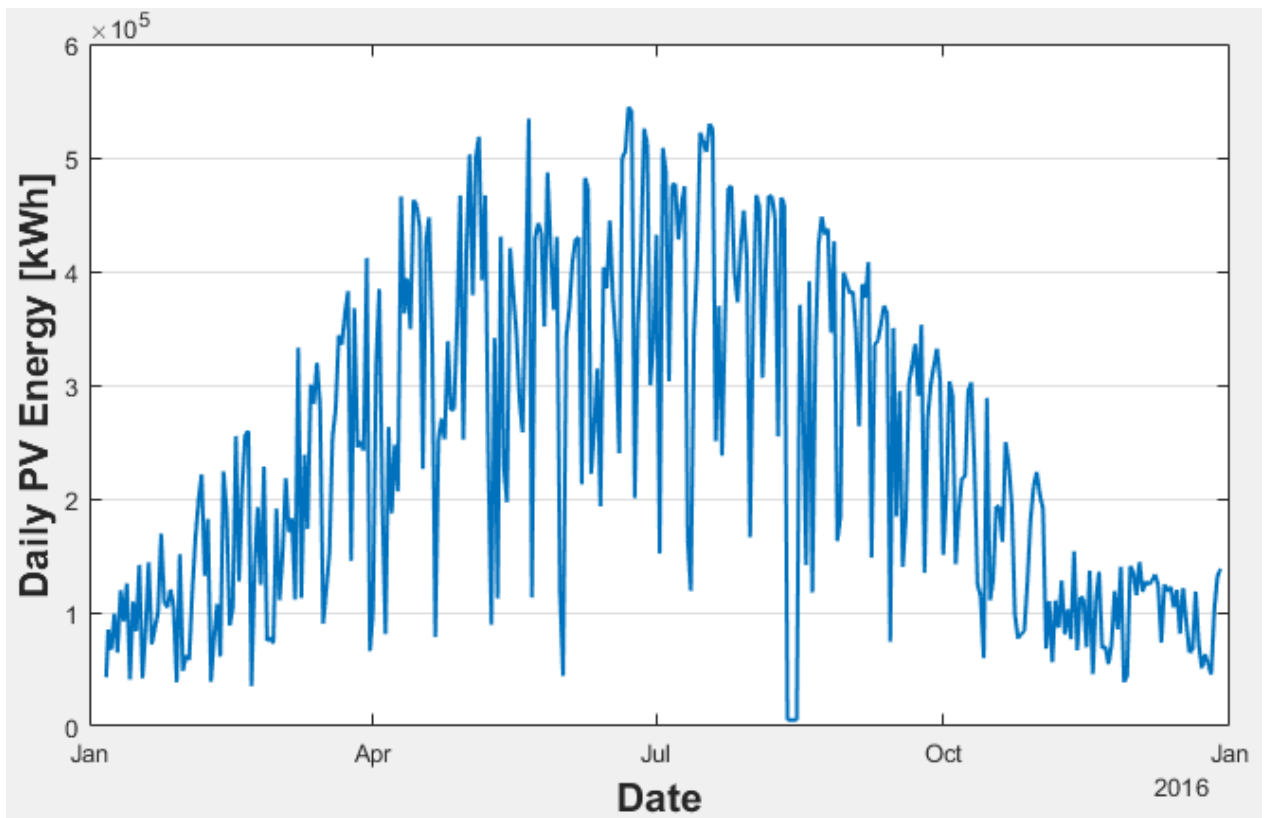





Figure 122: ADREAM's simulated PV Energy Production (2016), daily energy sum

ANNEX 4: BCS-815 battery cycling device specifications

Specifications

MODULES

| |  |  |  |
|-------------------------------|---|--|---|
| Channels | BCS-805 8 | BCS-810 8 | BCS-815 8 |
| Voltage | | | |
| Range | 0 V to 10 V | 0 V to 10 V | 0 V to 9 V |
| Resolution control | 150 μ V | 150 μ V | 150 μ V |
| measurement | 40 μ V (18 bit) | 40 μ V (18 bit) | 40 μ V (18 bit) |
| Accuracy | < ± 0.3 mV $\pm 0.01\%$ of setting | < ± 0.3 mV $\pm 0.01\%$ of setting | < ± 0.3 mV $\pm 0.01\%$ of setting |
| Slew rate | 150 kV/s | 150 kV/s | 150 kV/s |
| Current | | | |
| Max (continuous) per channel | ± 150 mA | ± 1.5 A | ± 15 A |
| Ranges | 5: 100 mA down to 10 μ A | 5: 1 A down to 0.1 mA | 5: 10 A down to 1 mA |
| Resolution control | Down to 800 pA | Down to 8 nA | Down to 80 nA |
| measurement | Down to 0.2 nA (18 bit) | Down to 2 nA (18 bit) | Down to 20 nA (18 bit) |
| Accuracy | < 0.05% of FSR $\pm 0.01\%$ of setting | < 0.05% of FSR $\pm 0.01\%$ of setting | < 0.5% of FSR $\pm 0.01\%$ of setting (10 A range) < 0.05% of FSR $\pm 0.01\%$ of setting (others) |
| Parallel ability | no | no | Yes Up to ± 120 A with 8 channels |
| EIS | | | |
| Built-in | On each module | On each module | On each module |
| Range | 10 kHz - 10 mHz | 10 kHz - 10 mHz | 10 kHz - 10 mHz |
| Measurement | | | |
| Acquisition time | 2 ms | 2 ms | 2 ms |
| Time base | 2 ms | 2 ms | 2 ms |
| Additional measurement | | | |
| Thermocouple | NA | K Type on each channel -25 $^{\circ}$ C +200 $^{\circ}$ C with accuracy of ± 2 $^{\circ}$ C | K Type on each channel -25 $^{\circ}$ C +200 $^{\circ}$ C with accuracy of ± 2 $^{\circ}$ C |
| Analog in | 1 (18 bit) on each module | 1 (18 bit) on each module | 1 (18 bit) on each module |
| Analog out | 1 (16 bit) on each module | 1 (16 bit) on each module | 1 (16 bit) on each module |
| Cell connection | | | |
| | 4 terminal leads + Guard | 4 terminal leads + Guard | 4 terminal leads |
| General | | | |
| Height | 1U | 2U | 4U |
| Weight | 5 kg | 10 kg | 23 kg |
| Power consumption | 60 W | 220 W | 1700 W |

* FSR: Full Scale Range

Pictures and specifications subject to change.

Specifications given with 2.5 m cell cable.

Cabinets of 38U, 24U, 12U and 6U are available.

ANNEX 5: datasheet of ENIX and PHET LFP cells

Battery specification / Fiche technique



18650 LIFEPO4 BATTERY 1500mAh 3.2V

Part No: ACL9011

TECHNICAL SPECIFICATIONS / CARACTÉRISTIQUES TECHNIQUES

| | | |
|-------------------------------|-------------------------------|---|
| BRAND NAME | MARQUE | ENIX |
| TECHNOLOGY | TECHNOLOGIE | Lithium Iron Phosphate |
| VOLTAGE | TENSION | 3.2V |
| DIMENSION | DIMENSION | 18.2 (Ø) x 64.8 (H) mm |
| WEIGHT | POIDS | 42g Approx. |
| STANDARD CAPACITY | CAPACITE STANDARD | 1550mAh - 0.5C (current value of 1500mA at 1C*) |
| CAPACITY RANGE | GAMME DE CAPACITE | 1450~1550mAh |
| CHARGE VOLTAGE | TENSION DE CHARGE | 4.2 ± 0.05 V |
| NOMINAL VOLTAGE | TENSION NOMINALE | 3.2V |
| ALTERNATING INTERNAL | RÉSISTANCE INTERNE | ≤80mΩ |
| DISCHARGE CUT-OFF VOLTAGE | TENSION DE COUPURE (DÉCHARGE) | 2.5V |
| CUT-OFF VOLTAGE | TENSION DE COUPURE (CHARGE) | 3.65±0.05V |
| CUT-OFF CURRENT | COURANT DE COUPURE | 0.01C |
| CYCLE CHARACTERISTIC | NOMBRE DE CYCLES MAX. | 2000 times |
| MAX.CONTINUOUS DISCH. CURRENT | COURANT DE DÉCHARGE MAX. | 4.5A |
| PULSE DISCHARGE CURRENT | COURANT DE POINTE MAX. | 10A, 5s |
| WORKING TEMPERATURE | TEMPÉRATURE DE FONCTIONNEMENT | Charge: 0 ~ 55°C Discharges: -20°C ~ 60°C |
| STORAGE TEMPERATURE | TEMPÉRATURE DE STOCKAGE | -20°C ~ 45°C |



PRODUCT DESCRIPTION / DESCRIPTION DU PRODUIT

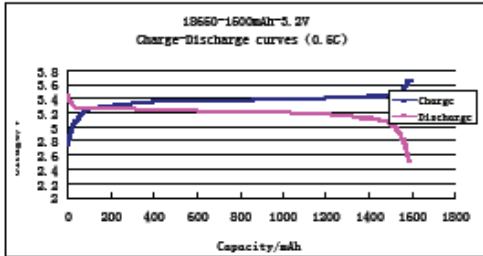
R: Quelques recommandations et précautions d'usages :

- Ne jamais essayer d'ouvrir un accumulateur,
- Ne pas jeter et suivre impérativement la procédure de recyclage,
- Ne pas exposer au feu, Ne pas percer,
- Ne pas effectuer de brasure à l'étain directement sur l'élément,
- Ne jamais assembler d'élément,
- Ne pas écraser,
- Ne jamais mettre le ou les éléments en court-circuit,
- Charger avec un chargeur adéquat et recommandé par nos soins,
- Bien respecter les courants de décharge.

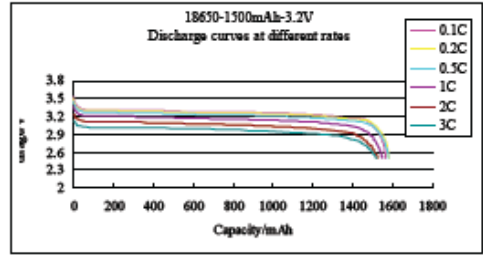
IK: Usage guidelines:

- Never try to open a battery
- Do not throw away, you must follow recycling procedure
- Do not burn
- Do not pierce
- Do not solder directly on cells
- Do not join cells
- Do not crush
- Do not short circuit
- Charge with an appropriate charger
- Respect discharge currents

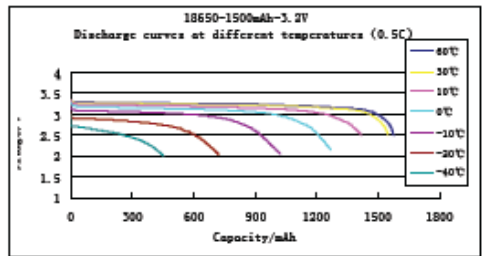
CHARGE/ DISCHARGE CURVES (0.5°C)
 COURBES DE CHARGE/DÉCHARGE (0.5°C)



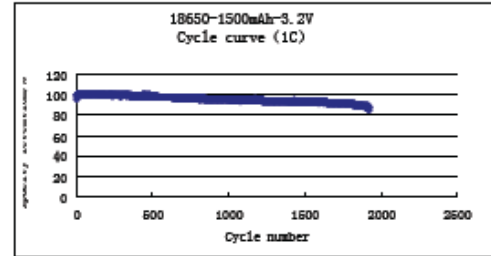
DISCHARGE CURVES AT DIFFERENT RATES
 COURBES DE DÉCHARGE À DIFFÉRENTS TAUX



DISCHARGE CURVES AT DIFFERENT TEMPERATURES 0.5°C
 COURBES DE DÉCHARGE À DIFFÉRENTES TEMPÉRATURE 0.5°C



CYCLE CURVE (1C CHARGE/10C DISCHARGE)
 COURBE DE CYCLE (1C CHARGE/10C DÉCHARGE)



ANNEX6: Complete results for the automatic characterization using ZFitGUI

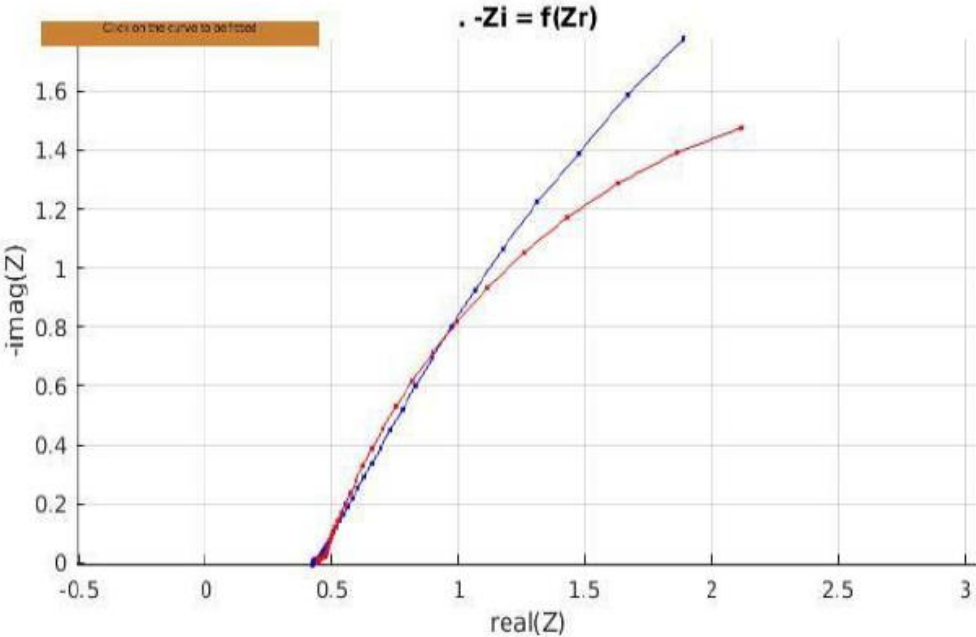


Figure 123: Results for the automated characterization of the complex impedance at 1.45V, using ZFitGUI

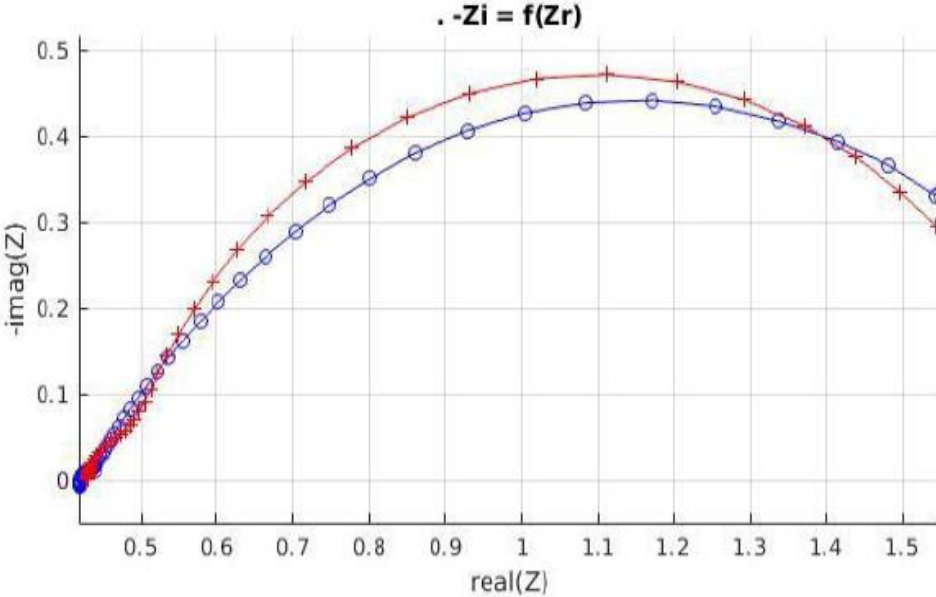


Figure 124: Results for the automated characterization of the complex impedance at 1.5V, using ZFitGUI

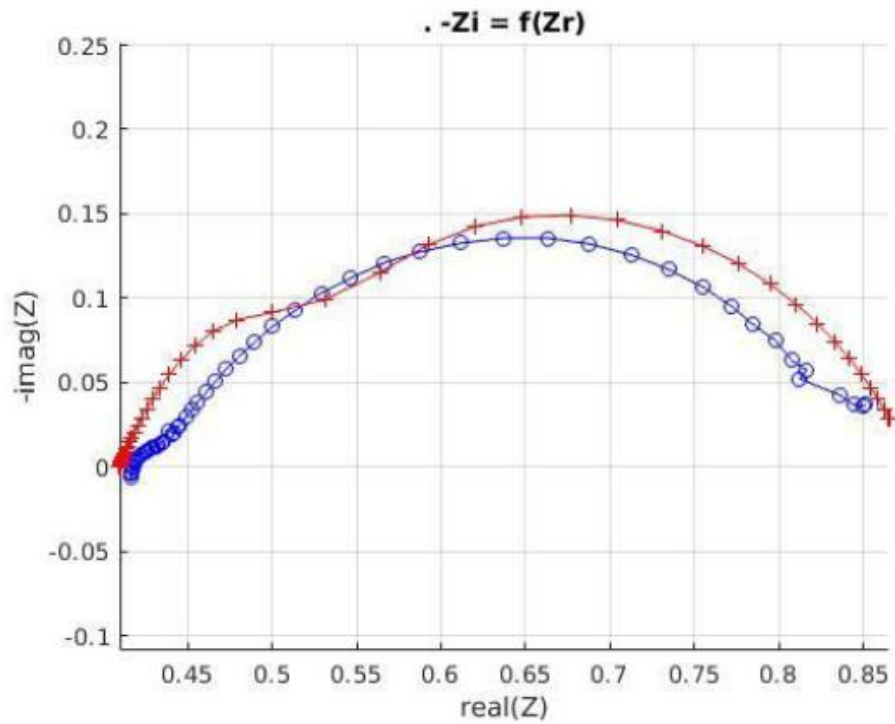


Figure 125: Results for the automated characterization of the complex impedance at 1.55V, using ZFitGUI

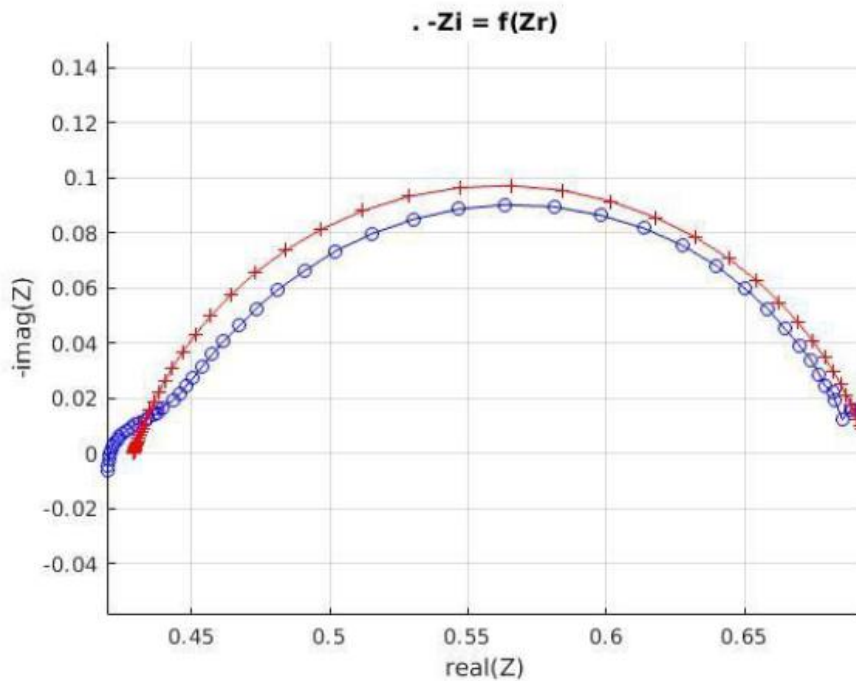


Figure 126: Results for the automated characterization of the complex impedance at 1.6V, using ZFitGUI

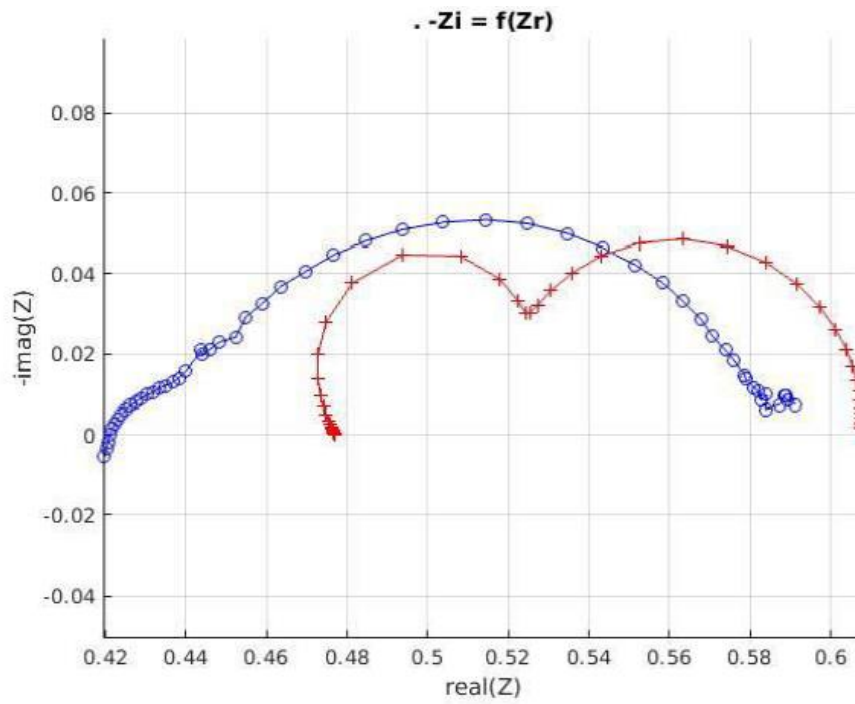


Figure 127: Results for the automated characterization of the complex impedance at 1.65V, using ZFitGUI

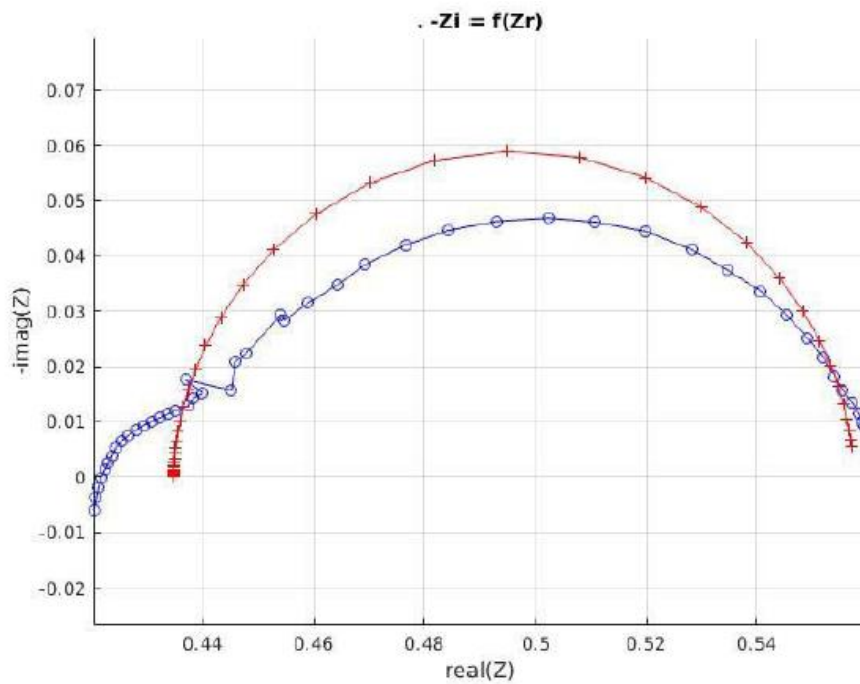


Figure 128: Results for the automated characterization of the complex impedance at 1.675V, using ZFitGUI

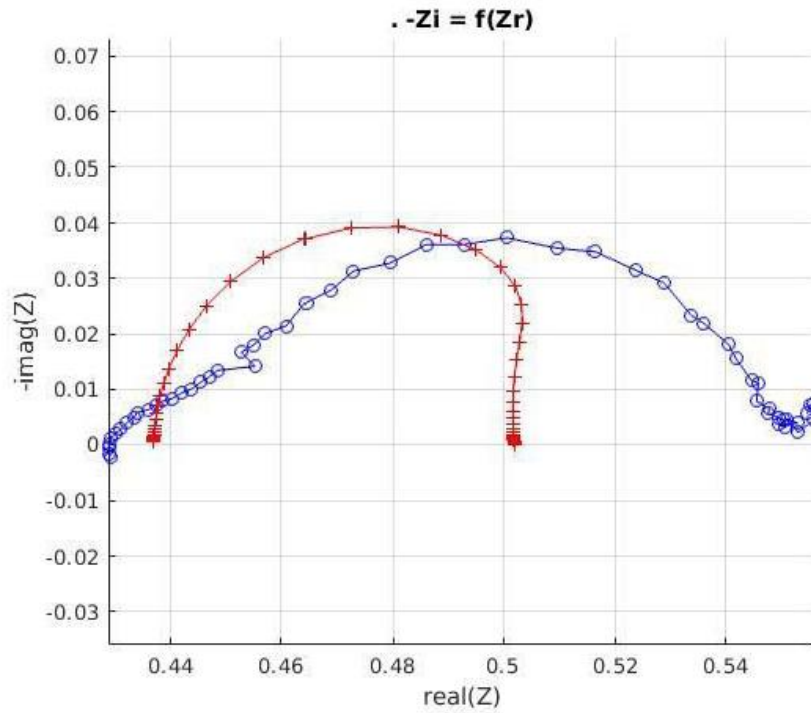


Figure 129: Results for the automated characterization of the complex impedance at 1.7V, using ZFitGUI

Tableau 1: Model parameters identified through automated characterization using ZFitGUI

| Tension (V) | Rs (Ohms) | Rp1 (Ohms) | P1 (Sans unité) | P2 (Sans unité) | Rp2 (Ohms) | P3 (Sans unité) | P4 (Sans unité) |
|-------------|-----------|------------|-----------------|-----------------|------------|-----------------|-----------------|
| 1.45 | 0.4441 | 0.01760 | 0.0139 | 1.147 | 4.589 | 0.4589 | 0.7602 |
| 1.50 | 0.4286 | 0.04983 | 0.08411 | 0.9470 | 1.243 | 0.3671 | 0.8269 |
| 1.55 | 0.4097 | 0.03478 | 3.693e-4 | 2.862 | 0.4336 | 0.2477 | 0.7743 |
| 1.60 | 0.4290 | 0.03134 | 2.522 | 0.8041 | 0.2353 | 0.1976 | 0.8087 |
| 1.65 | 0.4769 | 0.04064 | 6.892e-3 | 1.3800 | 0.09022 | 0.3149 | 1.031 |
| 1.675 | 0.4779 | -0.04342 | 0.0325 | -4.007 | 0.1232 | 0.09459 | 0.9720 |
| 1.70 | 0.5019 | 0.01097 | 0.1167 | 1.1290 | -0.0760 | 0.1471 | 1.012 |

Annex 7: Complete results for the manual characterization using ZFitGUI

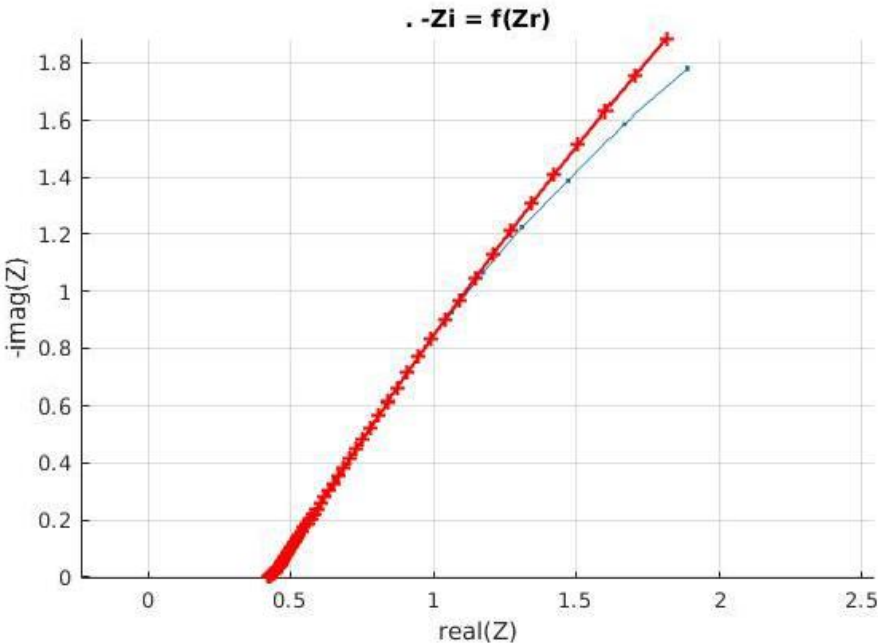


Figure 130: Results for the manual characterization of the complex impedance at 1.45V, using ZFitGUI

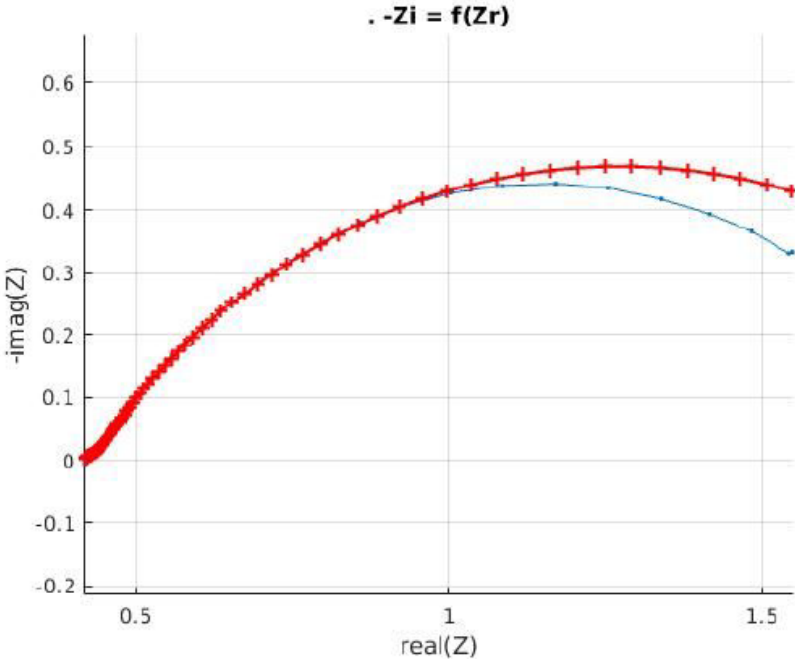


Figure 131: Results for the manual characterization of the complex impedance at 1.5V, using ZFitGUI

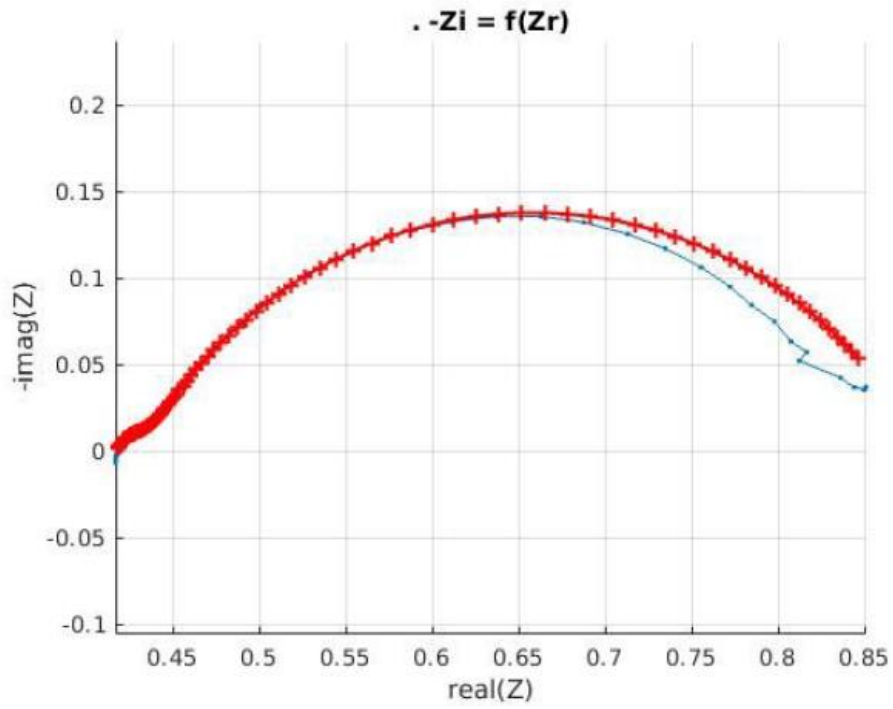


Figure 132: Results for the manual characterization of the complex impedance at 1.55V, using ZFitGUI

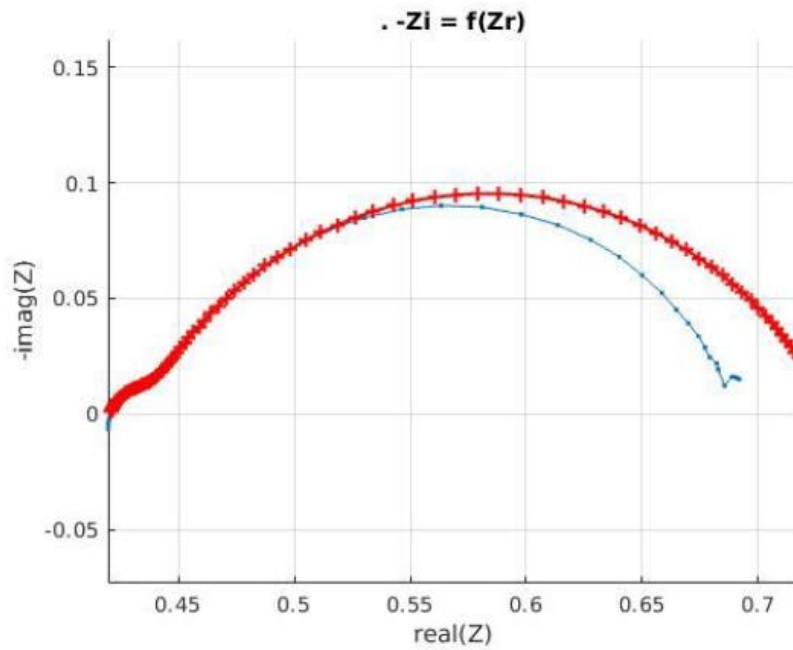


Figure 133: Results for the manual characterization of the complex impedance at 1.6V, using ZFitGUI

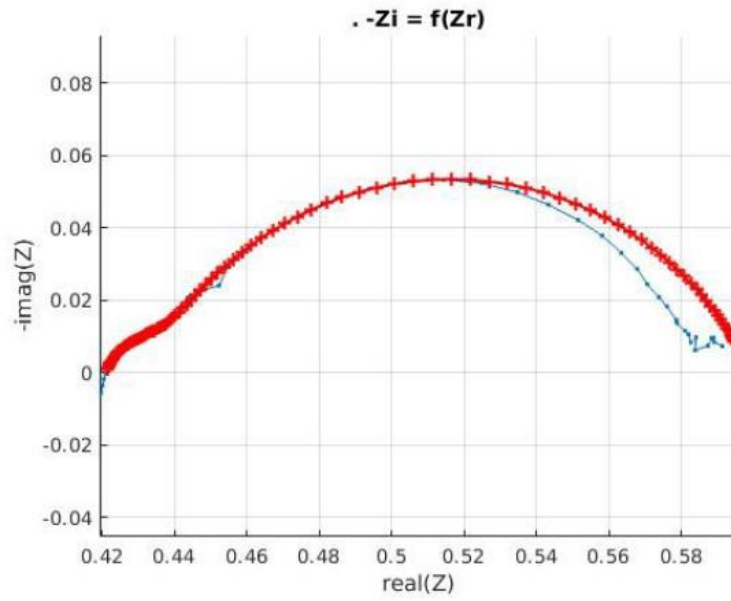


Figure 134: Results for the manual characterization of the complex impedance at 1.65V, using ZFitGUI

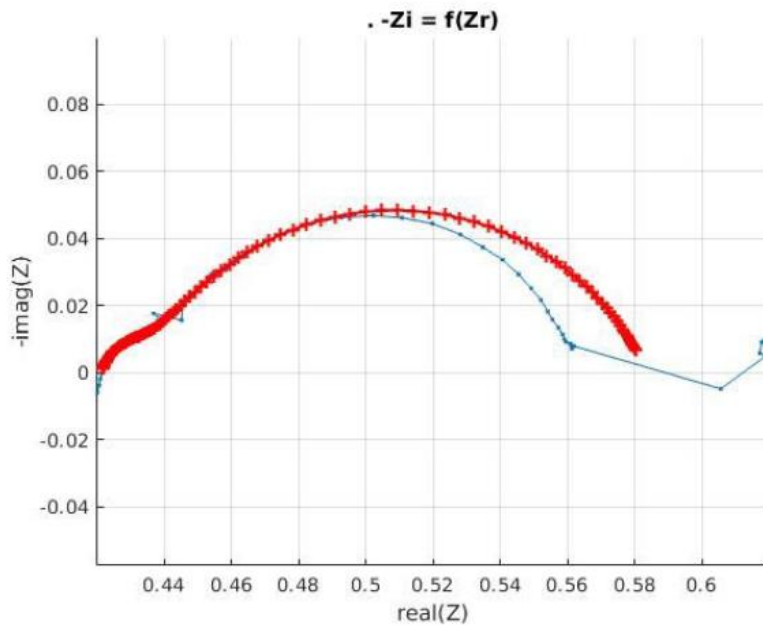


Figure 135: Results for the manual characterization of the complex impedance at 1.675V, using ZFitGUI

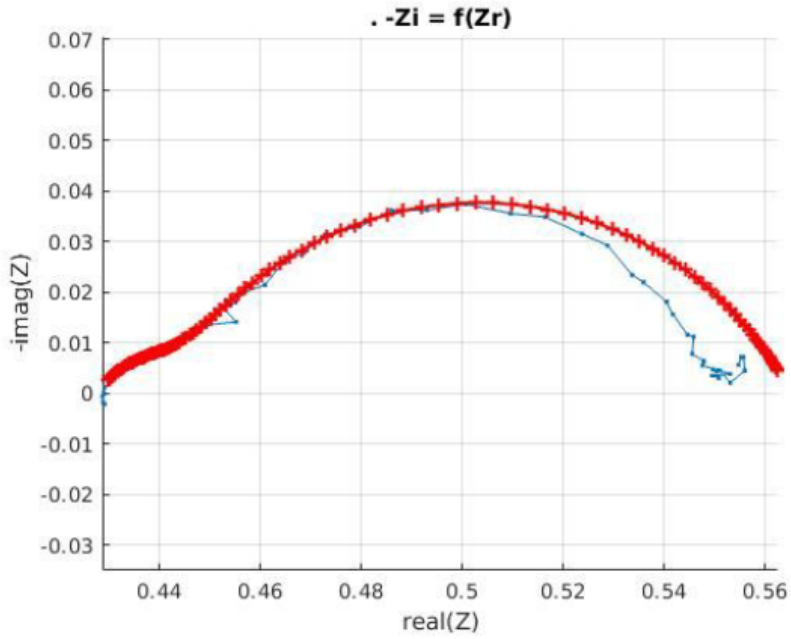


Figure 136: Results for the manual characterization of the complex impedance at 1.7V, using ZFitGUI

| Tension (V) | Rs (Ohms) | Rp1 (Ohms) | P1 (Sans unité) | P2 (Sans unité) | Rp2 (Ohms) | P3 (Sans unité) | P4 (Sans unité) |
|-------------|-----------|------------|-----------------|-----------------|------------|-----------------|-----------------|
| 1.45 | 0.4238 | 0.0187 | 0.064 | 0.80 | 9.20 | 0.52 | 0.71 |
| 1.50 | 0.4192 | 0.0187 | 0.040 | 0.80 | 1.40 | 0.35 | 0.72 |
| 1.55 | 0.4175 | 0.0187 | 0.038 | 0.80 | 0.414 | 0.25 | 0.74 |
| 1.60 | 0.4203 | 0.0187 | 0.035 | 0.80 | 0.252 | 0.15 | 0.79 |
| 1.65 | 0.4210 | 0.0187 | 0.0200 | 0.80 | 0.145 | 0.10 | 0.79 |
| 1.675 | 0.4210 | 0.0187 | 0.0130 | 0.80 | 0.124 | 0.05 | 0.81 |
| 1.70 | 0.4288 | 0.0187 | 0.0840 | 0.66 | 0.102 | 0.15 | 0.79 |

Annex 8: Complete results for the manual characterization using SpecificFit

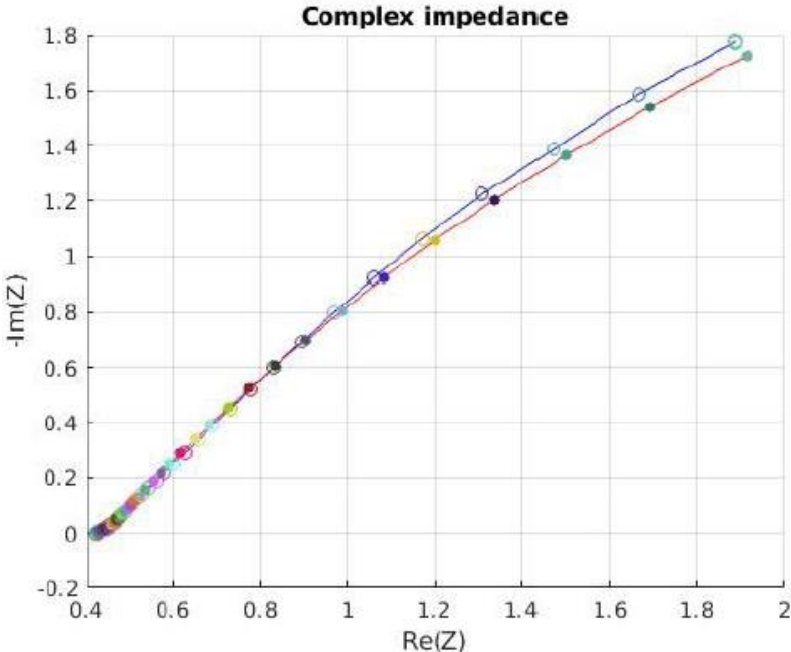


Figure 137: Results for the manual characterization of the complex impedance at 1.45V, using SpecificFit

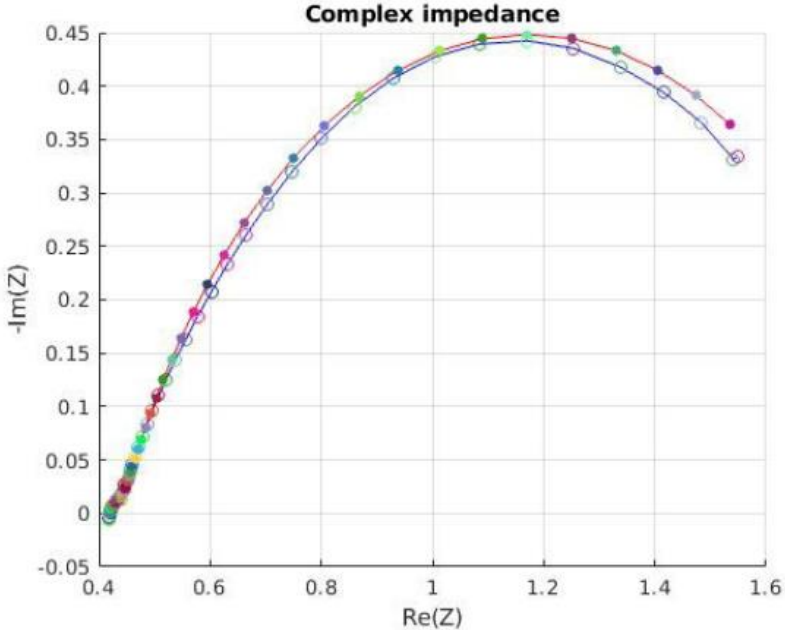


Figure 138: Results for the manual characterization of the complex impedance at 1.5V, using SpecificFit

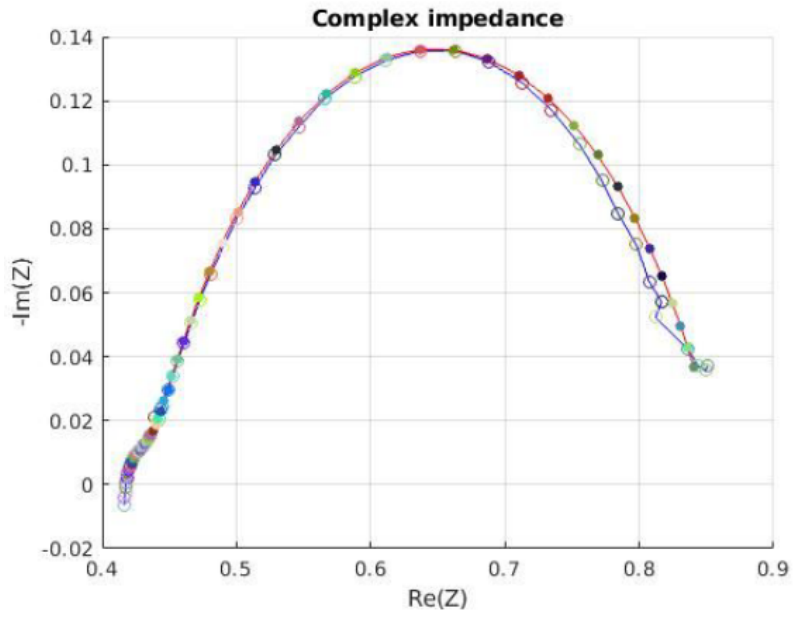


Figure 139: Results for the manual characterization of the complex impedance at 1.55V, using SpecificFit

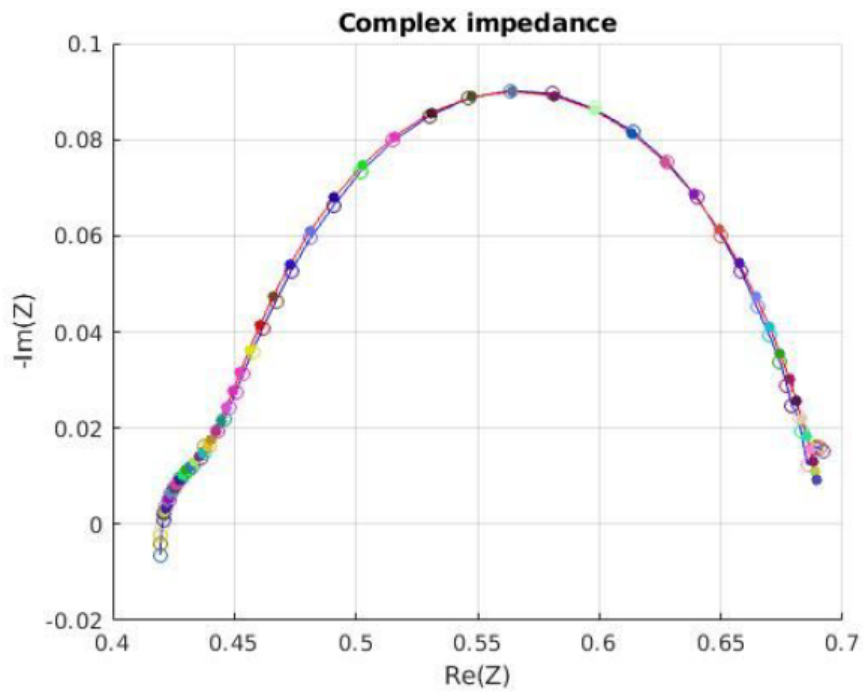


Figure 140: Results for the manual characterization of the complex impedance at 1.6V, using SpecificFit

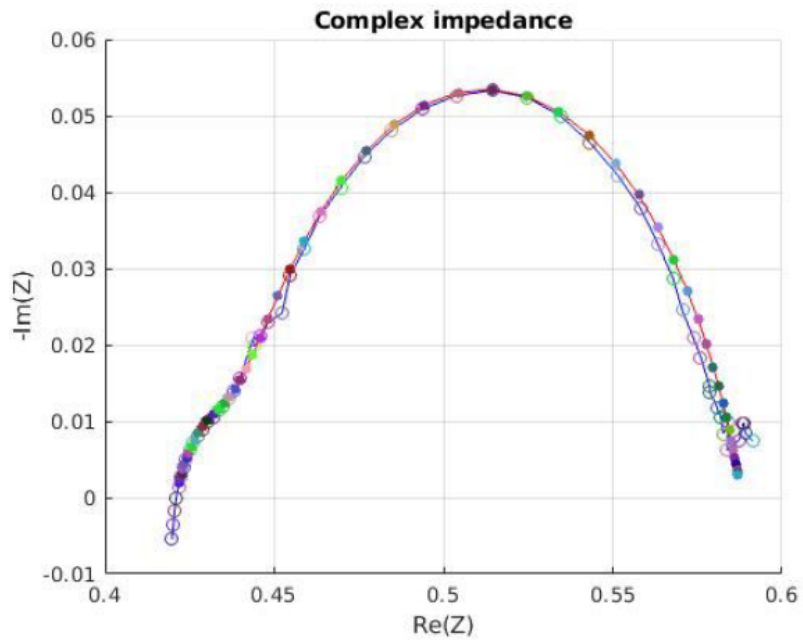


Figure 141: Results for the manual characterization of the complex impedance at 1.65V, using SpecificFit

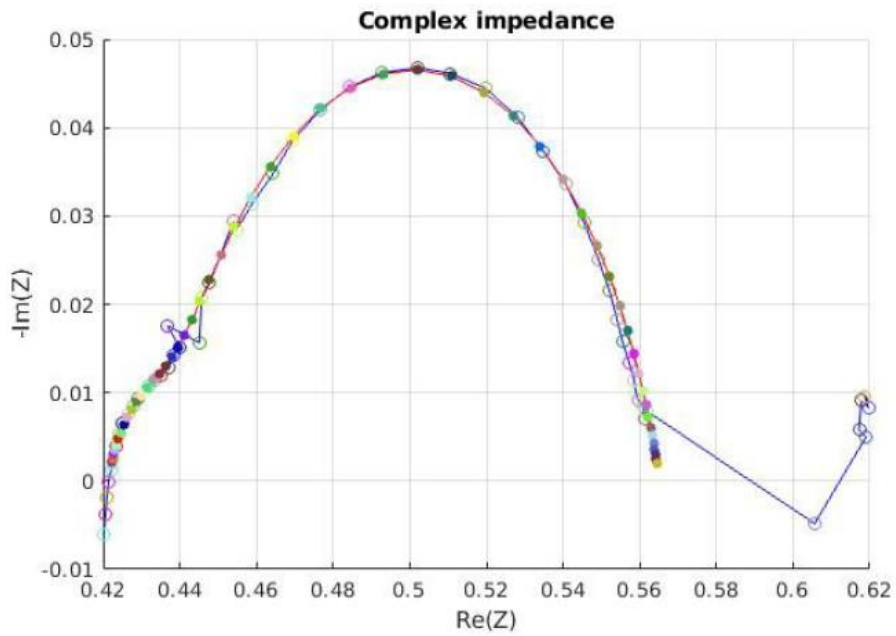


Figure 142: Results for the manual characterization of the complex impedance at 1.675V, using SpecificFit

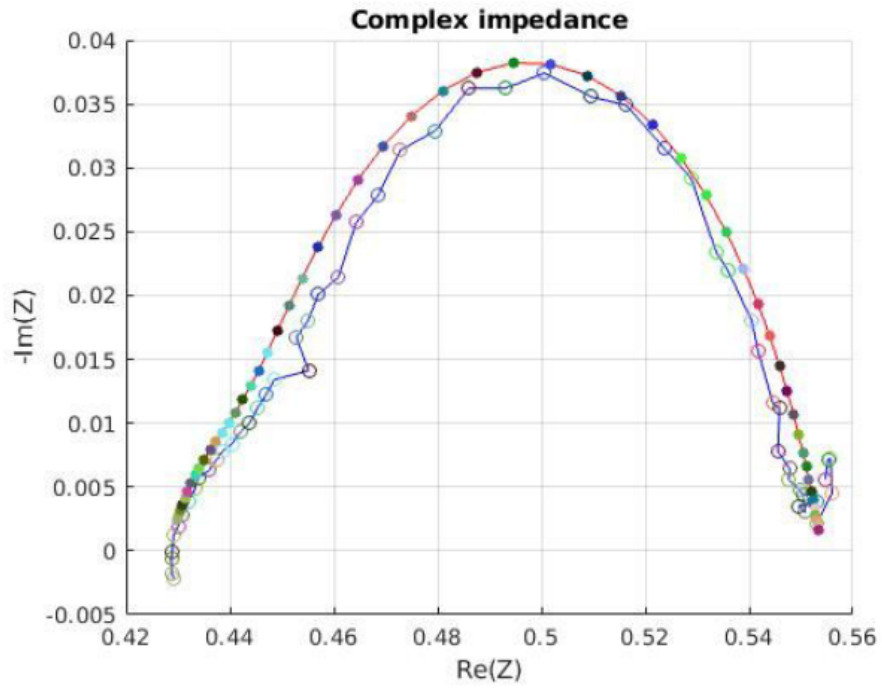


Figure 143: Results for the manual characterization of the complex impedance at 1.7V, using SpecificFit

Annex 9: Relations between parameters and supply voltage

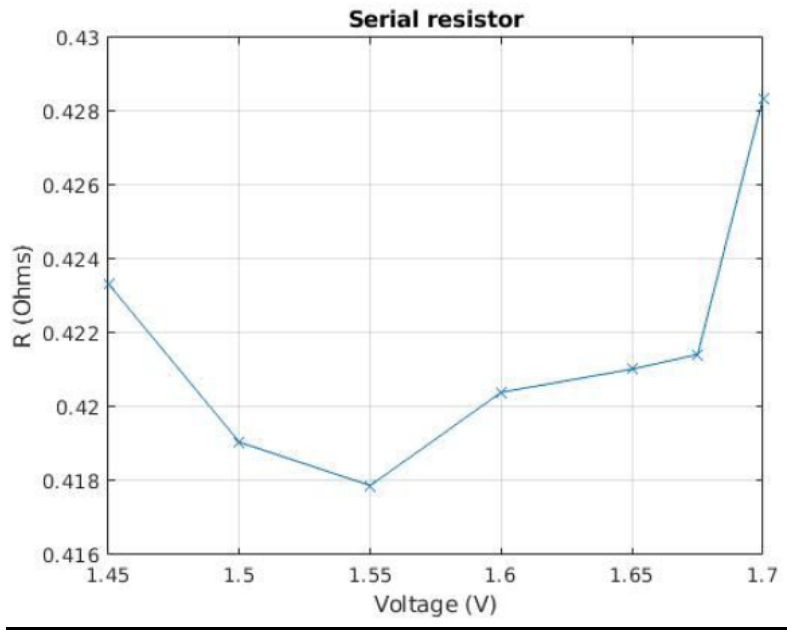


Figure 144: Relation between the series resistor and the supply voltage for the H-Tec cell

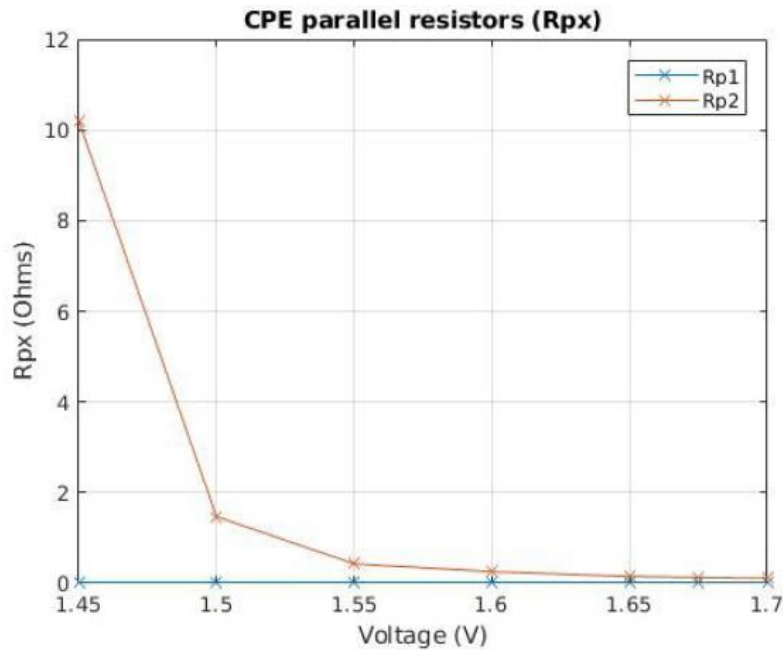


Figure 145: Relation between the parallel resistor Rp1 and the supply voltage for the H-Tec cell

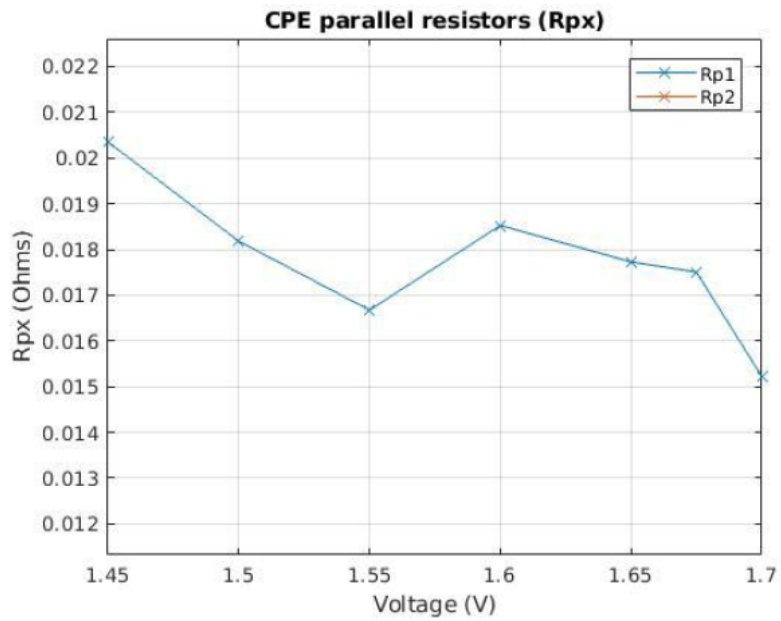


Figure 146: Relation between the parallel resistor Rp2 and the supply voltage for the H-Tec cell

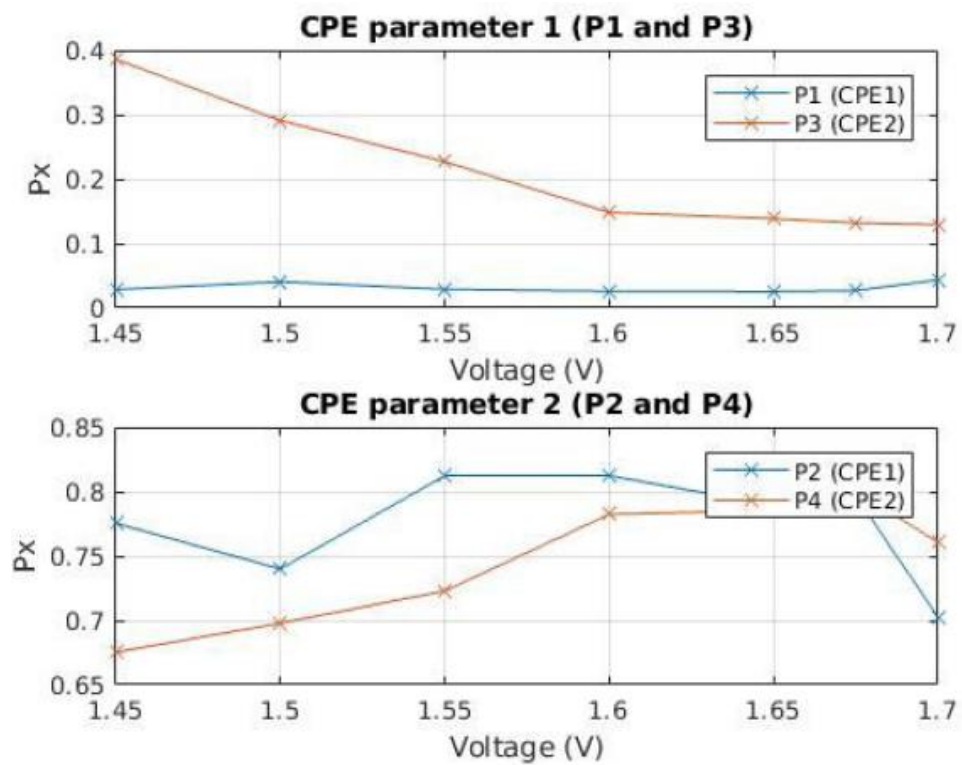
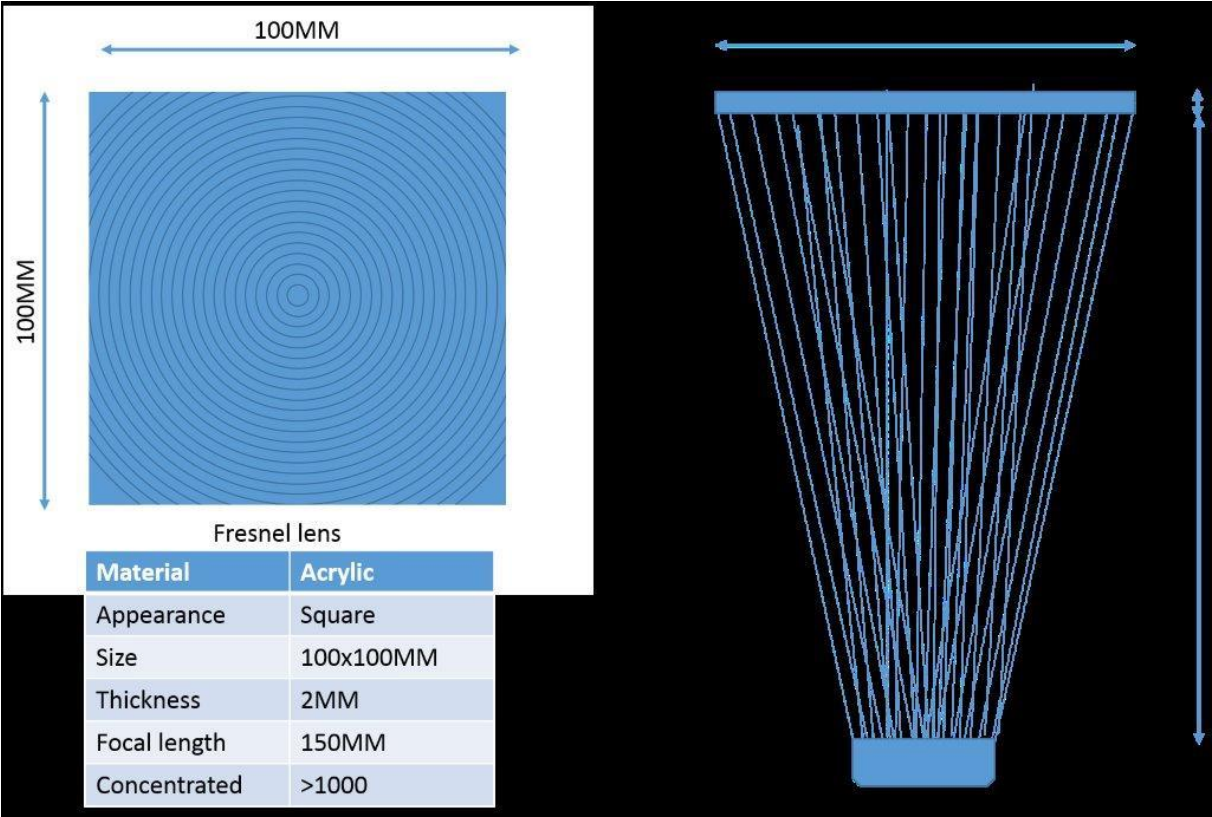


Figure 147: Relation between the CPE element parameters P1, P2, P3, P4 and the supply voltage for the H-Tec cell

ANNEX 10: Characteristics of the Fresnel lens



The diagram illustrates the physical characteristics and optical function of a Fresnel lens. On the left, a square lens with a 100MM side length is shown, featuring concentric circular ridges. On the right, a perspective view shows parallel light rays entering from the top and being focused into a small, concentrated spot at the bottom. A table below the lens image lists its material, appearance, size, thickness, focal length, and concentration.

Fresnel lens

| Material | Acrylic |
|--------------|-----------|
| Appearance | Square |
| Size | 100x100MM |
| Thickness | 2MM |
| Focal length | 150MM |
| Concentrated | >1000 |

ANNEX 11: Solar tracker motor specifications

| Mechanical Capabilities | |
|---|---|
| Number of turning axis | Dual-Axis |
| Hour Angle Limit | 100°, software and hardware limit 50°E to 50°W |
| Elevation angle | 15 - 90°, adjustable start |
| Type of hour-angle motor | Linear Motor SM4S510M2 with stroke of 510 mm |
| Type of elevation-angle motor | Linear Motor SM4S510M2 with stroke of 510 mm |
| Hour-angle shaft diameter and length | Ø48 mm, L=1400 mm (steel) |
| Backstructure size | 2 pcs of 1000 (H) mm & 4 pcs of 1000 (V) mm |
| Type of backstructure clamp | Toothed scissors grippers - 8 pcs |
| Tube diameter for mounting | Ø60 - 68 mm (not included with kit) |
| Max. dimensions of a solar panel | 2 pieces of 0,99 m x 1,65 m in total 3,3 m2 |
| Max. weight of a solar panel | 2 pcs per 20 kg |
| Estimated service life | 800-1000h of motor operation (DC motor replace on 8 years if each day one cycle), backup battery replace on 3-5 years if battery in, all other 25 years |
| Positioning System Data | |
| Tracking accuracy | <0.5° (optionally <0.1° - for additional payment) |
| Operating Protocol | TdAPS (Time derived Astronomical Positioning System) |
| Type of Positioning System | Servo driver positioner with TdAPS arc logic function calc. |
| Type of positioner | Din Rail positioner MICRO and exterior cables |
| Type of timer | GMT clock with EOT and calendar |
| Type of application program for supervision and setting | Solar tracking system monitor via web site |
| Setting and changing data via PC | Yes |
| Monitoring possibility via PC | Yes |
| Turned on the position sent from PC | Yes, it turn on position sent from PC, also all other setting can be commanded with string sent from PC |
| Turning time interval | 1min. - 15min. |
| Communication Data | |
| Type of communication interface | USB interface |
| Networking solution for control from centre | RS485 |
| Firmware - Software | |
| Upgrading possibility via PC | Yes, firmware via PC with help of Helios Analytics |
| Electrical Data | |
| Motor Power Supply | 24 VDC ± 15% (2.5A current capacity) SMPS must have 150% inrush current |
| Backup battery | CR 2512 coin |
| Standby consumption (when is not moving) | 20 mA ± 25% @ 24VDC |
| Power supply connection | 1 piece of 2 Wire Cable with an Internal Cu Conductor of 1.0mm2 (not included with kit) |
| Junction Box | 190 (L) x 140 (W) x 70 (H) mm with connection harness |
| Environmental Data | |
| Operating temperature | -25°C to +70°C (optionally with artic grease for temperatures from -40°C up to +70°C) |
| Operation at humidity | 0% to 100%, relative humidity |
| Max. safe wind speed | max. 144 km/h |
| Corrosion, weather and chemical resistance | |
| Hot-dip galvanizing (HDG, EN ISO 1461) | 75-100 m (equivalent of 50 years) |
| Packaging | |
| Dimensions of a packed product | 1 box of 165 (L) x 22 (W) x 27 (H) cm |
| Product weight | 41 kg |
| Quality Certificates | |
| International Protection Rating (IEC 60529) | IP63 |
| Electromagnetic Compatibility (EMC Directive 89/336/EEC) | Yes |
| Low Voltage Equipment Directive (EEC Council Directive 73/23/EEC) | Yes |
| Optional Properties | |
| Anti-Shadowing Function | Yes, included |
| HelioStat usage | Yes, for additional payment |

